HIGH THROUGHPUT STUDY OF FUEL CELL PROTON EXCHANGE MEMBRANES: POLY(VINYLIDENE FLUORIDE)/ACRYLIC POLYELECTROLYTE BLENDS AND NANOCOMPOSITES WITH ZIRCONIUM

A Thesis

Presented to

The Academic Faculty

By

Pedro José Zapata B.

In Partial Fulfillment

of the Requirements for the Degree

Doctor of Philosophy in the

School of Chemical and Biomolecular Engineering

Georgia Institute of Technology

May 2009

HIGH THROUGHPUT STUDY OF FUEL CELL PROTON EXCHANGE MEMBRANES: POLY(VINYLIDENE FLUORIDE)/ACRYLIC POLYELECTROLYTE BLENDS AND NANOCOMPOSITES WITH ZIRCONIUM

Approved by:

Dr. Carson Meredith, Advisor
School of Chemical and Biomolecular Engineering
Georgia Institute of Technology

Dr. Tom Fuller
School of Chemical and Biomolecular Engineering
Georgia Institute of Technology

Dr. William Koros
School of Chemical and Biomolecular Engineering
Georgia Institute of Technology

Dr. F. Joseph Schork
School of Chemical and Biomolecular Engineering
University of Maryland

Dr. David Mountz
Arkema, Inc.

Date Approved: March 25th, 2009

“Research is what I’m doing when I don’t know what I’m doing”

- Werner von Braun

Acknowledgements

It happened once and I said it would not happen again if I ever pursue another graduate degree … yet, here I am at the very last minute writing one of the hardest sections of this work. Maybe this is because I received help from others until the end, and I wanted to make sure I acknowledge their contributions; maybe is because I was purposely trying to avoid this section because I simply did not know what to write; or maybe is just because it happened that I was also writing all the other sections at this very last minute … . Regardless of whichever is the case, my whole graduate experience at GeorgiaTech has been an incredible journey of growing and learning, not only intellectually, but also personally; and for this there are many people I am grateful with.

First of all I would like to express my deepest gratitude to my advisor Dr. J. Carson Meredith, whose impressive broad-ranging knowledge is hardly matched, for his guidance and unwavering support. Thank you for your incessant motivation to never stop learning and especially for your infinite patience during all these years.

I would like to thank Dr. Tom Fuller, Dr. William Koros, Dr. Joseph Schork, and Dr. David Mountz for volunteering to serve in my thesis committee and offering valuable suggestions in the course of this work. I would also like to thank Arkema Inc. for providing financial support and materials.

To the Meredith Research group thank you for all the help … and making me complain about something every single time I entered the lab. I would specially like to thank Dr. Jing Su for all the wealth of knowledge shared about science, life, and philosophy; his impressive logical thinking is only matched by his extraordinary programming skills. I would also like to thank JungHyun Lee for all his help during the last stages of my research. To Keith Reed thanks for all the laughs and entertainment. To the entire group, my most sincere wishes that you have unimpeded progress to successful careers and lives.

My most special gratitude goes to my parents. Mis más profundos agradecimientos son para mis padres por haberme inculcado la importancia de los valores y la educación; y quienes me enseñaron que, sin importar las circunstancias, siempre hay que trabajar duro para alcanzar metas e ideales. Este logro es resultado de aquellas enseñanzas y sabios consejos. A Gladys, gracias por ser una segunda madre y por tu infinita paciencia durante todos estos años. To my brother Camilo, who is a role-model of hard-work, determination, and values that I strive to emulate; thank you for your wise advices and limitless support and motivation. Finally I would like to thank Hélène for her encouragement and endless motivation, for listening, for understanding, and for being an incredible source of strength and inspiration. I am truly fortunate to have you at my side.

Table of Contents

List of Tables

List of Figures

Summary

Sustainability is perhaps one of the most heard buzzwords in the post-20th century society; nevertheless, it is not without a reason. Our present practices for energy supply are largely unsustainable if we consider their environmental and social impact. In view of this unfavorable panorama, alternative sustainable energy sources and conversion approaches have acquired noteworthy significance in recent years. Among these, proton exchange membrane fuel cells (PEMFCs) are being considered as a pivotal building block in the transition towards a sustainable energy economy in the 21st century. The polyelectrolyte membrane or proton exchange membrane (PEM) is a vital component, as well as a performance-limiting factor, of the PEMFC. Consequently, the development of high-performance PEM materials is of upmost importance for the advance of the PEMFC field. In this work, alternative PEM materials based on semi-interpenetrated networks from blends of poly(vinyledene fluoride) (PVDF) (inert phase) and sulfonated crosslinked acrylic polyelectrolytes (PE) (proton-conducting phase), as well as tri-phase PVDF/PE/zirconium-based composites, are studied. To alleviate the burden resulting from the vast number of possible combinations of the different precursors utilized in the preparation of the membranes (PVDF: 5×, PE: 2×, Nanoparticle: 3×), custom high-throughput (HT) screening systems have been developed for their characterization. By coupling the data spaces obtained via these systems with the appropriate statistical

and data analysis tools it was found that, despite not being directly involved in the proton transport process, the inert PVDF phase plays a major role on proton conductivity. Particularly, a univocal inverse correlation between the PVDF crystalline characteristics (i.e., crystallinity and crystallite size) and melt viscosity, and membrane proton conductivity was discovered. Membranes based on highly crystalline and viscous PVDF homopolymers exhibited reduced proton conductivity due to precluded segmental motion and physical blockage of the PE chains during crosslinking. In addition, a maximum effective amount of PE (55-60wt%, neutralized form) beneficial for proton conductivity was revealed. Some of the aforementioned effects may possibly have been overlooked if a high-throughput study including plentiful combinations of multiple precursors hadn't been performed. In the case of composite membranes, despite the fact that nanoparticle dispersion was thermodynamically limited, a general improvement in proton conductivity was evidenced at low to medium nanoparticle loadings (0.5 to 1wt%) in comparison to non-hybrid PVDF/PE references. This beneficial effect was particularly noticeable in membranes based on PVDF homopolymers (7% to 14.3% increment), where the nanoparticles induced a "healing" effect by providing proton-conducting paths between non-crosslinked PE channels separated by dense PVDF areas resulting from large PVDF crystallites. In general, the results presented herein are promising for the development of new cost-effective alternative PEMs.

Chapter 1
Introduction

1.1 Sustainability and energy conversion

As with many scientific and technical research works, aside from most fundamental science-type research, the driving force behind them is something afar from just the desire for knowledge and the exhilaration of discovery. Sometimes concealed, this force is comprised by political, social, and/or economical needs; and is by and large the foremost drive pushing research forward. In the particular case of this work it takes the form of *sustainability and energy conversion* and all the political and social implications it involves. So before centering our attention in the focal point of this dissertation let's take a look at how sustainability and energy conversion concerns create a motivation and give significance to this work.

It is widely known that the actual energy economy is fossil-fuel based [1]. Coal, natural gas, and oil account for roughly 81% of the total world energy supply, while renewables such as geothermal, solar, and wind, among others, for less than 1% [2] (Figure 1.1). The implications of this scenery are substantial, particularly from the economical, political, and environmental points of view. For instance, it is predicted that the global fossil fluid fuel (i.e., natural gas and oil) supply will peak in 2015 [3, 4]; at this

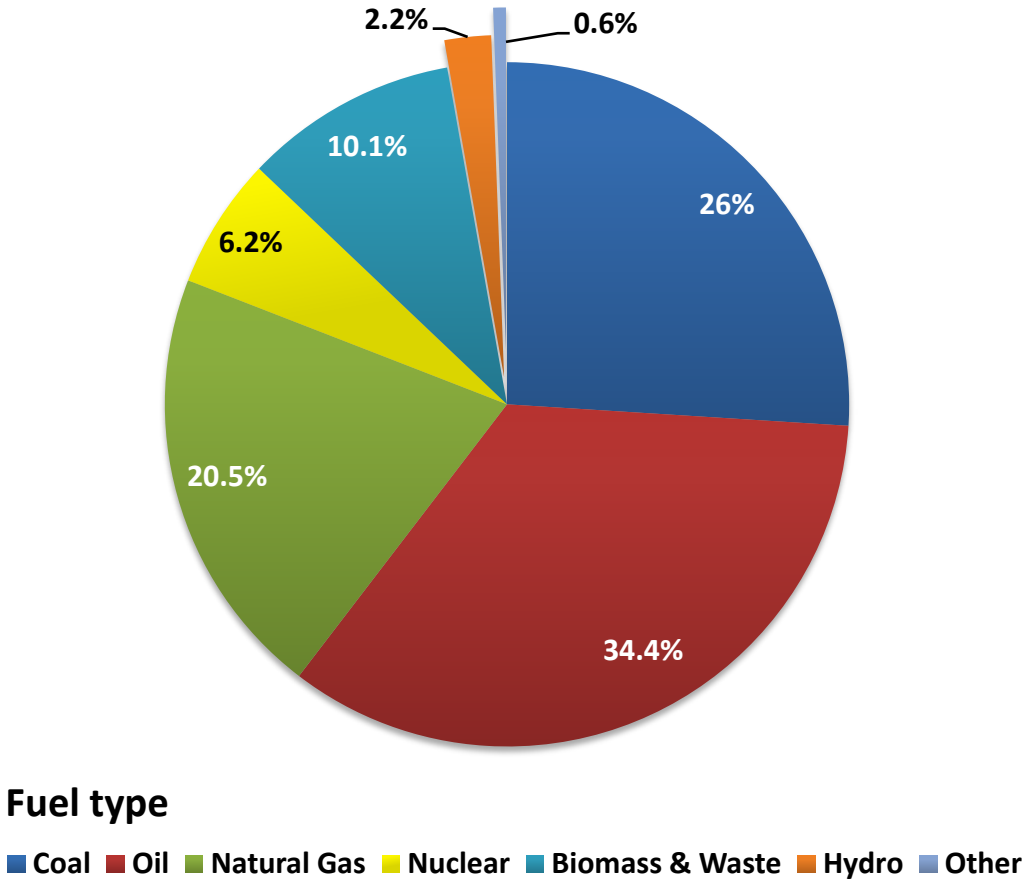

Figure 1.1 Total world primary energy supply by fuel type (source: IEA [2]).

point oil demand will outstrip supply and "low-priced" oil and gas won't be readily available. This will precipitate an energy shortage crisis unless a sustainable alternative fuel or energy source is available by then. What is more, 2008 saw the effects of preliminary estimates coming out of the oil industry that indicated a seemingly unbridgeable supply-demand gap opening up after 2007 [5]. The results: unstable oil market characterized by skyrocketing prices in record-short periods of time, and political tension throughout the globe. The other side of the spectrum is not much better either, fossil fuels face strong opposition because of environmental and health concerns. The utilization of fossil fuels is directly associated with the emission of pollutants (e.g., nitrogen dioxide, sulfur dioxide, etc) and greenhouse gases (e.g., carbon dioxide) that pose serious health threats, and have adverse environmental effects that can lead to the instability of the global ecosystem [3, 6, 7]. Ironically, fossil fuel-based electricity generation still constitutes approximately 71.7% of the total US electricity demand and 66.9% of the total world electricity Generation [2, 8].

Although it is hard to unambiguously define what "sustainability" means, a particularly good description is given in the definition "living off the interest and not the capital of natural resources" [9]. By that definition energy generation has been largely and obviously unsustainable for many years [1], relying heavily on the capital of natural fossil reserves. Higher standards of living in emerging economies are contributing to the increased use of energy for electric power generation and for personal automobile transportation. On the global scale, by 2015, world energy consumption will increase to 542 quadrillion BTU, 1.6 times more than the 1998 picture [10] (Figure 1.2). Sustainability

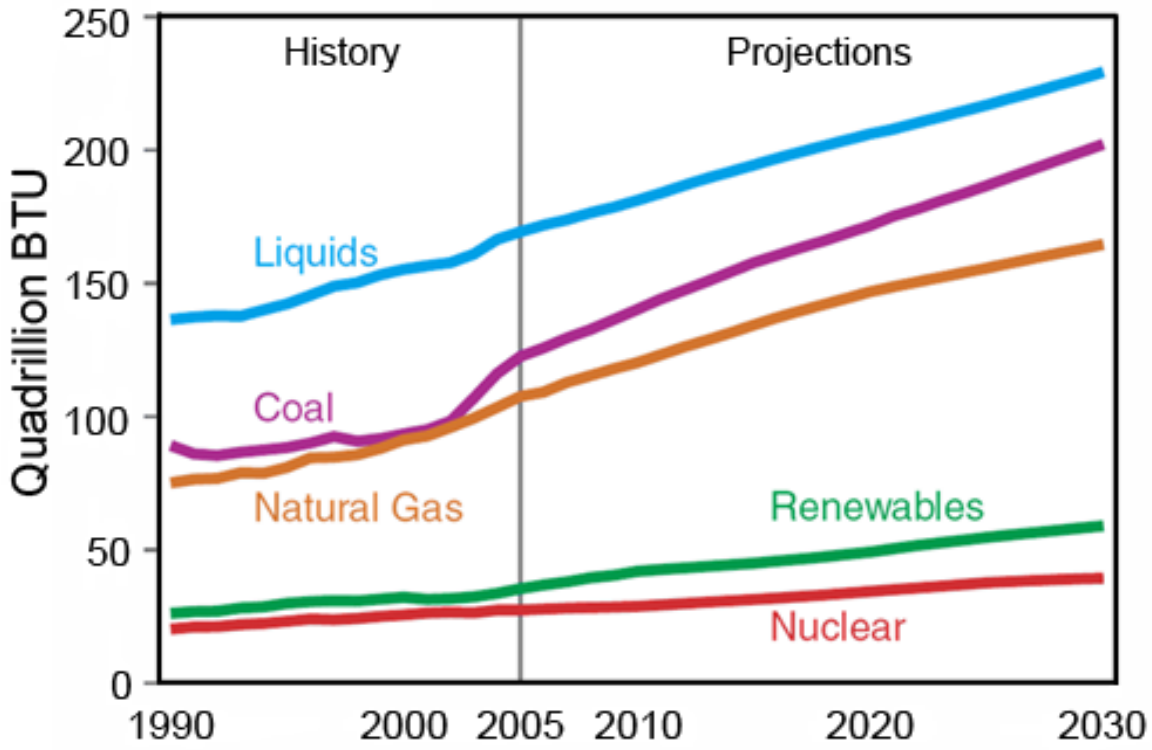

Figure 1.2 World marketed Energy use by fuel type (historical data since 1990 and projection to 2030) (source: EIA [8]).

models, which integrate social and environmental factors with planning and economic considerations, in conjunction with an increasing awareness of the influence of human activities on the environment, propose the development and adoption of alternative fuels and energy conversion technologies able to reduce dependence from oil and other fossil fuels.

Present energy sources and conversion practices, however, are starting to move in new directions to overcome the issues associated with the burn of fossil fuels while still providing high quality power and other energy services. Some of these new directions and alternatives include sources such as wind, geothermal, biomass, hydrogen, solar, and tidal; as well as conversion technologies like fuel cells, photovoltaics, turbines, and pelamis, among others. Amongst these myriad of alternative energy sources and conversion approaches hydrogen-based fuel cell technology has stood out during recent years as one of the potential keystones for future power generation. Fuel cells are significantly more efficient than most conventional energy conversion approaches based on internal combustion as they are not bounded by the Carnot efficiency (see section 1.3.3). In addition, byproduct emissions arising from the fuel cell operation are drastically lower [3, 11]. Being basically an energy conversion technique, the contribution of the fuel cell technology to energy sustainability depends heavily on the impact of the hydrogen procurement. However, experts in the field of sustainable energy suggest that hydrogen-based energy has the appropriate elements to meet requirements of high efficiency and low emissions [1, 7].

Fuel cells may fit into many different scenarios, including transportation, stationary energy generation, and mobile applications [12]. For example, in the transportation field, automobile manufacturers are seriously considering the fuel cell technology as one of their primary alternatives to tackle the environmental issues associated with emissions of internal combustion engines and overcome the instability of the oil market [13, 14]. In the case of mobile applications (e.g., portable electronic devices) fuel cells are an attractive alternative to alleviate the drawbacks linked with the capacity limitations of rechargeable batteries arising from the consumers demand of longer life in smaller form factors (e.g., personal media players, cell phones, and ultra-thin laptops). In addition, fuel cells are being considered as fundamental components in the development of highly integrated and efficient localized energy generation and storage systems with low environmental footprint [15] and for energy cogeneration [16]. Overall, it appears that hydrogen and fuel cells will play an important role in the large-scale integration of renewable energy into the future energy economy.

1.2 Fuel cells (overview)

Fuel cells are by no means a new technology; their invention dates back to the middle of the 19th century when Christian Friedrich Schönbein, a Swiss chemist, detailed their operational principle, and Sir William Robert Grove, a Welsh scientist, developed the 1st prototype (the Grove cell) using zinc and platinum electrodes in acid solutions separated by a porous ceramic material [4, 11, 17]. Then again, their development lacked

a drive for more than 100 years as primary energy sources were abundant, unrestricted, and inexpensive. In addition, the brief lifetime of early prototypes and the elevated costs incurred in their development delayed even more the interest in this technology. It wasn't until the escalation of the abovementioned social and environmental concerns that attention towards fuel cells became significant, especially during the last two decades as a result of direct funding for fuel cell research from the U.S. Department of Energy (DOE).

From a general perspective fuel cells are electrochemical devices in which the free energy of a chemical reaction is converted into electrical energy [11]. Although, both batteries and fuel cells are characterized by controlled chemical reactions in which a desired process occurs electrochemically (unwanted side reactions, including corrosion, are ideally absent or kinetically and/or thermodynamically minimized or suppressed), fuel cells are considered to be energy conversion-only devices whereas batteries serve as both energy storage and energy conversion systems. Opposite to batteries which need to be recharged with an external power source, fuel cells just need to be supplied with an appropriate fuel (e.g., hydrogen, methanol, etc).

All fuel cells contain an electropositive electrode (anode) and an electronegative electrode (cathode) separated by an electrolyte (Figure 1.3). The electrolyte is pivotal for the fuel cell operation as it has to effectively separate the anode (exposed to the fuel stream) and the cathode (exposed to the oxidant) gases and/or liquids, while mediating the electrochemical reaction through the swift conduction of a specific ion [18]. The complementary electric current generated in this process is used to perform work on an

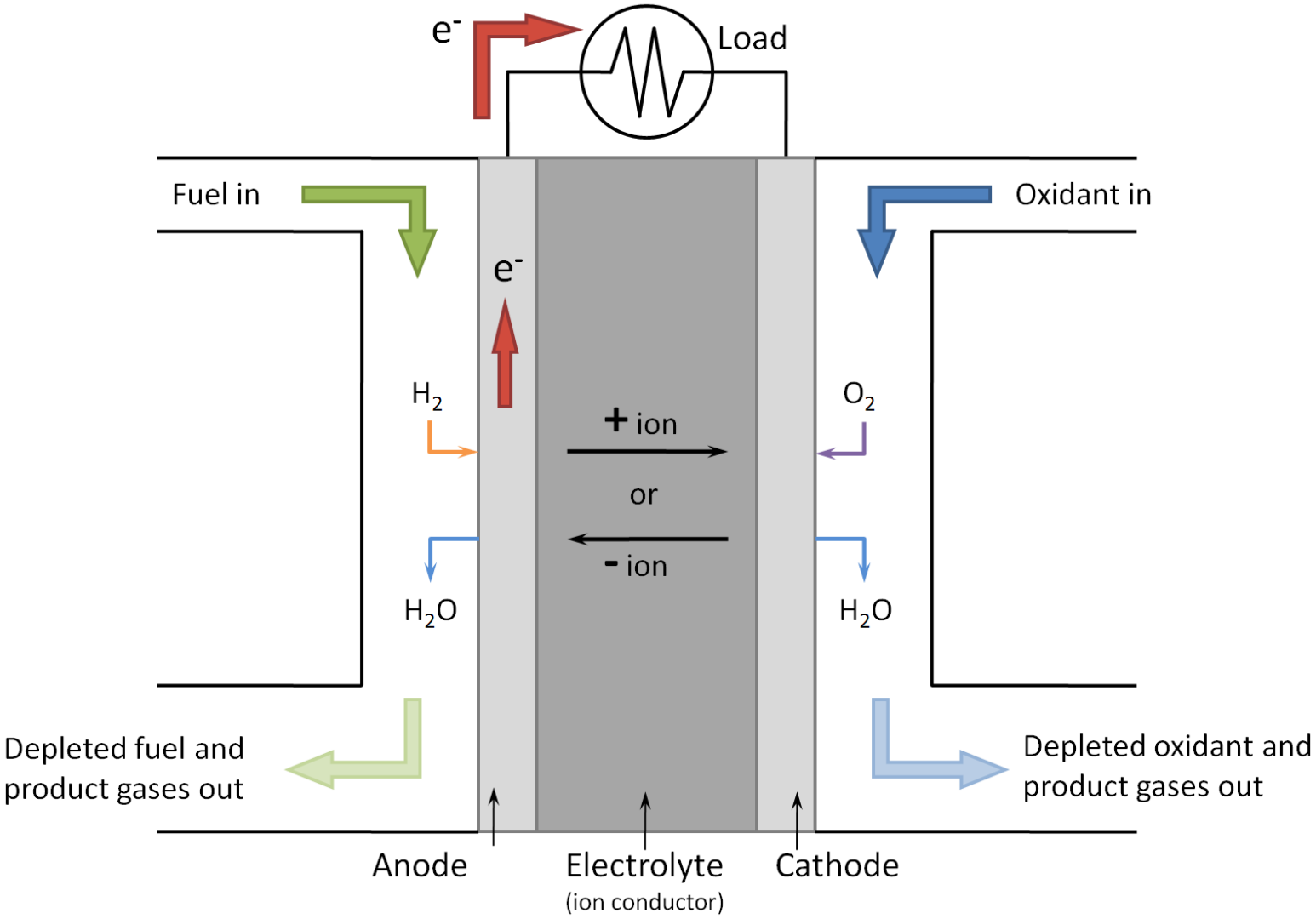

Figure 1.3 General schematic of an individual fuel cell.

external circuit (load). Habitually fuel cells are classified by their electrolyte type and sub-grouped by operating temperature (Table 1.1), being the most common the alkaline fuel cell (AFC), polymer electrolyte fuel cell (PEMFC), direct methanol fuel cell (DMFC), phosphoric acid fuel cell (PAFC), molten carbonate fuel cell (MCFC), and solid oxide fuel cell (SOFC). MCFC and SOFC are high-temperature fuel cells while PEMFC, DMFC, and PAFC are low-temperature fuel cells [3, 11, 18].

Although sharing a similar basic structure, the focus in terms of research and development on fuel cells is continuously shifting since it is unlikely that a single technology alone can meet all the requirements for each specific application. This has been particularly evident during the past 20 years when attention that was mainly directed towards MCFCs and PAFCs technologies for large-scale power generation as a direct result of oil price spikes and energy crisis in the 1970s, shifted throughout the 1990s due to the increased interest in transport applications (e.g., light duty vehicles). As a result, a greater deal of attention was given to PEMFC technology [19]. Nowadays PEMFCs are the leading low-temperature fuel cell type, and their technology (essentially hydrogen-based) has matured enough to surpass that of well established high-temperature fuel cells such as SOFCs (the prevailing high-temperature fuel cell technology) [3].

In general, due to the dissimilarity among the applications of the various fuel cell technologies, it is unlikely that on the long run they will all compete in the same market or the same type of application. Consequently, the success and evolution of each particular fuel cell technology will depend *directly* on the segment or market it targets, as

Table 1.1 Comparison of fuel cell technologies (charge carriers are shown in bold in the reactions column) [4, 11].

Fuel Cell Type	Electrolyte	Operating Temperature	Electrochemical Reactions	Applications	Advantages	Disadvantages
Polymer Electrolyte Membrane (PEMFC)	Hydrated polymeric ion exchange membranes	60-120°C	*A:* $H_2 \rightarrow 2\mathbf{H^+} + 2e^-$ *C:* $\frac{1}{2}O_2 + 2H^+ + 2e^- \rightarrow H_2O$ *Cell:* $H_2 + \frac{1}{2}O_2 \rightarrow H_2O$ (evap)	-Electricity -Portable power -Transportation	-Solid electrolyte reduces corrosion an and management problems -Low temperature -Quick start-up	-Low temperature requires expensive catalysts (platinum) -High sensitivity to fuel impurities
Alkaline (AFC)	Mobilized or immobilized potassium hydroxide in asbestos matrix	65-220°C	*A:* $H_2 + 2(\mathbf{OH^-}) \rightarrow 2H_2O + 2e^-$ *C:* $\frac{1}{2}O_2 + H_2O + 2e^- \rightarrow 2(OH^-)$ *Cell:* $H_2 + \frac{1}{2}O_2 \rightarrow H_2O$ (evap)	-Military -Space	-Fast cathode reaction = high performance	-Expensive removal of CO_2 from fuel and air streams required -Platinum catalysts
Phosphoric Acid (PAFC)	Immobilized liquid phosphoric acid in SiC	175-205°C	*A:* $H_2 \rightarrow 2\mathbf{H^+} + 2e^-$ *C:* $\frac{1}{2}O_2 + 2H^+ + 2e^- \rightarrow H_2O$ *Cell:* $H_2 + \frac{1}{2}O_2 \rightarrow H_2O$ (evap)	-Electric utility -Transportation	-Up to 85% efficiency in cogeneration of electricity and heat -Can use pure H_2 as fuel	-Platinum catalyst -Low current and power -Large size/weight
Molten Carbonate (MCFC)	Immobilized liquid molten carbonate in $LiAlO_2$	600-800°C	*A:* $H_2 + \mathbf{CO_3^{2-}} \rightarrow H_2O + CO_2 + 2e^-$ *C:* $\frac{1}{2}O_2 + CO_2 + 2e^- \rightarrow CO_3^{2-}$ *Cell:* $H_2 + \frac{1}{2}O_2 + CO_2 \rightarrow CO_2 + H_2O$ (gas)	-Electric utility	-High efficiency -Fuel flexibility -Can use a variety of cheap catalysts (stainless steel or nickel)	-High temperature enhances corrosion and breakdown of cell components
Solid Oxide (SOFC)	Perovskites (ceramics)	800-1000°C	*A:* $H_2 + \mathbf{O^{2-}} \rightarrow H_2O + 2e^-$ *C:* $\frac{1}{2}O_2 + 2e^- \rightarrow O^{2-}$ *Cell:* $H_2 + \frac{1}{2}O_2 \rightarrow H_2O$ (gas)	-Electric utility	-High efficiency -Fuel flexibility -Can use a variety of catalysts (nickel, ceramic, or steel)	-High temperature enhances breakdown of cell components

well as the requirements of the end-user [19]. On the whole, all types of fuel cells stand at an interesting stage and each system has its advocates and opponents, as well as its advantages and disadvantages. And while presently not economically competitive, except in a minority of niche markets, fuel cells are likely to become so in the near future.

This work is focused particularly on the study on new alternative electrolytes for polymer electrolyte membrane fuel cells (PEMFCs) (also designated as proton exchange membrane fuel cells). A detailed description of this type of fuel cells is presented next.

1.3 Polymer electrolyte membrane fuel cell (PEMFC)

1.3.1 Overview and general concepts

PEMFCs are a type of low-temperature fuel cell characterized by a solid polymer proton exchange membrane that serves as the electrolyte: the polyelectrolyte. Research and development of this type of fuel cell received a vital momentum boost (in both industry and academia) during the space race in the 1950s and 1960s when NASA chose the technology to power space missions. The 1st mission utilizing the new PEMFCs, developed by General Electric, was the Gemini V in 1965, which successfully doubled the flight time of prior similar battery-powered missions [4, 11, 20, 21]. Despite showing the potential of the PEMFC technology, the cells used had two significant drawbacks: extremely high costs (due mainly to the required platinum catalysts) and the prominently short life of the poly(styrene divinylbenzene) copolymer membranes used

as polyelectrolyte due to oxidative degradation of the polymer backbone. It wasn't until the late 1960s that interest in PEMFCs for applications outside the space program started to arise, when E.I. DuPont de Nemours & Company introduced a perfluorosulfonic acid-based polyelectrolyte under the trade name of Nafion® [22]. Although originally intended for use in chlor-alkali processes, the characteristics of Nafion® were more than appropriate for PEMFCs [11, 23]. Particularly, the main advantage of Nafion® membranes over the original polystyrene-based polyelectrolytes was the high resistance to oxidative degradation of its fluorinated backbone [21, 23]. However, it took another decade until the PEMFCs became a *real* viable energy conversion technology, when breakthroughs in electrode design allowed to substantially reduce the amount of platinum necessary in the cell catalyst layers.

Following the introduction and success of Nafion®, other types of perfluorosulfonic acid-based membranes were developed and introduced to the market. Some of these are Flemion® (Asahi Glass Co.), Aciplex® (Asahi Chemical), Hyflon® Ion (Solvay), GoreSelect® (W.L. Gore & Associates), and DowMembrane® (Dow Chemical Co.) [17]. Despite the increasing number of choices of polyelectrolytes, especially perfluorosulfonic acid polyelectrolytes, Nafion has remained the industry standard proton exchange membrane and almost all current research in the field of PEMFCs is focused on this type of electrolyte.

Regarding the operation of PEMFCs, as with all types of fuel cells, an oxidation reaction occurs at the anode whereas a reduction reaction takes place in the cathode. These electrochemical reactions result in a potential (voltage) gradient between the

electrodes. The polyelectrolyte located between the electrodes conducts ions between them while at the same time acting as a barrier for the reacting species of the fuel and oxidant streams (i.e., hydrogen and oxygen). It also must serve as an electronic insulator (electron barrier). When an external load is connected to the electrodes, the existing potential gradient resulting from the electrochemical reactions generates an electron flow that can be used as a source of electrical current. In a PEMFC hydrogen is oxidized at the anode to liberate two protons and two electrons. The protons enter the polyelectrolyte and are transported towards the cathode. The electrons travel through the external circuit reaching the cathode as well. At the cathode oxygen is reduced in presence of the electrons and recombines with the protons to form water as a byproduct of the reaction. The half-cell reactions of the hydrogen oxidation and the oxygen reduction, as well as the total or overall cell reaction are shown below:

Anode: $H_2 \rightarrow 2H^+ + 2e^-$

Cathode: $\frac{1}{2}O_2 + 2H^+ + 2e^- \rightarrow H_2O$

Cell (total): $H_2 + \frac{1}{2}O_2 \rightarrow H_2O$

Generally, both the oxidation and reduction reactions are carried out via heterogeneous catalysis.

1.3.2 PEMFC components

1.3.2.1 Electrodes

The electrodes in a PEMFC are generally composed of the same material as the electrolyte loaded with metallic catalysts dispersed in a conducting medium (usually carbon black) [24]. Due to the low operating temperatures of PEMFCs these catalysts are typically expensive noble metals (e.g., platinum) in order to attain acceptable reaction rates. The most common catalyst for PEMFCs is nanocrystalline platinum; although platinum-based alloys that incorporate other noble metals are being used to improve the tolerance to carbon monoxide poisoning. For example, ruthenium, in platinum-ruthenium alloys, permits the performance of the fuel cell to remain within acceptable margins even in presence of hundreds of parts-per-million of carbon monoxide in the anode fuel stream. The amount of precious metal necessary is determined by the amount of catalyst per active area and the ionomer content of the electrode, bounded by the PEMFC application requirements. For optimal current densities the catalyst area to electrode area ratio needs to be as high as possible. In addition, a "three-phase" boundary on the catalyst (Figure 1.4) formed by the gas supply on one hand, and the direct contact with both the proton and electron conductors in the other hand, is desired to maximize the reaction rate by moving away charges from the reaction sites towards the polymer electrolyte membrane (protons) an the external load (electrons) [11]. Another critical point that needs to be considered in the design of PEMFC electrodes is the distribution of free passages (or pores) in the electrode layer, so that it allows the

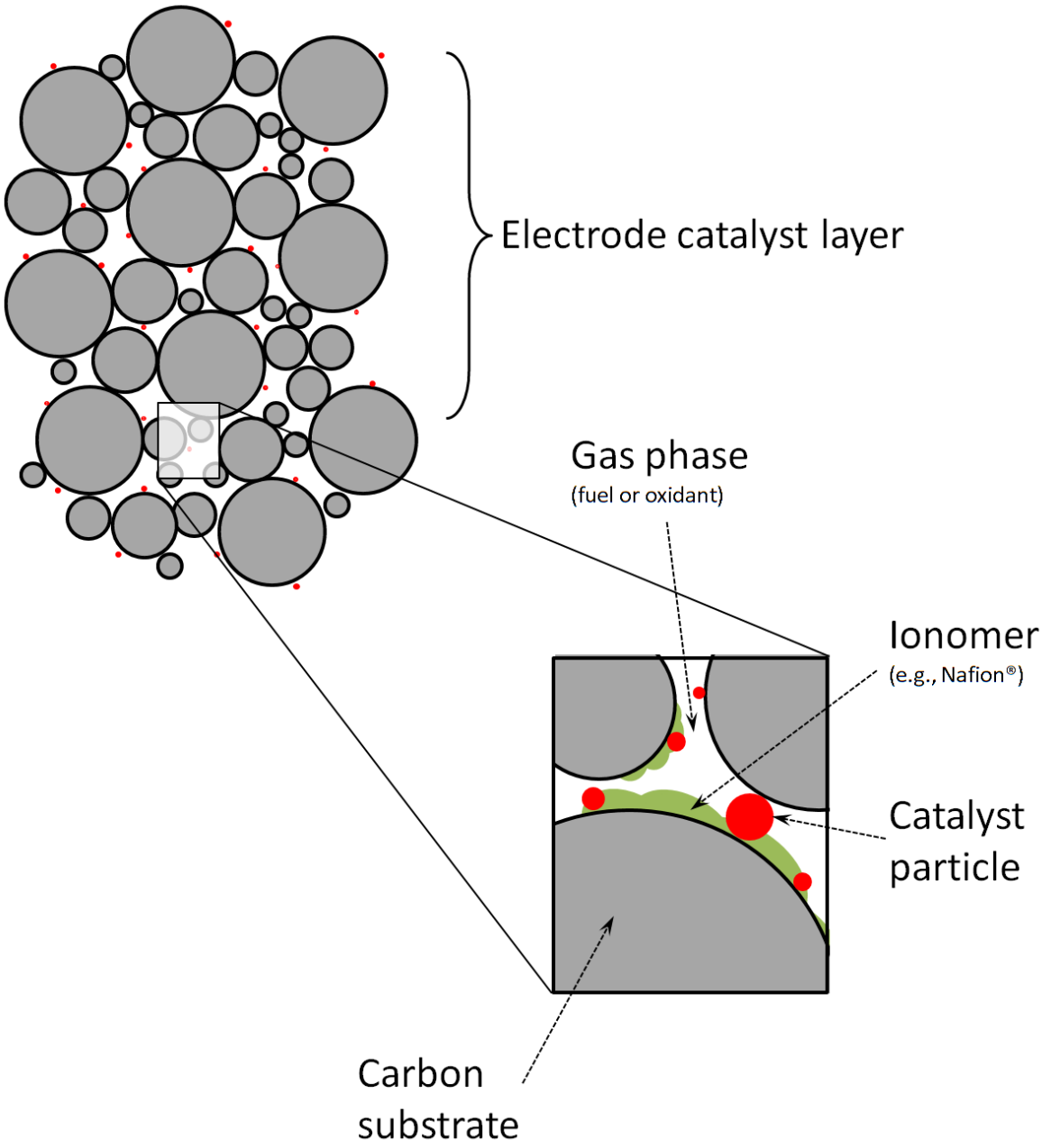

Figure 1.4 Schematic of the three-phase boundary between the catalyst particles and the gas phase, the ionomer, and the electron conductor (adapted from [11]).

reactant to easily reach the catalyst sites while allowing optimal water transport.

Electrodes are typically fabricated in the form of thin-film porous layers only a few microns thick due to the high costs of the noble metals they contain. As a result, their manufacturing process involves sophisticated methods (e.g., electrospraying) that permit build very thin layers of the proton conducting polymer impregnated with small carbon particles that have even smaller catalyst metal particles attached to them [24, 25]. The carbon support improves the utilization of the heterogeneous catalyst by increasing its useful surface area. This approach, in the case of platinum catalysts, allows for loadings in the range of just 0.5 mg/cm^2.

The electrodes are a vital component of the PEMFC as they are responsible for providing the cell working species (H^+ and e^-), and maintaining the potential gradient accountable for charge movement through the electrolyte and the external load (reduction of oxygen). Due to their significant effect on the performance of PEMFCs, the investigation of new catalysts and electrode manufacturing techniques are areas of intense research.

1.3.2.2 Polymer electrolyte membrane

While numerous different polymer electrolyte materials have been devised with equally varied fabrication approaches (section 1.3.4), polyelectrolyte membranes share a well defined attribute: the presence of negatively charged groups embedded in the polymer matrix. The occurrence of these groups gives the polyelectrolyte membranes an

acidic character and a hydrophilic behavior not typical in the majority of polymeric materials, which is the key for proton transport [11, 26]. Hydration of the hydrophilic channels inside the polymer electrolytes is a requirement for proton conduction as protonic charge carriers are solvated by very few types of species, among them water. Water solvated protons travel through the membrane via a mechanism denoted as Grotthuss diffusion or structure diffusion, where an excess solvated proton or protonic defect diffuses through the hydrogen bond network of water molecules inside the hydrophilic channels by sequential structural changes of Zundel ($H_5O_2^+$) and Eigen ($H_9O_4^+$) hydrated oxonium cations (solvation structures) [18, 27].

Due to the prerequisite of hydration for proton transport, polymer electrolyte membranes commonly have a small temperature range in which they are stable (Table 1.1), with the upper temperature limit is dictated by the point of membrane dehydration due to water evaporation. For this reason PEMFCs fall in the low-temperature fuel cell category and, as mentioned is the previous section, require expensive noble metal catalysts in order to achieve acceptable oxidation and reduction reaction rates at the electrodes.

The most common membrane for PEMFC is perhaps Nafion® [26] (Figure 1.5), manufactured by E.I. DuPont de Nemours & Company. Nafion® belongs to a family of membranes dubbed perfluorosulfonic acid membranes (also referred to as perfluorocarbon sulfonic acid membranes) (PFSA), which are characterized by a fluorinated backbone (poly(tetrafluoroethylene) in the case of Nafion®) with side chains that terminate in sulfonic acid groups. Apart from their proton conducting ability, the

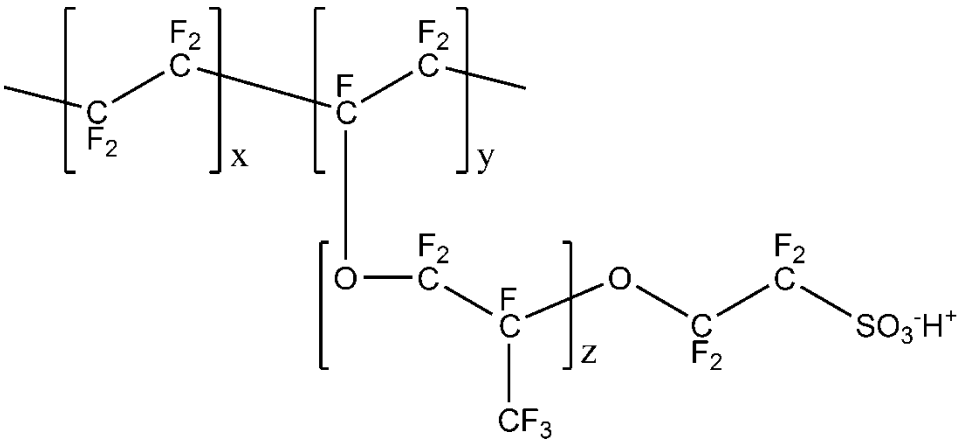

Figure 1.5 Nafion® chemical structure [22].

highly fluorinated structure of the backbone of PFSA membranes confers them greater resistance to degradation in the oxidative environment of PEMFCs, which translates in longer fuel cell lifetimes. Other characteristics such a good mechanical properties, satisfactory thermal stability, and reasonable swelling and barrier attributes; have made this type of membranes the most widely used and researched.

As emphasized before, PEMFCs find an extremely good fit in three main sectors: automotive, stationary, and portable power. Each of these applications exhibit unique operating conditions and material requirements; however there are several common prerequisites critical to all proton exchange membranes [23]:

- High protonic conductivity
- Low electronic conductivity
- Low permeability to fuel and oxidant

- Low water transport through diffusion and electro-osmosis
- Oxidative and hydrolytic stability
- Good mechanical properties in both the dry and hydrated states
- Competitive cost
- Capability for fabrication into membrane electrode assemblies (MEAs)

Extensive research is underway to address all these requirements and devise affordable materials with enhanced performance and extended lifetime. It will be, however, a significant research challenge to develop a material that encompasses all these properties at once. Since nearly all existing polymer electrolyte materials for PEMFCs rely on absorbed water and its interaction with acid groups to produce protonic conductivity, the biggest challenge, perhaps, will be to develop membranes that can operate efficiently at extreme temperatures. That is, membranes that work at temperatures above the boiling point of water and that can conduct protons with little or no water, and membranes that are functional at freezing and sub-freezing temperatures (extremely important for applications in the automotive industry).

Further information and details about materials for polymer electrolyte membranes can be found in section 1.3.4.

1.3.2.3 Membrane electrode assembly (MEA)

The unit constituted by the electrodes and membranes is the basic unit of the fuel cell, called the membrane electrode assembly (MEA) (Figure 1.6). In the membrane

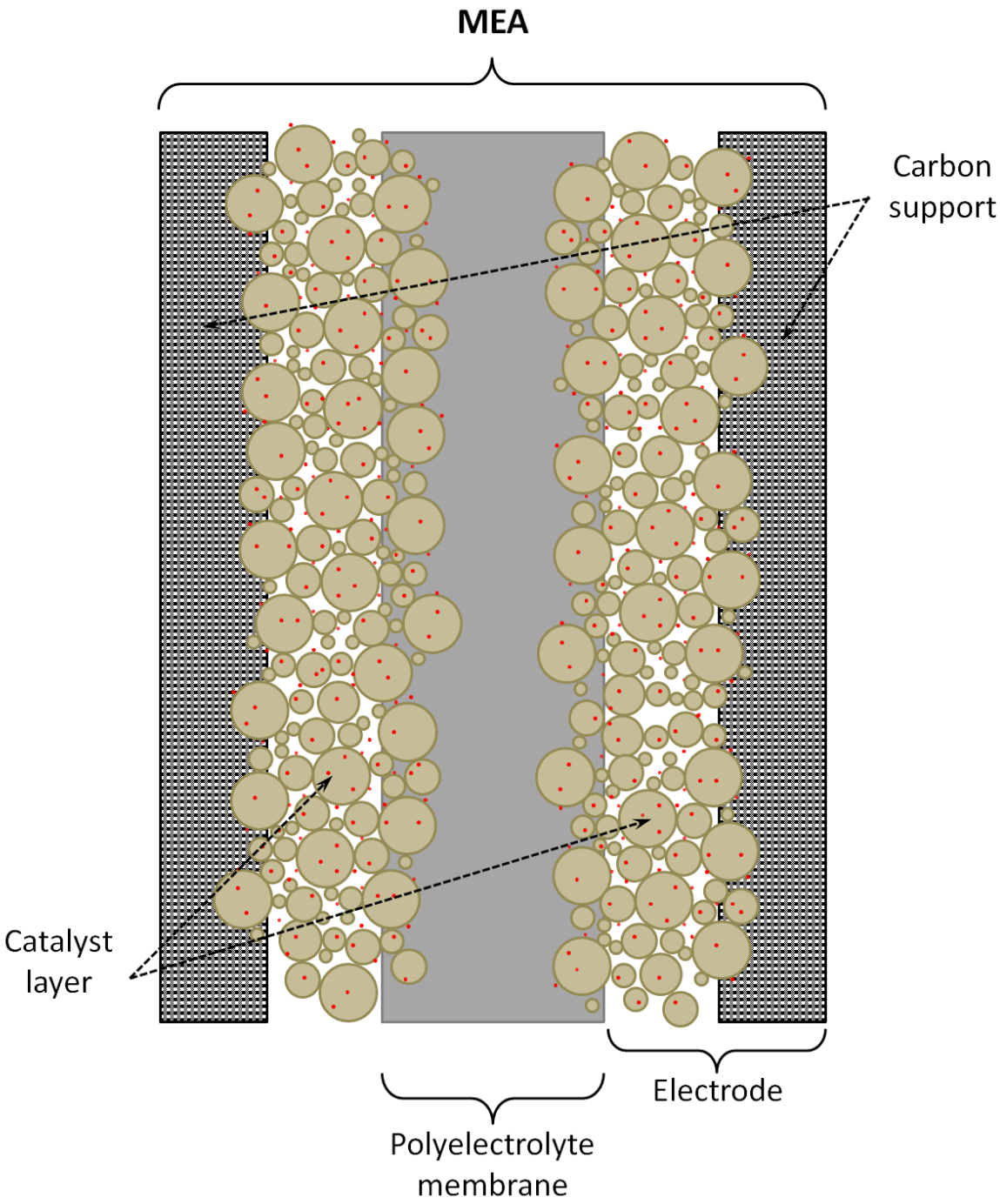

Figure 1.6 Schematic of the membrane electrode assembly (MEA).

electrode assembly the two electrically and ionically conductive electrodes containing the catalyst are bonded to the proton exchange membrane. There are two main techniques for bonding the electrodes to the proton exchange membrane. Both methods make use of a suspension called "catalytic ink" composed of the ion conducting polymer, copolymer, and/or blend of polymers diluted in a solvent (~5wt% polymer); and catalyst-impregnated carbon particles (usually Pt/C, ~20wt%). Other additives are usually added to ease processing. The first method consists in painting the ink directly onto the membrane following by solvent drying to form a thin porous catalyst layer or electrode. This method requires that the membrane is not soluble in the ink solvent. For the second method the selection of the ink solvent is independent of the membrane, as the ink is painted and dried onto a transfer substrate. Once the thin electrode layer is formed it is transferred to the polyelectrolyte membrane by hot-pressing at temperatures close to 150-200°C and pressures of 3000 psi. The electrode layer bonds to the membrane during the hot-pressing process using the ionomer itself as the binder [24].

The MEA is the fundamental unit of the fuel cell, reason why understanding the electrode and membrane structures, the interaction between them, and the effects of aging and degradation during fuel cell operation; as well as their effect on fuel cell performance, are of paramount importance.

1.3.2.4 Gas diffusion layers (GDL)

In an assembled PEMFC, the MEA is sandwiched between porous gas diffusion layers. As indicated by their name, these layers provide transport paths for the fuel and oxidant to the catalysts; however, they have many more purposes in addition to gas diffusion. In addition to provide a protective layer for the very thin catalyst layers of the electrodes, they form a thermal contact (to dissipate heat) between the electrodes and the flow field plates, provide an electrical connection between the electrodes and the current collectors, and remove excess product water to prevent flooding while maintaining appropriate MEA hydration levels [28, 29]. To achieve this, the gas diffusion layer material has to have high electrical and thermal conductivity, optimal hydrophobic/hydrophilic balance, adequate porosity, good chemical and mechanical stability in oxidative environments, and satisfactory durability.

As anticipated the properties of GDLs, particularly porosity and pore size distribution, have a prominent effect on the overall performance of the PEMFC. Usually they are made from carbon paper or carbon cloth, typically 100-300 μm thick. Any change in porosity or diffusion coefficient of the GDLs can lead to reduced fuel cell performance because of change of the diffusion overpotential [28]. For this reason, alternative GDLs materials to carbon paper or carbon cloth are being studied, as these are sensitive to pressure and easily deformed. Deformation under pressure can result in variable and/or reduced porosity that can be reflected in inferior cell performance. Some of the new approaches for GDLs include rigid metal-based structures, as well as variable structures consisting of a macroporous backing layer and a microporous diffusion layer

applied on one or both sides of the backing layer. Devising the right GDL material is, however, a daunting task as the material of choice has to exhibit a combination of all the aforementioned properties, and some of these properties are odds with each other.

A schematic of an individual fundamental unit for PEMFC, including the MEA (polyelectrolyte + electrodes) and the GDLs, is shown in Figure 1.7.

1.3.2.5 Bipolar plates and flow fields

Bipolar plates and flow fields carry out several functions of particular importance for low-temperature fuel cells. Just as the gas diffusion layers enclose or sandwich the MEA, the bipolar plates sandwich the unit comprised by the MEA and the GDLs. Facing the GDLs are the flow fields, which are channels engraved on the surface of the bipolar plates that provide a path between the GDLs and the fuel and oxidant feed streams. At the cathode side, these channels also serve as water-draining passages for removal of the reaction water produced during the operation of the PEMFC. The design of the flow fields is extremely important for optimal cell performance since normal operating conditions can be affected by issues arising from poor designs; for example, insufficient fuel supply to the anode or flooding of the cathode side [20, 30]. Most of the research in this area is focused on the geometry design and optimization of both the anode and cathode flow fields. As one would expect, the cathode flow field design is more critical, and more difficult, as water and oxygen counter-flow has to be considered. Most modern bipolar plates make use of internal manifolding for the flow field design, so that

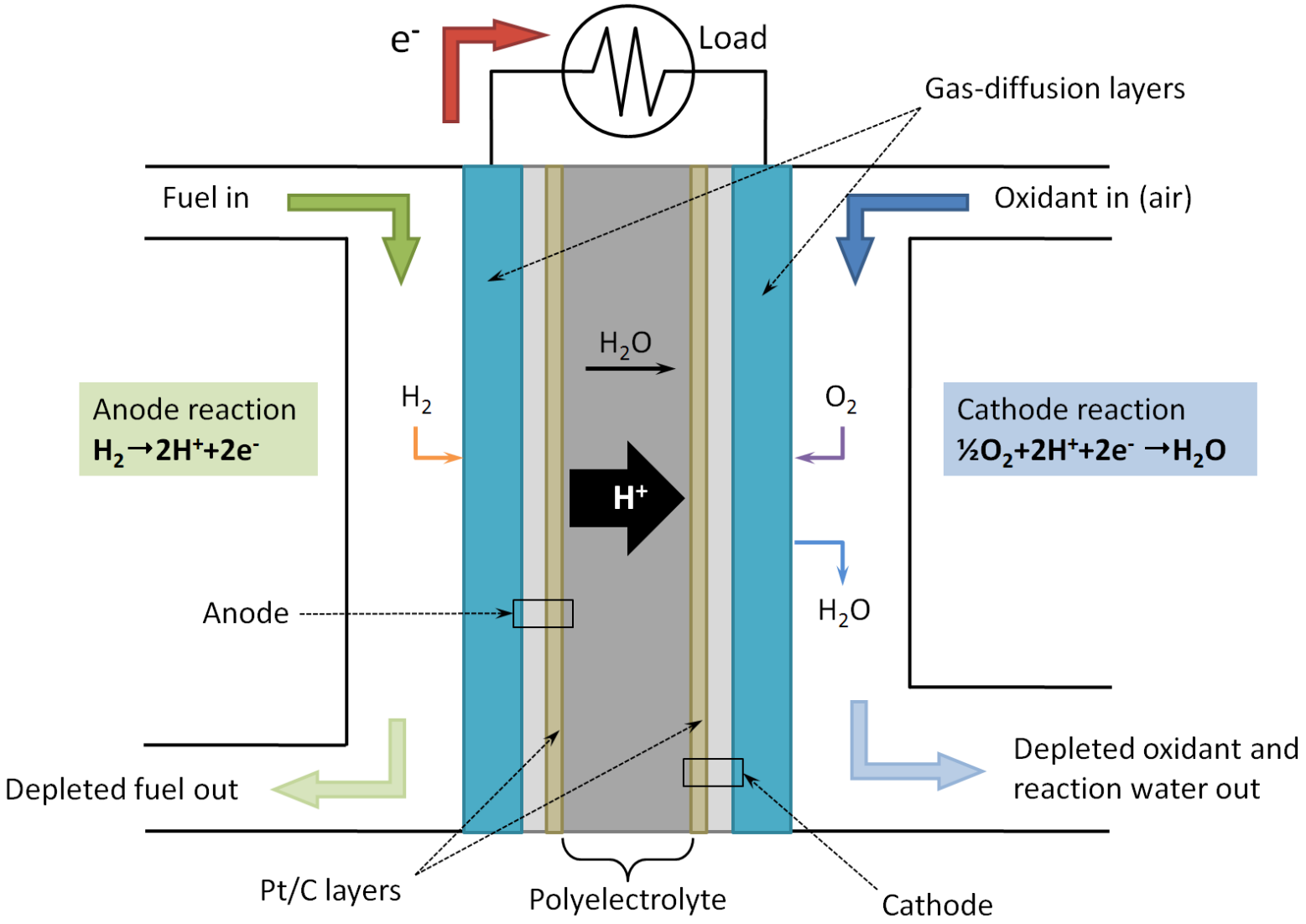

Figure 1.7 Fundamental PEMFC individual unit.

the species can keep flowing even when there are temporary blockages in some of the channels.

Excellent electrical and thermal conductivity, are other important requirements for bipolar plates as they provide the path for electric current (current collectors) and waste heat resulting from the electrodes reactions. Graphite is one of the most commonly used materials for bipolar plates since it is light, conductive, and have high resistance to corrosion. Stainless steel is used as well as it is easier to machine into desired geometries than graphite; however, it is more prone to corrosion [31].

Bipolar plates also serve as separators of reactants, form the electrical connection between unit cells, and constitute the mechanical structure of the PEMFC.

1.3.2.6 Fuel cell stack

The power output of a single PEMFC, as the basic individual unit illustrated in Figure 1.7, is generally too little (usually less than 500 mW) for practical applications. For this reason cells are physically connected in continuous arrays or stacks so that the voltages of all the cells are added. There are two typical types of fuel cell stack designs: monopolar and bipolar. The monopolar design has a positive/positive and negative/negative (anode/anode, cathode/cathode) cell arrangement where two contiguous cells are electrically isolated and share a gas stream (fuel or oxidant). Due to this arrangement the electrodes in this stack design have to be connected to one another at the edges, which gives the ability of using the stack as a "variable voltage" source

since only the number of cells necessary for a particular voltage demand are connected. This also makes this design more robust against failures since malfunctioning cell units can be disconnected without interrupting the global stack operation. However, current distribution tends to be significantly uneven in monopolar stacks with large electrodes or under high current loads.

The bipolar stack design, on the other hand, has high power density and low internal resistance due to direct electrical connection between contiguous unit cells through the bipolar plates (positive/negative or anode/cathode). However, a single failure from one of the cell units affects the whole stack. A schematic of a bipolar-type fuel cell stack is shown in Figure 1.8.

1.3.3 Fuel cell efficiency

In an internal combustion engine (ICE) energy conversion takes place accompanied by considerable temperature rise as combustion is typically extremely exothermic. The heat transfer from the reaction to the byproducts (combustion gases) and to the surroundings is a highly irreversible process that limits the overall efficiency of the ICE (generally not more than 50% for the most efficient engines). This efficiency is bounded by the Carnot efficiency, which is the maximum efficiency for a heat engine:

$$\eta_H = 1 - \frac{T_2}{T_1} \qquad 1.1$$

where T_1 and T_2 are the absolute operation temperatures of the heat engine. Contrary to internal combustion engines, and heat engines in general, fuel cells are not limited by the Carnot efficiency due to the isothermal chemical conversion of energy (no operation between a cold and hot side to produce work). Therefore, in theory, fuel cells can achieve higher efficiencies. The efficiency of fuel cells can be determined from the Gibbs free energy (useful energy) and the enthalpy change of the electrochemical reactions. Assuming that all the free energy can be transformed into electricity under reversible isothermal conditions, then the thermodynamic efficiency of the cell is given by:

$$\eta_r = \frac{\Delta G}{\Delta H} = 1 - \frac{T\Delta S}{\Delta H} \qquad 1.2$$

The entropy change (ΔS) in the reversible heat transfer to the surroundings term ($T\Delta S$) depends heavily on the reactants and products of the electrochemical reactions. However, besides the entropic energy losses under isothermal conditions accounted for in the thermodynamic efficiency, fuel cells exhibit a series of irreversible losses (also referred to as polarization effects, overpotentials, or overvoltages) that reduce their overall efficiency [30, 32, 33]. These losses are classified in three categories:

- Activation losses: Related to the activation energy of the electrochemical reactions at the electrodes (kinetic effects). These losses depend on multiple factors such as catalyst material and microstructure, the type of electrochemical

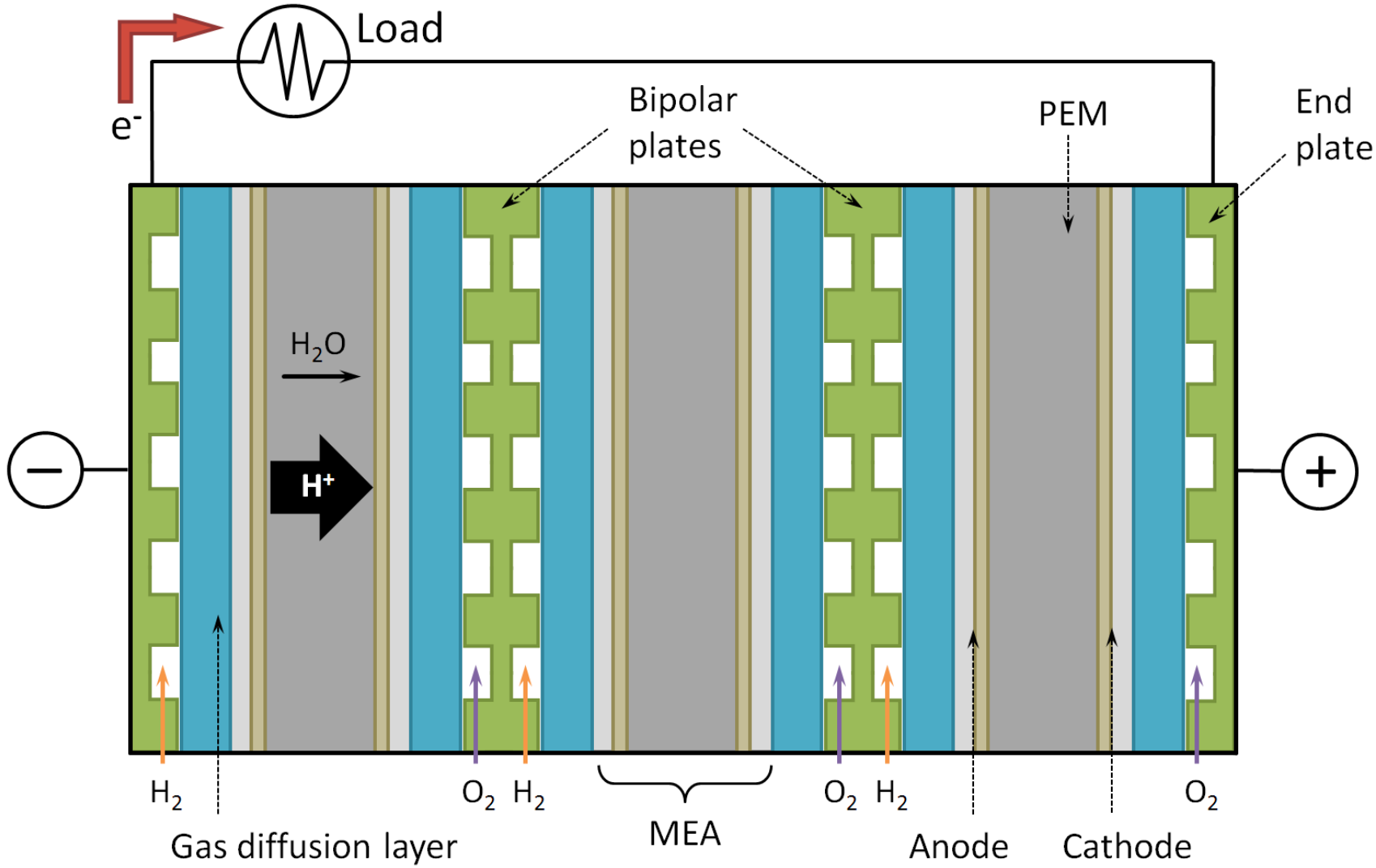

Figure 1.8 Schematic of a bipolar-type hydrogen PEM fuel cell stack (three unit cells are shown).

reactions, and reactants activity. Current density has little effect on this type of losses, except for operating conditions close to the cell open circuit voltage.

- Ohmic losses. Due to the resistance to the flow of ions in the electrolyte and electrodes, and to the flow of electrons in the electrodes and current collectors. Also, interfaces contact resistance. Ohmic losses are proportional to current density.
- Transport-related losses: Due to mass transport limitations of the reactants. These losses depend heavily on the current density, reactant activity, and electrode structure.

The effects of these losses on the performance of the fuel cell are evident in the generic voltage-current density diagram shown in

Figure 1.9, where the actual fuel cell voltage profile falls below the theoretical equilibrium voltage, or ideal reversible voltage (ΔU_0). Moreover, due to the low operating temperature of PEMFCs, even the open circuit voltage is less than the ideal reversible voltage as a large chemical activation polarization (activation losses) arises from the energy required to promote the electrochemical reactions of the reactants. The electrochemical efficiency (or voltage efficiency) of the fuel cell is related to ratio of these two profiles (ideal and real), and provides more information about the fuel cell than the thermodynamic efficiency (isothermal reversible efficiency, Equation 1.2), as it is directly related to the actual performance of the fuel cell [11]:

$$\eta_V = \frac{\Delta U_{cell}}{\Delta U_0} \tag{1.3}$$

where ΔU_{cell} is the real cell voltage. It is readily seen from Equation 1.3 and Figure 1.9 that fuel cell performance decreases as current density increases.

Other factors associated with the operation of the fuel cell need to be considered in order to fully describe the efficiency of the fuel cell. For example parasitic reactions can occur at the electrodes surfaces, or part of the reactants can participate in possible non-productive parallel side reactions, leading to lower current than theoretically possible. This is accounted for by the Faradaic efficiency, or current efficiency, defined as (for a hydrogen PEMFC):

$$\eta_f = \frac{jA}{2F\dot{n}_{H_2}} = \frac{I_{\text{ex}}}{I_{\text{max}}} \tag{1.4}$$

where j is the current density, A is the fuel cell active area, F is the Faraday's constant, and $\dot{n}_{H_2}$ is the hydrogen molar rate. I_{ex} and I_{max} are the experimental current and the maximal possible current respectively. There are additional factors that can further degrade the overall efficiency of the fuel cell such as parasitic power consumption of auxiliary devices, temperature difference between the cell and the fuel and oxidant streams, operation below 100% fuel utilization, incomplete electrochemical conversion of fuel mixtures (not common for PEMFCs), etc. Taking into account all these effects, the actual or overall fuel cell efficiency is given by [11, 32]:

$$\eta_{fc} = \eta_r \cdot \eta_V \cdot \eta_f \cdot \eta_S \cdot F_U \qquad 1.5$$

where η_r, η_V, and η_f are the thermodynamic efficiency, the electrochemical efficiency, and the faradaic efficiency respectively (given by Equations 1.2, 1.3, and 1.4 respectively). η_S and F_U are the additional efficiency due to power consumption of auxiliary devices, and fuel utilization factor respectively.

Regardless of all these factors involved in the efficiency of a PEMFC, overall electrical efficiencies of fuel cells are superior to that of heat engines. A comparison of typical fuel cell efficiencies (overall efficiencies) with conventional electric generation alternatives, such as gas turbines and diesel engines, is shown in Figure 1.10. It is important to notice that considerable gains in fuel cell efficiency can be attained by cogeneration (the simultaneous utilization of electricity and electricity), especially in fuel cells used for stationary power generation [11, 16].

1.3.4 Polymer electrolyte membranes: Commercial products and new materials

Historically, the development of polymer electrolytes has gone through several stages: from ionic polymers of poly(ethylene oxide)-salt complexes, and polystyrene sulfonated polymers (PSS) in the early days [11, 34], to PFSA copolymers such as Nafion®, Flemion®, and Aciplex® that, as previously mentioned, constitute the base of current PEMFCs technologies [11, 17, 35-37]. PFSA membranes possess acceptable mechanical integrity at low temperatures, good chemical stability, and high proton

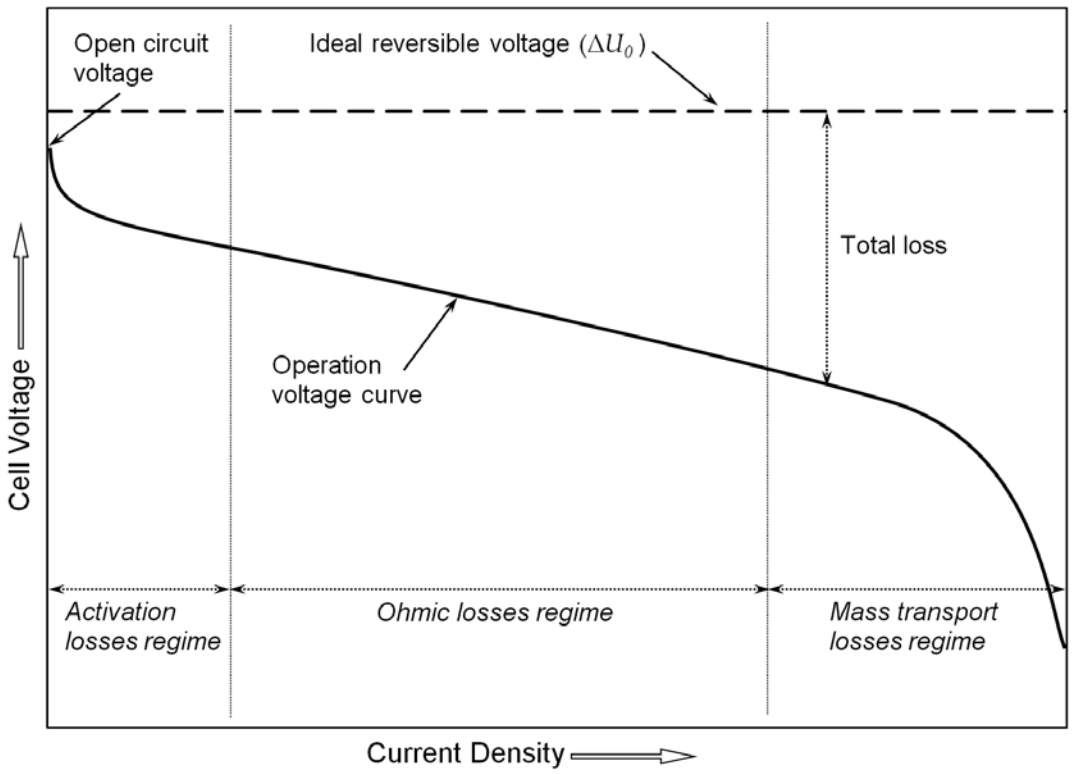

Figure 1.9 Generic diagram of fuel cell output voltage vs. output current density for a low temperature PEMFC. Ideal behavior and regions dominated by different losses are indicated (adapted from [30]).

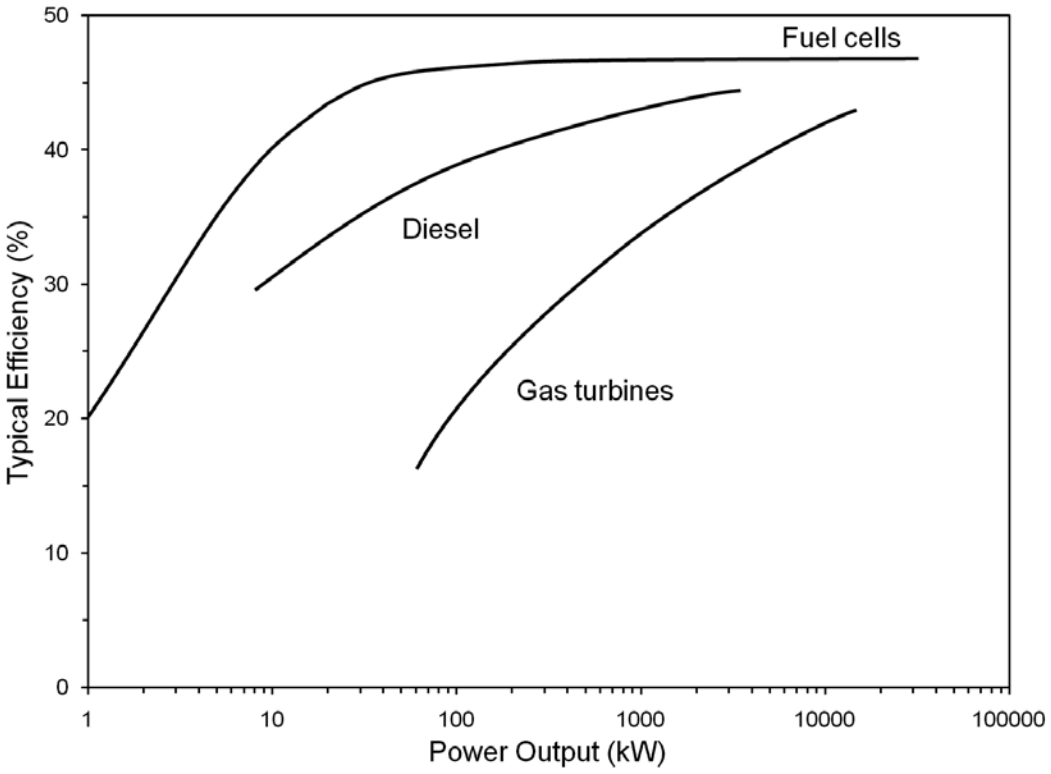

Figure 1.10 Typical efficiencies of power plants [33].

conductivity. However, as with most polymer electrolyte membranes they need to be significantly hydrated to provide an adequate environment for ion-hopping (Grotthuss diffusion) and convection mechanisms that are responsible for proton conduction [18, 27, 38-40]. Temperatures near or above 100°C are detrimental for the percolation pathways formed from water-filled channels connecting the ionic domains, resulting in dramatic drops in conductivity. These issues, combined with the high cost inherent to perfluorinated polymers, have become the driving force of an intense exploration of new material alternatives for polymer electrolyte membranes.

From the operational point of view, polyelectrolyte membranes used in PEMFCs should meet most, if not all, of the following properties in order to achieve high fuel cell efficiency [17, 41]:

- Chemical and electrochemical stability under operating conditions (oxidative environment)
- Mechanical strength and stability
- High perm-selectivity for non-ionized molecules and anions to maximize coulombic efficiency
- High proton conductivity to support high currents with minimal resistive losses

The suitability of a proton-conducting polymeric material as electrolyte in fuel cell applications is, however, not only dependant on its transport/barrier properties and its durability and reactivity. The necessity of economically attractive materials that can push the commercialization and large scale deployment of PEMFCs brings an additional

factor into the picture: Cost. The initial membranes developed for PEMFCs emphasized only performance and durability; now any comprehensive approach toward new polyelectrolyte materials should consider all relevant aspects, including both material properties and manufacturing costs.

Most current strategies towards new proton-conducting polymeric materials for PEMFCs are trying to extend the application limits, while preserving the specific advantages of well-established PFSA-based ionomer materials by slightly varying or modifying them. However, despite improvements, PFSA derived membranes still don't meet several of the major requirements needed for fuel cell commercial viability, including: long-term durability, dimensional stability at high temperature, low fuel crossover, and low cost [42]. Development of alternative PEM materials has been focused on partially fluorinated and non-fluorinated fully aromatic and/or aliphatic materials that can reduce the costs associated with the production of fluorinated-sulfonated monomers, the most cost intensive step in the production of PFSIs [17, 43]. To date several promising materials been devised [17, 35-37, 44-57]; yet, they remain at an experimental stage with laboratory-scale manufacturing volumes, which precludes their short term commercialization.

1.3.4.1 Commercial polymer electrolyte membranes

Several commercial polymer electrolyte products are available, although most of them are Nafion®-based or Nafion®-like PFSA-based electrolytes. Alternatives exist, but

are not as widely used as PFSA counterparts. Some of these commercially available membranes are:

Flemion®: PFSA fluoropolymer ion-exchange membrane introduced in 1975 by Asahi Glass Co. to be used for caustic soda production via chlor-alkali electrolysis. The functional (sulfonated) monomer unit of Flemion® is identical to that of Nafion®: $CF_2CFOCF_2CF(CF_3)OCF_2CF_2SO_3H$. Due to its electrolytic ion-exchange capacity Asahi Glass realized that it could be used in PEMFCs, so they started working on the development of electrode materials and MEAs using Flemion®. Recently, Asahi Glass introduce a newly developed Flemion®-based MEA that allows continuous operation for over 4,000 hours at a high temperature of 120°C, the first time it is done using a fluorine-based MEA.

Aciplex-F®: PFSA membrane introduced in 1975 by Asahi Kasei Chemicals Co. for chlor-alkali electrolysis. Aciplex-F®, as well as Nafion® and Flemion®, belongs to a family of ion-exchange perfluoropolymer membranes called "long-side-chain" (LSC) polymer due to the length of the functional monomer. Although very similar to Nafion® and Flemion® the sulfonated monomer unit of Aciplex-F® contains an extra fluorinated unit: $CF_2CFOCF_2CF(CF_3)OCF_2CF_2CF_2SO_3H$. The longer fluorinated side chain confers higher chemical stability to the membrane but reduces it ion-exchange capacity.

Hyflon® Ion: PFSA membranes developed by Solvay Solexis Inc. fabricated from the copolymer of tetrafluoroethylene (TFE) and a proprietary sulfonyl fluoride vinyl ether (SFVE) short-side-chain (SSC). The short side chain in Hyflon® Ion is very similar to that of the defunct Dow prototype membrane: $CF_2CFOCF_2CF_2SO_3H$. One of the main benefits of SSC ionomers is improved power output due to higher conductivity when compared to LSC counterparts. In addition, these types of membranes exhibit a higher ionic glass-transition temperature, which is a necessary condition operating cells at high temperatures without damaging the membrane [58].

Gore-Select®: PTFE–fluorinated ionomer composite membranes based on a PTFE microporous sheet reinforcement developed by Gore & Associates Inc. These composite membranes are micro-reinforced membranes in which non-ionically functional micro-porous PTFE medium (Gore-Tex®) is combined or impregnated with Nafion® [41]. Probably the main advantage of Gore-Select® membranes is their significantly mechanical strength when compared to other PFSA membranes; however, the membrane lower power output due to resistive losses originating from the non-ionically conducting PTFE support.

BAM3G: Ballard Advanced Materials 3rd Generation (BAM3G) membranes for PEMFC applications developed by Ballard Power systems. BAM3G are partially PFSA membranes based on sulfonated copolymers of α,β,β-trifluorostyrene and substituted

α,β,β-trifluorostyrene. They exhibit higher water retention, as well as superior PEMFC performance, than other PFSA due to their low equivalent weight (320–920) [41, 59].

Celtec-V® and Celtec-P®: Manufactured by PEMEAS GmbH (now BASF Fuel Cells GmbH). Celtec-V® is a proton exchange membrane based on polybenzimidazole (PBI) with an interpenetrating network of polyvinylphosphonic acid (PVPA). The polyelectrolyte PVPA is immobilized in the PBI matrix by interpenetration, crosslinking, and covalent bonding. The PBI matrix acts as a host material, whereas the continuous PVPA network serves as electrolyte. In the case of the Celtec-P® membranes the PBI is only doped with phosphoric acid [60]. The most noteworthy property of these membranes is their high operating temperature range (120-200°C). Multiple advantages over standard PFSA membranes arise from these elevated operational temperatures, including simple gas purification, facilitated water and thermal management, improved electrode tolerance to carbon monoxide poisoning, and reduced activation losses, among others.

Others membranes: Other commercially available PFSA and non-PFSA based membranes are PolyFuel's PolyFuel™ hydrocarbon-based membranes, FuMA-Tech's Fumapem® PFSA/PTFE copolymer-based membrane family, and Dais Analytic's sulfonated styrene-ethylene-butylene styrene copolymer membranes, among others.

1.3.4.2 New materials for polymer electrolyte membranes

The research field of polymer electrolyte membranes is tremendously active; owing to the surge in alternative energy technology programs. For instance, in the U.S., the Department of Energy has showed a considerable increase in interest and involvement in alternative energy technology-related projects. Ambitious targets and short periods of time to meet them are in general the common denominator of these programs, including those looking to push the development and deployment of fuel cell technology. As a result PEMFCs research has flourish and new polymer electrolyte material candidates thrive. It would certainly be impossible to address every single one of these materials so, just to give an idea of the breadth of alternatives being studied, a few will be mentioned.

The development of new membranes can be divided in six categories according to membrane type [41]:

- Per-fluorinated ionomer membranes
- Per-fluorinated ionomer composite membranes
- Partially per-fluorinated ionomer membranes
- Partially per-fluorinated ionomer composite membranes
- Non-per-fluorinated ionomer membranes
- Non-per-fluorinated ionomer composite membranes

and three categories according the membrane fabrication approach [23]:

- Copolymerization of monomers containing ionic-conducting moieties

- Modification of existing membranes/polymers to incorporate ionic-conducting features (e.g., aromatic sulfonation)
- Organic/inorganic and organic/organic composites or blends (the organic phase/phases of these composites can be fabricated following any of the two preceding methods)

Some of types of membranes currently in development include (detailed information of the membranes mentioned hereafter can be found elsewhere [17, 23, 41, 42, 59, 61]): homogeneous perfluorinated ionomer membranes (similar to Nafion®) where perfluorinated ionomers consist of a perfluoroalkyl side chain and a perfluoro alkyl ether side chain with a sulfonic acid group at its end. Micro-reinforced perfluorinated ionomer composite membranes (like Gore-Select®). Composites of perfluorinated ionomers with polythiophene or heteropolyacids like phosphotungstic acid, phosphomolybdenic acid or phosphotin acid. Grafted ionomer membranes based on styrene and divinylbenzene. A disadvantage of this type of membranes is the limited oxidation stability of their monomers due to the tertiary C–H bonds present in the styrene/divinylbenzene graft chains, which are sensitive to O_2 and hydrogen peroxide attack. Sulfonated or phosphonated Ionomer types based on poly(α,β,β-trifluorostyrene) and copolymers (like BAM3G membranes from Ballard). The disadvantage of this membrane type is the complicated production process for the monomer α,β,β-trifluorostyrene and the difficult sulfonation and phosphonation procedures for poly(α,β,β-trifluorostyrene) homopolymers and copolymers. Sulfonated

phenol-formaldehyde resins and sulfonated vinyl polymers. Phosphazene-based cation-exchange membranes. Homogeneous partially sulfonated arylene main-chain polymer membrane families. Some of these sulfonated arylene polymers families include: poly(phenylene ethers) like poly(2,6-dimethyl-1,4-phenylen ether) and poly(2,6-diphenyl-1,4-phenylen ether), poly(ether sulfone)s, poly(ether ketone)s (sPEK), poly(ether ether ketone)s (sPEEK), poly(phenylene sulfide)s, poly(phenylquinoxaline), poly(benzimidazole), and various poly(imide)s and poly(ether imide)s. These families of membranes exhibit the best chemical and mechanical stabilities after fluorinated polymer classes, and are able to reach long life spans; however, a general problem of homogeneous sulfonated arylene main-chain polymers is that these ionomers tend to swell to a large extent and thus lose mechanical stability when particular sulfonation thresholds are exceeded. Covalently cross-linked arylene main-chain ionomers and ionomer blends like sulfonated poly(styrene-co-divinyl benzene) ionomer membranes or covalent cross-linked sulfonated poly(ether sulfone). Ionically cross-linked ionomer networks obtained by mixing polymeric acids and polymeric bases to obtain networks which contain ionic cross-links formed by proton-transfer from the polymeric acid onto the polymeric base. Polymer/inorganic mineral acid composite membranes; a well-known example for this class of composite membranes is polybenzimidazole (PBI), which has phosphoric acid (or sulfuric acid) as proton-conducting electrolyte. This type of membranes show excellent proton conductivities, especially at temperatures of up to 130–150°C, well above the operational range of ionomers like Nafion®. H_3PO_4 composite membrane systems or "hydrogels" with high proton conductivities; for

example, poly(ethylene oxide)/poly(methyl methacrylate)/H_3PO_4 blends, poly(acryl amide)/poly(ethylene oxide)/H_3PO_4 blends, and poly(vinyl alcohol)/H_3PO_4 blends. Acidic polymer/low-molecular weight amphoter composite membranes capable of water-free proton conduction. An example of this type of membranes are blends of sulfonated polymers (e.g., sPEEK) with amphoteric compounds like imidazole or pyrazole. Imidazole and pyrazole function as both a base and as an acid and can transfer the proton from the acidic group to a basic nitrogen-base to form an imidazolium or pyrazolium cation. The cation can deliver the proton. Ionomer/inorganic oxide particle composite membranes. Nanostructured oxide materials (e.g., Nafion-SiO2 systems). Nanosize carbon materials (e.g., Nafion® doped with a mixture of fullerene and fullerenol). Crystalline solid electrolyte materials comprised of polymers doped with crystalline electrolytes like zirconyl phosphates (ZrP) and heteropolycompounds. Crystalline zirconium hydrophosphate in the form $Zr(HPO_4)_2 \cdot H2O$ and its related layered structures exhibit a high proton conductivity (more than 10^{-2} S/cm) across wide ranges of temperature (room temperature up to to 300°C). In addition, the ZrP additive enhances water retention characteristics and increases the maximum working temperature while reducing the membrane resistance. Thus, Nafion®-ZrP systems can reach conductivities in the order of 0.1 S/cm at 100°C and 100% humidity. Silica and molybdophosphoric acid modified Nafion®. Nafion®-polyfurfuryl alcohol nanocomposite membranes. Nafion® polypyrrole based membranes. Polyvinylidene fluoride + SiO_2 (or SiO_2 gel) + acid organic–inorganic composite membranes. Silanes/silica modified sPEEK. Irradiated sulfonated poly(ethylene-alt-tetrafluoro

ethylene) membranes. Asymmetric acrylic membranes. Functionalized polyvinylidene fluoride or low density polyethylene + styrene membranes.

Although the majority of these membranes exhibit excellent overall properties, application-related and design focus-related shortcomings exist. That is to say, for example, membranes particularly suitable for direct methanol fuel cells might not perform as well in hydrogen fuel cells, and vice versa. Concerning design focus, inexpensive membranes designed explicitly for short lifetime applications or to drive considerably small loads might not be adequate for long-term continuous operation and/or high power demanding systems. In this work we focus our attention on the study of reduced-cost membranes with characteristics and applicability comparable to that of Nafion® and other PFSA-based membranes.

1.4 Outline

A key issue in the field of polymer electrolyte materials, evident from the brief overview presented herein, is the overwhelming wide assortment of alternatives available; not to mention those yet to be discovered. As new candidate materials for PEMFCs electrolytes surface, it is urgent that characterization techniques keep up with the increased density of materials to characterize and/or optimize. Properties of interest are almost singular functions of the material design parameters; consequently, searching for an optimum, for example, is limited by the exponential decrease in probability of finding a better value as design parameters are varied. A step forward to alleviate this

limitation would be to introduce high-throughput techniques (HT) and combinatorial methodologies (CM) throughout the discovery, development, and optimization phases of new polymer electrolyte materials. HT and CM practices have been successfully used for decades in pharmaceutical and biomedical analysis to accelerate the development of new medicines. Lately, building on the gained know-how, these approaches have spread into the chemical industry as well as in multiple academic research fields. In the fuel cell area in particular, HT techniques have been widely used in the screening and optimization of catalysts [62-66]; however, little or no part has such approach taken in the development of new polymer electrolyte materials. HT and CM methodologies are already in place for the development and characterization of polymeric materials [67-73]; what's more, they have been used as optimization tools in membrane technology [74]. An important advance would be to introduce HT and CM methods tailored specifically for to the development, characterization, and optimization of polymer electrolytes. Towards this goal a new automated miniaturized high-throughput proton-conductivity screening system has been developed in this work. In addition, a refinement of a previously developed HT tool for mechanical characterization of free-standing polymer films [75], including new analysis algorithms, is presented to further expand the property characterization space of polymer electrolytes. On the combinatorial side a new microfluidic technique for the preparation of continuous-gradient combinatorial libraries of candidate materials for proton exchange membranes has been also developed and validated in this study (see appendix A).

Despite the large amount of promising material choices for polymer electrolytes, a considerable number may be considered to some extent "exotic materials" owing to multiple factors, including: expensive or uncommon reactants, convoluted synthesis mechanisms, complex scaling-up of the manufacturing process, low process yield, and/or elevated production costs, among others. To overcome some of these downsides a few polymer electrolyte developments have focused on the use and modification of commercially available and widespread engineering polymers (denoted as engineering plastics as well). Since the infrastructure to mass produce such polymers is already in place, changes to accommodate the variations introduced by the conversion of the engineering plastic to a polymer electrolyte are likely to be more straightforward (and probably cheaper) than scaling a whole new process from the ground up. What is more, most of these engineering polymers exhibit excellent mechanical and chemical stability properties that may probably pass on to the engineering polymer-based polyelectrolyte.

Two new types of polymer electrolytes based on poly(vinyledene fluoride) (PVDF) engineering plastics are presented in this work. The 1st type, which falls within the category of partially per-fluorinated ionomer composite (organic/organic) membranes (section 1.3.4.2), is based on a semi-interpenetrated network of PVDF and covalently crosslinked acrylic polyelectrolytes. The 2nd type corresponds to a "tri-phase" system where inorganic proton-conducting zirconium-based nanoparticles and microparticles are incorporated into the aforementioned PVDF/acrylic polyelectrolyte network to form an organic/organic/inorganic composite membrane. The primary goal of this study is to

characterize and determine property-structure relationships of such materials via HT techniques, in order to elucidate their suitability as polymer electrolyte membranes for PEMFCs.

The outline of this dissertation and a brief description of the chapters presented hereafter follow next:

- In Chapter 2, an innovative fully automated miniature high-throughput 4-electrode AC electrochemical impedance spectroscopy system for proton conductivity measurement (HTC) is presented. Design and modeling considerations of the system are described in detail. Thorough validation of the proton conductivity measuring capabilities of the HTC system is performed at several operational conditions by using Nafion® 112 standards. Measurements were also performed over 40 dissimilar types of PVDF/acrylic polyelectrolyte membranes to assess the sensitivity of the system to variations in membrane composition and preparatory conditions, and to determine the instrument usability for high-throughput screening purposes.
- In Chapter 3, the HTC system described in Chapter 2 is used in conjunction with a modified high-throughput apparatus for characterization of mechanical properties (HTMECH), to perform a comprehensive conductivity and mechanical high-throughput characterization of 80 different types of polymer electrolyte membranes fabricated from 5 dissimilar grades of PVDF and 2 distinct acrylic polyelectrolytes. Conductivity and mechanical data are analyzed with appropriate statistical tools and coupled with Fourier transform infra red

spectroscopy (FT-IR), X-ray diffraction, differential scanning calorimetry (DSC), and scanning electron microscopy (SEM) to develop structure-property relationships.

- In Chapter 4, the HTC and HTMECH techniques used in Chapter 3 are extended to novel tri-phase organic/organic/inorganic nano- and micro-composite polymer electrolyte membranes. Both mechanical and conductivity high-throughput characterizations are carried out on 50 dissimilar membranes manufactured from 5 different grades of PVDF, a single type of acrylic polyelectrolyte, and 3 distinct types of nanoparticles; namely, zirconium(IV) oxide (ZrO_2), zirconium(IV) hydroxide sulfated ($Zr(H_2SO_4)_4$), and zirconium(IV) hydrogenphosphate ($Zr(HPO_4)_2$). The effect of the presence of nanoparticles dispersed in the PVDF/acrylic polyelectrolyte matrix on conductivity and mechanical characteristics is investigated and compared to analogous two-phase organic/organic PVDF/acrylic polyelectrolyte semi-interpenetrated network membranes studied in Chapter 3.

1.5 References

1. Hart, D., *Sustainable energy conversion: fuel cells — the competitive option?* Journal of Power Sources, 2000. **86**: p. 23-27.
2. International Energy Agency, *World Energy Outlook 2008*. 2008: OECD/IEA. 578.
3. Irvine, J.T.S., *The Bourner lecture-Power sources and the new energy economy.* Journal of Power Sources, 2004. **136**: p. 203-207.

4. Sopian, K. and Daud, W.R.W., *Challenges and future developments in proton exchange membrane fuel cells.* Renewable Energy, 2006. **31**: p. 719-727.

5. *Energy Bulletin.* www.energybulletin.net, 04/2006

6. EPA, *The Benefits and Costs of the Clean Air Act 1990 to 2010 (EPA Report to Congress)*. 1999, United States Environmental Protection Agency, Office of Air and Radiation Policy. p. 654.

7. Johnston, B., Mayo, M.C., and Khare, A., *Hydrogen: the energy source for the 21st century.* Technovation, 2005. **25**: p. 569-585.

8. Energy Information Administration, *Electric Power Annual with data for 2007.* www.eia.doe.gov, 2009.

9. Schumacher, E.F., *Small Is Beautiful: Study of Economics as If People Mattered*. 1993: Vintage. 272.

10. Du Melle, F., *The global and urban environment: the need for clean power systems.* Journal of Power Sources, 1998. **71**: p. 7-11.

11. Carrette, L., Friedrich, K.A., and Stimming, U., *Fuel Cells-Fundamentals and Applications.* Fuel Cells, 2001. **1**(1): p. 5-39.

12. Kerres, J.A., *Blended and Cross-Linked Ionomer Membranes for Application in Membrane Fuel Cells.* Fuel Cells, 2005. **5**(2): p. 230-247.

13. Arita, M., *Technical Issues of Fuel Cell Systems for Automotive Application.* Fuel Cells, 2002. **2**(1): p. 10-14.

14. Preli, F., *Technical Challenges for Fuel Cells in Mobile Applications.* Fuel Cells, 2002. **2**(1): p. 5-9.

15. Williams, M.C., *Status and Promise of Fuel Cell Technology.* Fuel Cells, 2001. **1**(2): p. 87-91.

16. Alcaide, F., Cabot, P.-L., and Brillas, E., *Fuel cells for chemicals and energy cogeneration.* Journal of Power Sources, 2006. **153**: p. 47-60.

17. Meier-Haack, J., et al., *Membranes from sulfonated block copolymers for use in fuel cells (review).* Separation and Purification Technology, 2005. **41**: p. 207-220.

18. Kreuer, K.-D., et al., *Transport in Proton Conductors for Fuel-Cell Applications: Simulations, Elementary Reactions, and Phenomenology.* Chemical Reviews, 2004. **104**(10): p. 4637-4678.

19. Cropper, M.A.J., Geiger, S., and Jollie, D.M., *Fuel cells: a survey of current developments.* Journal of Power Sources, 2004. **131**: p. 57-61.

20. Appleby, A.J. and Foulkes, F.R., *Fuel Cell Handbook*. 1992, New Yotk: Van Nostrand Reinhold Co. 752.

21. Rajendran, R.G., *Polymer electrolyte membrane technology for fuel cells.* MRS Bulletin, 2005. **30**: p. 587-590.

22. Grot, W.G., *CF_2=$CFCF_2CF_2SO_2F$ and Derivatives and Polymers Thereof*. Patent No. U.S. 3,718,627. E.I. DuPont de Nemours & Company. 1973.

23. Hickner, M.A., et al., *Alternative Polymer Systems for Proton Exchange Membranes (PEMs).* Chemical Reviews, 2004. **104**: p. 4587-4612.

24. Wilson, M.S. and Gottesfeld, S., *Thin-film catalyst layers for polymer electrolyte fuel cell electrodes.* Journal of Applied Electrochemistry, 1992. **22**: p. 1-7.

25. Benítez, R., Soler, J., and Daza, L., *Novel method for preparation of PEMFC electrodes by the electrospray technique.* Journal of Power Sources, 2005. **151**: p. 108-113.

26. Heitner-Wirguin, C., *Recent advances in perfluorinated ionomer membranes: structure, properties and applications.* Journal of Membrane Science, 1996. **120**: p. 1-33.

27. Mauritz, K.A. and Moore, R.B., *State of Understanding of Nafion.* Chemical Reviews, 2004. **104**(10): p. 4535-4585.

28. Roshandel, R., Farhanieh, B., and Saievar-Iranizad, E., *The effects of porosity distribution variation on pem fuel cell performance.* Renewable Energy, 2005. **30**(10): p. 1557-1572.

29. Wang, C.-Y., *Fundamental Models for Fuel Cell Engineering.* Chemical Reviews, 2004. **104**: p. 4727-4766.

30. EG&G Technical Services Inc., *Fuel Cell Handbook*. 7th ed, ed. U.S. Department of Energy. 2004, Morgantown, WV: U.S. Department of Energy, Office of Fossil Energy, National Energy Technology Laboratory.

31. Davies, D.P., et al., *Stainless steel as a bipolar plate material for solid polymer fuel cells.* Journal of Power Sources, 2000. **86**(1-2): p. 237-242.

32. Blomen, L.J.M.J. and Mugerwa, M.N., *Fuel Cell Systems*. 2nd ed. 1993, New York: Springer-Verlag New York, LLC. 636.

33. Ramakumar, R., *Fuel cells-an introduction.* Power Engineering Society Summer Meeting, 2001. IEEE, 2001. **1**: p. 702-709.

34. Wright, P.V., *Polymer electrolytes - the early days.* Electrochimica Acta, 1998. **43**(10-11): p. 1137-1143.

35. Xing, P., et al., *Synthesis and characterization of poly(aryl ether ketone) copolymers containing (hexafluoroisopropylidene)-diphenol moiety as proton exchange membrane materials.* Polymer, 2005. **46**: p. 3257-3263.

36. Gómez-Romero, P., Asensio, J.A., and Borrós, S., *Hybrid proton-conducting membranes for polymer electrolyte fuel cells Phosphomolybdic acid doped poly(2,5-benzimidazole)—(ABPBI-$H_3PMo_{12}O_{40}$).* Electrochimica Acta, 2005. **50**: p. 4715-4720.

37. Swier, S., et al., *Polymer blends based on sulfonated poly(ether ketone ketone) and poly(ether sulfone) as proton exchange membranes for fuel cells.* Journal of Membrane Science, 2005. **256**: p. 122-133.

38. Commer, P., et al., *The effect of water content on proton transport in polymer electrolyte membranes.* Fuel Cells, 2002. **2**(3-4): p. 127-136.

39. Eikerling, M., et al., *Mechanisms of Proton Conductance in Polymer Electrolyte Membranes.* The Journal of Physical Chemistry B, 2001. **105**: p. 3646-3662.

40. Thampan, T.M., et al., *Systematic Approach to Design Higher Temperature Composite PEMs.* Journal of The Electrochemical Society, 2005. **152**(2): p. A316-A325.

41. Savadogo, O., *Emerging membranes for electrochemical systems Part II. High temperature composite membranes for polymer electrolyte fuel cell (PEFC) applications.* Journal of Power Sources, 2004. **127**: p. 135-161.

42. Kerres, J.A., *Development of ionomer membranes for fuel cells.* Journal of Membrane Science, 2001. **185**: p. 3-27.

43. Hickner, M.A. and Pivovar, B.S., *The Chemical and Structural Nature of Proton Exchange Membrane Fuel Cell Properties.* Fuel Cells, 2005. **5**(2): p. 213-229.

44. Alberti, G., et al., *New Preparation Methods for Composite Membranes for Medium Temperature Fuel Cells Based on Precursor Solutions of Insoluble Inorganic Compounds.* Fuel Cells, 2005. **5**(3): p. 366-374.

45. Curtin, D.E., et al., *Advanced materials for improved PEMFC performance and life.* Journal of Power Sources, 2004. **131**: p. 41-48.

46. Gode, P., et al., *Membrane Durability in a PEM Fuel Cell Studied Using PVDF Based Radiation Grafted Membranes* Fuel Cells, 2003. **3**(1-2): p. 21-27.

47. Harrison, W.L., et al., *Poly(Arylene Ether Sulfone) Copolymers and Related Systems from Disulfonated Monomer Building Blocks: Synthesis, Characterization, and Performance - A Topical Review.* Fuel Cells, 2005. **5**(2): p. 201-212.

48. Honma, I., et al., *A Sol-Gel Derived Organic/Inorganic Hybrid Membrane for Intermediate Temperature PEFC.* Fuel Cells, 2002. **2**(1): p. 52-58.

49. Karlsson, L.E. and Jannasch, P., *Polysulfone ionomers for proton-conducting fuel cell membranes 2. Sulfophenylated polysulfones and polyphenylsulfones.* Electrochimica Acta, 2005. **50**: p. 1939-1946.

50. Li, Q., et al., *PBI-Based Polymer Membranes for High Temperature Fuel Cells - Preparation, Characterization and Fuel Cell Demonstration.* Fuel Cells, 2004. **4**(3): p. 147-159.

51. Pan, M., et al., *Fabrication and Performance of Polymer Electrolyte Fuel Cells by Self-Assembly of Pt Nanoparticles.* Journal of The Electrochemical Society, 2005. **152**(6): p. A1081-A1088.

52. Schuster, M., et al., *About the Choice of the Protogenic Group in PEM Separator Materials for Intermediate Temperature, Low Humidity Operation: A Critical Comparison of Sulfonic Acid, Phosphonic Acid and Imidazole Functionalized Model Compounds.* Fuel Cells, 2005. **5**(3): p. 355-365.

53. Shin, J.-P., et al., *Sulfonated polystyrene/PTFE composite membranes.* Journal of Membrane Science, 2005. **251**(247-254).

54. Souzy, R., et al., *Proton-Conducting Polymer Electrolyte Membranes Based on Fluoropolymers Incorporating Perfluorovinyl Ether Sulfonic Acids and Fluoroalkenes: Synthesis and Characterization.* Fuel Cells, 2005. **5**(3): p. 383-397.

55. Tchicaya-Bouckary, L., Jones, D.J., and Rozière, J., *Hybrid Polyaryletherketone Membranes for Fuel Cell Applications.* Fuel Cells, 2002. **2**(1): p. 40-45.

56. Xiao, L., et al., *Synthesis and Characterization of Pyridine-Based Polybenzimidazoles for High Temperature Polymer Electrolyte Membrane Fuel Cell Applications.* Fuel Cells, 2005. **5**(2): p. 287-295.

57. Jalani, N.H., Dunn, K., and Datta, R., *Synthesis and characterization of Nafion®-MO_2 (M = Zr, Si, Ti) nanocomposite membranes for higher temperature PEM fuel cells.* Electrochimica Acta, 2005. **51**(3): p. 553-560.

58. Arcella, V., Troglia, C., and Ghielmi, A., *Hyflon Ion Membranes for Fuel Cells.* Industrial & Engineering Chemistry Research, 2005. **44**: p. 7646-7651.

59. Dobrovol'skii, Y.A., et al., *Proton-Exchange Membranes for Hydrogen-Air Fuel Cells.* Russian Journal of General Chemistry, 2007. **77**(4): p. 766-777.

60. Gubler, L., et al., *Celtec-V, A Polybenzimidazole-Based Membrane for the Direct Methanol Fuel Cell.* Journal of The Electrochemical Society, 2007. **154**(9): p. B981-B987.

61. Neburchilov, V., et al., *A review of polymer electrolyte membranes for direct methanol fuel cells.* Journal of Power Sources, 2007. **169**: p. 221-238.

62. Smotkin, E.S., et al., *High-throughput screening of fuel cell electrocatalysts.* Applied Surface Science, 2006. **252**: p. 2573-2579.

63. Liu, R. and Smotkin, E.S., *Array membrane electrode assemblies for high throughput screening of direct methanol fuel cell anode catalysts.* Journal of Electroanalytical Chemistry, 2002. **535**: p. 49-55.

64. Chu, Y.-H., et al., *Evaluation of the Nafion effect on the activity of Pt–Ru electrocatalysts for the electro-oxidation of methanol.* Journal of Power Sources, 2003. **118**: p. 334-341.

65. Cooper, J.S. and McGinn, P.J., *Combinatorial screening of thin film electrocatalysts for a direct methanol fuel cell anode.* Journal of Power Sources, 2006. **163**: p. 330-338.

66. Woo, Seong I., et al., *Current Status of Combinatorial and High-Throughput Methods for Discovering New Materials and Catalysts.* QSAR & Combinatorial Science, 2005. **24**(1): p. 138-154.

67. Meredith, J.C., Karim, A., and Amis, E.J., *High-Throughput Measurement of Polymer Blend Phase Behavior.* Macromolecules, 2000. **33**: p. 5760-5762.

68. Meredith, J.C., *A Perspective on High-Throughput Polymer Science.* Journal of Materials Science, 2003. **38**(22): p. 4427-4437.

69. Webster, D.C., *Combinatorial and high-throughput methods in macromolecular materials research and development.* Macromolecular Chemistry and Physics, 2008. **209**(3): p. 237-246.

70. Johnson, P.M., et al., *High throughput kinetic analysis of photopolymer conversion using composition and exposure time gradients.* Polymer, 2005. **46**: p. 3300-3306.

71. Ohtani, M., et al., *Development of high-throughput combinatorial terahertz time-domain spectrometer and its application to ternary composition-spread film.* Applied Surface Science, 2006. **252**(7): p. 2622-2627.

72. Guerrero-Sanchez, C., et al., *High-throughput experimentation in synthetic polymer chemistry: From RAFT and anionic polymerizations to process development.* Applied Surface Science, 2006. **252**(7): p. 2555-2561.

73. Sormana, J.-L. and Meredith, J.C., *High-Throughput Discovery of Structure-Mechanical Property Relationships for Segmented Poly(urethane-urea)s.* Macromolecules, 2004(37): p. 2186-2195.

74. Vandezande, P., et al., *High throughput membrane testing and combinatorial techniques: powerful new instruments for membrane optimisation.* Desalination, 2006. **199**: p. 395-397.

75. Sormana, J.-L., Chattopadhyay, S., and Meredith, J.C., *High-throughput mechanical characterization of free-standing polymer films.* Review of Scientific Instruments, 2005. **76**: p. 062214.

Chapter 2
High-Throughput Screening of Ionic Conductivity in Polymer Membranes

Reproduced with permission from Zapata, Pedro.; Basak, Pratyay.; and Meredith, J. C. *Electrochimica Acta*, **2009**, (accepted manuscript) doi:10.1016/j.electacta.2009.02.009.

Combinatorial and high-throughput techniques have been successfully used for efficient and rapid property screening in multiple fields. The use of these techniques can be an advantageous new approach to assay ionic conductivity and accelerate the development of novel materials in research areas such as fuel cells. A high-throughput ionic conductivity (HTC) apparatus is described and applied to screening candidate polymer electrolyte membranes for fuel cell applications. The device uses a miniature four-point probe for rapid, automated point-to-point AC electrochemical impedance measurements in both liquid and humid air environments. The conductivity of Nafion® 112 HTC validation standards was within 1.8% of the manufacturer's specification. HTC screening of 40 novel Kynar® poly(vinylidene fluoride) (PVDF)/acrylic polyelectrolyte (PE) membranes focused on varying the Kynar® type (5x) and PE composition (8x) using reduced sample sizes. Two factors were found to be significant in determining the

proton conducting capacity: (1) Kynar® PVDF series: membranes containing a particular Kynar® PVDF type exhibited statistically identical mean conductivity as other membranes containing different Kynar® PVDF types that belong to the *same* series or family. (2) Maximum effective amount of polyelectrolyte: increments in polyelectrolyte content from 55wt% to 60wt% showed no statistically significant effect in increasing conductivity. In fact, some membranes experienced a reduction in conductivity.

2.1 Introduction

Combinatorial synthesis and high-throughput screening techniques have become valuable alternative methodologies for development and characterization of new and advanced materials; including: catalysts, electrolytes, biodegradable and/or biocompatible materials, thin films and coatings, composites, and polymers, among others [1-11]. For numerous applications of some of these materials (e.g., ion exchange membranes for water purification, dye-sensitized solar cells, and proton exchange membranes) ionic conductivity is an essential property; however, high-throughput tools for screening ionic conductivity of polymeric combinatorial libraries have not been reported. The usefulness of a high-throughput conductivity (HTC) device can be appreciated by considering an example: proton exchange membranes for fuel cells. Fuel cells that utilize proton-conducting polymer electrolyte membranes (PEMs) have become attractive alternatives as energy sources for a wide variety of applications [12]. PEMs are inherently complex and the optimization of properties such as water sorption, swelling, proton conductivity, mechanical integrity, membrane selectivity, and

electrochemical stability is not trivial [13]. In particular, these properties are often at odds with one another and fine-tuning them via chemistry and processing is tedious. The application of combinatorial and high-throughput methods can offer significant efficiency and cost advantages to the discovery and optimization process. While a number of combinatorial synthesis strategies are potentially applicable to PEMs [2-6, 14-16], tools for rapid screening of properties relevant to PEMs are still needed. In this paper, we report the development of a HTC screening tool that is applicable to a range of advanced materials; however, we restrict attention to PEM materials in this report.

PEM proton conductivity is predominantly studied by AC electrochemical impedance spectroscopy (EIS) under a wide variety of environments (i.e., liquid water, water vapor, diluted acid, humidified gases, etc.) [17]. Traditionally, EIS measurements are carried out using conductivity cells consisting of a longitudinal geometry setup with 2 or 4 transverse platinum electrodes [18-21]. The need of fairly large homogeneous samples (e.g., 5cm by 1cm) renders this approach costly and time consuming, especially during the discovery stages of new polyelectrolytes when only small amounts of samples may be available. In addition the likelihood of overlooking effects on conductivity due to small changes in the polyelectrolyte structure or thickness variations is relatively high. High-throughput testing methodologies amenable to smaller sample sizes address the aforesaid limitations by reducing the time and cost associated with the experimentation involved in the development and/or characterization of new materials.

The automated EIS instrument we have developed was designed for rapid serial high-throughput characterization of ionic conductivity using a miniature four-point

probe, overcoming some of the issues common to conventional conductivity cells. The design of the HTC system follows the same principles as a high-throughput mechanical characterization (HTMECH) apparatus previously developed in our lab [22, 23], enabling relatively fast screening of small homogeneous and non-homogeneous (discrete or gradient combinatorial library) samples.

Following a detailed description of the HTC system design and operation, validation measurements performed on Nafion® 112 standards are presented to demonstrate the system's accuracy, repeatability, and sensitivity to small variations on membrane properties (e.g., thickness). Measurements performed over various custom Kynar®/acrylic polyelectrolyte PEMs are presented as well to show the utility of the HTC to rapidly characterize multiple compositions, while highlighting its potential to be used in conjunction with combinatorial methods (e.g., combinatorial PEM libraries with thickness or composition gradients) to speed up the screening process of novel materials for polymer electrolyte membrane fuel cells (PEMFCs).

2.2 Experimental

2.2.1 HTC apparatus

2.2.1.1 Theory and modeling considerations

Measuring the resistivity to the flow of AC or DC current is the generally accepted approach to determine the proton conductivity of membranes. Resistivity for homogeneous membranes with constant cross-sectional area is easily determined by:

$$\rho = R_0 \frac{A}{d} \qquad 2.1$$

where ρ is the membrane resistivity, R_0 is the ohmic resistance of the membrane (ratio of the voltage drop between the opposite edges of the sample and the current applied), d is the sample length (equivalent to the current path length), and A is the sample cross-sectional area. Commonly used for resistivity measurements under direct current (DC), Equation 2.1 is equally valid for alternating current (AC) measurements given that the ohmic resistance of the membrane is theoretically identical for both DC and AC conditions. Under AC conditions impedance spectroscopy is used to approximate the membrane ohmic resistance to the low-frequency limit of the complex impedance, where the total reactance is negligible:

$$Z_{(jw)} = \frac{V_{(jw)}}{I_{(jw)}} = Z'_{(w)} - jZ''_{(w)} \qquad 2.2$$

$$\rho\big|_{Z''\to 0} \approx Z_{(jw)} \frac{A}{d} \qquad 2.3$$

where $Z_{(jw)}$ corresponds to the complex impedance, $V_{(jw)}$ and $I_{(jw)}$ are the complex AC voltage and current, respectively; and $Z'_{(w)}$ and $Z''_{(w)}$ are the frequency-dependent resistance (real) and reactance (imaginary), respectively.

Impedance spectroscopy involves a perturbation with a monochromatic current signal (input) and measurement of the voltage response to (output). The ratio between the output and the input signals constitutes the system's complex impedance for the

corresponding perturbation frequency. The frequency dependence of the impedance defines the system transfer function that describes entirely the dynamic properties of a linear system [24, 25]. Electrochemical systems (e.g., proton-conductive membrane/electrodes system) are, however, inherently non-linear (i.e., doubling the current does not necessarily double the voltage). For non-linear systems complex transfer coefficients depend on both the frequency and the *amplitude* of the perturbation signal, and fail to render a unique description of the dynamic properties of the system. Electrochemical impedance spectroscopy (EIS) addresses the non-linearity of electrochemical systems by implementing local analysis of pseudo-linear responses to *small* amplitude perturbation signals, under the hypotheses of *linearity* (at the scale of the perturbation) and *steady state*, to estimate the system transfer function [24-27]. This is equivalent to limiting measurements to a very small portion of the system's non-linear potential-voltage profile, such that it appears to be linear.

Two-electrode and four-electrode configurations are customarily utilized for EIS; however, the four-terminal arrangement provides a separate path for the current carriers (working and counter electrodes) and the open voltage sensing terminals (reference electrodes) that effectively decreases charge transfer resistances and inductive impedance [18, 28]. As a result, reactance and non-ohmic resistances effects are minimized, facilitating the estimate of the true membrane ohmic resistance. Most four-electrode arrangements for proton-conductive membranes analysis (e.g., conductivity cells) have flat longitudinal electrodes that contact the sample along its entire width. The constant cross-sectional area along the current path of this configuration results in

constant current density and electric field strength that allows the direct use of Equation 2.3 to determine the membrane resistivity. In the case of point-contact type collinear four-electrode arrangements like the four-point probe (as illustrated schematically in Figure 2.1), however, current is injected and collected by the outer electrodes at *infinitesimal points* on the membrane surface, creating a dipole source that generates a field distribution inside the sample. Assuming a membrane material of uniform resistivity, a suitable model that accounts for the geometrical dependence of the current density and the potential induced by the dipole can be obtained by solving the steady state Laplace equation, or similarly, the equivalent electric field model given by:

$$E = \rho J \tag{2.4}$$

$$-\nabla\Phi = \rho\frac{I}{A} \tag{2.5}$$

where E is the applied electric field, defined as the gradient of the electric potential at any point on the membrane ($-\nabla\Phi$); and J is the current density, defined as the current per unit area normal to the current flow (I/A). Equation 2.5 can be solved rigorously via the method of images [29] or a Fourier-Bessel approach [30] to obtain a general model for the potential distribution over a membrane. However, for homogeneous membranes over non-conducting substrates and uniform thickness (h) *significantly smaller* than the inter-electrode spacing, one can assume cylindrical symmetry for the current flow at every contact point of the current-carrying electrodes (current flows

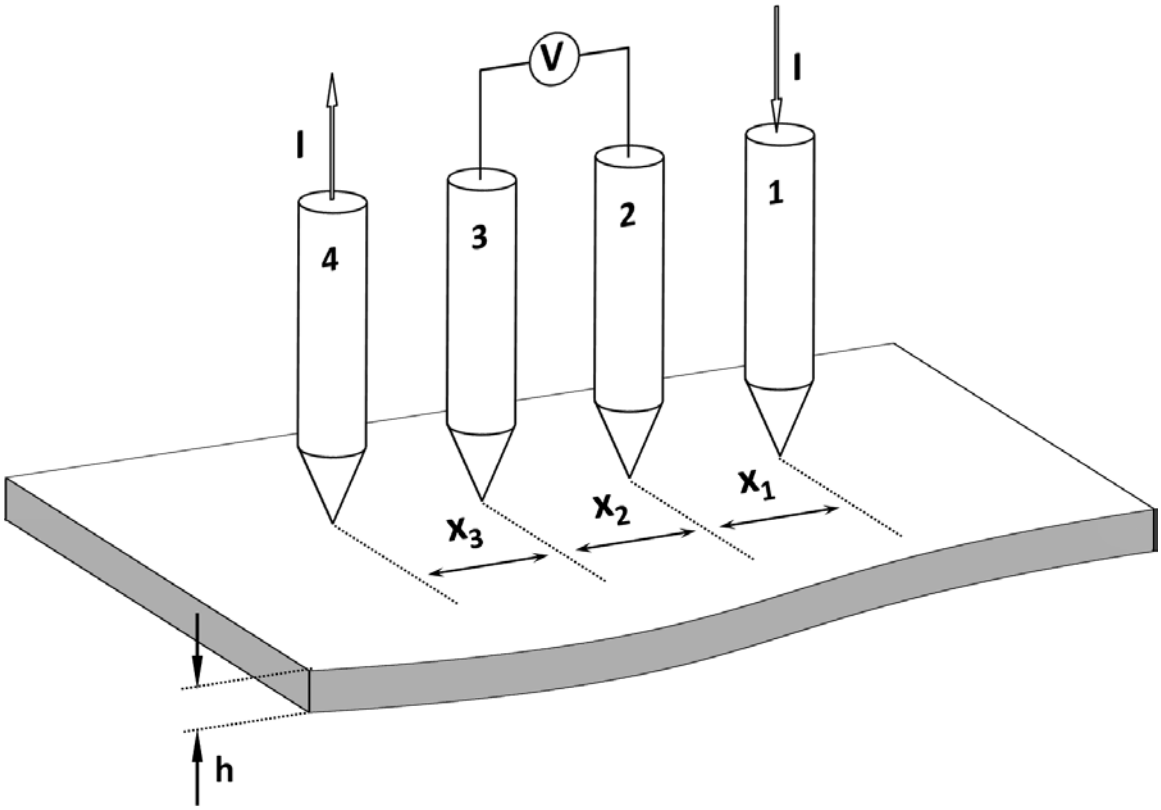

Figure 2.1 Schematic of the HTC collinear four-point probe arrangement for resistivity measurements over a homogeneous PEM of constant thickness *h*. Electrodes 2 and 3 correspond to the reference electrodes, while electrodes 1 and 4 constitute the current source and current collector respectively.

radially within discs of identical thickness as the membrane, as seen in Figure 2.2). Equation 2.5 is thus simplified to:

$$-\frac{d\Phi}{dr} = \frac{\rho I}{2\pi r h} \tag{2.6}$$

where r is the radial distance to a current-carrying contact point. Integration of Equation 2.6 is straightforward and leads to the floating potential at any arbitrary point on the membrane as a function of its distance to the current source:

$$\Phi - \Phi_0 = -\frac{\rho I}{2\pi h}\ln(r) \tag{2.7}$$

The total floating potential at a particular point on the membrane is given by the sum of the potentials induced by every current source or current collector electrode in contact with the membrane surface (current flowing in and current flowing out). Referring to Figure 2.2, the two outer electrodes of the four-point probe configuration carry currents of equal magnitude but opposite direction. Hence, the total floating potential of the reference electrodes is given by:

$$\Phi_2 = -\frac{\rho I}{2\pi h}\ln\left(\frac{x_1}{x_2 + x_3}\right) \tag{2.8}$$

$$\Phi_3 = -\frac{\rho I}{2\pi h}\ln\left(\frac{x_1 + x_2}{x_3}\right) \tag{2.9}$$

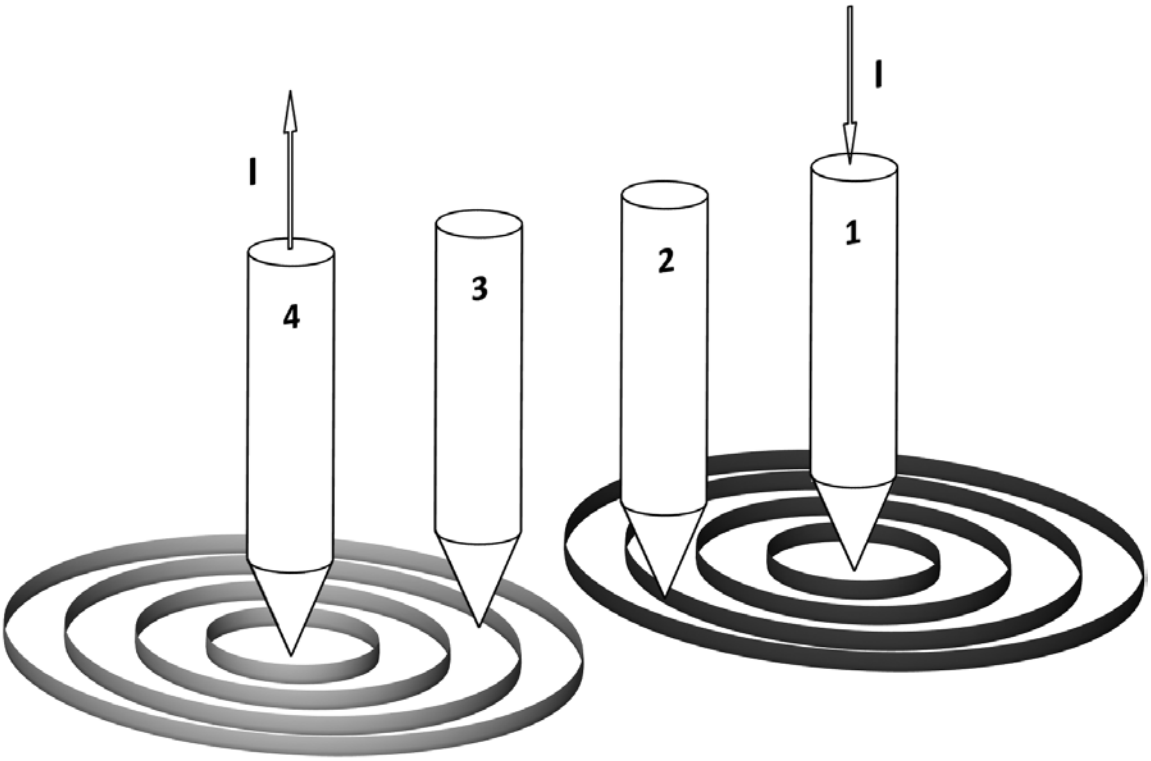

Figure 2.2 Representation of the current flow cylindrical symmetry at the current source and collector contact points. Rings represent the isocurrent surfaces perpendicular to the approximate radial current flow path.

where x_i are the distances between electrodes as indicated in Figure 2.1. The potential difference between the reference electrodes is then:

$$V = \Phi_2 - \Phi_3 = -\frac{\rho I}{2\pi h}\left[\ln\left(\frac{x_1}{x_2 + x_3}\right) - \ln\left(\frac{x_1 + x_2}{x_3}\right)\right] \qquad 2.10$$

From where membrane proton conductivity ($\sigma = 1/\rho$), including geometric correction factors (f_i) that account for edge effects due to small sample size and deviations from the assumed current flow cylindrical symmetry, is given by:

$$\sigma = -\frac{I}{V}\frac{1}{2\pi h}\left[\ln\left(\frac{x_1}{x_2 + x_3}\right) - \ln\left(\frac{x_1 + x_2}{x_3}\right)\right] f_1 f_2 \qquad 2.11$$

$$\sigma\big|_{Z'' \to 0} \approx -\frac{1}{Z_{(jw)}}\frac{1}{2\pi h}\left[\ln\left(\frac{x_1}{x_2 + x_3}\right) - \ln\left(\frac{x_1 + x_2}{x_3}\right)\right] f_1 f_2 \qquad 2.12$$

2.2.1.2 Design

An image of the HTC apparatus is shown in Figure 2.3 and Figure 2.4. As a proof of concept for the initial HTC design a commercially available miniature cylindrical four-point resistivity probe head (Jandel Engineering Ltd.) with equally separated tungsten carbide electrodes ($x_1 = x_2 = x_3 = x = 0.635$ mm) of 0.2 mm in diameter was utilized. For this particular case, where the point-type electrodes are equally spaced, Equation 2.12 is further simplified:

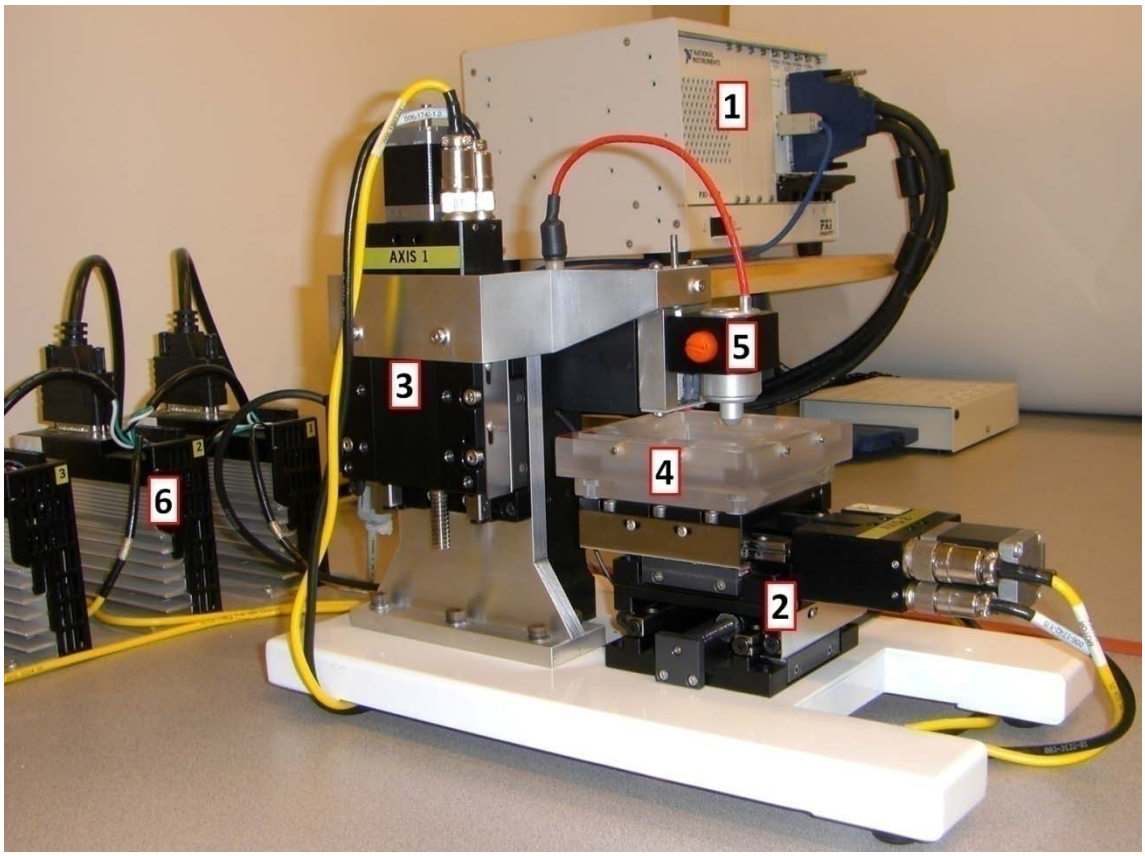

Figure 2.3 HTC apparatus. (1) Programmable stepper motion controller and multifunction DAQ system. (2) Motorized sample positioning X-Y stage. (3) Motorized vertical axis and optical encoder. (4) Sample holder (installed). (5) Four-point resistivity probe and thickness gauging probe retention mechanism (four-point resistivity probe shown connected). (6) Microstepping drives.

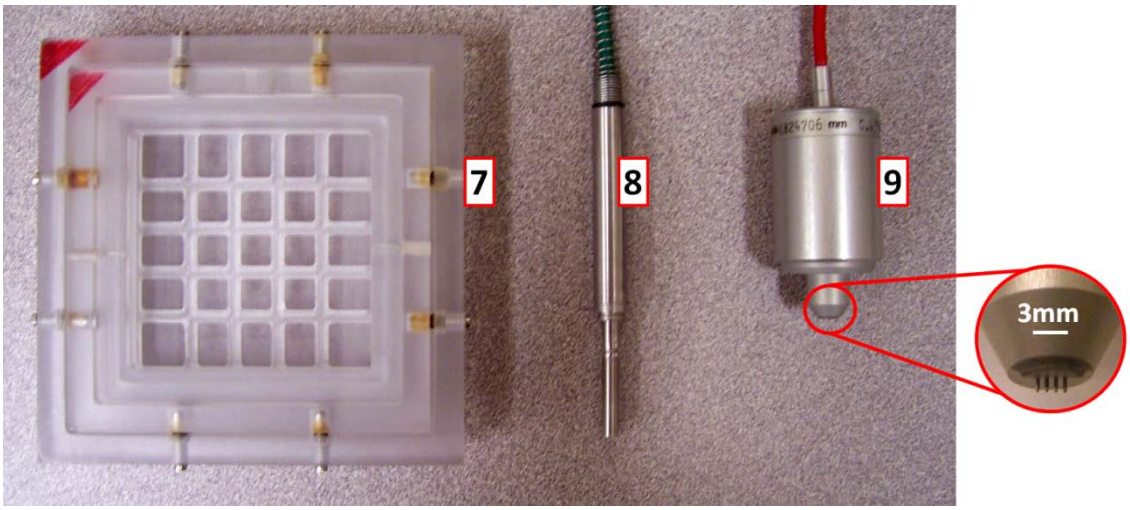

Figure 2.4 HTC apparatus (cont'd). (7) Sample holder (detached). Comprised of two parts: a reservoir/base (delimited by the outer rim), and a spring-loaded sample retention mechanism (grid). (8) Linear displacement digital gauging probe. (9) Miniature four-point resistivity probe.

$$\sigma\big|_{Z''\to 0} \approx \frac{1}{Z_{(jw)}} \frac{\ln(2)}{\pi h} f_1 f_2 \qquad 2.13$$

where $f_1 \cong f_2 \cong 1$ for $h/x \leq 0.5$ (thin membranes) and $d/x > 40$ (large lateral dimension d) [31, 32]. It is important to notice that the aforementioned model is based purely on the electrical behavior of the membrane and the geometry of the electrode array utilized for EIS, and does not account for the effect of the measurement circuit parasitic inductance on the voltage reading between the reference electrodes. The measurement circuit inductance, or residual inductance, arises from the changing magnetic flux within the loop of the circuit due to the alternating nature of the applied current. Its effect on the

voltage reading is frequency dependent and becomes dominant at very high frequencies; however, it approaches to zero at the low-frequency limit of the complex impedance where the ohmic resistance of the membrane is approximated to its complex impedance. The residual inductance can be determined by integrating the electric field around the loop of the measurement circuit [33]. Other additional electrical error sources that can potentially affect the precise measurement of membrane impedance, and that need to be corrected for, include capacitance and inductance of the electrode leads, stray capacitance between the electrodes, contact resistance between the electrodes and the membranes, and electromagnetic noise, among others [28]. The miniature four-point probe head is affixed to a vertical axis that consists of a precision grade 2.0 mm lead ballscrew Parker MX80S motorized linear slide (Parker Hannifin Co.).

Signal generation and reading are carried out with a PXI-6031E multifunction data acquisition (DAQ) system (National Instruments Co.). Specifically, the working and counter electrodes of the four-point probe are connected to a 100 kS/s 16-bit resolution analog output that allows for proper digitization of analog signals of frequencies of up to 50 kHz (sinusoidal signals); while the reference electrodes are connected to a high-impedance differential analog input with a maximum multiplexed sampling rate of 100 kS/s. Voltage readings are performed directly with the DAQ system, while the current flow through the working and counter electrodes is indirectly determined via the I-V method [34] by measuring the voltage drop across a very high precision 1070 Ω reference resistor.

The membrane sample holder was made of low-wear electrical-insulating polyoxymethylene in order to avoid boundary effects that can disrupt the current distribution on the membrane. The sample holder consists of two parts: a reservoir-like base that can be filled with water or acidic solutions for submerged measurements, and a 5 x 5 spring-loaded grid-like retention mechanism that provides uniform pressure on the sample to prevent slippage. The system provides 25 testing locations of 7 mm x 7 mm each and a maximum sample size of approximately 58 mm x 58 mm. It is important to note that the number of available testing locations is a limitation given by the size of the four-point probe head, and that further miniaturization of the four-electrode assembly will allow for a considerable increase in the number of testing locations. The sample holder is mounted over an automated X-Y stage consisting of two orthogonal 1.0 mm lead leadscrew Parker MX80S motorized linear slides (Parker Hannifin Co.) that allows precise sample positioning from one testing location to another. All linear slides are driven by individual Parker E-AC microstepping drives (Parker Hannifin Co.) and controlled using a PXI-7334 four-axis programmable stepper motion controller (National Instruments Co.). The HTC is also equipped with a flat-tip 0.12 μm resolution Omega GP901-2 linear displacement digital gauging probe with low spring constant (Omega Engineering, Inc.), attached to the vertical axis, for localized membrane thickness characterization prior to conductivity tests. The low spring constant of the displacement probe helps minimize the error in conductivity calculations arising from membrane compression when measuring the thickness of swollen membranes. The vertical axis was

coupled with a 0.1 μm resolution RGH24 Renishaw optical encoder (Renishaw plc.) to ensure repeatability of sequential positioning cycles of the displacement probe.

A custom LabVIEW™ program was developed to automate and control the HTC system (sample and probe positioning; and data acquisition, manipulation, analysis, and storage).

2.2.1.3 Signal analysis

Due to their small level the signals used in EIS are frequently overshadowed by noise and harmonics, as well as coupled with DC-offsets. To decouple the required signal from these unwanted parasitic components a sine correlation extraction approach [35, 36] is utilized. A schematic of the principle of this technique applied to the HTC is shown in Figure 2.5. The technique correlates the system's response to an excitation signal $P(t) = P_0 \sin wt$ with two reference signals of normalized unitary amplitude and identical frequency to the excitation signal. The reference signals are in phase and in quadrature (out of phase 90°) with *P(t)* respectively:

$$\mathrm{Re} = \frac{2}{T}\int_0^T Q(t)\sin wt\, dt \qquad 2.14$$

$$\mathrm{Im} = \frac{2}{T}\int_0^T Q(t)\sin\left(wt + \frac{\pi}{2}\right) dt \qquad 2.15$$

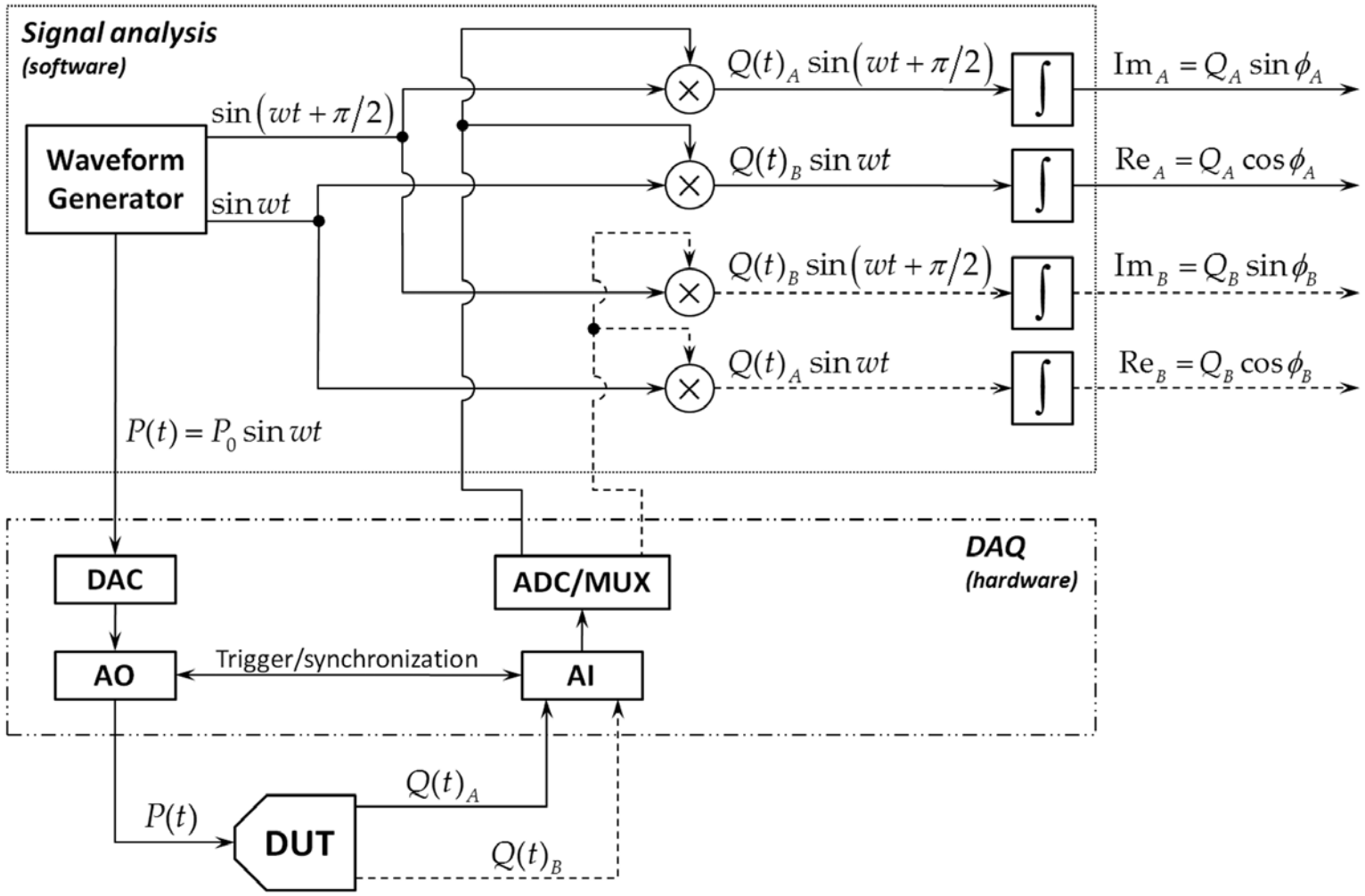

Figure 2.5 Schematic of the HTC sine correlation signal analysis principle. Subscripts *A* and *B* indicate the source of the response signal (*A*: membrane under test, *B*: reference resistor).

where $Q(t) = n(t) + Q_{DC} + Q_0 \sin\left[wt + \phi(w)\right] + \sum_n Q_n \sin\left[nwt + \phi_n(w)\right]$ is the system response signal (comprised of noise, DC-offset, a fundamental tone, and high order harmonics), Re and Im are the "real" and "imaginary" parts of the extracted signal respectively, and T is the integration time, which is equivalent to an integer number of periods of the excitation signal. The correlation rejects harmonics as the only non-zero integral corresponds to the fundamental tone (1st harmonic), while noise is minimized by averaging the signal over the integration time. Since the sine correlation approach is a complex bandpass filter centered at the frequency of the excitation signal, total noise elimination is only possible for an infinite integration time where filter bandwidth ($B_W = 1/T$) becomes infinitely narrow. Thus:

$$\mathrm{Re} = \lim_{T\to\infty} \frac{2}{T} \int_0^T Q(t) \sin wt \, dt = Q_0 \cos\phi(w) \qquad 2.16$$

$$\mathrm{Im} = \lim_{T\to\infty} \frac{2}{T} \int_0^T Q(t) \sin\left(wt + \frac{\pi}{2}\right) dt = Q_0 \sin\phi(w) \qquad 2.17$$

In practice, as an infinite integration time is not possible, it is defined by selecting an acceptable filter bandwidth (filter selectivity). Furthermore, selectivity can be tuned to balance the signal-to-noise ratio of the extracted signal and the computation time required to perform the integration. The phase of the signal is calculated using a four-quadrant inverse tangent to account for the sign of Re and Im and minimize phase wrapping:

$$\phi(w) = \arctan 2\left[\frac{\mathrm{Im}}{\mathrm{Re}}\right] \qquad 2.18$$

The membrane complex impedance is calculated from the sine correlation filtered voltage and current signals:

$$Z_{(jw)} = |Z|e^{j\varphi} = \frac{V_0 e^{j(wt+\phi_V)}}{I_0 e^{j(wt+\phi_I)}} \qquad 2.19$$

where V_0 and I_0 are the voltage and current amplitude, ϕ_V and ϕ_I are the voltage and current phase, and $|Z|$ and φ are the impedance modulus and phase respectively. Equating real and imaginary parts, the latter are given by:

$$|Z| = \frac{V_0}{I_0} \qquad 2.20$$

$$\varphi = \phi_V - \phi_I \qquad 2.21$$

2.2.2 Membrane preparation

Different grades of Kynar® poly(vinylidene fluoride) (PVDF) (Arkema, Inc.), namely, Kynar® 500, Kynar® 731, Kynar® 2801, Kynar® 2821, and Kynar® 2851; were dissolved in 1-methyl-2-pyrrolidinone (NMP) (Sigma-Aldrich Co., assay≥99.5%) to a total concentration of 10 wt% per solution. An acrylic polyelectrolyte (PE) consisting of a random copolymer of 2-sulfoethyl methacrylate (SEM) (69.39wt%), 2-hydroxyethyl methacrylate (HEMA) (15.27wt%), methyl methacrylate (MMA) (7.67wt%), and styrene

(7.67wt%) (Figure 2.6) was mixed with each Kynar® PVDF solution at multiple dissimilar ratios of Kynar® PVDF to PE. Desmodur N-3300A (Bayer AG.), a 1,6-hexamethylene diisocyanate-derived triisocyanate crosslinker, was added to the mixtures at a 1:0.8 OH:NCO ratio, or 80 mol% of the stoichiometric amount of crosslinker needed to react with all the PE hydroxyl groups. The final mixtures were coated using a knife-edge apparatus onto silicon <100> substrates (Silicon, Inc.) previously cleaned for 2 hours in Piranha solution (70% H_2SO_4, 9% H_2O_2, 21% H_2O) at 80°C. The coated films were cured in a convection oven at 175°C for 20 minutes, while the conversion of isocyanate groups into urea linkages was confirmed via FT-IR spectroscopy using a Bruker IRscope II (Bruker Optics Inc.). The final films constituted homogeneous Kynar®/PE proton-conductive membranes of uniform thickness (~20-25μm) with contents of neutralized form PE ranging from 25wt% to 65wt% (equivalent to ~17wt% to ~48wt% acid form PE) for each grade of Kynar® PVDF.

2.2.3 Membrane protonation

Kynar®/PE membranes were detached of the silicon substrates previous to protonation using a dilute soap solution, consisting of alkyl ammonium surfactants. Free-standing membranes were initially washed in a 1M HCl solution at 80°C for 2 hours, followed by a 15-minute wash in DI water. The acid-washed membranes were protonated by immersing them in a 1M H_2SO_4 solution at 80°C for 2 hours, followed by several washes with DI water to remove the excess sulfuric acid solution from the

membranes (15-minute DI water washes are done continuously until the pH of the rinse water is above 4).

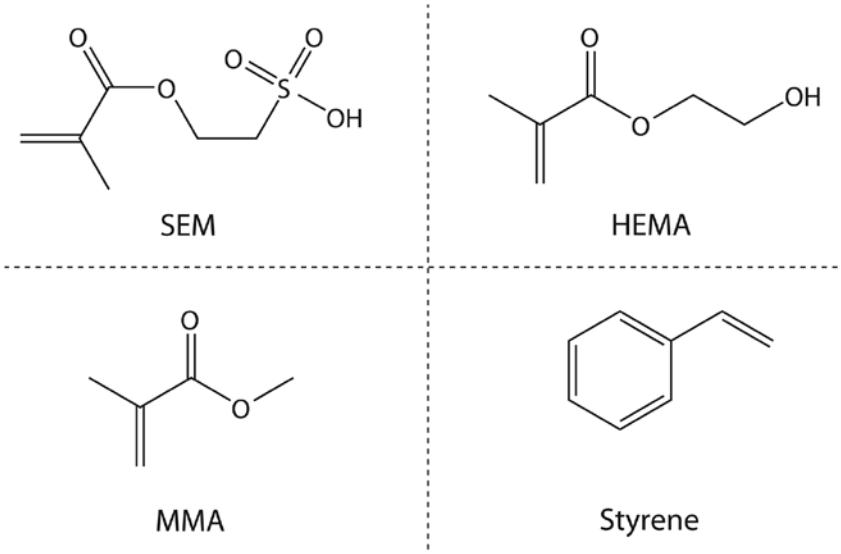

Figure 2.6 Acrylic polyelectrolyte constitutive monomers.

2.2.4 Membrane conditioning and conductivity measurement

Protonated Kynar®/PE membranes and Nafion® 112 perfluorosulfonic acid (PFSA) membranes (DuPont), used as a validation standard, were conditioned in boiling DI water for 1 h to allow complete swelling of the samples prior to conductivity measurements. Once conditioned, the membranes were placed in the sample holder and held in place using the spring-loaded retention mechanism. Two types of measurement were carried out, namely, submerged (liquid environment) and relative humidity. For

submerged conductivity measurements the sample holder reservoir was filled with 18.2 MΩ water at 25°C until the membrane sample was completely covered. Conductivity of Nafion® in its hydrated state originates only from the mobile protons transported through fixed anion structures and contribution from the conductivity of the 18.2 MΩ water is low enough as to be neglected. For relative humidity conductivity measurements the whole HTC system was enclosed in a controlled humidity chamber. Local membrane thickness of the swollen membrane samples is measured prior to conductivity assays using the automated digital gauging probe to account for thickness variation from point to point over the sample. Conductivity measurements were performed in potentiostatic mode with an AC excitation signal amplitude of 30 mV (~20 mV RMS). Tests were divided in two classes: frequency sweeps measurements and standard conductivity readings. For frequency sweeps measurements each testing location over the membranes was excited with sequential AC signals of varying frequency ranging from 1 Hz to 12500 Hz (the upper limit of the frequency range is restricted by the multiplexed analog input sampling rate of the PXI-6031E DAQ). The integration time of the input and output signals varied from a minimum of 100 cycles up to approximately 6500 cycles depending on the frequency of the AC signal. For standard conductivity readings membrane samples were excited with a 1 kHz AC signal at each testing location with an integration time of 5000 cycles following a 5 s stabilization period. Membrane impedance was calculated via the sine correlation technique described above, and conductivity was evaluated using Equation 2.13 with $f_1 = f_2 = 1$ given that $h/x \leq 0.5$ and $d/x > 40$ for all the samples.

2.2.5 Statistical analysis

Kynar® PVDF/PE conductivity data was analyzed by unbalanced univariate ANOVA (unbalanced univariate general linear model, type III sums of squares); $p < 0.05$ was defined as significant (5% significance level). Data homoscedasticity (homogeneity of variance) was assayed using Levene's test. The Tukey HSD post hoc test was used for pairwise comparisons to determine homogeneous subsets of significant factors. Tamhane's T2 post hoc test was used for pairwise comparisons in the case of unequal variances and unequal group sizes. All results are expressed as mean ± standard error of the mean (S.E.M.).

2.3 Results and discussion

2.3.1 Validation – Nafion® 112 ex-situ conductivity

Nafion® properties have been exhaustively studied for the last couple of decades, making it an appropriate standard for the HTC validation experiments. Following the HTC assembly and programming, initial EIS measurements were performed over homogeneous Nafion® 112 samples equilibrated in 18.2 MΩ water. A Bode plot of the four-point probe EIS results over a frequency range of 1 to 12500 Hz for Nafion® 112 at 25°C is shown in Figure 2.7. A transition from a flat constant profile on the high frequency side to a steep continuous increment towards low frequencies is readily observed below 500 Hz for the impedance modulus. Similarly, in the same frequency range of non-constant impedance the phase angle exhibits a sigmoid shape, while

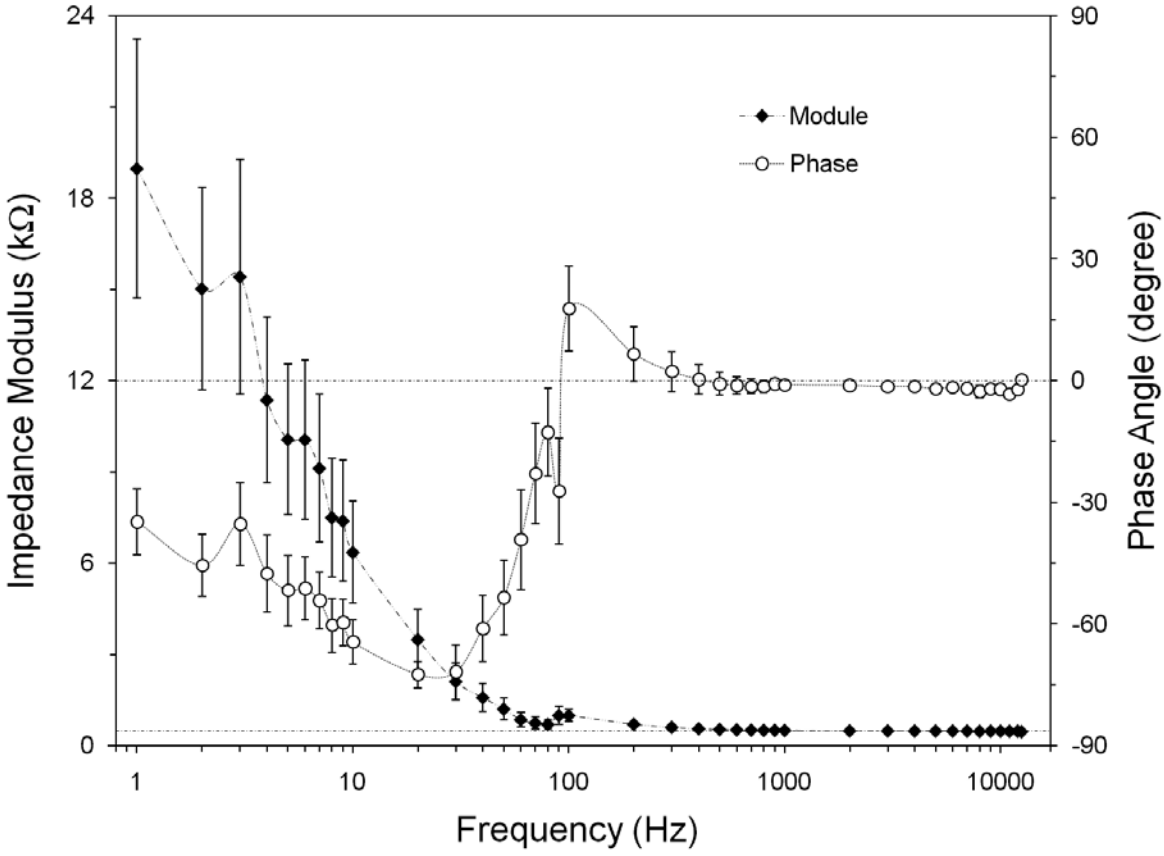

Figure 2.7 Impedance modulus and phase angle Bode plot representation for water equilibrated Nafion® 112 derived from HTC four-point probe EIS measurements in the frequency range from 1Hz to 12.5kHz. Test conditions: 18.2 MΩ water at 25°C. Values are averages ± S.E.M. (n=12).

having a constant value around 0° above 500Hz. This result seems to contradict the near purely resistive behavior typical of water equilibrated Nafion® over wide frequency ranges (1 to 10^5 Hz) [18], and diverges from the expected approximation of the membrane ohmic resistance to the low-frequency limit of the complex impedance where the effect of the parallel-equivalent capacitive element (inter-electrode capacitance) due to the dielectric capacity of the membrane becomes negligible. It is important to notice, however, that the operating frequency range of I-V method used to determine the current flow, and hence the membrane impedance, is known to be limited at the low end of the frequency spectrum [34]. Limitation that is exacerbated by small level signals such as those used in EIS (mV and μA range), and confirmed by elevated noise levels in the unfiltered voltage signal measured across the reference resistor at frequencies below 500 Hz.

Despite being exceptionally robust against noise and high order harmonics, sine correlation filtering of the reference resistor voltage signal in the low frequency range proved to be particularly erratic, explaining the high variability of the impedance and phase data in this frequency range (Figure 2.7) and suggesting that the signal was effectively overshadowed by the noise. This was verified by the power spectral density of the signal (not shown); where the power of the fundamental frequency peak decreased steadily with the frequency of the perturbation signal, up to the point where the peak was completely undistinguishable from the rest of the spectrum (below 100Hz). The use of an additional zero-phase bandpass filter around the perturbation signal frequency, prior to signal correlation, to enhance the voltage signal-to-noise ratio at low

frequencies proved to be ineffective. The effect of the drop in the detected voltage amplitude is directly reflected on the current flow estimation causing the increase in the calculated membrane impedance witnessed at low frequencies. In addition, below 100Hz, voltage readings across the reference resistor fell under 50μV (equivalent to a current of approximately 50nA), below the range accuracy of the DAQ system, contributing as well to the instability/inaccuracy of the readings.

An AC impedance measurement procedure with a wider applicable frequency range such as the autobalancing bridge, the most suitable technique for wide frequency coverage (20 Hz to 110 MHz) [34]), can potentially overcome the aforementioned limitations; however, it could not be implemented in the actual HTC design due to bandwidth limitations of the multiplexed analog input of the DAQ system.

Despite the stated issues in the low frequency range the behavior of water equilibrated Nafion® 112 at 25°C was basically resistive above 800 Hz, with a constant impedance of 484.05 ± 9.37 Ω and a flat phase angle profile within 2.5° (Figure 2.7) free of residual impedances that arise from the measurement circuit parasitic inductance (effect expected to be considerable at very high frequencies). Impedance values at 1000 Hz were therefore chosen as a suitable approximation to the membranes ohmic resistance in order to calculate their conductivity.

Subsequent to the HTC tuning, preliminary conductivity tests were performed over homogeneous Nafion® 112 samples submerged in 18.2 MΩ water. The tests were carried out following the same fashion of traditional methods by considering a constant average membrane thickness across the whole sample. Thickness of the wet membrane

was measured with a Mitutoyo 293-344 low-torque flat head digital micrometer (Mitutoyo Co.) at several locations over the swollen sample and then averaged prior to EIS analysis. Abnormally high conductivity values of 106.2 ± 0.76 mS/cm were obtained for Nafion® 112 in 18.2 MΩ water at 20°C, suggesting lower than normal impedance readings arising from very small amplitude response signals, whose amplitude might have been further dampened by the filtering process due to poor signal-to-noise ratios. However, this effect was ruled out as the ratio of multiple membrane impedance values calculated at 1000Hz and different perturbation voltages remained equal to one at voltages up to 600mV, above which noticeable deformation of the response signals was indicative of the system drifting from a linear behavior.

As it is evident from the conductivity model presented in Equation 2.13, besides impedance, the membrane conductivity is directly dependent on the sample thickness. In addition, it is well known that after hydration Nafion® membranes swell considerably and exhibit noticeable dimensional changes in both the X-Y plane and thickness when compared to their dry geometry [37, 38]. Therefore, the wet thickness is critical to obtain the true membrane conductivity. The elevated conductivity witnessed for Nafion® 112 during the preliminary conductivity tests was consequently indicative that the sample was being compressed when measuring its thickness, despite caution was taken not to exert excessive force on the wet membrane with the micrometer jaws during the measurements. For this reason, in order to minimize the compressive force exerted on the swollen membrane samples, localized thickness measurements were performed at each test site using the digital gauging probe described in the HTC design

section. The 0.1 μm resolution optical encoder affixed to the vertical axis ensured a wet thickness measuring repeatability better than ± 1 μm between consecutive readings, as shown in Figure 2.8.

Figure 2.9 illustrates the substantial conductivity decrease at several testing locations of an individual membrane sample when using localized thickness measurements instead of assuming a constant average wet thickness for the whole membrane. The use of localized thickness measurements yielded an average conductivity of 77.7 ± 0.51 mS/cm for the same Nafion® 112 samples submerged in 18.2 MΩ water at 20°C that previously exhibited a value close to 110 mS/cm. This result supports the hypothesis of membrane compression during thickness measurements and highlights the importance of proper membrane wet thickness readings for accurate conductivity estimation. In addition, the implementation of such localized thickness measurements allowed the creation of Nafion® 112 wet thickness maps (example shown in Figure 2.10) that, regardless of an almost constant native dry thickness of 51 ± 0.68 μm, revealed differences of up to 10μm between different locations of otherwise considered homogeneous membranes. These wet thickness variations are likely explained by an uneven water distribution in the membrane due to anisotropy in the Nafion® structure [17, 37, 39-41] that imbalances the distribution of sulfonic acid groups and leads to anisotropic membrane swelling. As seen in Figure 2.9, the latter can lead to deviations of up to 30% or more in local conductivity calculations when assuming a constant membrane wet thickness.

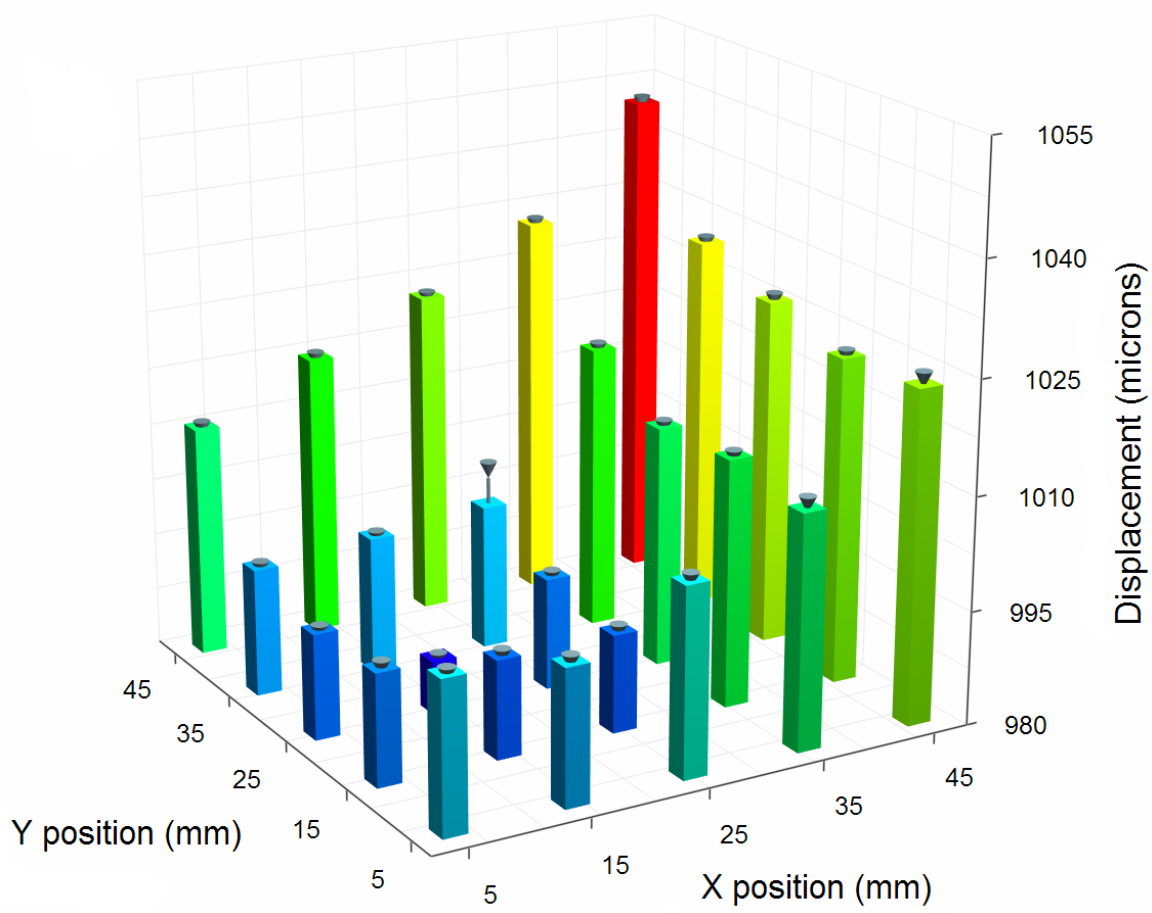

Figure 2.8 Absolute displacement of the digital gauging probe at multiple locations over a swollen Nafion® 112 membrane. The Z-axis scale has been zoomed-in to facilitate the visualization of the measurements repeatability. Values are averages ± S.E.M. (indicated by error bars delimited with inverted cone markers, n=10).

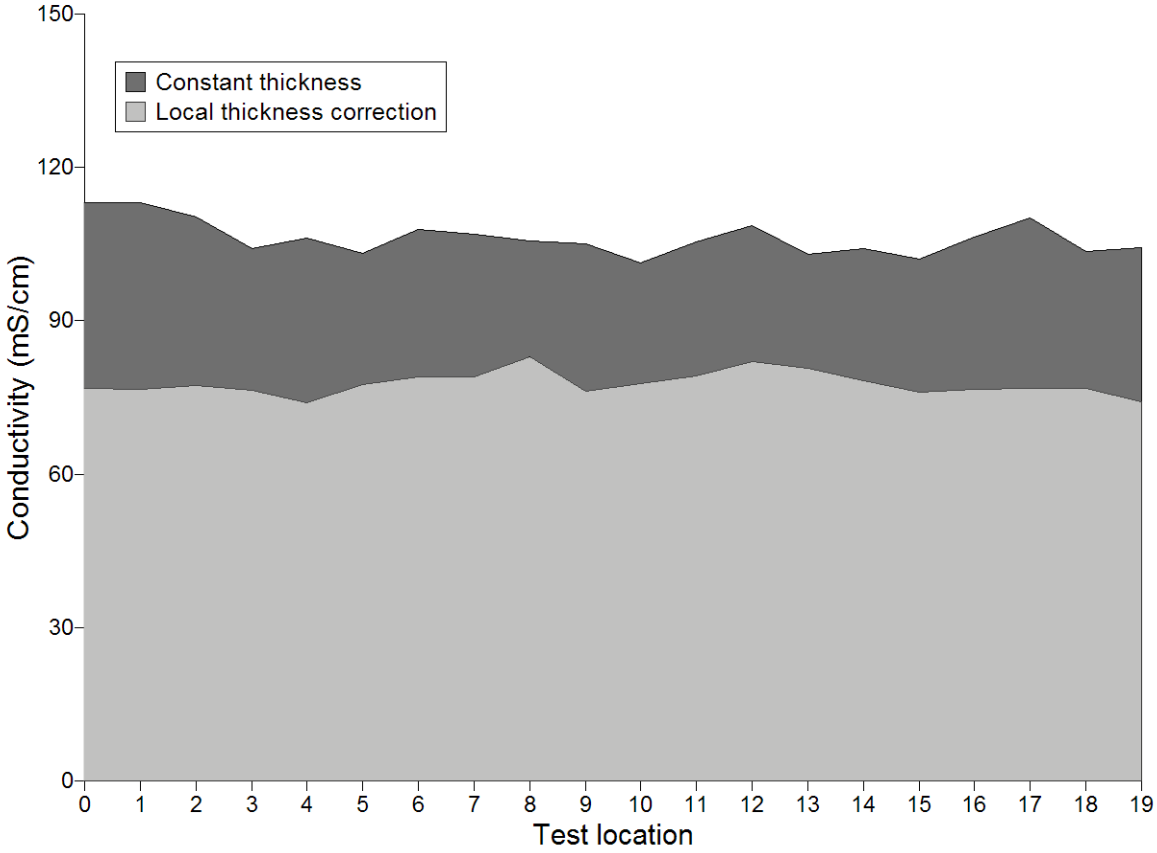

Figure 2.9 Contrast between the effect of constant average thickness (dark gray) and local thickness (light gray) on the conductivity estimation of water equilibrated Nafion®112 (single sample, identical testing locations for both cases). Test conditions: 18.2 MΩ water at 20°C. Excitation signal frequency: 1000Hz.

While some authors claim that Nafion® is isotropic [42, 43], the discrepancies between their results and this work may be attributed to a difference of scale. Large scale measurements (e.g., electrodes that contact the membrane surface in its entirety) may average or mask the effect of a small level of structural anisotropy, if any, in the Nafion® membrane that may possibly only become evident with small scale localized measurements (e.g., HTC).

The lack of correlation between a particular thickness map distribution (Figure 2.10) and its associated impedance map (Figure 2.11), which results in a variable conductivity distribution over the membranes (Figure 2.12), constitutes another potential indicative of membrane anisotropy. Although recent studies [17, 43-45] propose that the proton conductivity of Nafion® and other proton-conductive materials is *not* an intensive (bulk) property and increases almost linearly with membrane thickness, no directly proportional association between corresponding thickness and conductivity maps supporting this hypothesis was noticed. Further HTC studies involving multiple Nafion® grades (besides 112) or using custom proton conducting thickness gradient libraries, could, however, be performed to ascertain the functional relation between average conductivity and membrane thickness.

As anticipated, the conductivity of Nafion® 112 utilizing localized thickness measurements remained stable at frequencies above 800Hz (Figure 2.13) having an average value of 84.5 ± 0.54 mS/cm at 1000 Hz for samples submerged in 18.2 MΩ water at 25°C (average from a total of 108 readings over 12 samples coming from three different lots). This value is within 1.8% of the 83 mS/cm Nafion® 112 conductivity

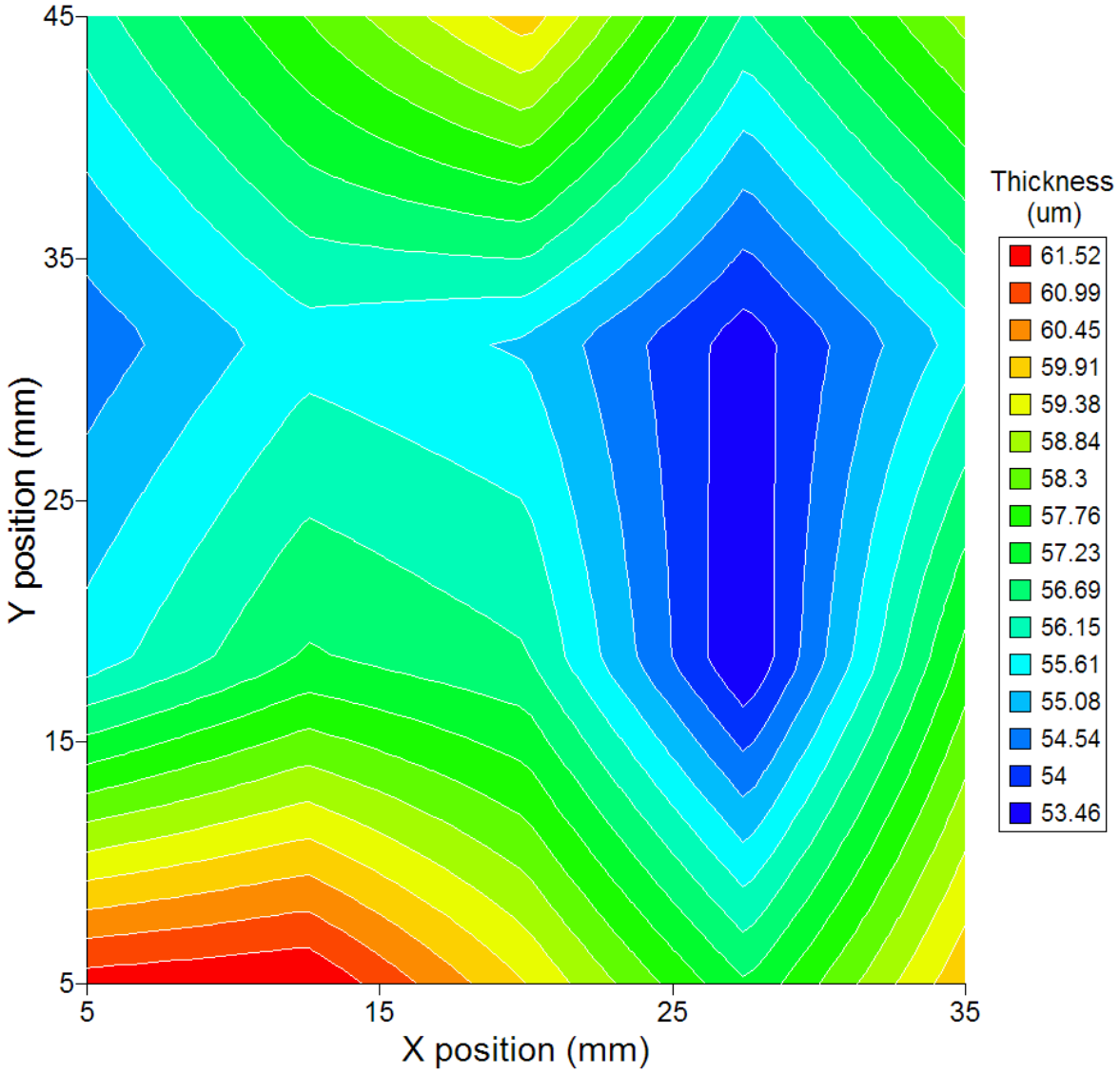

Figure 2.10 Thickness map for water equilibrated Nafion® 112. Values constituting the contour map are averages of each property at 20 locations over a single sample. Test conditions: 18.2 MΩ water at 25°C. Excitation signal frequency: 1000Hz.

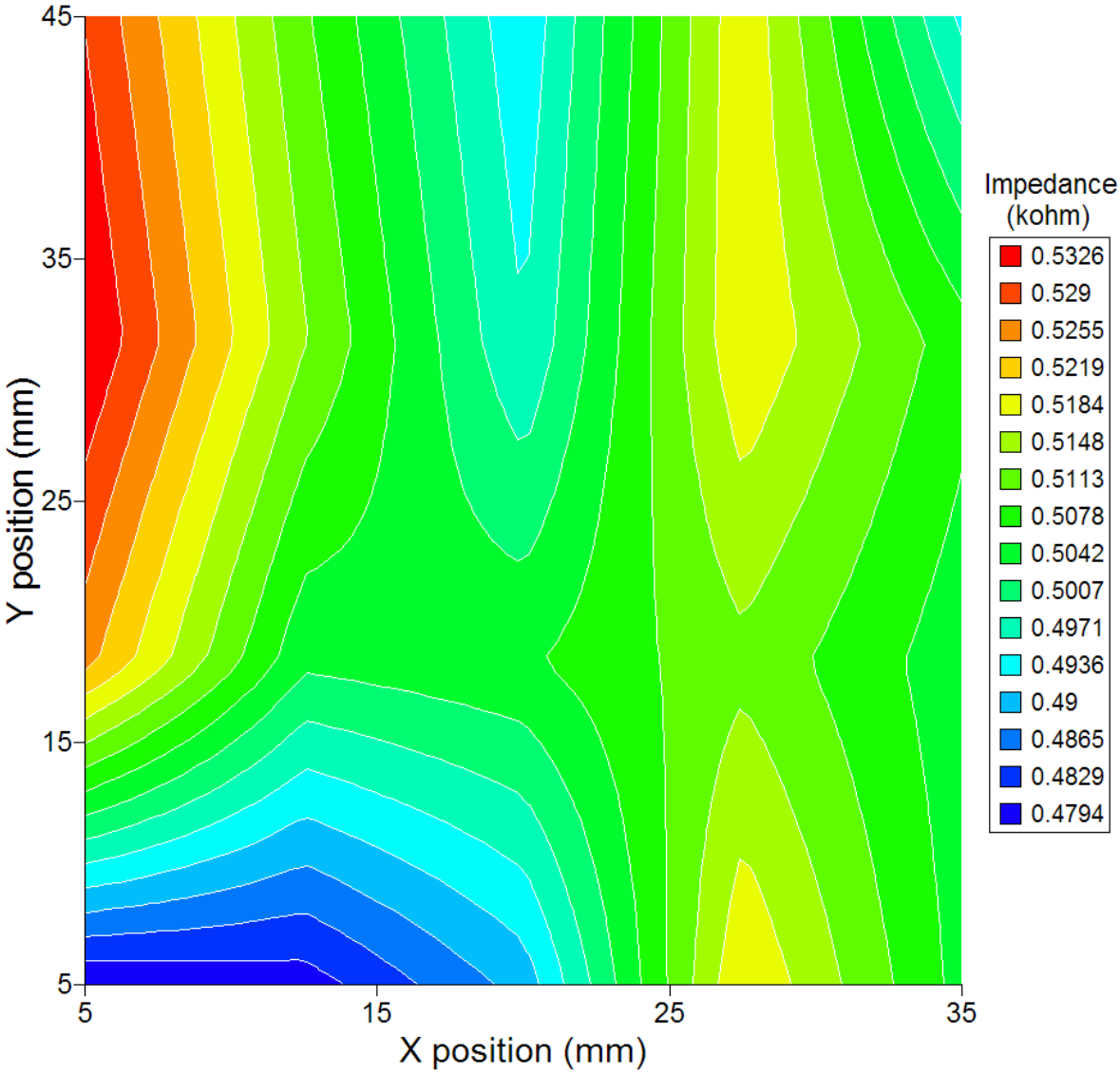

Figure 2.11 Impedance map for water equilibrated Nafion® 112. Values constituting the contour map are averages of each property at 20 locations over a single sample. Test conditions: 18.2 MΩ water at 25°C. Excitation signal frequency: 1000Hz.

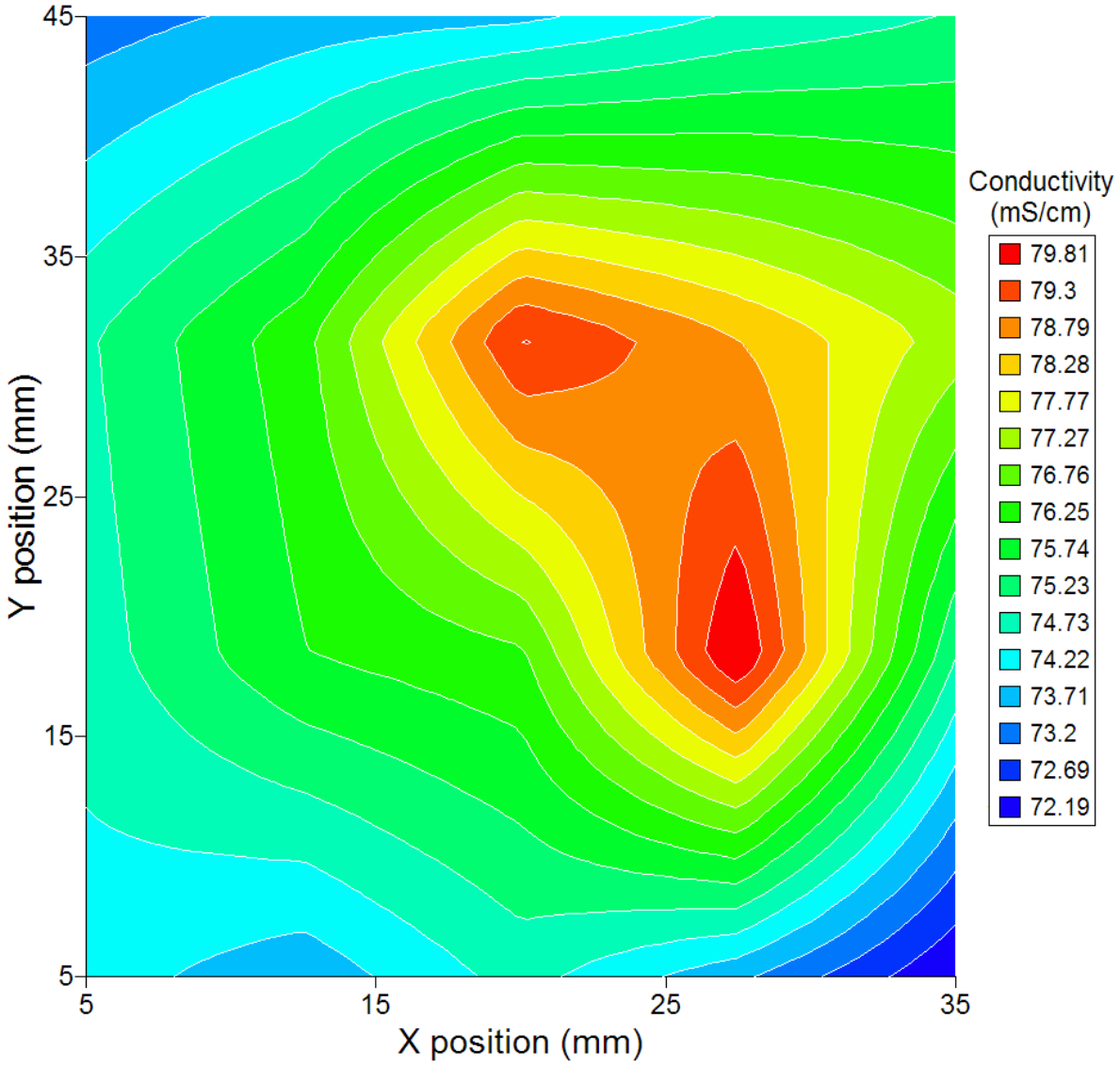

Figure 2.12 Conductivity map for water equilibrated Nafion® 112. Values constituting the contour map are averages of each property at 20 locations over a single sample. Test conditions: 18.2 MΩ water at 25°C. Excitation signal frequency: 1000Hz.

reported by the manufacturer [46] under identical testing conditions, and verifies the suitability of the HTC for performing high-throughput conductivity measurements at small scale via a miniature four-point probe. It is important to notice that although thickness variations exist across the Nafion® 112 membranes as previously indicated, their effect on the reported average conductivity is diluted by the large number of measurements performed. Also, while results are well within proximity to the manufacturer reported specifications, it is necessary to point out that no standard procedure has been established yet for measuring proton conductivity of PEMs [28].

DC measurements at different voltages were conducted for completeness, and to further corroborate the AC impedance-based results, by obtaining the membrane resistance from the slope of the generated potential-current profile. However, contrary to AC measurements where the current reverses continuously; high perturbation voltages (reaching values higher than 1 V-DC) were required to maintain the current above the range accuracy of the DAQ. Due to the small inter-electrode spacing, these voltages (even as low as 200 mV-DC) were enough to electrolyze water, which was evident from the almost instantaneous formation of bubbles and gas pockets below the membrane samples. Voltage and current readings dropped continuously while a particular DC voltage was applied to the membrane suggesting local drying of the sample due to increasing exposure to the gas pockets formed by electrolysis over the duration of the readings. Since it is critical that the membrane water content remains invariable during the course of the experiments, the construction of a unique membrane

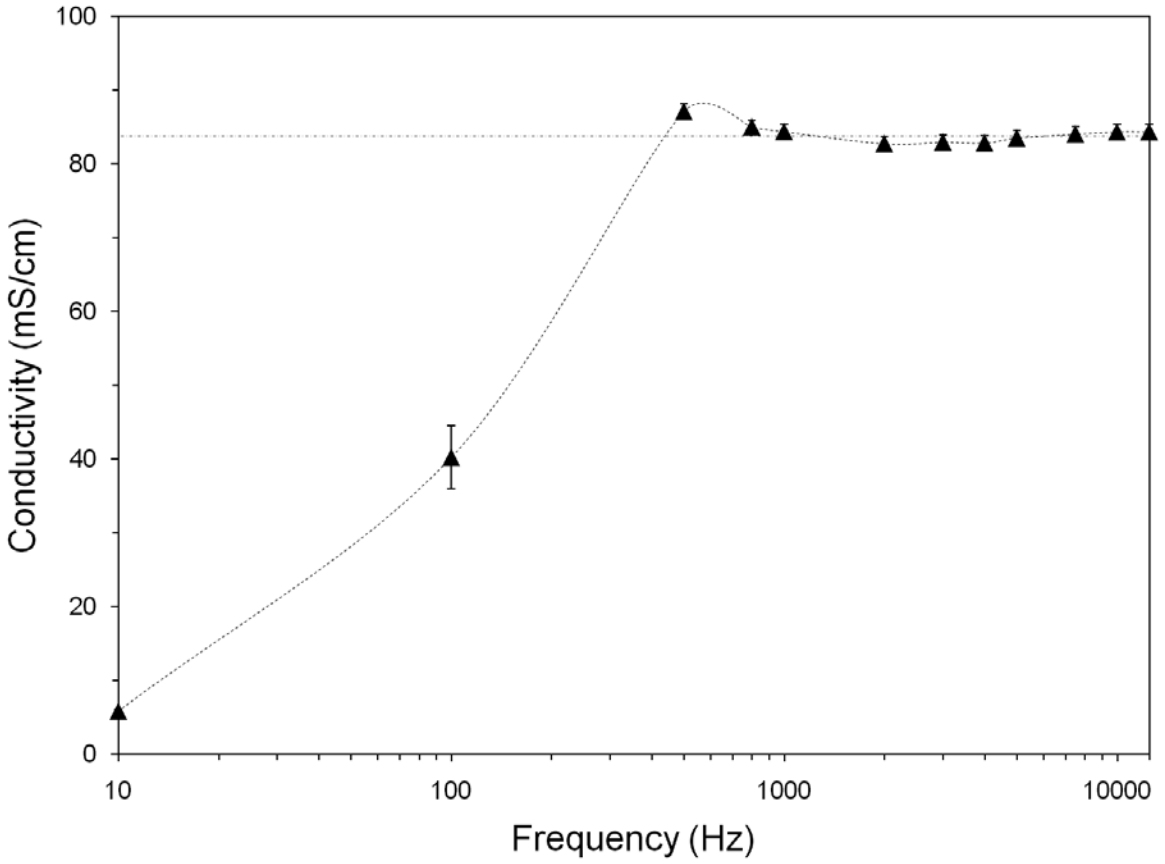

Figure 2.13 Conductivity of water equilibrated Nafion® 112 derived from HTC four-point probe EIS measurements at different excitation signal frequencies (10Hz to 12.5kHz). Test conditions: 18.2 MΩ water at 25°C. Values are averages ± S.E.M. (n=108).

potential-current plot to obtain the membrane resistance was not possible. This hindrance arises from the coupled effect of the miniature electrode geometry utilized and the I-V technique used to determine the current flowing through the membrane; constituting a limitation of the actual HTC design.

Figure 2.14 shows the conductivity of Nafion® 112 for multiple relative humidity conditions. An almost perfect exponential relation between conductivity and relative humidity in the range of 40% to 100% RH is indicative of the expected strong effect of membrane hydration on conductivity. As extensively known, proton mobility in Nafion® and other PFSA membranes depends heavily on the hydration level of the membrane [19, 28, 37, 41, 47-49], as transport of hydrated oxonium cations (solvated protons in the form of $H_{2n+1}O_n^+$), particularly Zundel $H_5O_2^+$ and Eigen $H_9O_4^+$ structures, is dominated in the bulk water by the hydration-dependent Grotthuss mechanism of structural diffusion.

Due to water condensation over the HTC above 95% RH, the last data point (100% RH) in Figure 2.14 corresponds to the conductivity of Nafion® 112 submerged in water at the same temperature of the rest RH data points. This point, however, does not necessarily reflect the real conductivity at 100% RH due to a phenomenon dubbed Schroeder's Paradox [50, 51], in which the amount of water uptake by a PEM equilibrated with water vapor differs from that of a membrane saturated with liquid water. Then again, its unexpected seamless fit into the conductivity-RH profile (instead of an abrupt jump) could actually be indicative of the absence of the paradox effect as a result of an identical thermal history of all the Nafion® 112 membranes used in this

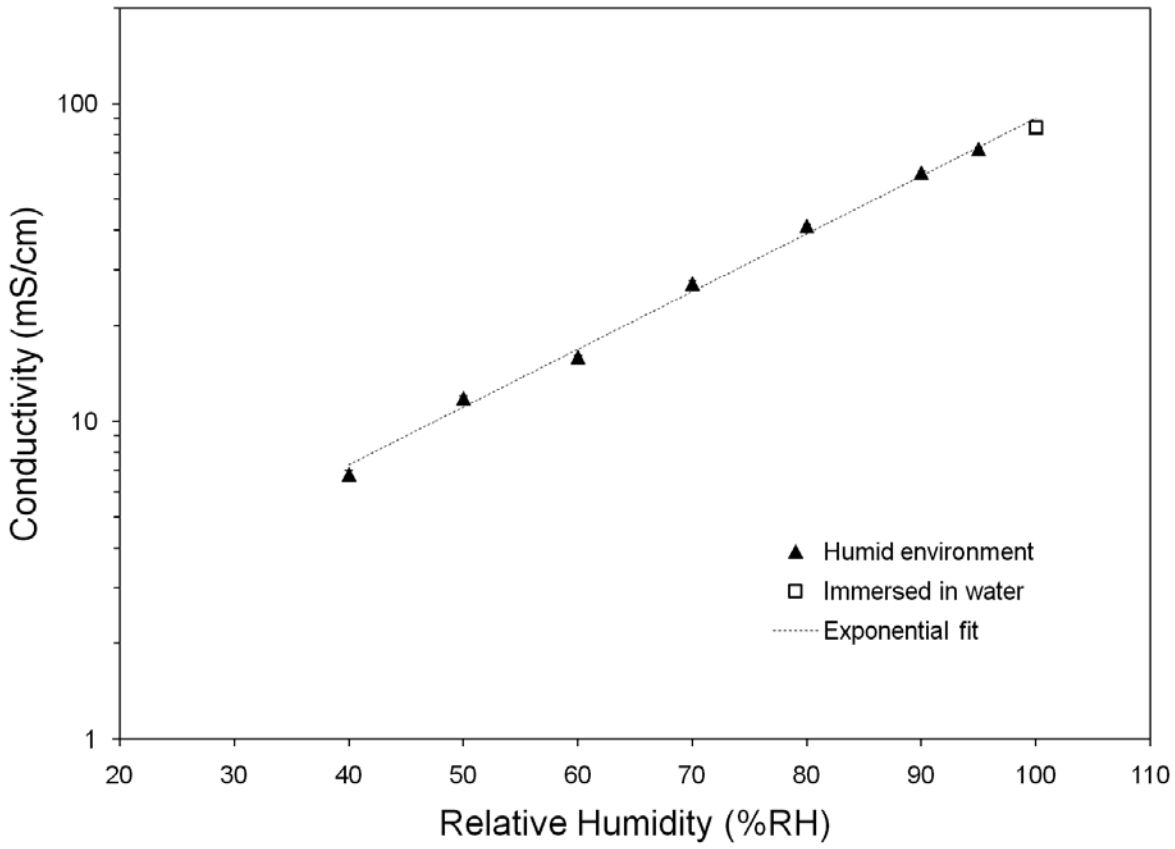

Figure 2.14 Conductivity of Nafion® 112 as a function of relative humidity at 25°C derived from HTC four-point probe EIS measurements. (▲) non-condensing relative humidity environment (40 to 95%RH). (□) liquid water environment. (---) exponential fit (r^2=0.9959). Excitation signal frequency: 1000Hz. Values are averages ± S.E.M. (n=9).

work (membrane conditioning in boiling DI water for 1 h). Constant thermal history has been shown to have the ability to effectively override the Schroeder's Paradox effect [52]. Moreover, results from a novel model [51] indicate that much smaller membrane channels are able to fill with water when the membrane is exposed to a saturated liquid water environment as opposed to saturated vapor. This result and the possible absence of the Schroeder's Paradox effect observed at 100% RH, could be indicative that small channels filled during the membrane conditioning step, which will not normally get filled in a saturated vapor atmosphere, remain full while the membranes are kept exposed to vapor conditions above a particular RH that prevents the channels from drying. Consequently conditioned membranes exposed to saturated vapor could eventually reach the same water content as membranes exposed directly to liquid water, and hence, exhibit the same conductivity. Regardless if this hypothesis holds, the almost perfect exponential relation between conductivity and relative humidity shown in Figure 2.14, which highlights the aforementioned importance of hydration on proton conductivity, is in excellent agreement with previous studies [28, 48, 49] and confirms the effectiveness of the HTC for both liquid and humid environments.

2.3.2 Kynar® PVDF/Acrylic polyelectrolyte membranes

The conductivity of multiple dissimilar Kynar® PVDF/PE membranes, obtained from serial high-throughput four-point probe EIS tests performed subsequent to the HTC validation procedure, is shown in Figure 2.15. A strong, almost linear, direct relationship between conductivity and PE content is evident throughout the whole

spectrum of Kynar® PVDF grades utilized as mechanical supports for the crosslinked network of PE channels. Also, an unforeseen manifest variation in conductivity among membranes with identical PE content but different Kynar® PVDF grade is observed, indicating an apparent influence of the latter on membrane conductivity.

An unbalanced univariate general linear model (GLM) test of the Kynar® PVDF/PE conductivity data (unequal group sizes) confirmed the aforementioned hypotheses as a statistically significant main effect of PE content was found ($F_{(7,404)} = 356.59$, $p < 0.001$), indicating that conductivity increases with PE content. There was also a main effect of Kynar® PVDF grade ($F_{(4,404)} = 35.99$, $p < 0.001$) showing a variation in conductivity depending on the Kynar® PVDF grade. Moreover there was an interaction between PE content and Kynar® grade ($F_{(28,404)} = 5.01$, $p < 0.001$), that emphasizes the effect of the later on the proton conducting characteristics of the membranes. Complementary simple effects tests showed that conductivity was statistically identical for membranes with a PE content 25wt% regardless of the Kynar® PVDF grade ($F_{(4,404)} = 1.012$, $p > 0.05$). However, for PE contents of 30wt% and above conductivity varied depending on the Kynar® PVDF type ($4.57 \leq F_{(4,404)} \leq 16.84$, $p < 0.001$).

Pairwise multiple comparisons using the Tukey HSD post hoc test to assess significantly different means among groups of significant factors revealed four homogeneous subsets for the Kynar® PVDF grade ($\alpha = 0.05$): subset 1 = Kynar® 500, subset 2 = Kynar® 731, subset 3 = Kynar® 2821, and subset 4 = Kynar® 2801 + Kynar® 2851. These subsets seem to indicate a possible global effect on conductivity characteristic for each particular Kynar® series (i.e., 500, 700, and 2800). However, the

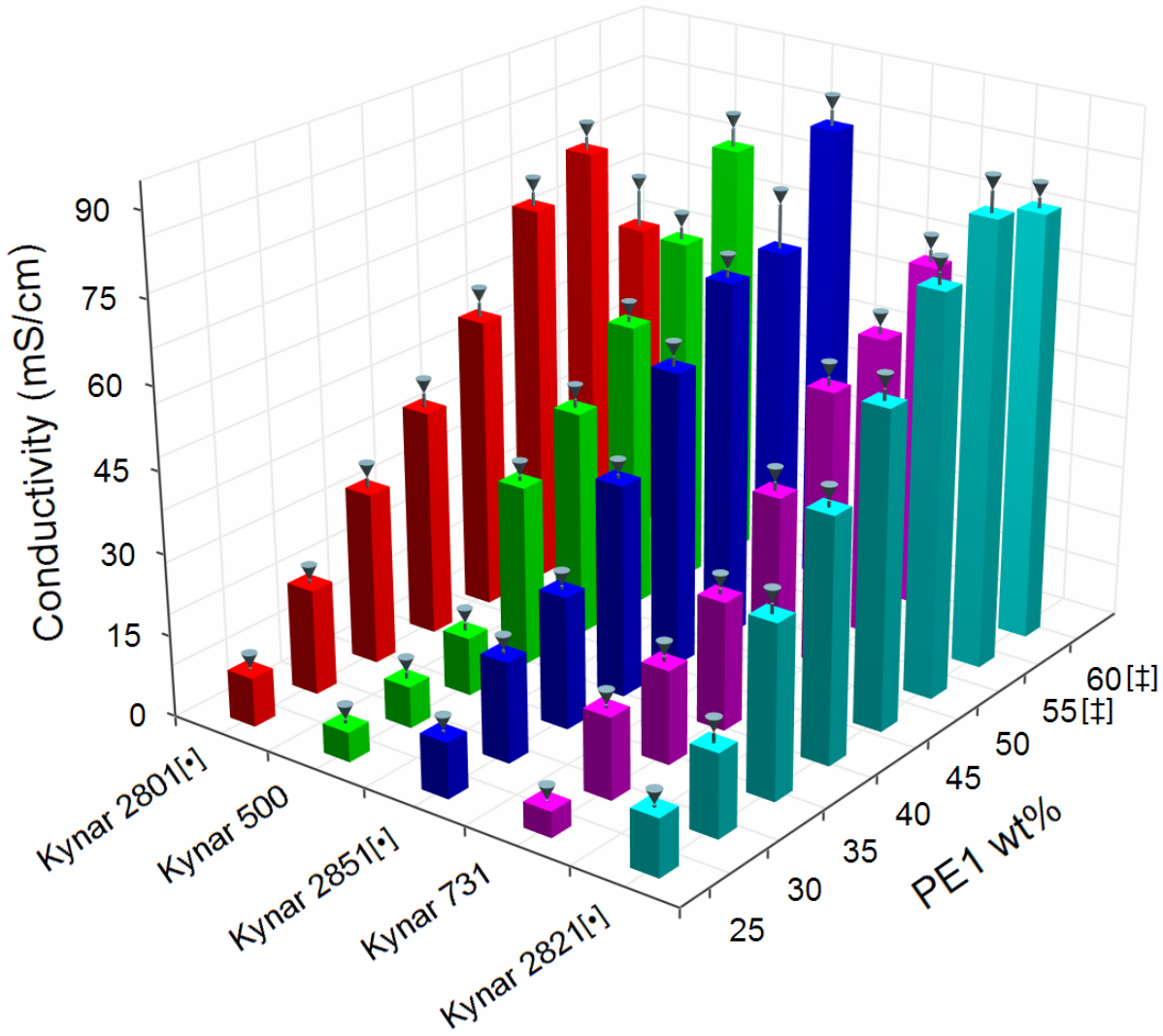

Figure 2.15 Conductivity of Kynar® PVDF/acrylic polyelectrolyte membranes for various Kynar® grades as a function of polyelectrolyte content. Polyelectrolyte content is expressed as the weight percentage in the final membrane of neutralized form polyelectrolyte. Range: 25 to 60wt% neutralized form polyelectrolyte (equivalent to 16.8 to 47.7wt% acid form polyelectrolyte). [•] and [‡] designate homogeneous subsets of Kynar® grade and of PE content, respectively (Tamhane's T2 post hoc test, $\alpha = 0.05$); factor levels significantly different from the rest (single element subsets) have no marker. Values are averages ± S.E.M. (indicated by error bars delimited with inverted cone markers, n=2-24)

Tukey HSD method is not exact if group sizes are not equal. Furthermore, although distribution tests showed an acceptable deviation degree of the conductivity data from normality, Levene's test of homogeneity of variance revealed that variances across groups were not equal (heteroscedastic data). Consequently, additional confirmatory pairwise multiple comparisons were performed via Tamhane's T2 post hoc test (appropriate for unequal variances and group sizes). It is important to point out that the univariate general linear model is relatively robust to heteroscedasticity and to skewed distributions; therefore, although Type I errors may increase, the significant main effects observed are not necessarily affected by the heteroscedasticity of the conductivity data.

Tamhane's T2 test results ($\alpha = 0.05$) revealed no significant difference on the effect on conductivity of Kynar® 2821 and 2801 ($p = 0.937$), and Kynar® 2821 and 2851 ($p = 0.976$); as a result, the previous homogeneous subsets 3 and 4 collapsed into a single subset. Kynar® 500 and 731 means remained significantly different from the rest. The new subset, comprised only by the Kynar® 2800 series, gives strength to the hypothesis of a global effect on the conductivity of Kynar® PVDF/PE membranes that is characteristic for each particular Kynar® series. In contrast, conductivity of membranes with a PE content of 55wt% and 60wt% were statistically identical ($p = 1.00$), suggesting a maximum effective amount of PE above which its effect on membrane conductivity is negligible, or even slightly detrimental as noticed on membranes containing Kynar® 2801 and 2821.

Presumably, differences in the Kynar® crystallinity may explain the variation in conductivity among the membranes containing different Kynar® types. For instance,

Kynar® 500 and 731 are PVDF homopolymers, while Kynar® 2801, 2821, and 2851 are copolymers of PVDF and hexafluoropropylene (HFP). It has been shown that when copolymerized with HFP, PVDF crystallinity, as well as glass transition temperature, is reduced considerably when compared to PVDF homopolymer counterparts [53]. The direct effect of the non-conducting phase crystallinity on conductivity is not well understood and depends on a combination of factors. For example, conductivity of styrene grafted-sulfonated PVDF membranes has been found to increase as crystallinity decreases [54]. On the contrary, conductivity of polymer gel electrolytes of $LiBF_4$ based on PVDF homo- and copolymers increased with crystallinity for high porosity membranes, and decreased as crystallinity increased for low-porosity membranes [55]. In the particular case of this study Kynar® crystallinity is likely to have an effect on the thermodynamics and kinetics of micro-phase separation of the membrane accountable for the formation of the ion conducting channels. Delineation of these effects is the subject of ongoing work [56]. Nevertheless, based on the GLM marginal means (un-weighted means) for the different types of Kynar®, and the content of HFP in the Kynar® copolymers it is safe to speculate that reduced Kynar® crystallinity results in increased conductivity. Specifically, the maximum conductivity marginal mean (Mu = 49.538) corresponds to membranes based on Kynar® 2821, which in turn has the highest content of HFP (PVDF:HFP ≈ 90:10). It is important to notice that although the HFP content of Kynar® 2801 is almost identical to that of Kynar® 2821, the melt viscosity of the former is much higher (15-20 kP vs. 5-10 kP), which can hinder the formation of ion conducting channels.

2.4 Conclusions

A high-throughput automated electrochemical impedance spectroscopy apparatus (HTC) based on a miniature four-point probe has been designed to measure ionic conductivity of thin film materials (e.g., polymer electrolyte membranes for fuel cell applications). Validation of the device using Nafion® 112 as a standard demonstrated its suitability to measure proton conductivity of PEM materials in both liquid water and variable-humidity air environments at multiple AC excitation frequencies. Particularly, the conductivity of the Nafion® 112 was within ± 1.8% of the value reported by the manufacturer under identical testing conditions. Localized thickness and impedance measurements performed during the system validation, owing to the reduced size of the measuring probes (~3mm), allowed the creation of detailed irregular single-membrane Nafion® 112 property maps that indicated a probable uneven distribution of sulfonic acid groups in the membrane (membrane anisotropy). This ability to perform localized measurements by means of the HTC has the potential, in conjunction with combinatorial samples, to accelerate screening and optimization of new PEM materials by orders of magnitude.

HTC characterization of novel Kynar® PVDF/acrylic polyelectrolyte membranes of various compositions, proved to be a fast and effective way to assay new PEM materials using reduced sample sizes. Specifically, two unanticipated significant factors were found to intervene and/or limit the proton conducting capacity of the membranes when analyzing HTC data:

- Kynar® PVDF series: membranes containing a particular Kynar® PVDF type exhibited statistically identical mean conductivity than other membranes containing different Kynar® PVDF types that belong to the *same* series or family.
- Maximum effective amount of polyelectrolyte: Increment in polyelectrolyte content from 55wt% to 60wt% showed no statistically significant effect in increasing conductivity. In fact, some membranes experienced a reduction in conductivity.

These results provide useful information to construct hypotheses that can be used towards an explanation of a maximum effective amount of PE, the interaction between the acrylic polyelectrolyte and Kynar® PVDF, and the effect of the structure and properties of the latter (e.g., crystallinity, homo- and copolymer configurations, viscosity, etc.) on the membrane ionic conductivity.

2.5 References

1. Sormana, J.-L. and Meredith, J.C., *High-Throughput Screening of Mechanical Properties on Temperature-Gradient Polyurethaneurea Libraries.* Macromolecular Rapid Communications, 2003. **24**(1): p. 118-122.
2. Chisholm, B.J. and Webster, D.C., *The development of coatings using combinatorial/high throughput methods: a review of the current status.* Journal of Coatings Technology and Research, 2007. **4**(1): p. 1-12.
3. Genzer, J. and Bhat, R.R., *Surface-Bound Soft Matter Gradients.* Langmuir, 2008. **24**: p. 2294-2317.
4. Kohn, J., Welsh, W.J., and Knight, D., *A new approach to the rationale discovery of polymeric biomaterials.* Biomaterials, 2007. **28**(29): p. 4171-4177.

5. Meredith, J.C., *Advances in Combinatorial and High-Throughput Screening of Biofunctional Polymers for Gene Delivery, Tissue Engineering, and Anti-Fouling Coatings.* Journal of Materials Chemistry, 2009. **19**: p. 34-45.

6. Webster, D.C., *Combinatorial and high-throughput methods in macromolecular materials research and development.* Macromolecular Chemistry and Physics, 2008. **209**(3): p. 237-246.

7. Rajan, K., *Combinatorial Materials Sciences: Experimental Strategies for Accelerated Knowledge Discovery.* Annual Review of Materials Research, 2008. **38**: p. 299-322.

8. Smotkin, E.S., et al., *High-throughput screening of fuel cell electrocatalysts.* Applied Surface Science, 2006. **252**: p. 2573-2579.

9. Cooper, J.S. and McGinn, P.J., *Combinatorial screening of thin film electrocatalysts for a direct methanol fuel cell anode.* Journal of Power Sources, 2006. **163**: p. 330-338.

10. Liu, R. and Smotkin, E.S., *Array membrane electrode assemblies for high throughput screening of direct methanol fuel cell anode catalysts.* Journal of Electroanalytical Chemistry, 2002. **535**: p. 49-55.

11. Devenney, M., Donne, S.W., and Gorer, S., *Application of combinatorial methodologies to the synthesis and characterization of electrolytic manganese dioxide.* Journal of Appled Electrochemistry, 2004. **34**: p. 643-651.

12. Cropper, M.A.J., Geiger, S., and Jollie, D.M., *Fuel cells: a survey of current developments.* Journal of Power Sources, 2004. **131**(1-2): p. 57-61.

13. Mauritz, K.A. and Moore, R.B., *State of Understanding of Nafion.* Chemical Reviews, 2004. **104**: p. 4535-4585.

14. Meredith, J.C., Karim, A., and Amis, E.J., *High-Throughput Measurement of Polymer Blend Phase Behavior.* Macromolecules, 2000. **33**: p. 5760-5762.

15. Meredith, J.C., et al., *Combinatorial Materials Science for Polymer Thin-Film Dewetting.* Macromolecules, 2000. **33**: p. 9747-9756.

16. Meredith, J.C. and Amis, E.J., *LCST phase separation in biodegradable polymer blends: poly(D,L-lactide) and poly(ε-caprolactone).* Macromolecular Chemistry and Physics, 2000. **201**(6): p. 733-739.

17. Slade, S., et al., *Ionic Conductivity of an Extruded Nafion 1100 EW Series of Membranes.* Journal of The Electrochemical Society, 2002. **149**(12): p. A1556-A1564.

18. Cahan, B.D. and Wainright, J.S., *AC Impedance Investigations of Proton Conduction in Nafion.* Journal of The Electrochemical Society, 1993. **140**(12): p. L185-L186.

19. Zawodzinski, T.A., et al., *Determination of Water Dlffusion Coefficients in Perfluorosulfonate Ionomeric Membranes.* Journal of Physical Chemistry, 1991. **95**: p. 6040-6044.

20. Elabd, Y.A., Walker, C.W., and Beyer, F.L., *Triblock copolymer ionomer membranes Part II. Structure characterization and its effects on transport properties and direct methanol fuel cell performance.* Journal of Membrane Science, 2004. **231**(1-2): p. 181-188.

21. Vona, M.L.D., et al., *SPEEK/PPSU-based organic–inorganic membranes: proton conducting electrolytes in anhydrous and wet environments.* Journal of Membrane Science, 2006. **279**(1-2): p. 186-191.

22. Sormana, J.-L., Chattopadhyay, S., and Meredith, J.C., *High-throughput mechanical characterization of free-standing polymer films.* Review of Scientific Instruments, 2005. **76**: p. 062214.

23. Sormana, J.-L. and Meredith, J.C., *High-throughput dynamic impact characterization of polymer films.* Material Research Innovations, 2003. **7**: p. 295-301.

24. Vladikova, D. *The Technique of the Differential Impedance Analysis Part I: Basics of the Impedance Spectroscopy*. in *Proceedings of the International Workshop "Advanced Techniques for Energy Sources Investigation and Testing"*. 2004. Sofia, Bulgaria.

25. Urquidi-Macdonald, M., Real, S., and Macdonald, D.D., *Applications Of Kramers-Kronig Transforms In The Analysis Of Electrochemical Impedance Data-III: Stability And Linearity.* Electrochimica Acta, 1990. **35**(10): p. 1559-1566.

26. Gomadam, P.M. and Weidner, J.W., *Analysis of electrochemical impedance spectroscopy in proton exchange membrane fuel cells.* International Journal of Energy Research, 2005. **29**: p. 1133-1151.

27. Barsoukov, E. and Macdonald, J.R., eds. *Impedance Spectroscopy: Theory, Experiment, and Applications*. 2nd ed. 2005, Wiley-Interscience: Hoboken, New Jersey. 616.

28. Lee, C.H., et al., *Importance of Proton Conductivity Measurement in Polymer Electrolyte Membrane for Fuel Cell Application.* Industrial & Engineering Chemistry Research, 2005. **44**: p. 7617-7626.

29. Valdes, L.B., *Resistivity Measurements on Germanium for Transistors.* Proceedings of the IRE, 1954: p. 420-427.

30. Albers, J. and Berkowitz, H.L., *An Alternative Approach to the Calculation of Four-Probe Resistances on Nonuniform Structures.* Journal of The Electrochemical Society, 1985. **132**(10): p. 2453-2456.

31. Smits, F.M., *Measurements of Sheet Resistivity with the Four-Point Probe.* Bell System Technical Journal, 1958. **37**: p. 711-718.

32. Uhlir, A.J., *The Potentials of Infinite Systems of Sources and Numerical Solutions of Problems in Semiconductor Engineering.* Bell System Technical Journal, 1955. **34**: p. 105-128.

33. Bowler, J.R. and Bowler, N., *Theory of four-point alternating current potential drop measurements on conductive plates.* Proceedings of the Royal Society A, 2007. **463**: p. 817-836.

34. *Agilent Technologies Impedance Measurement Handbook (Agilent application note 5950-3000)*. 2006, Agilent. p. 126.

35. Gabrielli, C. and Keddam, M., *Progres recents dans la mesure des impedances electrochimiques en regime sinusoidal.* Electrochimica Acta, 1974. **19**: p. 355-362.

36. Gabrielli, C., *Identification of electrochemical processes by frequency response analysis (Solartron Analytical Technical Report 004/83)*. 1998, Solartron. p. 130.

37. Morris, D.R. and Sun, X., *Water-Sorption and Transport Properties of Nafion 117 H.* Journal of Applied Polymer Science, 1993. **50**: p. 1445-1452.

38. Gebel, G., Aldebert, P., and Pineri, M., *Swelling study of perfluorosulphonated ionomer membranes.* Polymer, 1993. **34**(2): p. 333-339.

39. Casciola, M., et al., *On the decay of Nafion proton conductivity at high temperature and relative humidity.* Journal of Power Sources, 2006. **162**: p. 141-145.

40. Gardner, C.L. and Anantaraman, A.V., *Studies on ion-exchange membranes. II. Measurement of the anisotropic conductance of Nafion.* Journal of Electroanalytical Chemistry, 1998. **449**: p. 209-214.

41. Choi, P., Jalani, N.H., and Datta, R., *Thermodynamics and Proton Transport in Nafion II. Proton Diffusion Mechanisms and Conductivity.* Journal of The Electrochemical Society, 2005. **152**(3): p. E123-E130.

42. Nouel, K.M. and Fedkiw, P.S., *Nafion-based composite polymer electrolyte membranes.* Electrochimica Acta, 1998. **43**: p. 2381-2387.

43. Silva, R.F., Francesco, M.D., and Pozio, A., *Tangential and normal conductivities of Nafion membranes used in polymer electrolyte fuel cells.* Journal of Power Sources, 2004. **134**(1): p. 18-26.

44. Tsampas, M.N., et al., *The effect of membrane thickness on the conductivity of Nafion.* Electrochimica Acta, 2006. **51**: p. 2743-2755.

45. Dimitrova, P., et al., *Transport properties of ionomer composite membranes for direct methanol fuel cells.* Journal of Electroanalytical Chemistry, 2002. **532**: p. 75-83.

46. *DuPont Nafion PFSA Membranes Product Information*, in *NAE101*. 2004, DuPont. p. 2.

47. Seeliger, D., Hartnig, C., and Spohr, E., *Aqueous pore structure and proton dynamics in solvated Nafion membranes.* Electrochimica Acta, 2005. **50**: p. 4234-4240.

48. Sone, Y., Ekdunge, P., and Simonsson, D., *Proton Conductivily of Nafion 117 as Measured by a Four-Electrode AC Impedance Method.* Journal of The Electrochemical Society, 1996. **143**(4): p. 1254-1259.

49. Sumner, J.J., et al., *Proton Conductivity in Nafion 117 and in a Novel Bis[(perfluoroalkyl)sulfonyl]imide lonomer Membrane.* Journal of The Electrochemical Society, 1998. **145**(1): p. 107-110.

50. Choi, P. and Datta, R., *Sorption in Proton-Exchange Membranes An Explanation of Schroeder's Paradox.* Journal of The Electrochemical Society, 2003. **150**(12): p. E601-E607.

51. Elfring, G.J. and Struchtrup, H., *Thermodynamic considerations on the stability of water in Nafion.* Journal of Membrane Science, 2007. **297**: p. 190-198.

52. Onishi, L.M., Prausnitz, J.M., and Newman, J., *Water-Nafion Equilibria. Absence of Schroeder's Paradox.* Journal of Physical Chemistry B, 2007. **111**: p. 10166-10173.

53. Moggi, G., Bonardelli, P., and Bart, J.C.J., *Synthesis and properties of some hexafluoropropene-1,1-difluoroethene copolymers.* Polymer Bulletin, 1982. **7**: p. 115-122.

54. Holmberg, S., et al., *Structure and properties of sulfonated poly [(vinylidene fluoride)–g-styrene] porous membranes.* Journal of Materials Chemistry, 1996. **6**(8): p. 1309-1317.

55. Michot, T., Nishimoto, A., and Watanabe, M., *Electrochemical properties of polymer gel electrolytes based on poly(vinylidene fluoride) copolymer and homopolymer.* Electrochimica Acta, 2000. **45**: p. 1347-1360.

56. Zapata, P. and Meredith, J.C., *High Throughput Study of Novel PVDF/Acrylic Polyelectrolyte Semi-Interpenetrated Network Proton Exchange Membranes.* To be submitted for publication, 2009.

Chapter 3
High-Throughput Study of Novel PVDF/Acrylic Polyelectrolyte Semi-Interpenetrated Network Proton Exchange Membranes

The proton exchange membrane (PEM) is a fundamental component of the polymer electrolyte membrane fuel cell (PEMFC); a promising alternative energy conversion approach for low to medium power applications. Existing commercially available PEMs are predominantly based on perfluorosulfonic acid polymers (PFSA) (e.g., Nafion®), which are characterized by elevated costs owing to convoluted manufacturing processes. In this study the viability of semi-interpenetrating ionomer-polymer networks from blends of poly(vinylidene fluoride) (PVDF) and covalently crosslinked sulfonated acrylic polyelectrolytes (PE) as potential PEM materials is examined. A total of 80 dissimilar PVDF/PE membranes, prepared from five different grades of Kynar® PVDF (homo- and copolymers) and two types of PE, were

characterized in terms of proton conductivity and mechanical properties using custom-developed high-throughput screening tools. In addition to PE type and content, the crystalline characteristics (i.e., crystallinity and crystallite size) and melt viscosity of the inert PVDF phase were found to play a major role on proton conductivity. Particularly, membranes based on highly crystalline and viscous PVDF homopolymers exhibited the lowest proton conductivity due to precluded segmental motion and physical blockage of the PE chains during crosslinking. Mechanical properties of the membranes were dominated by the PVDF grade incorporated. Membranes based on stiffer PVDF homopolymers exhibited higher elastic modulus and tensile strength; while those based on the more flexible copolymers were tougher. In general PVDF/PE membranes compared favorably to Nafion®, having conductivities in excess of 130 mS/cm (vs. 84.5 mS/cm for Nafion®) and mechanical properties 2 to 5 times higher in some cases. The selection of a particular PVDF/PE membrane, however, implies a tradeoff between conductivity and mechanical properties that is determined by the requirements of the PEMFC final application.

3.1 Introduction

Nowadays, owing to numerous factors that span from environmental awareness and health-related issues to major social and political conflicts, the energy economy has started to move towards technologies that can overcome the multiple problems associated with the extraction and use of fossil fuels, while still providing high quality

power and other energy services [1-4]. Among these technologies fuel cells stand out as one of the most viable alternatives, and are anticipated to be one of the basic building blocks in the transition towards a sustainable energy economy in the 21st century [3-7].

The use of fuel cells is envisioned in many dissimilar applications that range from portable electronics to transportation to stationary power generation. However, unavoidably, power requirements vary to a great extent from one application to another, resulting in the necessity of various types of fuel cell technologies tailored for specific markets according to their power output. In the small to medium power markets (e.g., laptop computers and light duty vehicles, respectively), proton exchange membrane fuel cells (PEMFCs), also referred to as polymer electrolyte membrane fuels cells, have gained a great deal of attention [5, 6, 8].

At the heart of the PEMFC is the proton exchange membrane (or polymer electrolyte membrane) that gives the characteristic name to this particular fuel cell technology. The proton exchange membrane (PEM) serves as a solid electrolyte barrier that separates the fuel cell fuel and oxidant streams, while providing a path for fast transport of the protons resulting from the anodic oxidation of the fuel. Although this may sound as simple task to accomplish, the PEM has to meet a myriad of other requirements for robust fuel cell operation, thus becoming often one of the performance-limiting components in PEMFCs. Among these requirements are: low electronic conductivity, low permeability to both fuel and oxidant, low water transport, high hydrolytic stability under the oxidative fuel cell environment, and excellent mechanical integrity; not to mention competitive cost [7, 9-13].

Perfluorosulfonic acid (PFSA) polymer electrolyte membranes such as DuPont's Nafion® have been the platform of choice for the development of PEMFCs in the past [9, 10, 13]; however, Nafion® and other PFSA-based membranes are considerably expensive and have operational limitations such as high fuel crossover and relatively poor mechanical integrity when swollen (in the hydrated state) [9, 10]. Extensive research is underway to address these limitations and meet the aforementioned PEM requirements in order to devise affordable materials with enhanced performance and extended lifetime. Although a large branch of the fuel science still focuses on PFSA-based membranes, present-day PEM research also involves the development of alternative PEM materials based on the functionalization, particularly sulfonation, of high-performance hydrocarbon polymers such as polyimides (PI), poly(ether ether ketone)s (PEEK), poly(ether sulfone)s (PES), polybenzimidazole (PBI), and other polyaromatics [10]. A different approach that can provide a potential cost-effective alternative to PFSA membranes involves the blending of a proton-conducting component with a highly stable and mechanically sound inert component (generally an engineering thermoplastic) that provides improved mechanical and thermal stability to the membrane [9, 14-16].

Although less common than post-sulfonation strategies, polymer blending is gaining ground as promising methodology for the development of PEMs. For instance, recent studies including PEMs based on methylmethacrylate (MMA) compatibilized poly(vinylidene fluoride) (PVDF) and styrene-ethylene/butylene-styrene (SEBS) blends [17]; poly(2,6-dimethyl-1,4-phenylene oxide) (PPO) acid-base blends [18]; sulfonated

poly(arylene ether), PES, and polysulfone (PSF), or PBI blends [16]; sulfonated poly(ether ketone ketone) (SPEKK) and PES (or SPEKK with a different sulfonation level) blends [15]; and poly(styrene-*b*-vinylbenzylphosphonic acid) (PS-*b*-PVBPA) and PPO blends [14]; have shown the feasibility of the technique. The key advantage of polymer blending resides in the ability to combine the properties of two or more different polymers; which in turn can result in a considerable decoupling of mechanical and proton-conducting properties. Moreover, the use of accessible commercial polymers is an added advantage since synthesis of new polymers is not required, thus reducing the costs associated with the development of new PEM materials.

PVDF is a commercially available and widespread engineering thermoplastic that exhibits remarkable chemical resistance in highly oxidative and extreme acidic environments, as well as exceptional electrochemical stability and mechanical toughness; making it an excellent candidate mechanical support (inert matrix) of blended PEMs. In fact, PVDF has been recently used in new PEM materials designs including blending with SEBS [17] (as previously mentioned), and PVDF supported free-radical polymerized methacrylic and *p*-styrenesulfonic acid membranes [19]. Its suitability as porous support for direct methanol fuel cell PEMs has also been assayed [20]. In this work we evaluate the practicability of ionomer-polymer semi-interpenetrated networks (SIPN) obtained by compatibilized blends of PVDF (inert matrix, mechanical support phase) and covalently crosslinked sulfonated acrylic polyelectrolytes (PE) (proton-conducting phase) as potential PEM material candidates. In particular proton-conducting and mechanical properties are examined for a wide

variety of membranes based on two types of acrylic polyelectrolytes of different equivalent weight and multiple dissimilar PVDF grades.

Exploratory research comprising *de novo* material syntheses generally involves extensive variable spaces that encompass both material properties and processing conditions. To alleviate this burden high-throughput screening techniques are utilized for the characterization of PVDF/PE membranes as they provide a suitable framework to address large variable spaces. Namely, a high-throughput mechanical testing apparatus (HTMECH) based on a previous design [21] is used for characterization of mechanical properties, and a recently developed AC electrochemical impedance spectroscopy high-throughput conductivity measuring device (HTC) [22] is used for proton-conductivity characterization. High-throughput methods have been recently utilized in the fuel cell area in the study of catalysts for use in PEMFCs [23], and a comprehensive application of these techniques to the study of other PEMFC components such as the proton exchange membrane can offer significant cost and efficiency advantages to the discovery and optimization stages of the global PEMFC design and development process.

3.2 Experimental

3.2.1 Membrane preparation, protonation, and conditioning

Proton-conducting SIPN membranes were prepared from numerous grades of Kynar® poly(vinylidene fluoride) (PVDF) and two dissimilar novel sulfonated acrylic polyelectrolytes (PE) consisting of a random copolymer of 2-sulfoethyl methacrylate

(SEM) (~69wt%), 2-hydroxyethyl methacrylate (HEMA) (~15wt%), methyl methacrylate (MMA) (~8wt%), and styrene (~7wt%) in the case of polyelectrolyte No.1 (PE1); and a random copolymer of SEM (~90wt%) and HEMA (~10wt%) in the case of polyelectrolyte No.2 (PE2) (Figure 3.1). The different Kynar® PVDF grades utilized, specifically Kynar® 500, Kynar® 731, Kynar® 2801, Kynar® 2821, and Kynar® 2851 (all in a fine powder form) (Arkema Inc.); were dissolved in 1-methyl-2-pyrrolidinone (NMP) (Sigma-Aldrich Co., assay ≥99.5%) to a total concentration of 10wt% per solution. These solutions were mixed at multiple PVDF to PE ratios with individual stock solutions (25wt% total solids in NMP) of each polyelectrolyte. PVDF/PE mixtures were combined with Desmodur N-3300A (Bayer AG.), a 1,6-hexamethylene diisocyanate-derived triisocyanate crosslinker, at a 1:0.8 OH:NCO ratio for PE1 and 1:0.9 OH:NCO ratio for PE2 (80 and 90mol% of the stoichiometric amount of crosslinker needed to react with all the polyelectrolyte hydroxyl groups respectively). The final blends were thoroughly mixed at room temperature under an inert nitrogen atmosphere for approximately 30 min, followed by a brief degassing by sonication (~5 min) before film coating. Coating was performed using a knife-edge apparatus [24, 25] to spread liquid PVDF/PE films onto silicon <100> substrates (Silicon, Inc.) previously cleaned for 2 h in Piranha solution (70% H_2SO_4, 9% H_2O_2, 21% H_2O) at 80°C. The resulting films were cured at 175°C for 20 min in a forced convection oven to crosslink the PE and remove excess NMP. Conversion of isocyanate groups into urea linkages was estimated via Fourier transform infrared (FT-IR) spectroscopy (section 3.2.4.3) by tracking the disappearance of the -NCO peak (2260 cm^{-1}), in order to confirm the completeness of the PE crosslinking reaction. Cured

PVDF/PE membranes were detached from the silicon substrates by immersion in DI water at room temperature. Composition of final membranes ranged from 25wt% to 65wt% neutralized form PE (equivalent to ~17wt% to ~48wt% acid form PE in the case of PE1, and ~15wt% to 44%wt acid form PE in the case of PE2) for each grade of Kynar® PVDF and each PE.

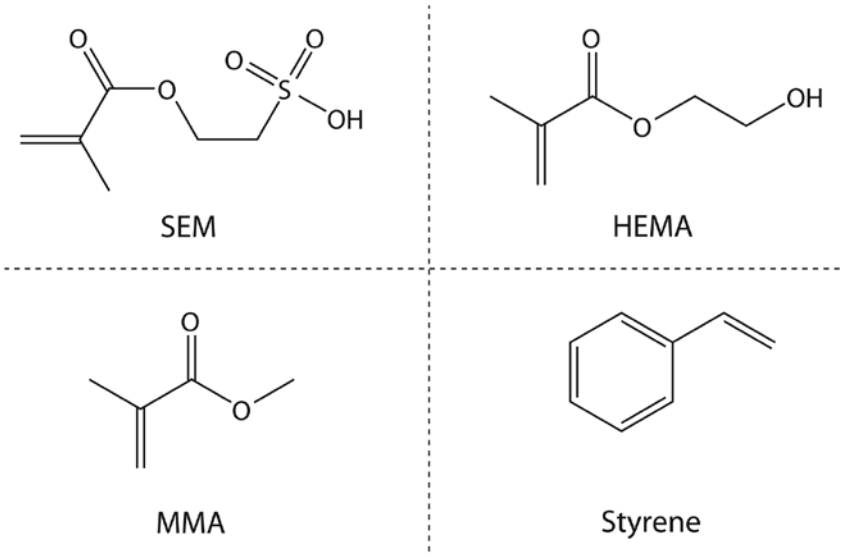

Figure 3.1 Acrylic polyelectrolyte constitutive monomers. PE1: SEM (69wt%) + HEMA (15wt%) + MMA (8wt%) + Styrene (7wt%). PE2: SEM (90wt%) + HEMA (10wt%).

Prior to protonation, free-standing membranes were washed in a 1M HCl solution at 80°C for 2 h, followed by a 15-minute rinse in DI water. The acid-washed membranes were protonated by immersion in 1M H_2SO_4 at 80°C for 2 h, followed by removal of

excess sulfuric acid by several successive 15-minute rinses in DI water until the pH of the rinse water was above 4. Conditioning of protonated PVDF/PE membranes, as well as Nafion® 112 standards used as reference, was carried out by immersion in boiling 18.2 MΩ water for 1 h to allow complete membrane swelling. Swollen membranes were stored in 18.2 MΩ water until conductivity measurements were performed.

3.2.2 High-throughput conductivity measurement

Proton conductivity measurements were performed by AC electrochemical impedance spectroscopy (EIS) using a custom fully automated high-throughput conductivity measuring device (HTC) [22]. Briefly, the conditioned membrane to be tested is placed in an electrically insulating sample holder and held in place with a grid-like retention mechanism. The sample holder assembly is filled with 18.2 MΩ water to fully cover the membrane and avoid dehydration. The water-immersed membrane is excited via a small AC signal using a miniature 4-point probe (point-contact collinear electrodes), that creates a dipole source with cylindrically symmetric iso-current surfaces within the membrane. The response voltage is measured via the inner point-electrodes, which allows determining the membrane complex impedance. Proton conductivity is estimated from the calculated complex impedance by means of the following model:

$$\sigma\big|_{Z''\to 0} \approx -\frac{1}{Z_{(jw)}2\pi h}\left[\ln\left(\frac{x_1}{x_2+x_3}\right)-\ln\left(\frac{x_1+x_2}{x_3}\right)\right] \qquad 3.1$$

where σ is the membrane proton conductivity, $Z_{(j\omega)}$ is the membrane complex impedance, h is the membrane thickness, and x_i are the inter-electrode distances of the 4-point probe.

Conductivity measurements for all membranes, including Nafion® 112 standards, were performed using the HTC in potentiostatic mode with an excitation signal of 1000 Hz and 30 mV (~20 mV RMS), and a response signal integration time of 5000 cycles following a 5 second stabilization period.

3.2.3 High-throughput measurement of mechanical properties

Characterization of PVDF/PE membranes mechanical properties was performed using an automated modified high-throughput mechanical testing apparatus (HTMECH) based on a previous design [21]. A general overview of the process is as follows: the membrane is mounted on a sample holder consisting of a pair of grid-like steel isolation plates affixed to a linear motor. The holder/membrane assembly is moved at a predefined speed towards a hemispherical-tip shaft connected to a high-sensitivity load cell. As the membrane is indented by the shaft or "needle" the force exerted on load cell is recorded, generating a force vs. time profile that depicts the evolution of the membrane axisymmetric biaxial deformation and fracture process. Analysis of this profile, performed using a custom developed algorithm [26] based on undecimated wavelet transforms and non-causal zero-phase IIR filters for signal conditioning and denoising, and profile scaling and second derivative techniques for characterization;

allows the assessment of the material mechanical properties (e.g., elastic modulus, tensile strength, elongation at break, and toughness).

Mechanical characterization tests for all membranes and Nafion®112 standards were performed at a constant speed of 10 mm/s using a 1.24 mm diameter needle (needle to isolation plate hole diameter ratio: 0.413). Sampling rate of the load cell signal was set to 5000 samples per second. All membranes were tested in a fully hydrated state.

3.2.4 PVDF and membranes characterization

3.2.4.1 Differential scanning calorimetry (DSC)

Thermal characterization of PVDF powders via DSC was carried out using a DSC Q20 (TA Instruments). PVDF samples (approx. 5 mg each), enclosed in hermetic aluminum pans, were subjected to three temperature cycles (heating-cooling-heating) within a temperature interval of -40°C to 200°C at a heating/cooling rate of 10°C/min. All tests were performed under an inert nitrogen atmosphere.

3.2.4.2 X-Ray diffraction (XRD)

X-ray diffraction spectra of PVDF powders and proton conducting membranes were recorded using a PANalytical X'Pert PRO diffractometer (PANalytical). The incident beam configuration consisted of a Cu-anode tube (λ CuKα_1 = 1.540598 Å,λ CuKα_2 = 1.544426 Å) operated at 45 kV and 40 mA with a fixed 1/16°(0.19 mm) divergence slit, a 0.04 rad Soller slit, and a nickel β-filter to remove CuKβ radiation. The

detector, a PANalytical X'Celerometer, was equipped with a 10 mm anti-scatter slit and a 0.04 rad Soller slit. Data was collected over a 2θ range of 2°-70° using a step size of 0.008°.

3.2.4.3 Fourier transform infrared spectroscopy (FT-IR)

Infrared absorption spectra of PVDF films and proton conducting membranes were collected at room temperature with a Bruker IRscope II (Bruker Optics Inc.) for reflection mode and a Bruker Equinox 55 spectrometer (Bruker Optics Inc.) for transmission mode, both coupled with a KBr beam splitter. The spectra were recorded in the range of 400-5000 cm^{-1} at a resolution of 4 cm^{-1} and averaged 128 times.

3.2.4.4 Scanning electron microscopy (SEM)

High resolution images of proton conducting membranes were obtained using a LEO 1530 thermally assisted field emission scanning electron microscope (LEO Electron Microscopy Group), operated at 10keV. Samples for SEM imaging where prepared by cryogenic breaking in liquid nitrogen followed by vacuum metallization with gold.

3.2.5 Statistical analysis

An unbalanced univariate general linear model (GLM) (2 and 3-way, type III sums of squares) was used for evaluation of significant factors; $p < 0.05$ was defined as significant (5% significance level). Levene's test was used to determine data sets

homogeneity of variance (homoscedasticity); while data sets normality was assessed using the Shapiro-Wilk test. Pairwise comparisons of significant factors from 3-way GLM tests were performed by comparisons of unweighted means of main effects with Sidak-adjusted confidence intervals; while Tamhane's T2 post hoc test was utilized for pairwise comparisons of significant factors from 2-way GLM tests. All results are expressed as mean ± standard error of the mean (± S.E.M.) or as mean ± 95% confidence intervals, according to indicated.

3.3 Results and Discussion

3.3.1 Proton conductivity

Proton conductivity from HTC screening of 80 different types of proton conducting membranes, prepared from various grades of Kynar® PVDF and several weight fractions of acrylic polyelectrolytes, is shown in Figure 3.2 and Figure 3.3. An initial qualitative evaluation of the visual data presented in the figure calls attention to an apparent correlation between conductivity and PE content for both polyelectrolytes and each Kynar® grade. Also revealed is the dissimilarity between membranes containing one or the other polyelectrolyte, and how these PVDF/PE membranes compare to Nafion® 112 (semi-transparent planes in Figure 3.2 and Figure 3.3) at identical testing conditions. PE2-based membranes compare more favorably to Nafion® 112 as they reach comparable or higher conductivities (up to 25-30 mS/cm more in some cases) than Nafion® at PE2 contents of 45wt% and above. Conversely, only PE1 membranes

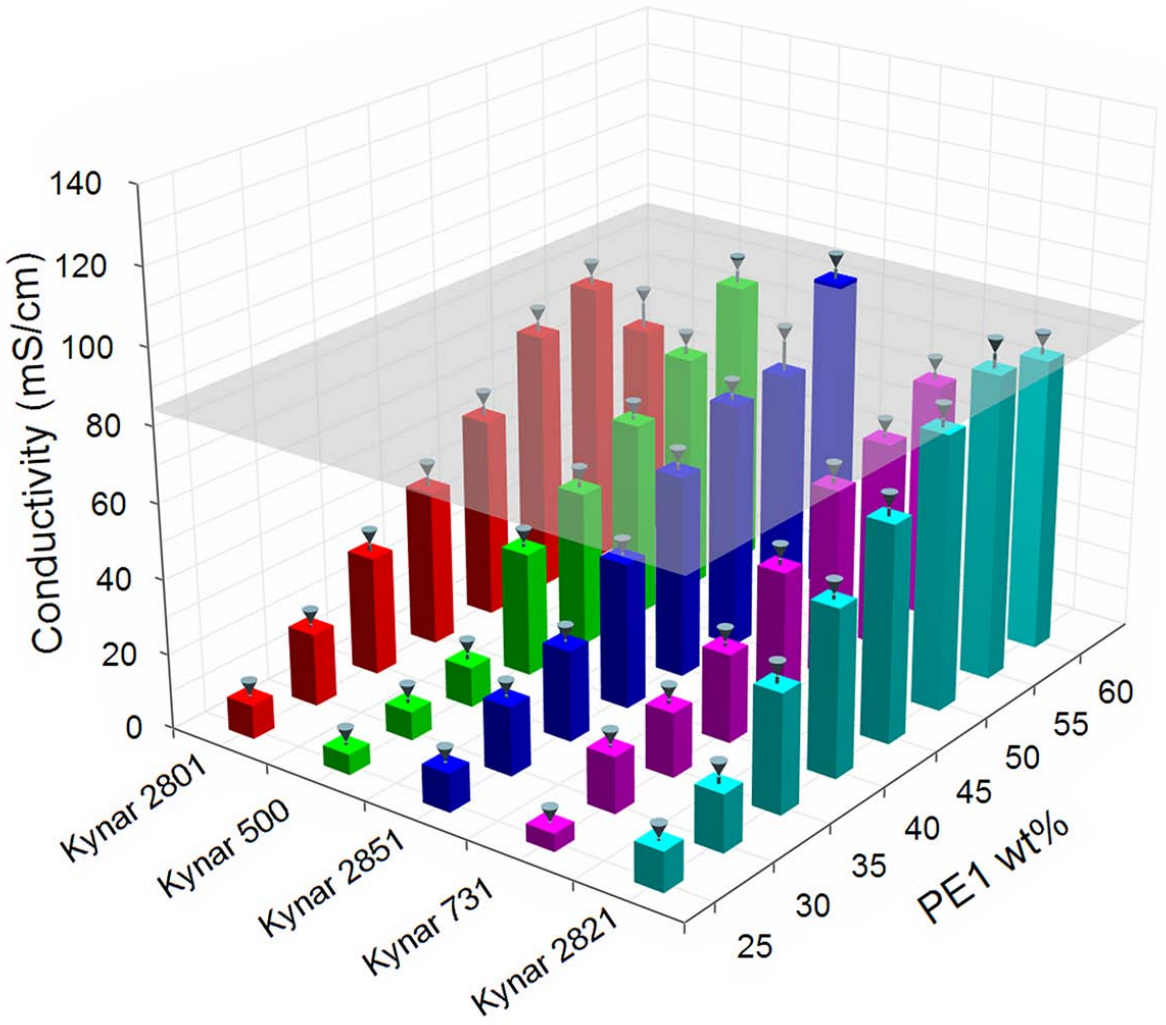

Figure 3.2 Conductivity of Kynar® PVDF/PE1 membranes for various Kynar® grades and PE1 mass fractions: range: 25 to 60wt% neutralized form PE1 (equivalent to approx. 17 to 48wt% acid form PE1). PE1 content in the figure is expressed as the weight percentage of neutralized form PE1 in the final membrane Test conditions: 18.2 MΩ water at 25°C. Excitation signal: 1000Hz, 30mV. Semitransparent planes correspond to the average conductivity of Nafion® 112 (84.5 ± 0.54 mS/cm [22]) at identical testing conditions. Values are averages ± S.E.M. (indicated by error bars delimited with inverted cone markers) (n=2-24).

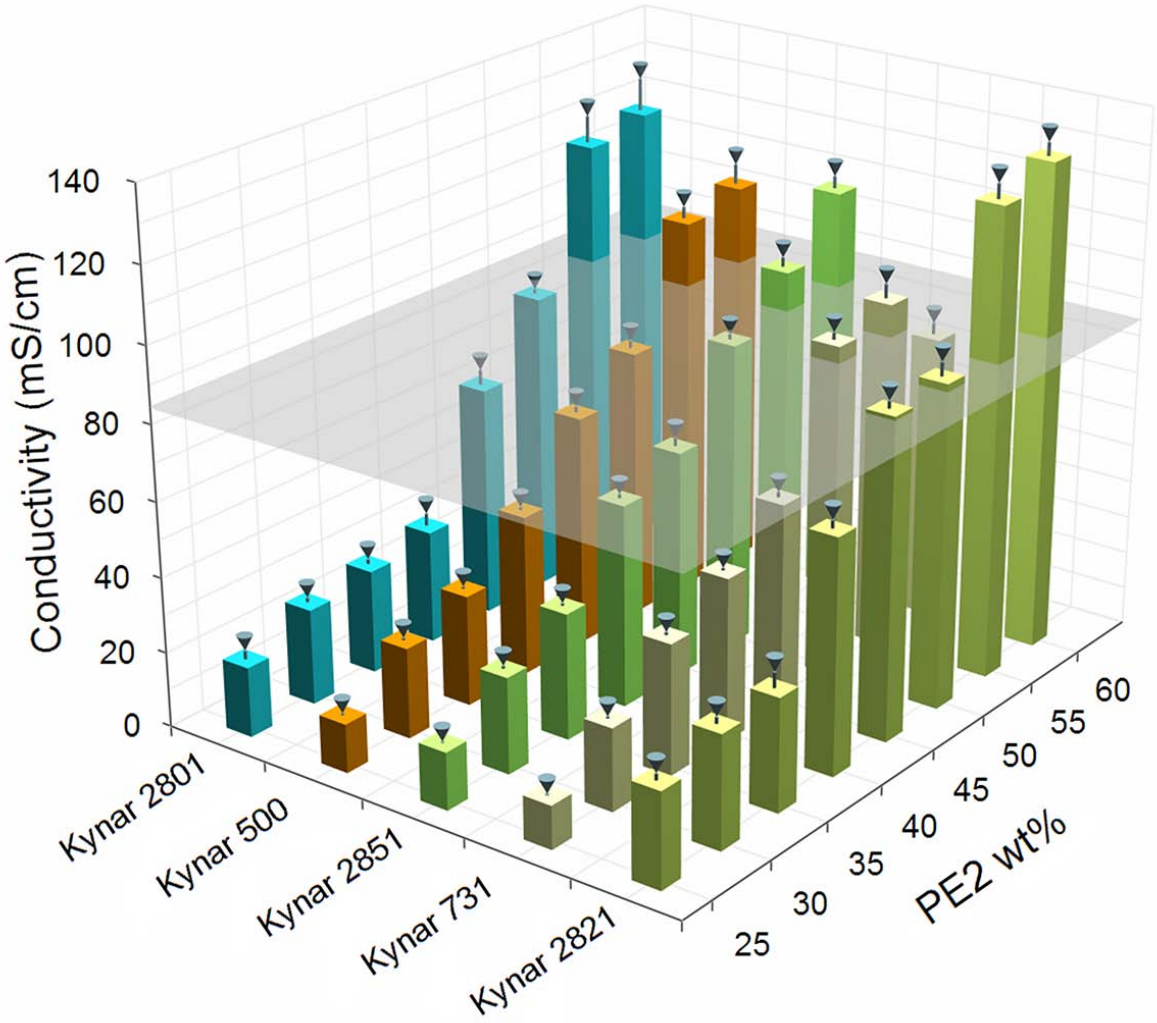

Figure 3.3 Conductivity of Kynar® PVDF/PE2 membranes for various Kynar® grades and PE2 mass fractions: range: 25 to 60wt% neutralized form PE2 (equivalent to approx. 15 to 44wt% acid form PE2). PE2 content in the figure is expressed as the weight percentage of neutralized form PE2 in the final membrane Test conditions: 18.2 MΩ water at 25°C. Excitation signal: 1000Hz, 30mV. Semitransparent planes correspond to the average conductivity of Nafion® 112 (84.5 ± 0.54 mS/cm [22]) at identical testing conditions. Values are averages ± S.E.M. (indicated by error bars delimited with inverted cone markers) (n=4-16).

containing Kynar® 2821 or 2851 attain conductivities in the same order as Nafion® 112. In general, membranes containing PE2 exhibit higher conductivity than their PE1 counterparts at identical PE mass fraction, expected from the lower equivalent weight of the former (280 gr PE1/mol SO_3H for PE1 vs. 216 gr PE2/mol SO_3H for PE2) which translates in lower activation energy of proton mobility. However, the differences in conductivity between membranes are not restricted exclusively to the PE content and appear to be influenced by the PVDF grade as well. To evaluate the effect of these factors on the PVDF/PE membranes properties, and assay the dissimilarities between membranes in a quantitative manner, the conductivity data generated from the HTC screening was analyzed using an unbalanced GLM. As anticipated the PE content and PE type play a major role on proton conductivity, as the analysis revealed statistically significant effects of PE content ($F_{(7,815)} = 1154.01$, $p < 0.001$), directly related to the evident rise in conductivity with increasing PE mass fraction; and PE type ($F_{(1,815)} = 807.92$, $p < 0.001$), related to the aforementioned equivalent weight difference between the polyelectrolytes. A significant effect of PVDF grade on proton conductivity was also evident ($F_{(4,815)} = 84.51$, $p < 0.001$). Interestingly, a partial eta squared statistic (η_p^2) (which reports the "practical" significance of a factor on the dependent variable) of 0.293 indicates a considerable effect size of PVDF grade; that is, PVDF grade by itself accounts for about 30% of the overall variance, suggesting that the PVDF grade has actually an *important* effect on the membrane proton conductivity. Significant interaction effects between PE type and PVDF grade ($F_{(4,815)} = 6.37$, $p < 0.001$), PE content and PVDF grade ($F_{(28,815)} = 6.7$, $p < 0.001$), and PE type and PE content ($F_{(7,815)} = 38.29$, $p < 0.001$); were also

present. Ensuing simple main effects tests performed separately at fixed levels of the significant factors verified the interactions, including the influence of PVDF grade on proton conductivity for PE1 contents above 30wt% ($4.92 \leq F_{(4,815)} \leq 18.11$, $p < 0.001$) and PE2 contents above 35wt% ($6.97 \leq F_{(4,815)} \leq 56.02$, $p < 0.001$); the effect of PE type for all PVDF types (particularly for PE contents of 35wt% and above ($4.26 \leq F_{(1,815)} \leq 250.87$, $p < 0.001$); and the impact of PE content at all levels of PVDF grade and PE type.

Pairwise comparisons by unweighted means of PE content at a 5% significance level ($\alpha = 0.05$) with Sidak-adjusted confidence intervals showed that conductivity of membranes with a PE content of 55wt% and 60wt% are statistically indistinguishable ($p = 0.661$) regardless of the polyelectrolyte type. This is in line with our previous findings from membranes based solely on PE1 [22], and suggests the existence of an optimal amount of PE content in the vicinity of 55-60wt% above which any gain in proton conductivity is marginal or even unattainable. Presumably, this effect is associated with the coalescence of PE chains observed at high weight fractions of PE in the membranes (Figure 3.4 and Figure 3.5, only one representative image per polyelectrolyte type is shown at high PE to visualize the difference between clusters of each PE type. Figure 3.6 is provided as contrast due to the absence of PE clusters), which in turn may be directly related with the neutralization degree of the polyelectrolyte (for this particular study both polyelectrolytes have a degree of neutralization of 0.95). At elevated PE concentrations the un-neutralized sulfonic acid groups have higher probability of coming in close range one to another before covalent crosslinking of the PE, resulting in the coalescence of PE chains to form PE clusters. In addition, this outcome may explain

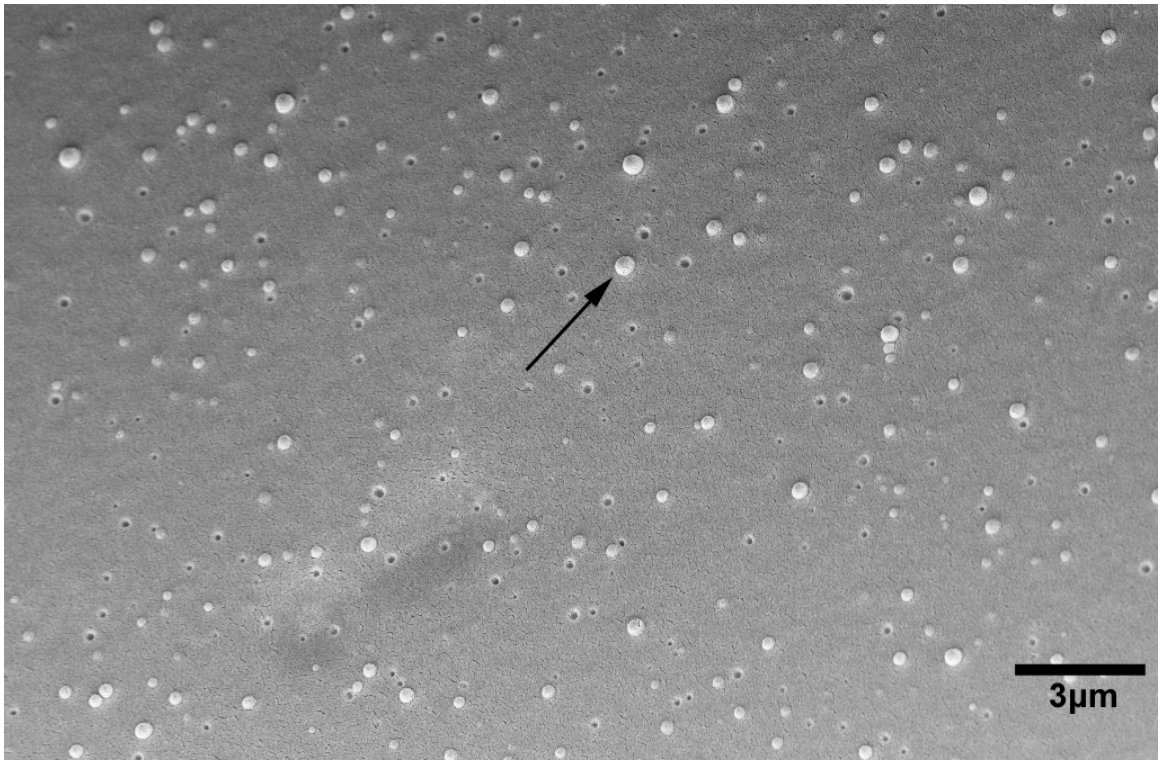

Figure 3.4 SEM image of the cross-sectional area of a Kynar® 2851/PE1 membrane with 60wt% neutralized form PE1, EHT 10 kV. Arrow indicates a representative PE1 cluster resulting from the coalescence of PE1 chains.

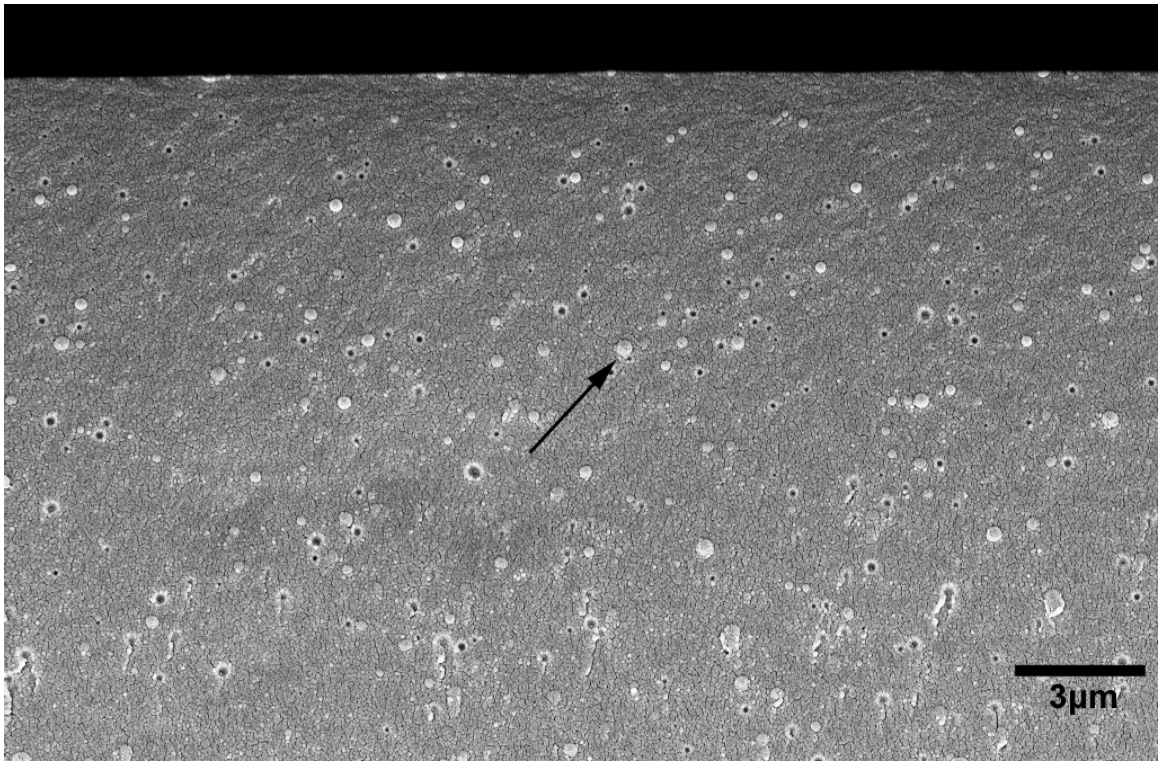

Figure 3.5 SEM image of the cross-sectional area of a Kynar® 500/PE2 membrane with 60wt% neutralized form PE2, EHT 10 kV. Arrow indicates a representative PE2 cluster resulting from the coalescence of PE2 chains

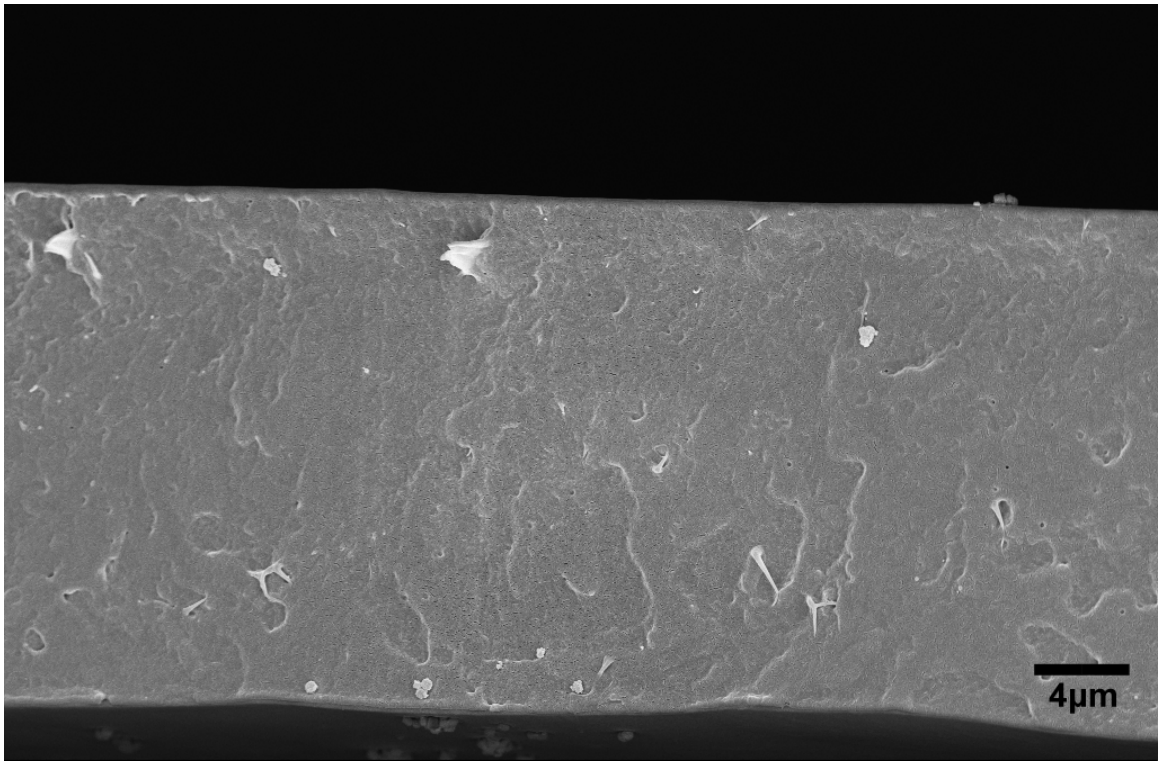

Figure 3.6 SEM image of the cross-sectional area of a Kynar® 2801/PE1 membrane with 25wt% neutralized form PE1, EHT 10 kV. Image is provided as contrast to Figure 3.4 and Figure 3.5 due to the absence of PE clusters (artifacts in the image are the result of the cryogenic fracture).

the slight haziness noticed on most of the membranes with elevated PE content owing to light scattering from the PE clusters embedded in the membranes.

In contrast pairwise comparisons of unweighted means of PVDF type exposed an interesting result: the presence of four homogeneous subsets where only Kynar® 2851 and 2801 constituted a non-single member subset. Previously, in our study of PVDF/PE1 membranes [22], the homogeneous subsets coincided with the family to which each PVDF type belonged; that is, membranes containing PVDF:HFP (hexafluoropropylene) copolymers (Kynar® 2801, 2821, and 2851) constituted a homogeneous subset, while those containing PVDF homopolymers (Kynar® 500 and 731) constituted each a separate subset. The departure of Kynar® 2821 from a homogeneous subset for PE1-based membranes to an individual subset for PE2-based membranes is readily seen in Figure 3.7, which displays the comparison of global and individual (PE1 and PE2) unweighted means of conductivity by PVDF type. This divergence is not completely unexpected as it is supported by the aforementioned significant interaction effect between PE type and PVDF grade. However, albeit the differences among homogeneous subsets of PE1 and PE2 membranes, it is important to notice that the overall trend of unweighted means depicted in Figure 3.7 is almost identical for both polyelectrolytes. This similarity is a clear indicator that membrane proton conductivity is closely related to the PVDF properties and that the effect of a specific PVDF grade on conductivity is comparable across all acrylic polyelectrolytes used. For instance, regardless of the PE type, high proton conductivity was favored in membranes containing PVDF:HFP copolymers when compared to those containing PVDF homopolymers. Furthermore, the highest

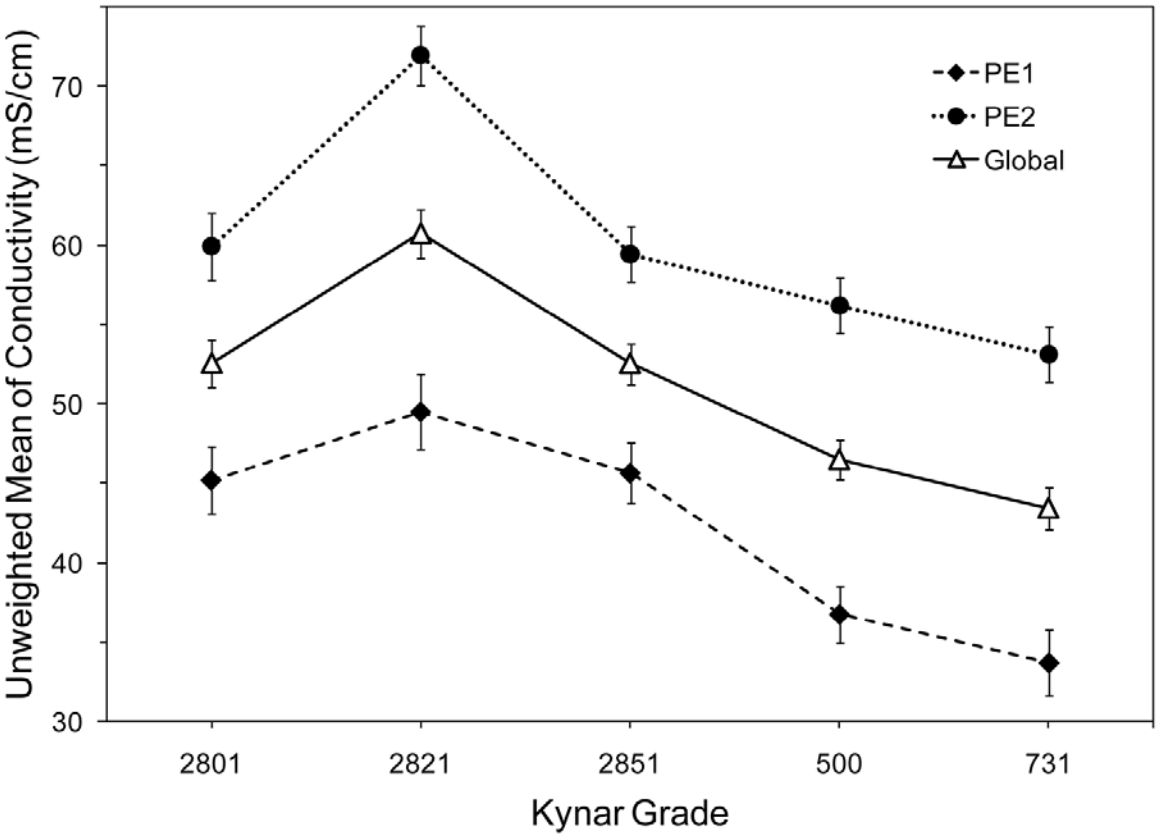

Figure 3.7 Unweighted means of conductivity as a function of Kynar® grade estimated from 2-way (PE1 and PE2 profiles), and 3-way (global profile) univariate unbalanced GLM analysis (full factorial model). Error bars represent the upper and lower bounds of 95% confidence intervals.

conductivity always corresponded to membranes based on Kynar® 2821, while the lowest to those based on Kynar® 731.

PVDF is an extensively studied semi-crystalline polymer notorious for the complex polymorphism of its crystalline phase [27-32] (some properties of the PVDF grades used in this study are shown in Table 3.1). There are at least four known PVDF crystal phases; namely, α (phase II), β (phase I), γ (phase III), and δ (phase IV, or polar phase II), which are dependent on numerous factors including mechanical and thermal history, as well as processing conditions. Furthermore, it is known that the use of a co-monomer such as HFP can disrupt the ordering of the PVDF chains, thus reducing its degree of crystallinity [27, 33, 34]. The degree of crystallinity and type of crystalline phase of PVDF can affect its bulk properties (e.g., mechanical strength, glass transition and melting temperatures), as well as its interaction with other polymers (e.g., miscibility, phase separation). Information about crystallinity, and crystalline structure in general, of the different PVDF grades can be obtained directly from their corresponding XRD spectra (shown in Figure 3.8). All the spectra profiles exhibit relatively similar semi-crystalline morphologies with a broad amorphous halo and crystalline reflections (Bragg peaks) located at the following scattering angles (2θ): 18.34°±0.07°, 19.89°±0.07°, and 26.61°±0.14° (Table 3.2). These locations are associated with the reflections (020), (110), and (021) typical of the PVDF α-phase [30-32, 35, 36], the most thermodynamically stable (lowest energy state) due to its TGTG' arrangement. This indicates that the crystalline phase type for both homo- and copolymer samples is identical and that differences in crystallinity among them are due to the size and amount of crystallites. XRD spectra

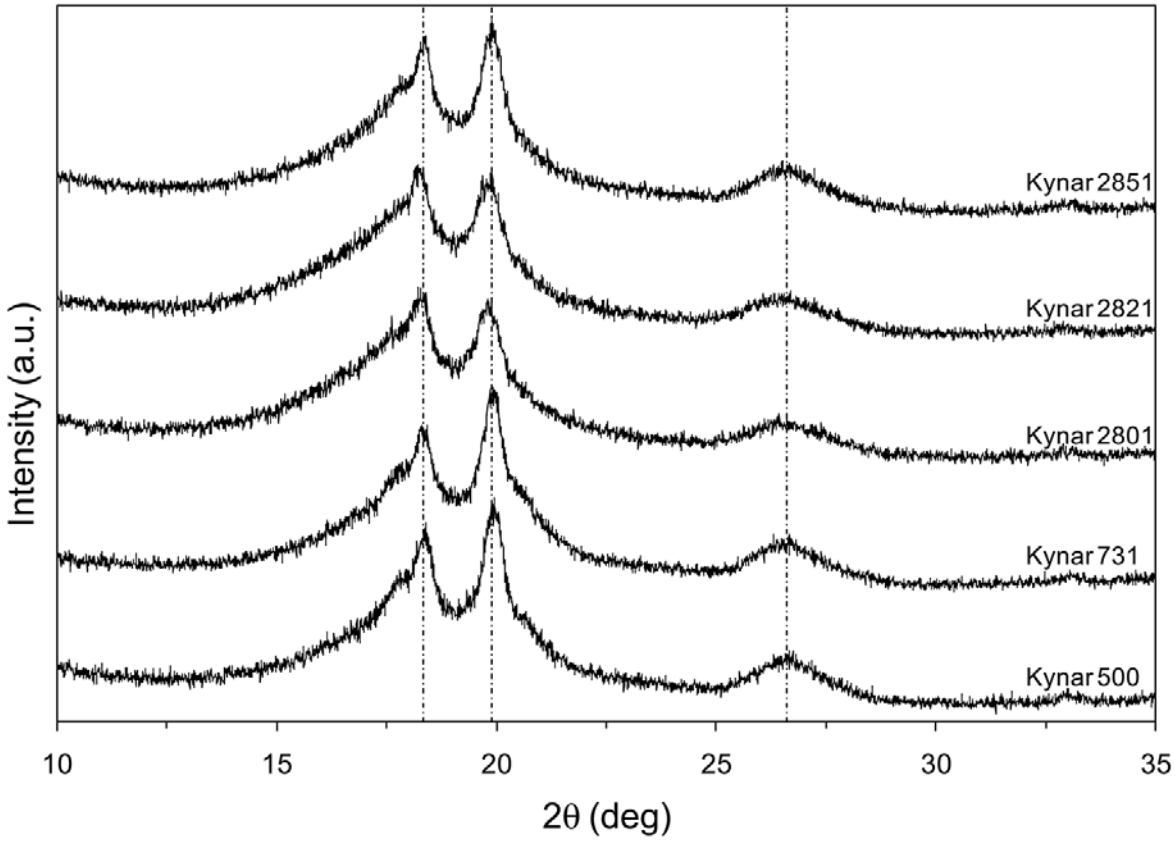

Figure 3.8 Wide angle X-ray diffraction spectra of Kynar® PVDF powders (as received from the manufacturer). Vertical lines indicate α-phase crystalline reflections at scattering angles (2θ) 18.34° (020), 19.89° (110), and 26.61° (021).

Table 3.1 Characteristics and properties of the different Kynar® PVDF grades used in this study

PVDF grade	Type	Comonomer	Comonomer wt%	Melt viscosity (kP)	Mw [a] (g/mol)
Kynar® 500	Homopolymer	–	–	31.42	523,000
Kynar® 731	Homopolymer	–	–	16.92	462,000
Kynar® 2801	Copolymer	HFP	~10	19.77	470,000
Kynar® 2821	Copolymer	HFP	~10	8.6	–
Kynar® 2851	Copolymer	HFP	~5	24.8	454,700

[a]Values found in the literature can vary as much as 350,000 g/mol for the same PVDF grade. Consequently, the molecular weight values presented for each PVDF type correspond to the mode of values from multiple sources, and should not be considered as exact.

Table 3.2 Wide angle X-ray diffraction (WAXD) of pure PVDF powders

PVDF grade	*hkl* (020)		*hkl* (110)		*hkl* (021)		*D*(Å)[a]
	2θ(°)	*d*(Å)	2θ(°)	*d*(Å)	2θ(°)	*d*(Å)	
Kynar® 500	18.38	4.83	19.95	4.45	26.75	3.33	183.58
Kynar® 731	18.43	4.82	19.96	4.45	26.70	3.34	200.15
Kynar® 2801	18.27	4.86	19.80	4.49	26.44	3.37	164.56
Kynar® 2821	18.27	4.86	19.89	4.47	26.69	3.34	152.36
Kynar® 2851	18.38	4.83	19.89	4.47	26.50	3.36	159.55

[a]Crystallite sizes derived from baseline-corrected (110) crystalline reflections.
(θ) Bragg angle. (*d*) Interplanar spacing. (*D*) Crystallite size approximation from Scherrer's equation.

were baseline-corrected and smoothed using a fast Fourier transform (FFT) filter, followed by Voigt and Gaussian peak fitting (Peakfit, Systat Software Inc.) to deconvolute the crystalline peaks from the amorphous halo. The size of coherently diffracting crystalline domains (crystallites) was approximated from the broadening of their diffraction peaks via Scherrer's equation (Eq. 2) [37] (ignoring instrument-related peak broadening effects):

$$D = \frac{K\lambda}{\beta_{2\theta}\cos\theta_0} \qquad 3.2$$

where D is the average crystallite size perpendicular to a particular *hkl* plane, $\beta_{2\theta}$ is the angular width at half maximum of the peak associated with the *hkl* plane, θ_0 is the peak centroid Bragg angle, λ is the CuKα wavelength, and K is the Scherrer shape factor (taken as ~0.94, assuming that a cube-shaped monodisperse crystallites model is valid for the general case). Overall, calculation of crystallite size was robust to ambiguities of the peak fitting and deconvolution process, revealing smaller crystallites in the matrix of the PVDF copolymers than in the homopolymers (Table 3.2).The smallest crystallites correspond to Kynar® 2821 (152.4 Å), while the largest to Kynar® 731 (200.2 Å). Conversely, crystallinity fluctuated considerably depending on the data processing and manipulation of the spectra; as a result, it was quantified via DSC.

Calculation of the Kynar® PVDF crystallinity was carried out using the following simple model (a more rigorous approach can be found elsewhere [38]):

$$X_C(\%) = \frac{\Delta H_f}{\Delta H_m^0} \times 100 \qquad 3.3$$

where ΔH_f is the enthalpy of fusion of the PVDF sample calculated by integration of the fusion endotherms of the DSC heating profiles (presented in Figure 3.9), and ΔH_m^0 is the standard enthalpy of fusion of 100% crystalline PVDF. In lieu of individual standard enthalpies of fusion for each of the PVDF grades, a typical accepted value of 104.7 J/g [35, 39] was used. Hence the crystallinities calculated are *relative* values. The lack of exothermic recrystallization peaks in all DSC profiles indicates no additional heat-induced crystallization of the amorphous phase; therefore, no further adjustment of the calculated enthalpies of fusion was necessary. Crystallinity values, along with thermal characteristics including crystallization enthalpies and temperatures (from DSC cooling ramps, not shown), are presented in Table 3.3. Following the same trend of crystallite size, copolymers exhibit a lower degree of crystallinity than the homopolymer counterparts. Particularly, Kynar® 2821 is ranked at the bottom with the smallest crystallites and lowest crystallinity (152.4 Å and 24.8%); in addition, it also has the lowest melting and crystallization temperatures (144.9°C and 97.2°C). In contrast, Kynar® 731 has the largest crystallites and highest crystallinity (200.2 Å and 69.1%), in addition to the highest melting and crystallization temperatures (169.1°C and 135.2°C). Remarkably, the aforementioned trend of unweighted means of proton conductivity follows the exact opposite behavior; that is, Kynar® 2821 based membranes have the highest average conductivity, while those containing Kynar® 731 have the lowest

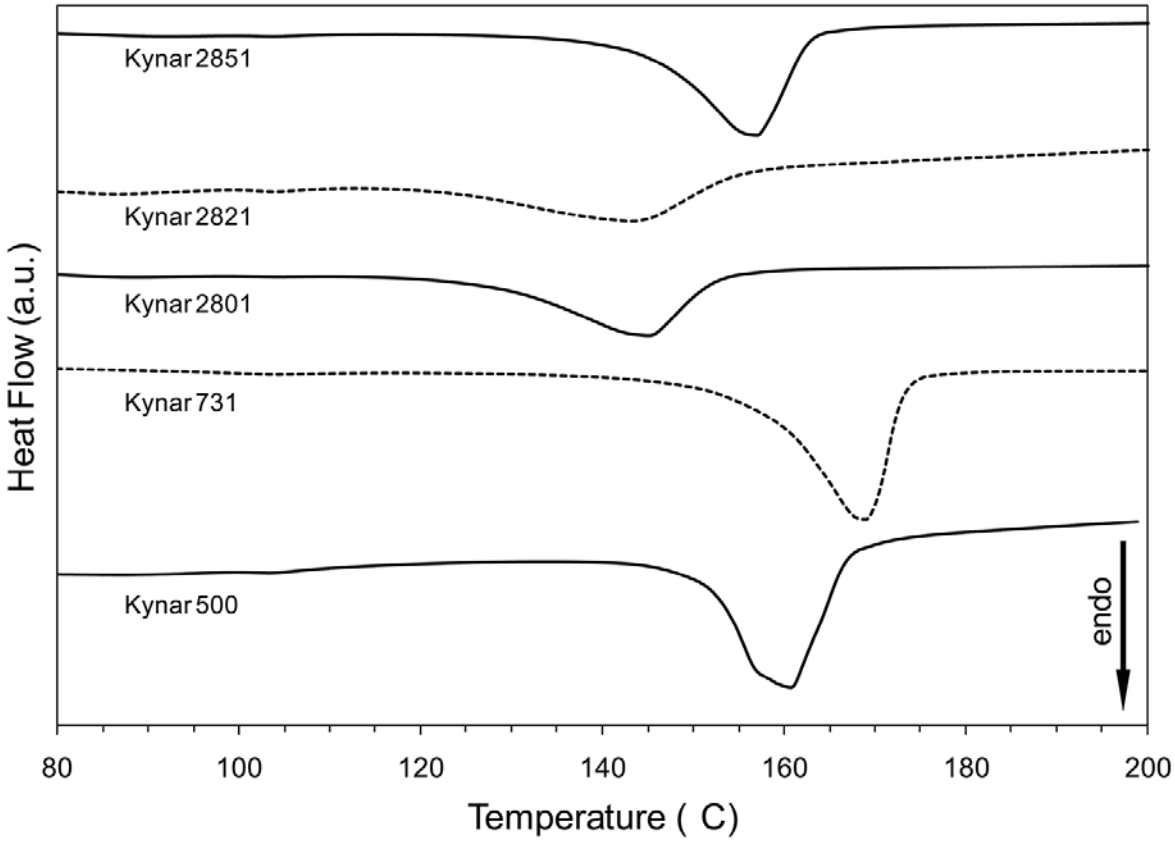

Figure 3.9 DSC heating profiles of Kynar® PVDF powders (as received from the manufacturer) (heating rate: 10°C/min).

Table 3.3 Thermal characteristics of pure PVDF powders (DSC)[a]

PVDF grade	T_m (°C)	ΔH_f (J/g)	T_C (°C)	ΔH_C (J/g)	X_C (%)
Kynar® 500	162.39	53.07	125.96	85.94	50.69
Kynar® 731	169.05	72.30	135.17	94.49	69.05
Kynar® 2801	146.68	38.83	101.60	57.85	37.09
Kynar® 2821	144.85	25.96	97.18	53.30	24.79
Kynar® 2851	158.31	51.07	120.40	68.82	48.78

[a] Heating and cooling rates were 10°C/min.
(T_m) Melting peak temperature. (ΔH_f) Enthalpy of fusion. (T_C) Crystallization temperature. (ΔH_C) enthalpy of crystallization.

conductivity. This relationship applies as well for the PVDF grades in between, with conductivity decreasing as crystallinity, crystallite size, and melting and crystallization temperatures increase (Figure 3.10). Furthermore, the end of the Kynar® 731 fusion endotherm is slightly above the curing temperature of the membranes (~177-178°C vs. 175°C), indicating that the Kynar® 731 is not completely melted during the curing process. This may indicate a competition between PVDF crystallization and PVDF-PE phase separation processes that restricts the formation of ion conducting channels, explaining in part the lower conductivity of Kynar® 731 based membranes.

Additional XRD spectra of pure PVDF solvent-cast films from NMP (175°C, 20min) and PVDF/PE membranes are shown in Figure 3.11 and Figure 3.12 respectively. The locations of the crystalline peaks in the neat PVDF films spectra show that upon cooling

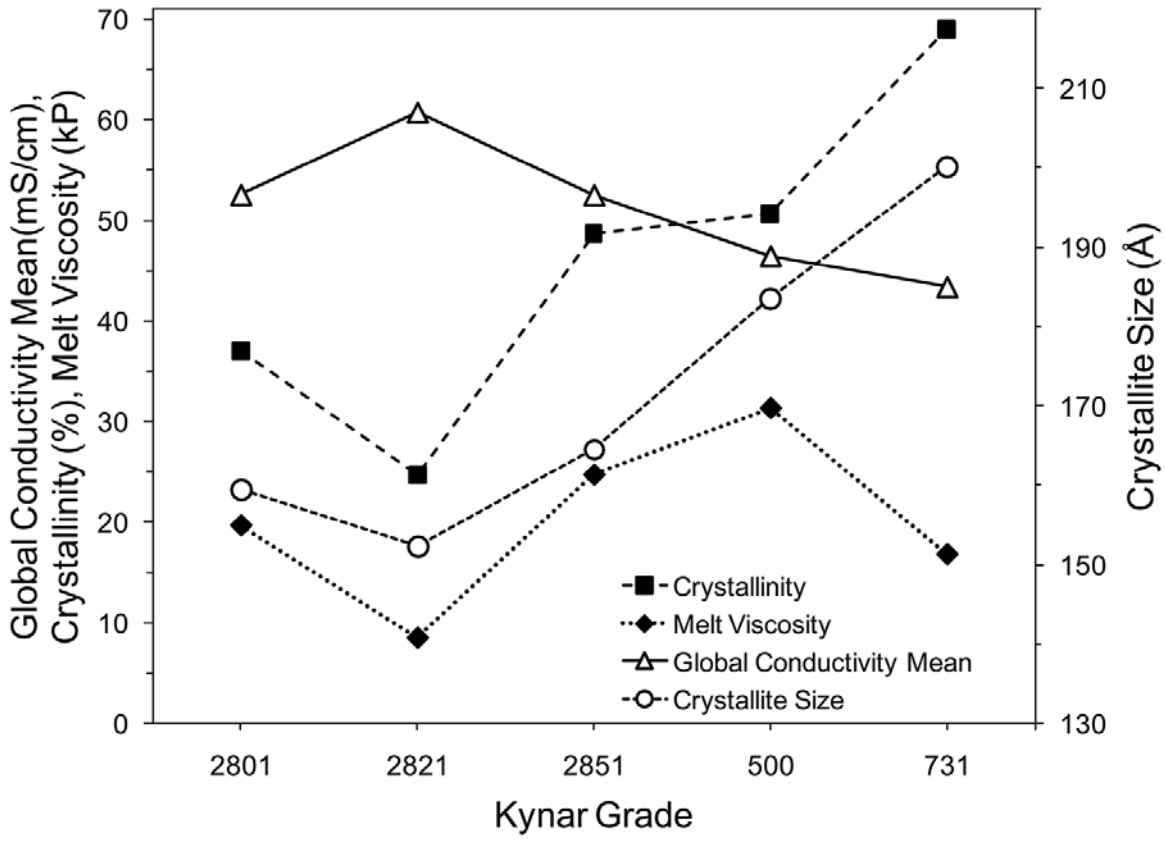

Figure 3.10 Comparison between global conductivity mean (unweighted mean) and PVDF crystallinity, crystallite size, and melt viscosity by PVDF type.

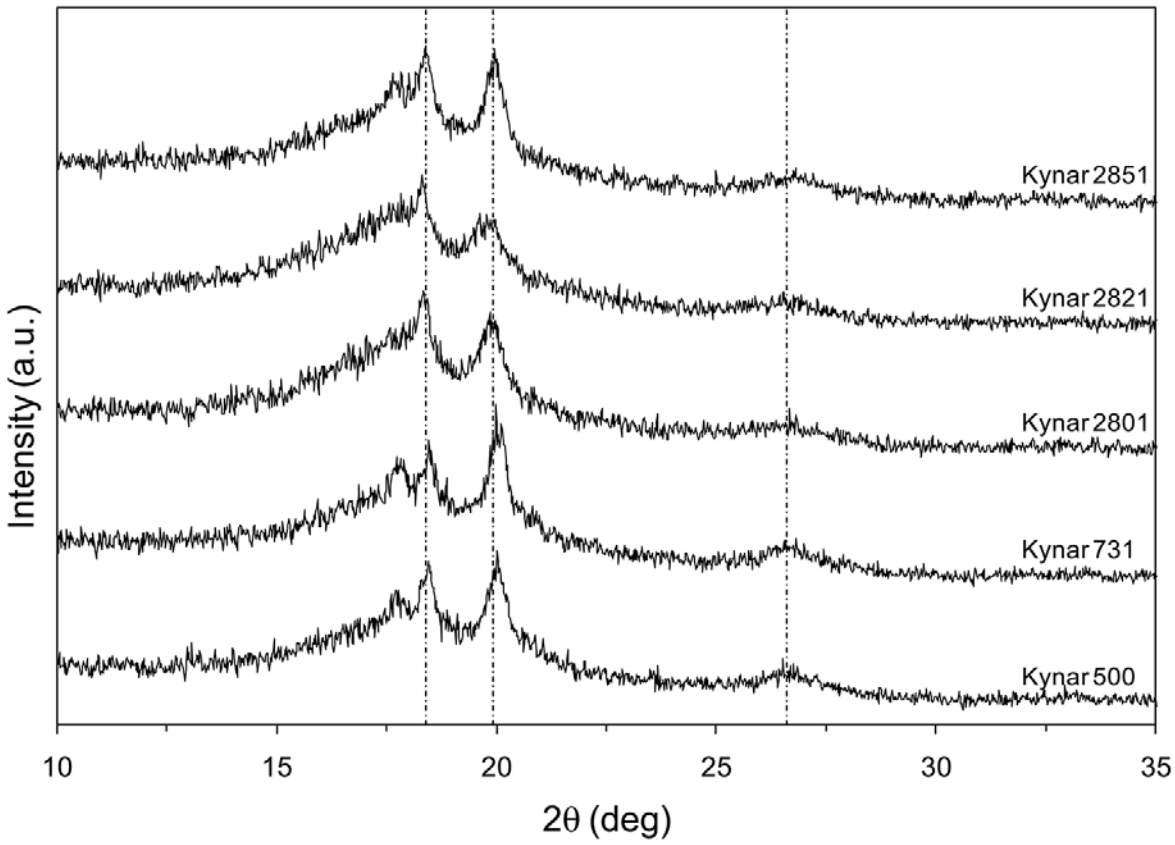

Figure 3.11 Wide angle X-ray diffraction spectra of NMP solvent-cast Kynar® PVDF films. Vertical lines indicate α-phase crystalline reflections at scattering angles (2θ) 18.34° (020), 19.89° (110), and 26.61° (021). Spectra are not corrected for sample thickness.

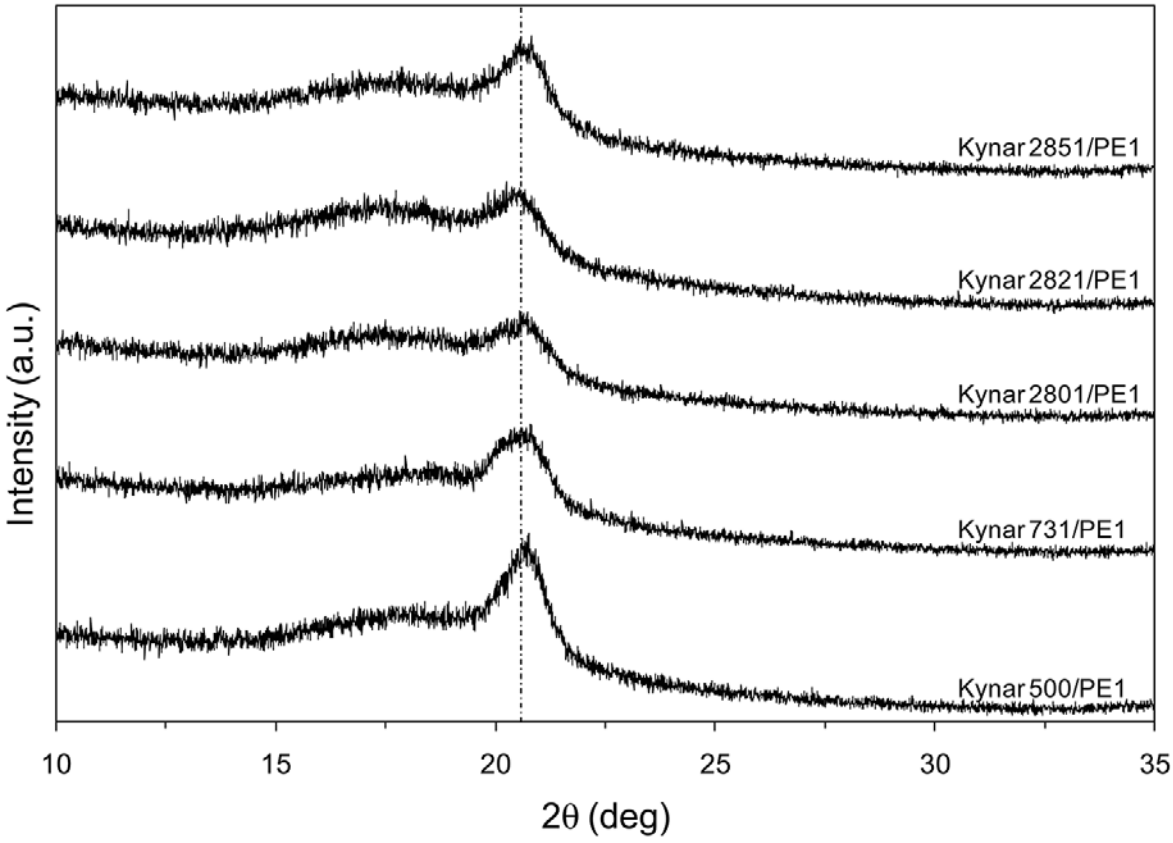

Figure 3.12 Wide angle X-ray diffraction spectra of Kynar® PVDF/PE1 membranes (only representative spectra of membranes containing 50wt% neutralized form PE1 are shown. Membranes containing PE2 and different PE mass fractions exhibited identical behavior). Vertical line indicates a β-phase crystalline reflection at a scattering angle (2θ) of 20.58° (110)+(200). Spectra are not corrected for sample thickness.

from the molten state all the PVDF grades crystallize back to the α-phase (scattering angles (2θ): 18.4°±0.06°, 19.93°±0.1°, and 26.61°±0.12°, Table 3.4). This is supported by FT-IR spectra of the PVDF films (Figure 3.13) which exhibit well defined α-phase absorption bands at 408, 489, 614, 764, 796, 855, 976, and 1070 cm^{-1} [30, 31, 40], as well as the non-polar trans-gauche CF_2 bending at 532 cm^{-1}, with no evidence of β or γ crystals; behavior consistent with previous studies where the α-phase is predominant when PVDF is cooled from the melt [30, 31, 41]. Despite crystallizing to the same phase type as the original PVDF powders, it is important to notice that the broader and shallower crystalline reflections (from baseline corrected XRD spectra) indicate a strong effect of the fast quenching of the films (175°C to room temperature in less than 30 s) on their crystallinity and crystallite size (i.e., reduced crystallinity and smaller crystallites). Contrary to PVDF-only films, PVDF/PE membranes exhibit markedly different crystalline structure as their XRD spectra display only one strong crystalline reflection at a scattering angle of approximately 20.58°±0.05°, typical of the sum of the diffraction in the (110) and (200) planes of the β-phase [28, 30, 36] (Table 3.4). FT-IR corroborates the variation in the PVDF crystalline structure due to PE incorporation in the PVDF/PE membranes (Figure 3.14), as the spectra display absorption bands at 445, 472, 490, and 842 cm^{-1}, including the ferroelectric all-trans conformation CF_2 bending band at 510 cm^{-1}; distinctive of the β-phase [30, 40]. The change of PVDF polymorph indicates a manifest perturbation of PVDF crystalline structure due to the presence of PE; however, this change from a non-polar α-phase to a polar β-phase is not unreasonable due to the polar

Table 3.4 WAXD of pure PVDF films and PVDF/PE[a] films

Sample	*hkl* (020)		*hkl* (110)[b]		*hkl* (021)		*hkl* (200)[b]	
	2θ(°)	*d*(Å)	2θ(°)	*d*(Å)	2θ(°)	*d*(Å)	2θ(°)	*d*(Å)
Kynar® 500	18.46	4.81	20.03	4.43	26.52	3.36	–	–
Kynar® 731	18.47	4.80	19.99	4.44	26.54	3.36	–	–
Kynar® 2801	18.34	4.84	19.85	4.47	26.68	3.34	–	–
Kynar® 2821	18.32	4.84	19.79	4.49	26.53	3.36	–	–
Kynar® 2851	18.40	4.82	19.97	4.45	26.80	3.33	–	–
Kynar® 500/PE1	–	–	β →		–	–	20.61	4.31
Kynar® 731/PE1	–	–	β →		–	–	20.55	4.32
Kynar® 2801/PE1	–	–	β →		–	–	20.57	4.32
Kynar® 2821/PE1	–	–	β →		–	–	20.51	4.33
Kynar® 2851/PE1	–	–	β →		–	–	20.63	4.31

[a]Representative PVDF/PE films shown in this table correspond to membranes containing 50wt% PE1. PVDF polymorph change from α to β phase was evident in all membranes containing either type of polyelectrolyte at all PVDF to PE ratios. [b]Reflections from the sum of the diffractions in planes (110) and (200) for β-phase PVDF are shown in the column corresponding to plane (200); plane (100) reflections are denoted as "β →" for this phase.
(θ) Bragg angle. (*d*) Interplanar spacing.

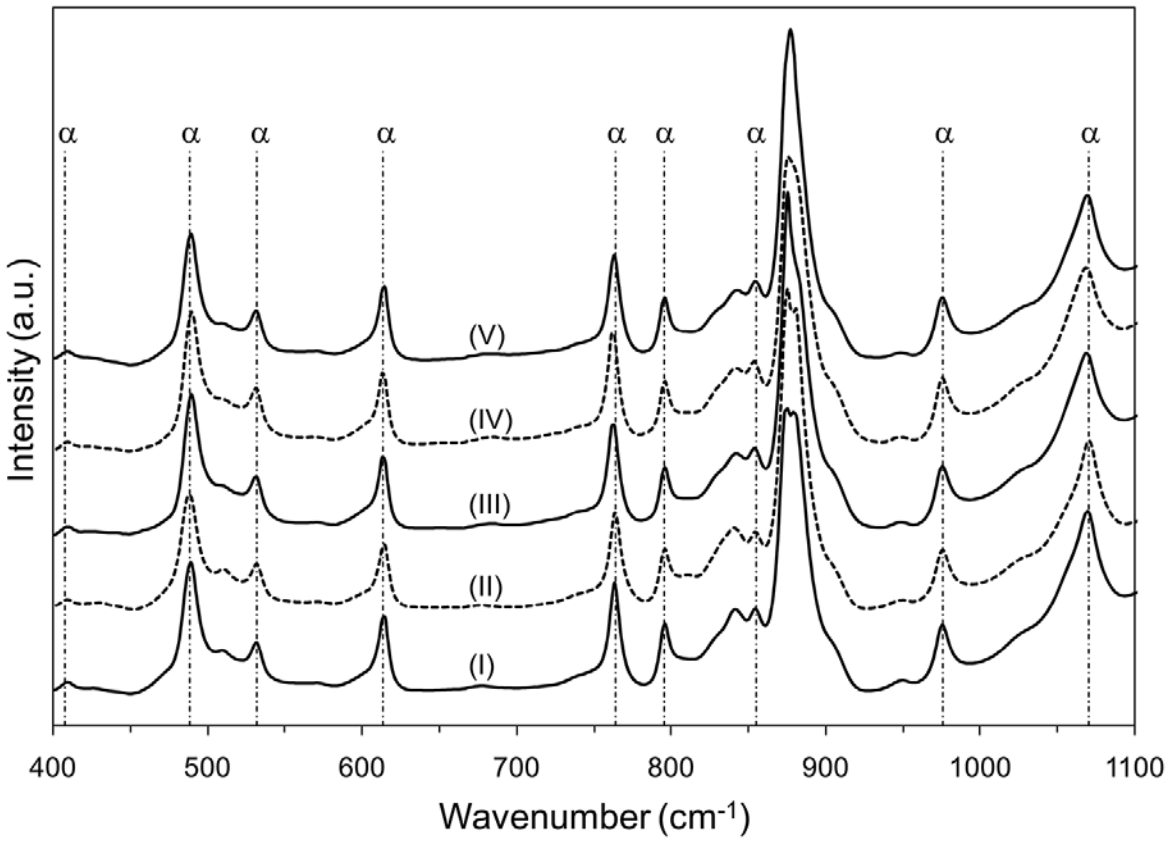

Figure 3.13 FT-IR spectra in the range of 400 to 1100 cm^{-1} of NMP solvent-cast Kynar® PVDF: (I) 500, (II) 731, (III) 2801, (IV) 2821, and (V) 2851. Vertical lines indicate typical α-phase absorption bands.

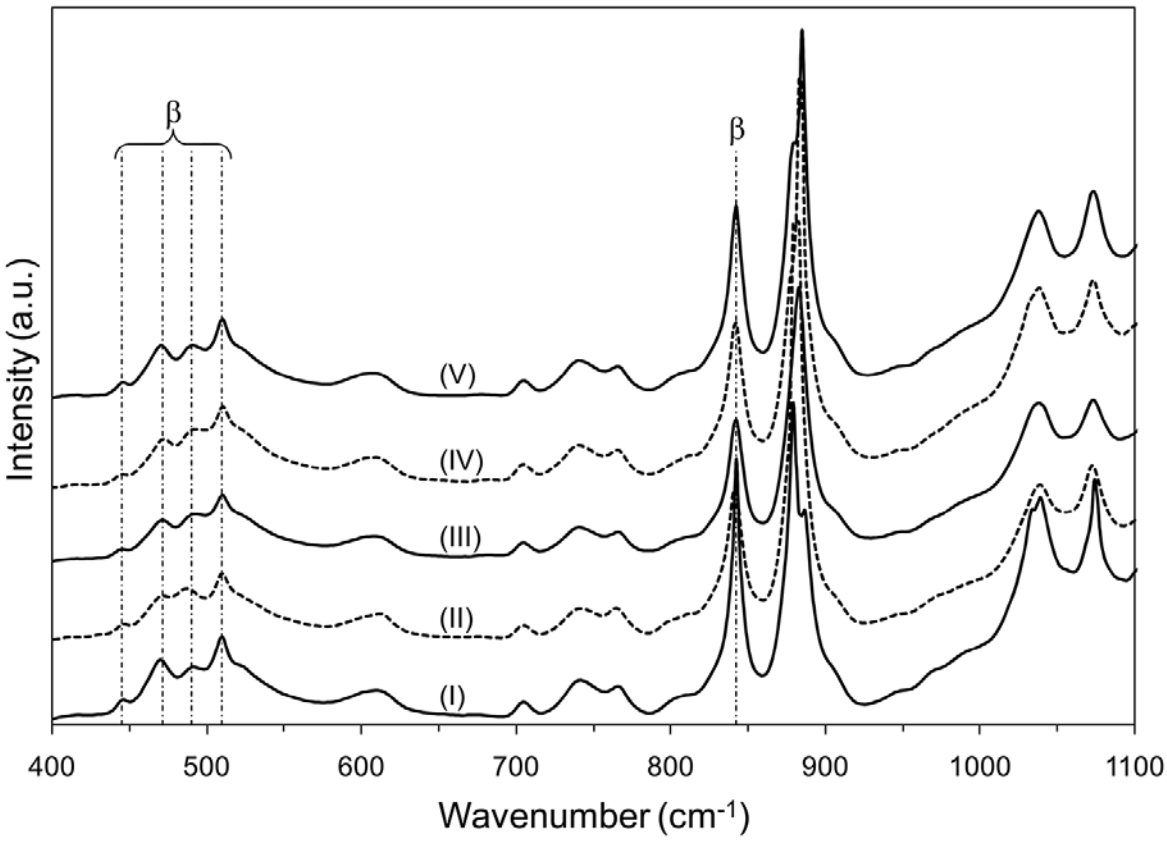

Figure 3.14 FT-IR spectra in the range of 400 to 1100 cm^{-1} of Kynar® PVDF/PE1 membranes (only representative spectra of membranes containing 50wt% neutralized form PE1 are shown. Membranes containing PE2 and different PE mass fractions exhibited identical behavior): (I) 500/PE1, (II) 731/PE1, (III) 2801/PE1, (IV) 2821/PE1, and (V) 2851/PE1. Vertical lines indicate typical β-phase absorption bands.

nature of the PE. Similar behavior has been observed for PVDF in presence of polar media such as salts or other type of electrolytes [42, 43]. It is not known, however, if the type of crystalline phase of the original PVDF (prior to blending with PE) and that of the PVDF in the final membranes have any particular effect on proton conductivity.

The strong inverse relationship between the conductivity of PVDF/PE membranes and some of the crystalline characteristics of the inert PVDF phase, suggests an important effect of on the thermodynamics and kinetics of nanophase separation responsible for the formation of ion-conducting channels. Particularly, we hypothesize that even though PVDF is in the molten state (except Kynar® 731, which is only partially molten) during curing of the solvent-cast PVDF/PE membranes, the length of the process is relatively short to allow long-range rearrangement of the polymer chains (approx. 20 min). As a result, areas corresponding to locations where crystallites were initially situated before melting remain densely packed with PVDF chains throughout the curing process. These dense PVDF areas constitute an impediment for the segmental motion of PE chains, as well as a physical blockage, that hampers their mobility, rearrangement, and interconnection during crosslinking (Figure 3.15), resulting in less branched and interconnected proton conducting channels that are likely to be responsible for reduced conductivity. A similar structural effect has been previously observed on other type of ionomers, where the ionic species are excluded from the crystalline domains causing a concentration of the former outside lamellar regions [44]. What is more, decreased PE mobility and rearrangement is seemingly exacerbated by a synergistic effect between crystallinity and the high melt viscosity of the PVDF (Figure 3.10); namely, Kynar® 500:

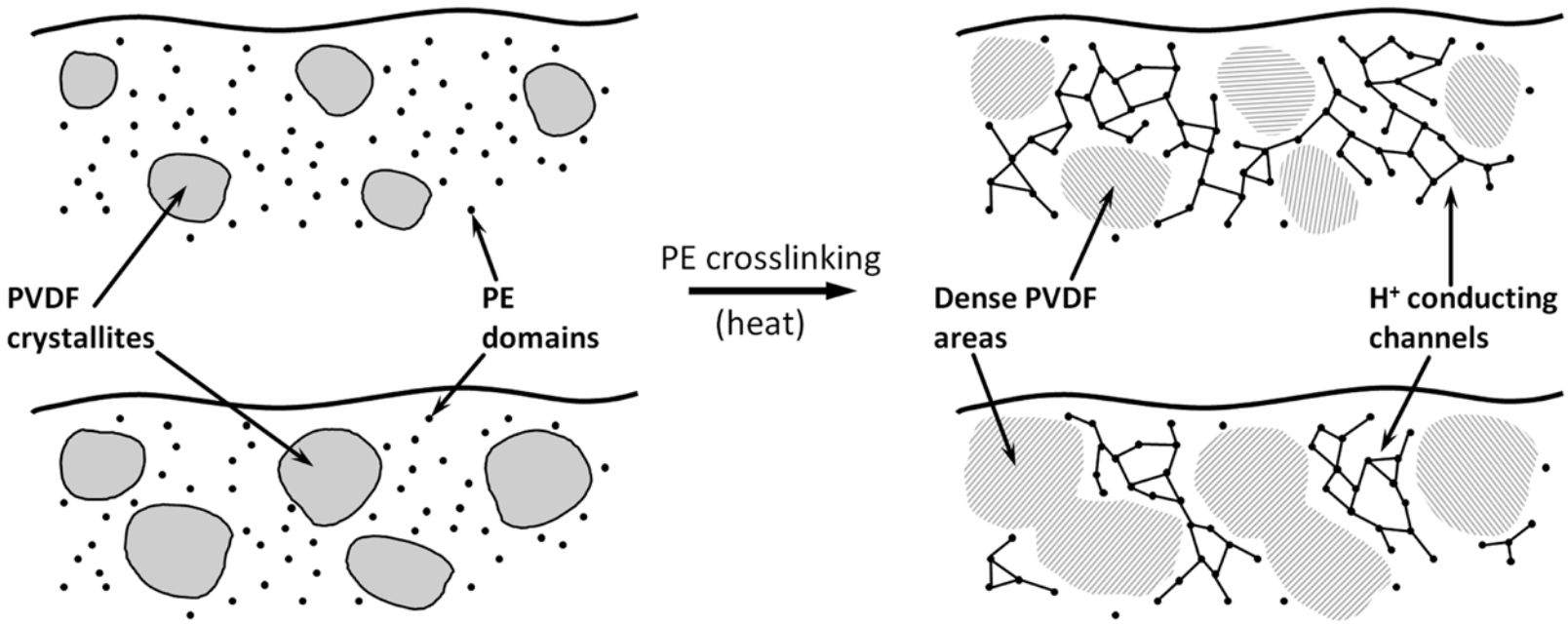

Figure 3.15 Cartoon schematic of the morphology transition of a solvent-based PVDF/PE blend containing individual PE domains and PVDF crystallites, into a membrane of semi-interpenetrated PVDF structures and crosslinked proton conducting channels, after heat-induced crosslinking. The upper and bottom images correspond to low and high crystallinity PVDF respectively, illustrating the effect of crystallinity and crystallite size in the formation of proton conducting channels.

31.42 kP, Kynar® 731: 16.92 kP, Kynar® 2801: 19.77 kP, Kynar® 2821: 8.60 kP, and Kynar® 2851: 24.80kP; which might explain why, regardless of an almost identical crystallinity (50.69% vs. 48.78%), Kynar® 500 has a lower average conductivity than Kynar® 2851. Also, despite having a lower melt viscosity when compared to Kynar® 500, it is important to remember that Kynar® 731 is not completely molten throughout the curing process giving rise to a possible competition between PVDF crystallization and PVDF-PE phase separation; as previously stated. The effect of reduced mobility of PE chains in high crystallinity PVDF matrices is further supported by the size of the PE clusters formed at high polyelectrolyte mass fractions (Figure 3.4 and Figure 3.5); namely, clusters in the lower crystallinity PVDF:HFP copolymers reached a maximum size of ~450 nm for 60wt% PE and ~410 nm for 55wt% PE, whereas the maximum cluster size for a 60wt% PE in any of the homopolymers was only in the order of ~355nm.

Albeit longer curing/heating time periods may seem as a reasonable approach to improve the conductivity of membranes manufactured with highly crystalline PVDF, it proved ineffective since the length of the curing process follows the completion of PE crosslinking reaction (see section 3.2.1, membrane preparation). Consequently, the network of crosslinked proton-conducting channels is already formed after 20 minutes and further heating doesn't have a considerable effect on the PE network configuration. Additional annealing of finished membranes at the PVDF α-phase relaxation temperature (~90°C) and above (130°C and 170°C) for 5 h and 11 h proved to be equally unsuccessful. That is, no statistically significant increase in conductivity was observed in membranes annealed at 90°C; whereas annealing at 130°C and 170°C was prominently

detrimental for proton conductivity regardless of the duration (inset Figure 3.16). The diminution in conductivity was accompanied by a manifest change in the PVDF crystalline phase evident from the FT-IR spectra of annealed membranes (Figure 3.16). Specifically, the spectra of membranes annealed at 130°C exhibit IR band broadening compared to the spectrum of a non-annealed reference membrane, while membranes annealed at 170°C display a mix of α- and β-phase structures. In contrast, the FT-IR spectra of membranes annealed at the α-phase relaxation temperature virtually overlap with the spectrum of the non-annealed reference membrane (β-phase). The manifestation of IR broadening is perhaps explained by dipolar interactions [45] and may indicate the onset of the partial ferroelectric to paraelectric transition seen at 170°C. Presumably, the associated decrease in conductivity can be attributed to PVDF segregation towards the membrane surface during annealing, resulting in a low surface energy polymer-rich layer depleted of ionic domains (similar to fluoro-rich layers found on the surface of Nafion® [44]). This hypothesis coincides with a manifest strong wettability reduction (dry surface) noticed in membranes annealed at 130°C and 170°C. As temperature increased from 130°C to 170°C the low energy PVDF layer thickened hindering conductivity even further and allowing the formation of non-polar α-phase PVDF away from PE domains. What is more, SEM imaging of high PE concentration membranes annealed at elevated temperatures displays a perceptible reduction of PE clusters towards the membranes surface (Figure 3.17), which might be an indicative of the speculated formation and thickening of a PVDF-rich layer. A gradual color progression (from clear to brownish) of the membranes was noticed as well with

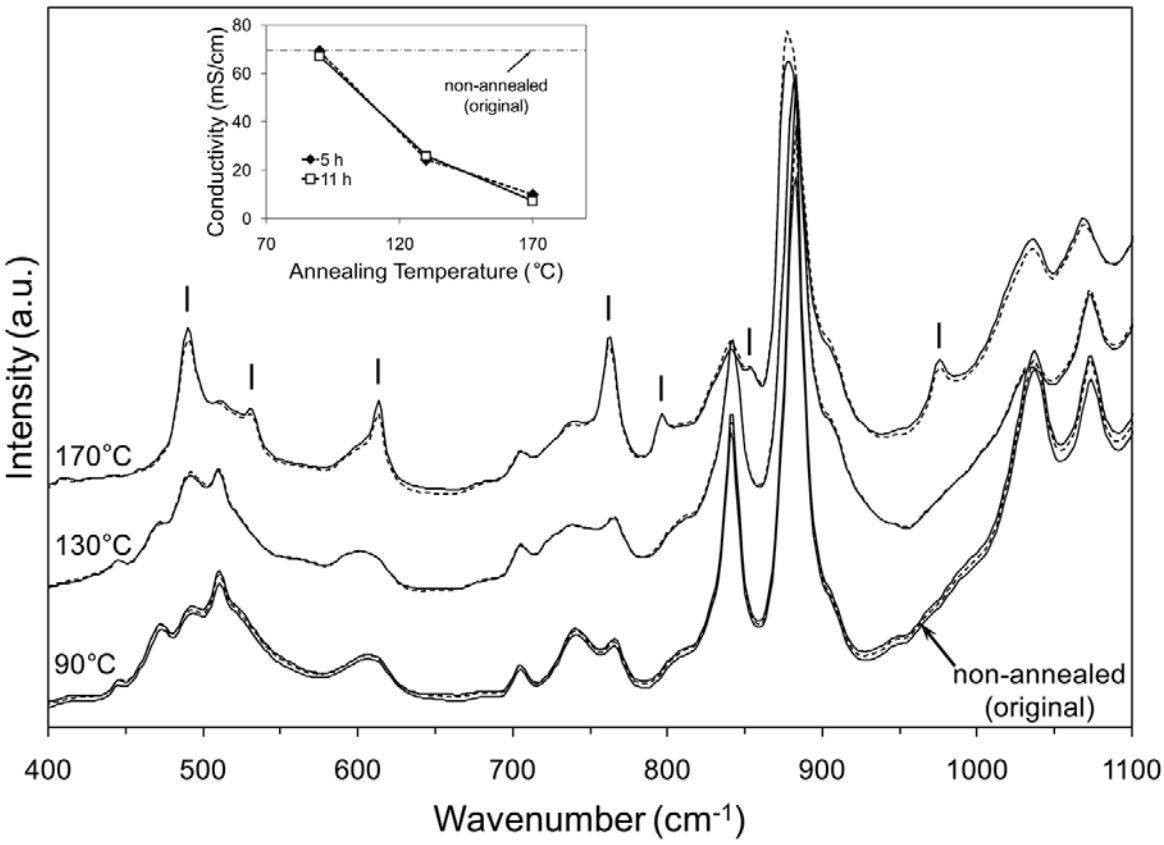

Figure 3.16 Representative FT-IR spectra of PVDF/PE membranes annealed at 90°C, 130°C and 170°C for 5 h (**.....**) and 11 h (▬▬). Vertical markers on the 170°C spectra indicate the appearance of α-phase bands. Inset: conductivity of annealed membranes as a function of annealing temperature. Spectra and conductivity data correspond to Kynar® 731/PE1 (60wt%) membranes.

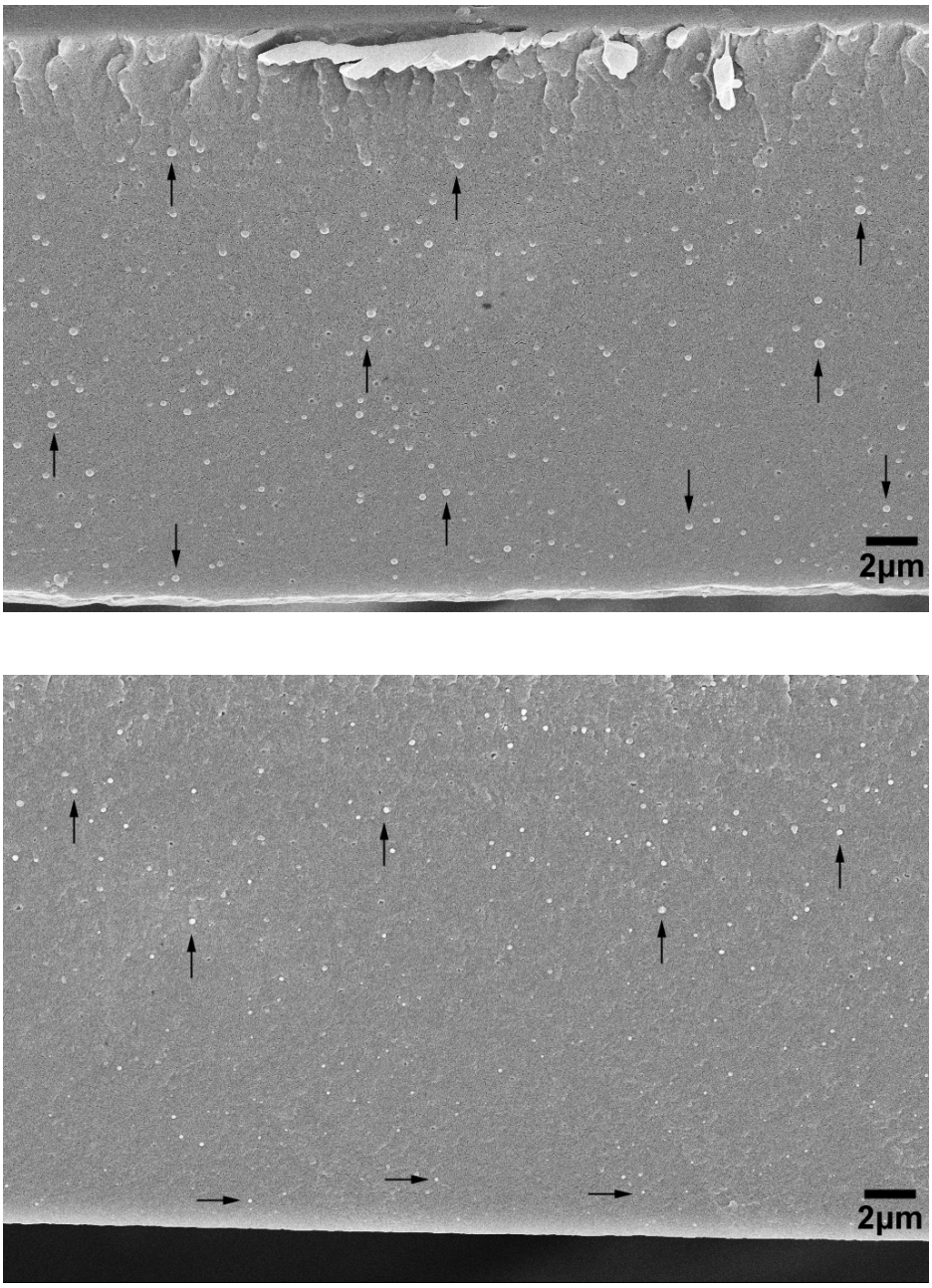

Figure 3.17 SEM images (EHT 10 kV) of the cross-sectional area of Kynar® 731/PE1 (60wt%) membranes: non-annealed (top) and annealed at 170°C (bottom). The non-annealed sample displays well distributed PE clusters (vertical arrows) across the membrane thickness; whereas the annealed sample exhibits a noticeable PE cluster size and number distribution from big and numerous (vertical arrows) to small and scarce (horizontal arrows) towards de membrane surface.

increasing annealing temperature, suggesting the formation of conjugated C=C bonds arising from PVDF dehydrofluorination in the presence of PE.

Supplementary crystallinity characterization of the different PVDF grades; particularly, the crystallite-thickness distribution and transition layers between the amorphous and crystalline domains, can be carried out via small angle X-ray scattering (SAXS) long-period measurements (not performed in this study) to further elaborate on the relationship between crystalline properties of PVDF and proton conductivity of PVDF/PE membranes.

In general, based on the preceding high-throughput study of PVDF/PE SIPN membranes, lower PVDF crystallinity is translated in better membrane performance (from the standpoint of proton conductivity). In fact, contrary to what would be the conventional approach to enhance proton conductivity by only increasing the content of PE, the results suggest that the use of other PVDF grades with lower crystallinity (e.g., copolymers with higher content of HFP) for the manufacturing of the membranes could be a plausible method to boost conductivity (especially as there is no statistically significant conductivity rise above 55wt% PE). In addition, prolonged heat pre-treatment (prior to PVDF-PE blending) of highly crystalline PVDF types above their melting temperature, followed by ultrafast quenching to preclude crystallite growth, could serve to circumvent the unfavorable effect of high crystallinity on conductivity; allowing the use of these PVDF types in the manufacturing of PVDF/PE membranes with adequate proton conductivity. However, besides proton conductivity, the use of a particular

PVDF type is also constrained by the required mechanical and fuel barrier properties of the membrane.

3.3.2 Mechanical properties

Representative force vs. time profiles from HTMECH characterization of PVDF/PE membranes are shown in Figure 3.18 (a total of approximately 1750 of these profiles were recorded and analyzed for this study). In order to obtain the true mechanical response of the materials, as briefly mentioned in the experimental section, raw force vs. time profiles undergo denoising and conditioning followed by analysis via a custom algorithm [26] to remove artifacts arising from background noise, natural vibration frequencies of the system, and harmonic oscillations from the motion of the linear motors. As otherwise stated, denoising of all raw profiles was carried out via either undecimated wavelet transform with multiple-level rescaling to estimate noise variance (noise was not assumed white), universal threshold, and an orthogonal Haar wavelet type; or a non-causal zero-phase IIR filter using 1st order Chebyshev coefficients, a passband ripple of 0.2-0.3 dB, and a cutoff frequency of 10 Hz. Bisquare fitting sensitivity was set to 95% for linear fitting of elastic modulus. It is important to underline that contrary to uniaxial deformation, typical of conventional mechanical characterization systems, membranes undergo axisymmetric biaxial deformation in HTMECH tests. A possible advantage of this type of deformation may be the reduction of structural anisotropy effects, related to potential uneven distributions of PVDF-rich domains and crosslinked PE structures, on the measured membrane properties.

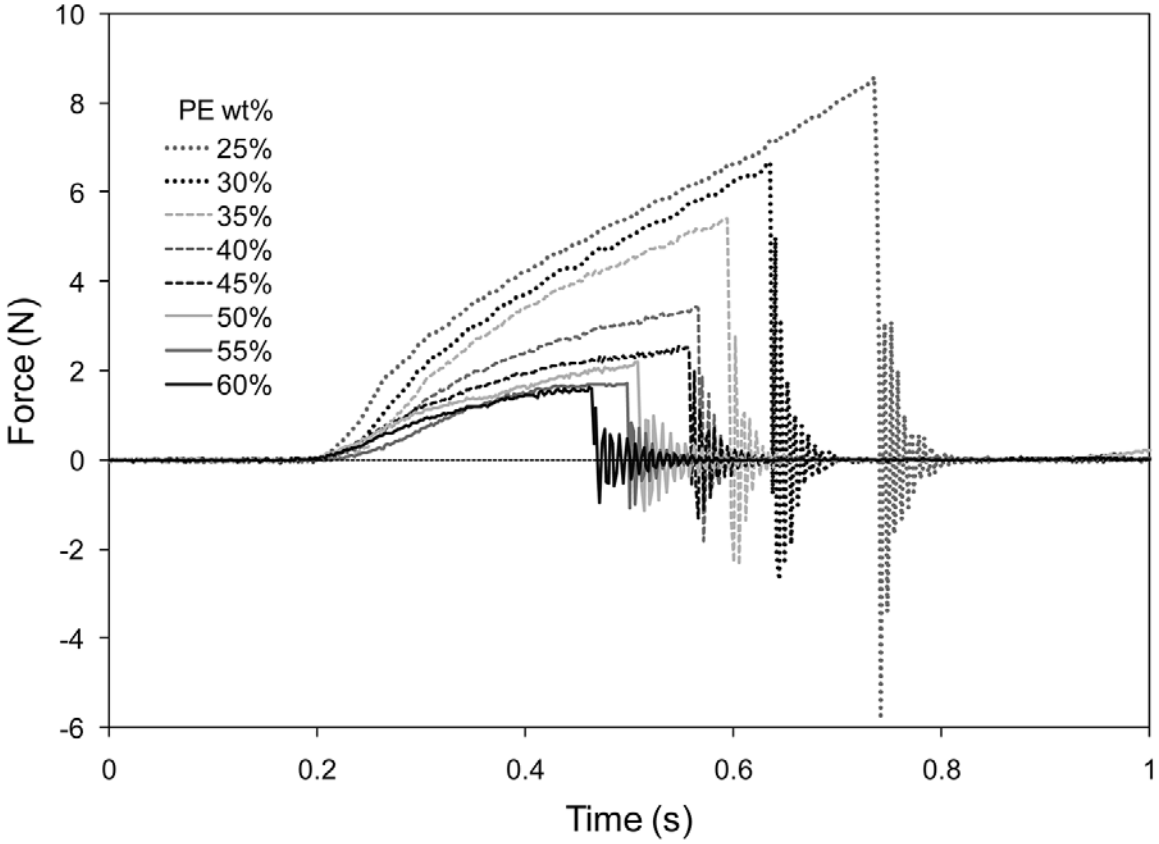

Figure 3.18 Representative HTMECH force vs. time profiles of PVDF/PE membranes. Approximately 1750 profiles were utilized to determine the mechanical properties of the membranes. Profiles correspond to Kynar® 2851/PE2 membranes.

However, care must be taken if the results presented herein are to be compared to uniaxial tensile tests, as differences in mechanical response should be expected between both deformation models. For instance the biaxial "engineering" elastic modulus obtained from HTMECH characterization is predicted to be approximately twice the Young's modulus measured under uniaxial tension [46]. In addition, other geometry-dependent factors such as non-affine membrane deformation arising from the very dissimilar mechanical characteristics of the blend components (i.e., PVDF and acrylic PE), and non-linear stress response, might stress the difference between biaxial and uniaxial characterization approaches. To simplify the analysis model, membrane deformation was assumed to follow a linear profile; however, radial, tangential, and bending stresses in the membranes when undergoing biaxial deformation depend directly upon the load, sample geometry (needle to isolation plate hole diameter ratio), and material properties, and may result in non-linear deformation profiles that must be solved numerically. Additional considerations about the HTMECH system and testing methodology can be found elsewhere [21, 47].

For the sake of simplicity the elastic modulus, the ultimate tensile strength, and toughness were chosen among all the mechanical properties resulting from the HTMECH data analysis to describe the mechanical behavior of the PVDF/PE membranes (additional properties are available as supplementary information). The corresponding profiles of these properties as a function of PE mass fraction are shown in Figure 3.19 through Figure 3.24. A similar GLM statistical analysis to that performed for conductivity tests revealed statistically significant effects of PE content

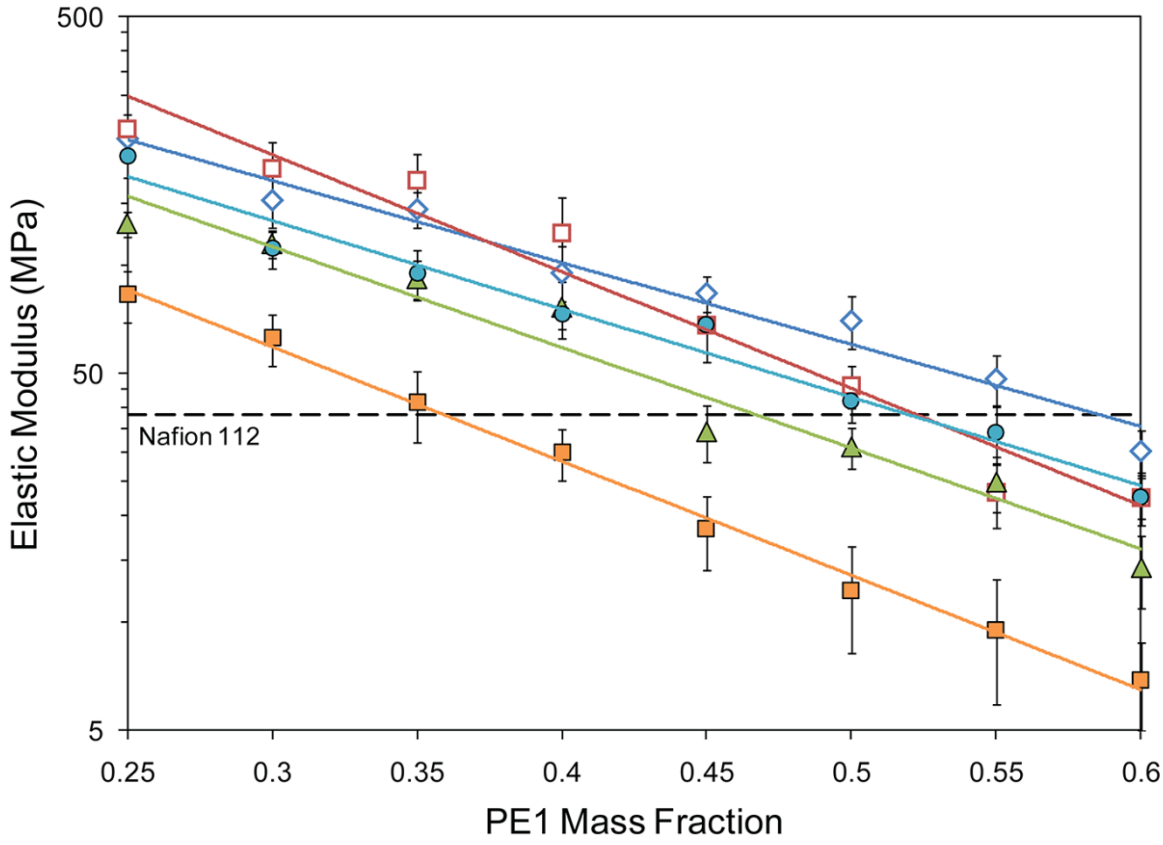

Figure 3.19 Parametric log-scale plot of biaxial elastic modulus of PE1-based membranes by Kynar® grade (500 —◇—, 731 —□—, 2801 —△—, 2821 —■—, and 2851 —●—) as a function of polyelectrolyte mass fraction. All membranes were tested in a hydrated state. Polyelectrolyte content is expressed as the mass fraction of neutralized form polyelectrolyte in the final membrane. Values are averages ± 95% confidence intervals. Solid lines correspond to exponential trend lines.

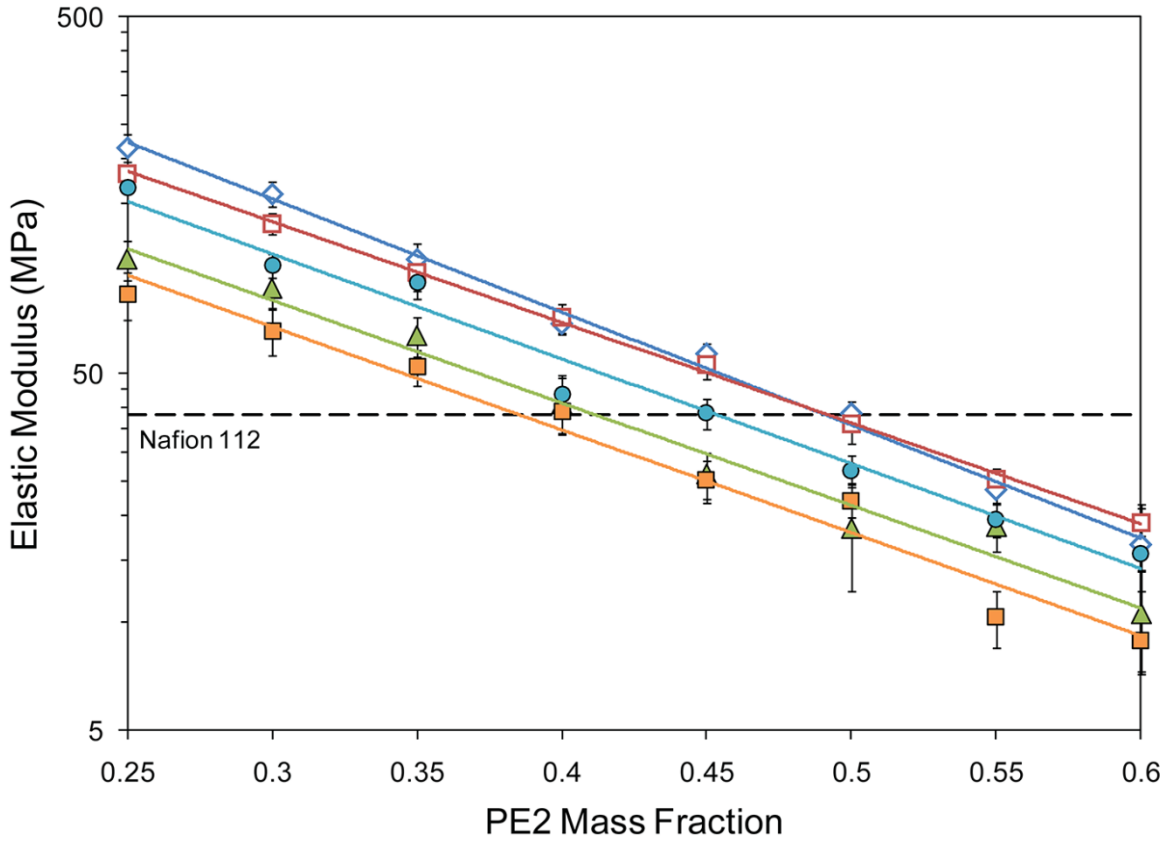

Figure 3.20 Parametric log-scale plot of biaxial elastic modulus of PE2-based membranes by Kynar® grade (500 —◇—, 731 —□—, 2801 —△—, 2821 —■—, and 2851 —●—) as a function of polyelectrolyte mass fraction. All membranes were tested in a hydrated state. Polyelectrolyte content is expressed as the mass fraction of neutralized form polyelectrolyte in the final membrane. Values are averages ± 95% confidence intervals. Solid lines correspond to exponential trend lines.

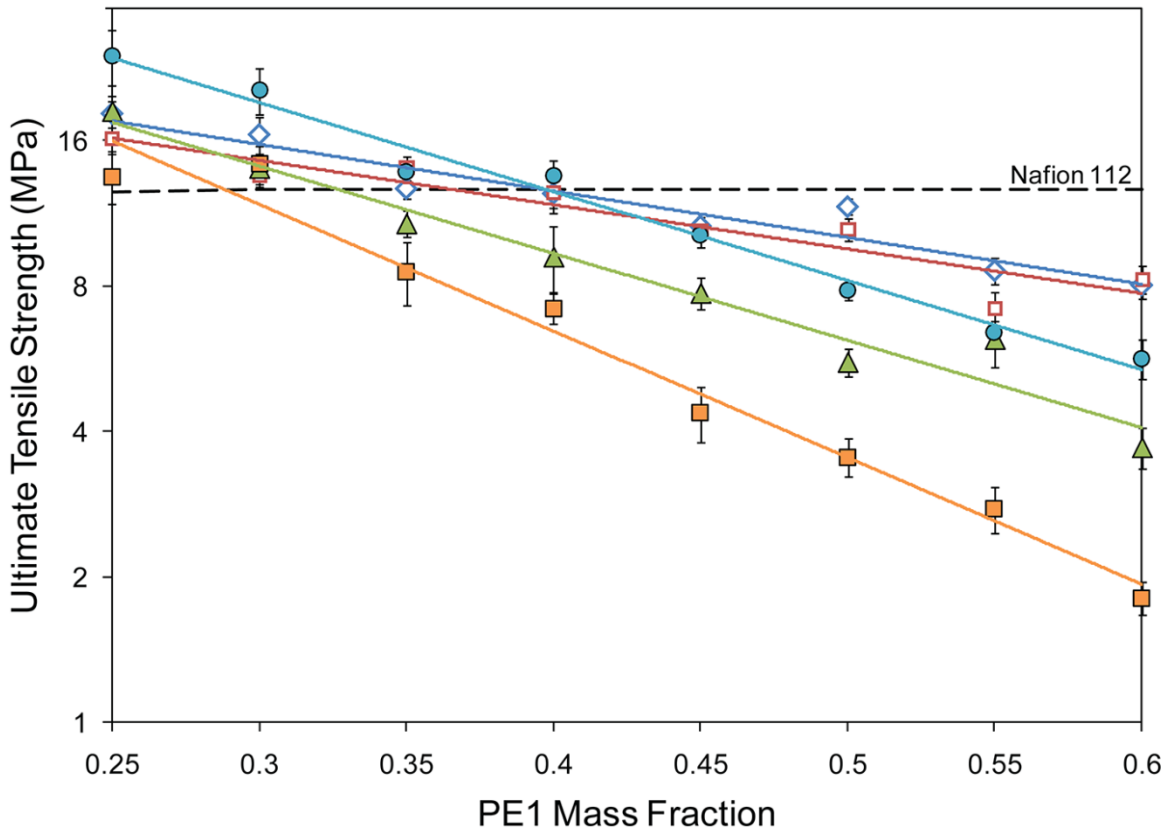

Figure 3.21 Parametric log-scale plot of ultimate tensile strength (biaxial) of PE1-based membranes by Kynar® grade (500 —◇—, 731 —□—, 2801 —△—, 2821 —■—, and 2851 —●—) as a function of polyelectrolyte mass fraction. All membranes were tested in a hydrated state. Polyelectrolyte content is expressed as the mass fraction of neutralized form polyelectrolyte in the final membrane. Values are averages ± 95% confidence intervals. Solid lines correspond to exponential trend lines.

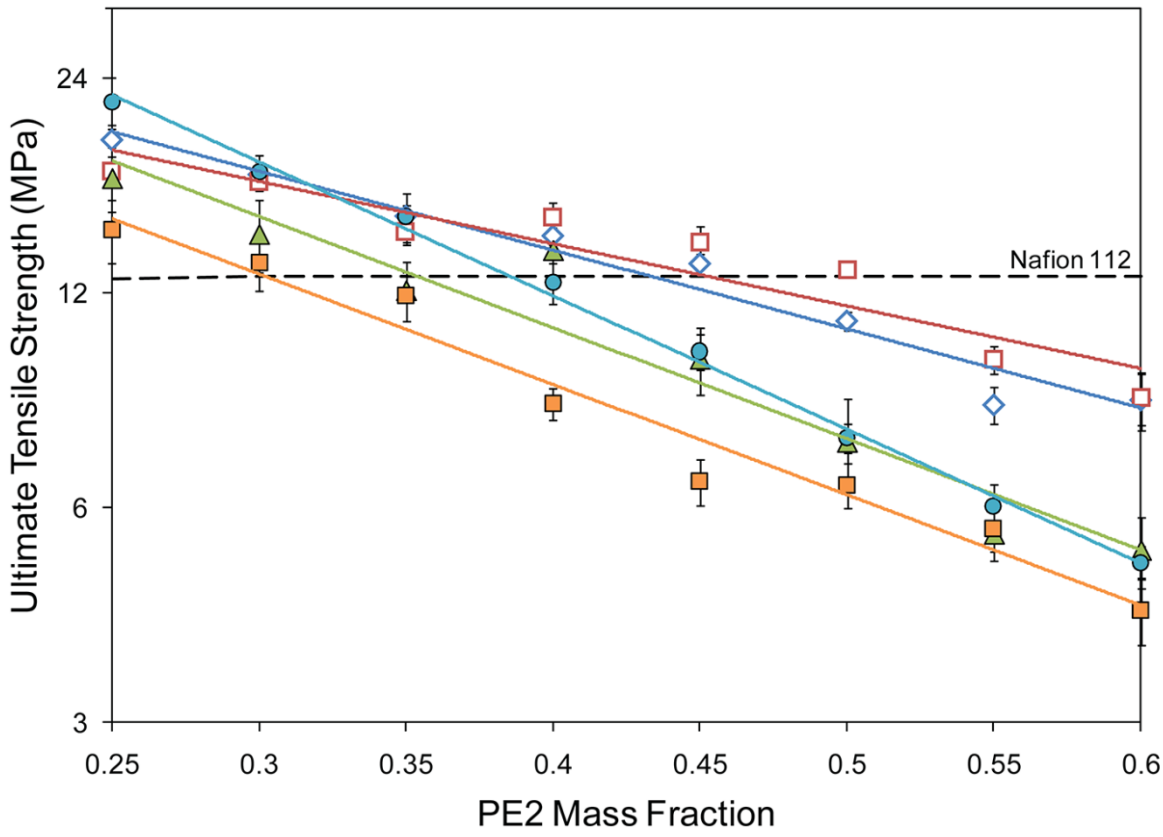

Figure 3.22 Parametric log-scale plot of ultimate tensile strength (biaxial) of PE2-based membranes by Kynar® grade (500 —◇—, 731 —□—, 2801 —△—, 2821 —■—, and 2851 —●—) as a function of polyelectrolyte mass fraction. All membranes were tested in a hydrated state. Polyelectrolyte content is expressed as the mass fraction of neutralized form polyelectrolyte in the final membrane. Values are averages ± 95% confidence intervals. Solid lines correspond to exponential trend lines.

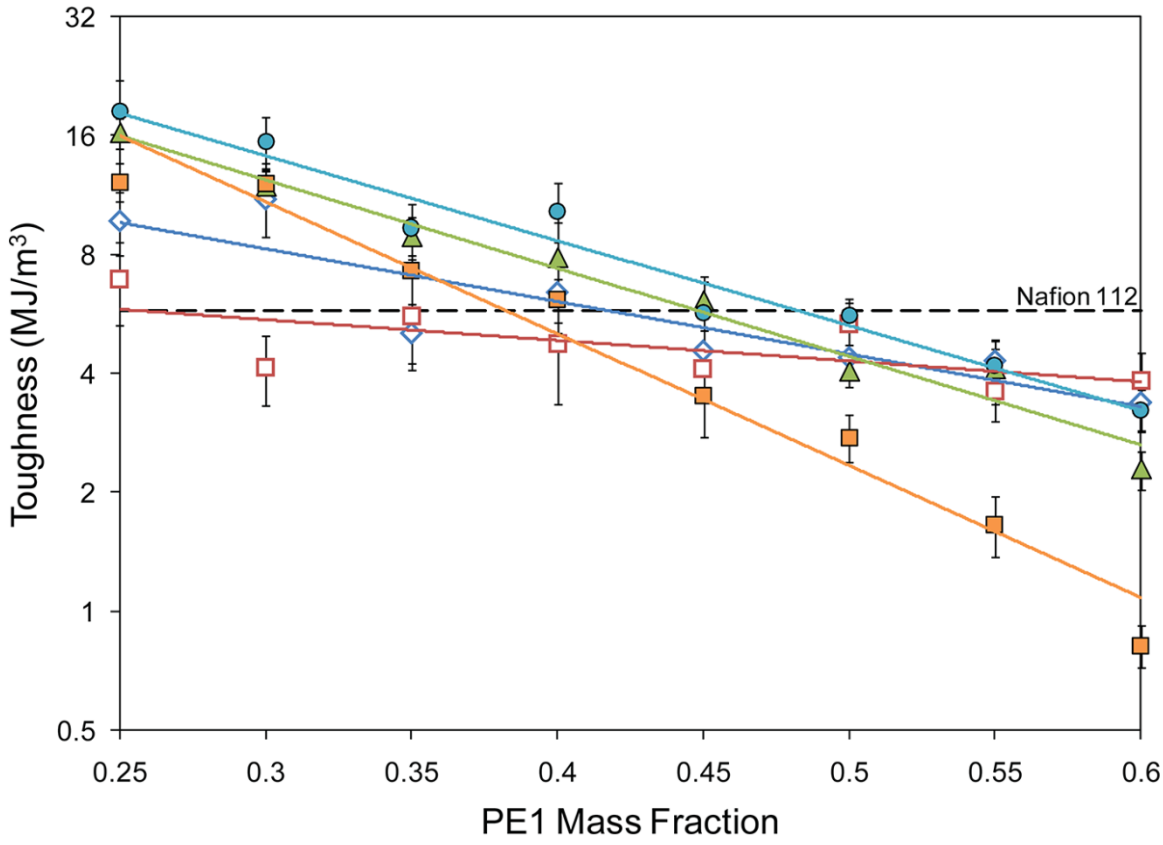

Figure 3.23 Parametric log-scale plot of toughness of PE1-based membranes by Kynar® grade (500 —◇—, 731 —□—, 2801 —△—, 2821 —■—, and 2851 —●—) as a function of polyelectrolyte mass fraction. All membranes were tested in a hydrated state. Polyelectrolyte content is expressed as the mass fraction of neutralized form polyelectrolyte in the final membrane. Values are averages ± 95% confidence intervals. Solid lines correspond to exponential trend lines.

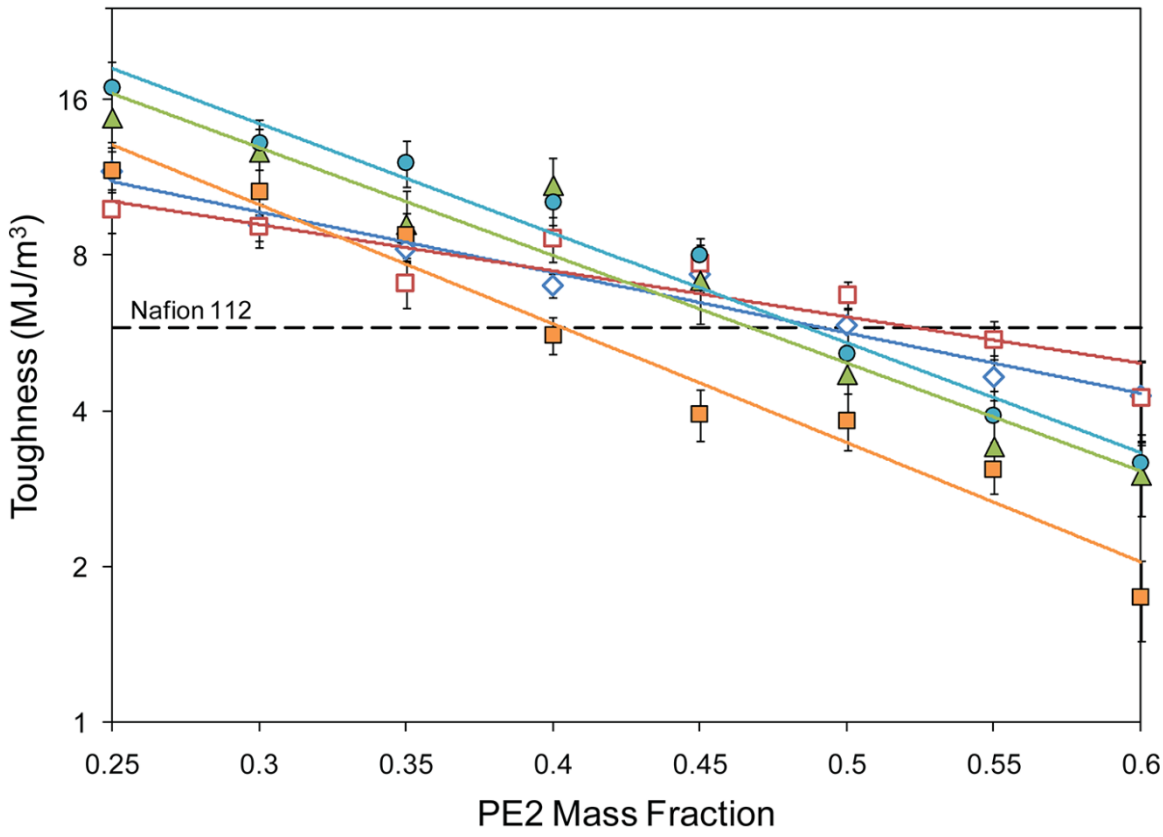

Figure 3.24 Parametric log-scale plot of toughness of PE2-based membranes by Kynar® grade (500 —◇—, 731 —□—, 2801 —△—, 2821 —■—, and 2851 —●—) as a function of polyelectrolyte mass fraction. All membranes were tested in a hydrated state. Polyelectrolyte content is expressed as the mass fraction of neutralized form polyelectrolyte in the final membrane. Values are averages ± 95% confidence intervals. Solid lines correspond to exponential trend lines.

($F_{(7,1657)}$ = 940.44, p < 0.001), PE type ($F_{(1,1657)}$ = 207.55, p < 0.001), and PVDF grade ($F_{(4,1657)}$ = 349.49, p < 0.001) on membrane elastic modulus; significant effects of PE content ($F_{(7,1657)}$ = 799.92, p < 0.001), PE type ($F_{(1,1657)}$ = 106.89, p < 0.001), and PVDF grade ($F_{(4,1657)}$ = 291.60, p < 0.001) on membrane ultimate tensile strength; as well as significant effects of PE content ($F_{(7,1657)}$ = 396.94, p < 0.001), PE type ($F_{(1,1657)}$ = 53.92, p < 0.001), and PVDF grade ($F_{(4,1657)}$ = 91.76, p < 0.001) on membrane toughness. Significant interactions effects of each and every one of the factors exist as well for all the mechanical properties (p < 0.001), and were corroborated by subsequent simple effects analysis (omitted here due to length). Although a significant factor, the size effect of the PE type on the mechanical properties is weak ($0.03 \leq \eta_p^2 \leq 0.11$); which was evident in the simple effects analysis where at several fixed levels of PVDF type and PE content the difference in mechanical behavior of PE1 and PE2 membranes was statistically negligible. This was anticipated as the mechanical strength of both PE types is extremely low when compared to that of PVDF (an engineering plastic); consequently, the effect of either PE type on the mechanical properties of the membranes depends mainly on the amount of PVDF it "displaces", and not significantly on its own mechanical properties. In other words, PE domains act as defects that are detrimental for the membrane mechanical integrity. The higher the PE mass fraction the higher number of defects (larger amount of PVDF displaced), and consequently the further the deterioration of mechanical properties; evident in all the profiles.

Homopolymer-based membranes exhibited the highest elastic moduli over the range of PE mass fractions in comparison with copolymer-based ones. This is attributed

to the added flexibility in the copolymer chains by the HFP co-monomers. For instance, copolymer-based membranes were noticeably more flexible in the dry state than their homopolymer-based counterparts (the latter being particularly brittle at high PE concentrations). Similarly, the ultimate tensile strength of the PVDF/PE membranes was generally higher for those containing PVDF homopolymers, and only at very small PE mass fractions some copolymers, particularly Kynar® 2851, exhibited a higher value. This coincides with the occurrence of what seems to be strain-induced crystallization characterized by a slope increment beyond the initial plastic flow at the end of several force vs. time profiles of copolymer based membranes with low PE content. Strain-induced crystallization can lead to hardening which in turn can increase the tensile strength of the membrane. Opposite to the elastic moduli and the general trend of ultimate tensile strength values, toughness was higher in the copolymer-based membranes between low to medium PE mass fractions, owing to a more flexible structure of the copolymer PVDF matrix that allows for better absorption of the impact energy from the HTMECH hemispherical shaft (higher resistance to failure). Interestingly, toughness in the homopolymer-based membranes seems to diminish at a slower pace than for the copolymer-based ones (smaller slope), being higher for the former above medium PE mass fractions. This might be related to added ductility to the PVDF matrix by the PE domains that allow for better impact energy dissipation and improved membrane failure threshold. In fact, addition of PE to homopolymer-based membranes resulted in improved strain at break (not shown); whereas the presence of PE was always detrimental for strain at break of copolymer-based membranes,

suggesting a different interaction mechanism between the PVDF and PE phases in homo- and copolymer-based membranes. Presumably, this difference may be rooted on the previously proposed model of variable distribution of PE and PVDF domains that depends on the inert matrix original crystallinity and crystallite size, as well as melt viscosity (Figure 3.15).

A remarkably good exponential-decay fit, analog to the Maxwell model for polymer stress and strain behavior as a function of time, was found for all the mechanical properties as a function of the PE mass fraction (trend lines in Figure 3.19 through Figure 3.24). Although similar exponential decaying relationships exist for the yield stress of polymer suspensions as a function of the suspension concentration [48], we are not aware of any blend model, or experimental studies for that matter, that elucidate the nature of this particular type of mechanical property/composition association; specially if we take into account the non-typical biaxial deformation origin of the mechanical properties presented in this study. Interestingly, the goodness of fit of the exponential profiles of the homopolymers was on average lower than that of the copolymers; that is, the exponential decaying fit explains better the observed mechanical properties of the copolymers, alluding to the model of dissimilar interaction mechanisms between PE and PVDF homo- and copolymers. In contrast, no defined relationships were found for membrane conductivity as a function of PE content (the best approximations corresponded to quadratic models; however, correlation coefficients were particularly low: < 0.7).

In general, opposite to the conductivity behavior, copolymer-based membranes exhibited the worst mechanical properties. In fact, membranes containing Kynar® 2801, which attained the highest average conductivity, had the lowest average elastic modulus, ultimate tensile strength, and toughness. It is important to notice, however, that in the dry state copolymer-based membranes were less brittle and more easily handled. When compared to the average Nafion® 112 mechanical properties (reference horizontal lines in Figure 3.19 through Figure 3.24) the PVDF/PE membranes perform satisfactorily, having a similar average range of mechanical properties at medium PE mass fractions. On the contrary, at low PE contents the mechanical properties of PVDF/PE membranes can reach values as high as five times (elastic modulus), two times (ultimate tensile strength), or three times (toughness) those in Nafion® 112 due to the high PVDF to PE ratio. At a glance membranes containing Kynar® 2801 or 2851 and PE2 in the range of 40 to 50wt% provide the best trade-off of conductivity and mechanical properties; whereas Kynar® 2821 and 500 provide the best individual conductivity and mechanical properties respectively. However, due to the "property-map" data generation type resulting from high-throughput HTC and HTMECH screening, the conductivity information shown in Figure 3.2 and Figure 3.3 can be coupled with the mechanical data to create response surfaces that can be overlapped to choose the appropriate proton-conducting and mechanical properties for a particular membrane design.

3.4 Conclusions

Novel membranes of semi-interpenetrated networks of Kynar® PVDF and covalently crosslinked sulfonated acrylic polyelectrolytes were prepared from five different Kynar® PVDF grades and two dissimilar types of polyelectrolytes blended at numerous Kynar® to PE ratios. The proton conductivity and mechanical properties of the membranes were assayed by means of custom designed electrochemical impedance spectroscopy and biaxial axisymmetric deformation high-throughput screening tools (HTMECH and HTC) respectively.

As anticipated membrane conductivity exhibited a conventional behavior, being higher in membranes containing the PE with lower equivalent weight, and increasing as the amount of PE increased. Nevertheless, statistical analysis of the conductivity data revealed a maximum effective amount of polyelectrolyte of approximately 55-60wt% above which there was no statistically significant change in conductivity. This conductivity plateau was linked to the coalescence of ion conducting domains at high PE mass fractions in the membrane. In addition, even though a considerable decoupling of proton conductivity from the properties of the inert phase was initially expected, a significant effect of Kynar® PVDF grade indicated that conductivity was strongly favored in membranes containing PVDF:HFP copolymers in comparison to those containing PVDF homopolymers. Further analysis revealed a direct correlation between proton conductivity and several physical properties of the PVDF phase such as: crystallinity, crystallite size, and melt viscosity. Specifically, conductivity was found to decrease with increased crystallinity, crystallite size, and melt viscosity of the PVDF

phase. The maximum overall conductivity was attained by membranes containing Kynar® 2821 PVDF:HFP copolymer (X_C = 24.8%, D = 152.4 Å, η_M = 8.6 kP), while the lowest by those based on Kynar® 731 PVDF homopolymer (X_C = 69.1%, D = 200.2 Å, η_M = 16.9 kP). A model based on the impediment of the PE segmental motion during the crosslinking process by a synergistic effect of high viscosity and dense PVDF areas formed by molten crystallites is proposed to explain this behavior. Annealing of PVDF/PE membranes at temperatures above the PVDF α-phase relaxation temperature resulted in the apparent formation of a PVDF-rich surface layer exhibiting a partial ferroelectric to paraelectric phase transition, accompanied by a substantial reduction of proton conductivity.

Mechanical properties were mainly dictated by the PVDF grade. Elastic modulus and ultimate tensile strength were generally higher in membranes containing stiffer PVDF homopolymers than in those that incorporate more flexible PVDF:HFP copolymers (only in a few cases at low PE content copolymer-based membranes exhibited higher tensile strength as a result of strain-induced crystallization). Toughness was higher in copolymer-based membranes in the range of low to medium PE content (25 to 45wt%) due to the ability of the more flexible PVDF:HFP system to absorb the impact energy of the test.

In general PVDF/PE membranes compare favorably against Nafion® 112, reaching conductivities as high as 130 mS/cm (at 25°C in water) and mechanical properties that can be several times higher than those of Nafion® 112. However, the selection of a

particular PVDF/PE membrane, and hence the tradeoff between conductivity and mechanical characteristics, will be dictated by the requirements of its final application.

3.5 References

1. Melle, F.D., *The global and urban environment: the need for clean power systems.* Journal of Power Sources, 1998. **71**: p. 7-11.

2. Irvine, J.T.S., *The Bourner lecture-Power sources and the new energy economy.* Journal of Power Sources, 2004. **136**: p. 203-207.

3. Johnston, B., Mayo, M.C., and Khare, A., *Hydrogen: the energy source for the 21st century.* Technovation, 2005. **25**: p. 569-585.

4. Hart, D., *Sustainable energy conversion: fuel cells — the competitive option?* Journal of Power Sources, 2000. **86**: p. 23-27.

5. Cropper, M.A.J., Geiger, S., and Jollie, D.M., *Fuel cells: a survey of current developments.* Journal of Power Sources, 2004. **131**: p. 57-61.

6. Sopian, K. and Daud, W.R.W., *Challenges and future developments in proton exchange membrane fuel cells.* Renewable Energy, 2006. **31**: p. 719-727.

7. Kerres, J.A., *Development of ionomer membranes for fuel cells.* Journal of Membrane Science, 2001. **185**: p. 3-27.

8. Whittingham, M.S., Savinell, R.F., and Zawodzinski, T., *Introduction: Batteries and Fuel Cells.* Chemical Reviews, 2004. **104**(10): p. 4243-4244.

9. Kerres, J.A., *Blended and Cross-Linked Ionomer Membranes for Application in Membrane Fuel Cells.* Fuel Cells, 2005. **5**(2): p. 230-247.

10. Meier-Haack, J., et al., *Membranes from sulfonated block copolymers for use in fuel cells.* Separation and Purification Technology, 2005. **41**: p. 207-220.

11. Kreuer, K.-D., et al., *Transport in Proton Conductors for Fuel-Cell Applications: Simulations, Elementary Reactions, and Phenomenology.* Chemical Reviews, 2004. **104**(10): p. 4637-4678.

12. Hickner, M.A., et al., *Alternative Polymer Systems for Proton Exchange Membranes (PEMs).* Chemical Reviews, 2004. **104**: p. 4587-4612.

13. Hickner, M.A. and Pivovar, B.S., *The Chemical and Structural Nature of Proton Exchange Membrane Fuel Cell Properties.* Fuel Cells, 2005. **5**(2): p. 213-229.

14. Cho, C.G., et al., *Fuel cell membranes based on blends of PPO with poly(styrene-b-vinylbenzylphosphonic acid) copolymers.* Journal of Membrane Science, 2008. **308**: p. 96-106.

15. Swier, S., et al., *Polymer blends based on sulfonated poly(ether ketone ketone) and poly(ether sulfone) as proton exchange membranes for fuel cells.* Journal of Membrane Science, 2005. **256**(1-2): p. 122-133.

16. Arnett, N.Y., et al., *Hydrocarbon and partially fluorinated sulfonated copolymer blends as functional membranes for proton exchange membrane fuel cells.* Journal of Power Sources, 2007. **172**: p. 20-29.

17. Mokrini, A., Huneault, M.A., and Gerard, P., *Partially fluorinated proton exchange membranes based on PVDF–SEBS blends compatibilized with methylmethacrylate block copolymers.* Journal of Membrane Science, 2006. **283**: p. 74-83.

18. Fu, R.-Q., et al., *PPO-based acid–base polymer blend membranes for direct methanol fuel cells.* Journal of Membrane Science, 2008. **322**: p. 331-338.

19. Moszczyński, P., et al., *Interpenetrating ionomer–polymer networks obtained by the in situ polymerization in pores of PVdF sponges as potential membranes in PEMFC applications.* Journal of Power Sources, 2007. **173**: p. 648-656.

20. Quartarone, E., et al., *Relationships between microstructure and transport properties of proton-conducting porous PVDF membranes.* Journal of Power Sources, 2007. **168**: p. 126-134.

21. Sormana, J.-L., Chattopadhyay, S., and Meredith, J.C., *High-throughput mechanical characterization of free-standing polymer films.* Review of Scientific Instruments, 2005. **76**: p. 062214.

22. Zapata, P., Basak, P., and Meredith, J.C., *High-Throughput Screening of Ionic Conductivity in Polymer Membranes.* Electrochimica Acta, 2009. **10.1016/j.electacta.2009.02.009**.

23. Whitacre, J.F., Valdez, T.I., and Narayanan, S.R., *A high-throughput study of PtNiZr catalysts for application in PEM fuel cells.* Electrochimica Acta, 2008. **53**: p. 3680-3689.

24. Meredith, J.C., Karim, A., and Amis, E.J., *Combinatorial Methods for Investigations in Polymer Materials Science.* MRS Bulletin, 2002. **27**(4): p. 330-335.

25. Meredith, J.C., et al., *Combinatorial Materials Science for Polymer Thin-Film Dewetting.* Macromolecules, 2000. **33**: p. 9747-9756.

26. Zapata, P. and Meredith, J.C., *in preparation.*

27. Jayasuriya, A.C., Schirokauer, A., and Scheinbeim, J.I., *Crystal-Structure Dependence of Electroactive Properties in Differently Prepared Poly(vinylidene fluoride/hexafluoropropylene) Copolymer Films.* Journal of Polymer Science: Part B: Polymer Physics, 2001. **39**: p. 2793-2799.

28. Gregorio, R.J. and Ueno, E.M., *Effect of crystalline phase, orientation and temperature on the dielectric properties of poly (vinylidene fluoride) (PVDF).* Journal of Materials Science, 1999. **34**: p. 4489-4500.

29. Wang, Y., Cakmak, M., and White, J.L., *Structure Development in Melt Spinning Poly(viny1idene Fluoride) Fibers and Tapes.* Journal of Applied Polymer Science, 1985. **30**: p. 2615-2632.

30. Gregorio, R.J., *Determination of the α, β, and γ Crystalline Phases of Poly(vinylidene fluoride) Films Prepared at Different Conditions.* Journal of Applied Polymer Science, 2006. **100**: p. 3272-3279.

31. Mhalgi, M.V., Khakhar, D.V., and Misra, A., *Stretching Induced Phase Transformations in Melt Extruded Poly(vinylidene fluoride) Cast Films: Effect of Cast Roll Temperature and Speed.* Polymer Engineering and Science, 2007. **47**(12): p. 1992-2004.

32. Newman, B.A. and Scheinbeim, J.I., *Polarization Mechanisms in Phase II Poly(vinylidene fluoride) Films.* Macromolecules, 1983. **16**: p. 60-68.

33. Moggi, G., Bonardelli, P., and Bart, J.C.J., *Synthesis and properties of some hexafluoropropene-1,1-difluoroethene copolymers.* Polymer Bulletin, 1982. **7**: p. 115-122.

34. Cui, Z.-Y., et al., *Preparation of PVDF-HFP Microporous Membranes via the Thermally Induced Phase Separation Process.* Journal of Macromolecular Science, Part B: Physics, 2009. **48**: p. 41-54.

35. Tazaki, M., et al., *Crystallization and Gelation of Poly (vinylidene fluoride) in Organic Solvents.* Journal of Applied Polymer Science, 1997. **65**: p. 1517-1524.

36. Satapathy, S., et al., *Crystallization of β-phase Poly (vinylidene fluoride) films using dimethyl sulfoxide (DMSO) solvent and at suitable annealing condition.* arXiv, 2008. **arXiv:0808.0419v1**.

37. Birkholz, M., *Thin Film Analysis by X-Ray Scattering*. 2006, Weinheim: Wiley-VCH Verlag GmbH & Co. KGaA. 378.

38. Kong, Y. and Hay, J.N., *The enthalpy of fusion and degree of crystallinity of polymers as measured by DSC.* European Polymer Journal, 2003. **39**: p. 1721-1727.

39. Cao, J.-H., Zhu, B.-K., and Xu, Y.-Y., *Structure and ionic conductivity of porous polymer electrolytes based on PVDF-HFP copolymer membranes.* Journal of Membrane Science, 2006. **281**: p. 446-453.

40. Bachmann, M.A., et al., *An Infrared Study of Phase-III Poly(vinylidene fluoride).* Journal of Applied Physics, 1979. **50**: p. 6106-6112.

41. Lovinger, A.J., *Ferroelectric Polymers.* Science, 1983. **220**(4602): p. 1115-1121.

42. Abbrent, S., et al., *Crystallinity and morphology of PVdF–HFP-based gel electrolytes.* Polymer, 2001. **42**: p. 1407-1416.

43. Jiang, Z., Carroll, B., and Abraham, K.M., *Studies of some poly(vinylidene fluoride) electrolytes.* Electrochimica Acta, 1997. **42**(17): p. 2667-2677.

44. McLean, R.S., Doyle, M., and Sauer, B.B., *High-Resolution Imaging of Ionic Domains and Crystal Morphology in Ionomers Using AFM Techniques.* Macromolecules, 2000. **33**: p. 6541-6550.

45. Painter, P.C., et al., *Infrared Band Broadening and Interactions in Polar Systems.* Macromolecules, 1999. **32**(6): p. 2055-2057.

46. Sormana, J.-L. and Meredith, J.C., *High-throughput screening of mechanical properties on temperature-gradient polyurethaneurea libraries.* Macromolecular rapid communications, 2003. **24**(1): p. 118-122.

47. Sormana, J.-L. and Meredith, J.C., *High-Throughput Discovery of Structure-Mechanical Property Relationships for Segmented Poly(urethane-urea)s.* Macromolecules, 2004. **37**(6): p. 2186-2195.

48. Utracki, L.A., *Polymer Blends Handbook*. 2003, New York: Springer-Verlag New York, LLC.

Chapter 4
Organic/Inorganic Composite Proton Exchange Membranes from Zirconium-Based Solid Acids and PVDF/Acrylic Polyelectrolyte Blends

Nowadays, organic/inorganic composite (or hybrid) proton exchange membranes (PEMs) are receiving great attention owing to the multiple benefits that may arise by the incorporation or inorganic nanofillers into the polymeric matrix of the membranes. Our previous work showed that entirely polymeric membranes based on blends of poly(vinylidene fluoride) (PVDF) and covalently crosslinked sulfonated acrylic polyelectrolytes (PE) compare favorably against perfluorosulfonic acid-based counterparts (e.g., Nafion®) in terms of proton conductivity and mechanical properties. In this study our primary efforts are centered in further enhance these properties by the insertion of various zirconium-based nanoparticles into the PVDF/PE matrix, giving place to *tri-phase* organic/organic/inorganic composite membranes. Dispersion of

nanoparticles in the polymer matrix was thermodynamically limited as unfavorable particle-polymer interactions resulted in severe aggregation of the solid-phase at high particle loadings (5wt%). Nevertheless, a general improvement in proton conductivity was evidenced in composite membranes with low to medium nanoparticle loadings (0.5 to 1wt%), in comparison to non-hybrid PVDF/PE references. This beneficial effect was particularly noticeable in membranes manufactured from highly crystalline PVDF homopolymers (7% to 14.3% increment), where the nanoparticles induced a "healing" effect by providing proton-conducting paths between non-crosslinked PE channels separated by dense PVDF areas arising from large PVDF crystallites. Similarly, tensile properties were enhanced at identical particle loadings (19.5% to 22.5% elastic modulus increment); especially in membranes containing more flexible PVDF:HFP copolymers, where a reinforcing stiffening effect was evident. Albeit addressing nanoparticle dispersion issues is imperative, the results presented herein are promising for the development of cost-effective alternative composite PEMs.

4.1 Introduction

Owing to the multiple drawbacks associated with the use of traditional energy sources and energy conversion technologies, and in view of the unfavorable panorama of the actual energy economy, alternative sustainable energy sources and conversion approaches have acquired noteworthy significance in recent years [1-3]. One of such alternatives is the proton exchange membrane fuel cell (PEMFC), which constitutes a

promising high-efficiency energy conversion alternative to provide power for mobile and stationary applications; and which is considered to be pivotal for the transition towards a sustainable global energy economy [1-4].

One of the key components of the PEMFC is the polymer electrolyte, or proton exchange membrane (PEM). The PEM is a proton-conducting polymeric solid that provides a proton transport vehicle between the anode and the cathode, while simultaneously serving as a barrier to prevent cross-leaks between the fuel and oxidant streams. Besides these proton transport and gas barrier properties, the PEM needs to satisfy other essential requirements for the appropriate operation of the fuel cell, including: low electronic conductivity, low water transport, high hydrolytic stability, and excellent mechanical integrity, among several others [5, 6].

Over the past years a profuse amount of research endeavors have focused on developing new cost-effective and operational sound PEM materials with the purpose of closing the breach between the actual PEMFC technology (based primarily on perfluorosulfonic acid (PFSA) membranes [3-5]) and commercialization targets (e.g., DOE targets for portable fuel cells [3]). Numerous approaches are being considered in the development of these new PEM materials, including: modification of PFSA-based membranes, functionalization of high-performance hydrocarbon polymers, polymer blends of inert and ionic conductive precursors, and organic/inorganic composite membranes, just to mention a few [5, 7-11]. Among these, organic/inorganic composite or hybrid proton exchange membranes have gained momentum at an incredible pace. The reason behind this resides in the synergistic beneficial effects in proton conductivity,

mechanical properties, thermal stability, membrane humidification, and fuel crossover reduction that may arise by introducing inorganic nanofillers in the polymer matrix of the membranes [9-20].

Inorganic candidate materials for use in composite proton exchange membranes include: metal oxides (e.g., SiO_2, TiO_2, ZrO_2, and Al_2O_3) [9, 10, 12], solid acids such as sulfates and phosphates [9, 11-13, 17-19, 21], and nanoclays (e.g., montmorillonite) [20]. Among these, solid acids appear to have the most potential owing to their proton-conducting properties, as well as their hydrophilicity and self-humidification characteristics [6, 9, 13]. Of particular interest are tetravalent metal acids based on zirconium, particularly zirconium phosphate [11, 13, 15, 16, 22], which can preserve its proton conductivity up to 300°C [6]; and sulfated zirconia [12, 17], which is one of the strongest solid superacids known and can retain sulfonic acid groups responsible for proton conduction up to 500°C [12, 23].

Recently proton exchange membranes from semi-interpenetrated networks of PVDF and covalently crosslinked sulfonated acrylic polyelectrolytes were studied and characterized using high-throughput techniques [8, 24]. These PVDF/PE blended membranes exhibited acceptable proton conducting and mechanical properties comparable or better than Nafion® standards. Here, we examine the possibility of improving these properties even further by incorporating zirconium-based nanofillers (i.e., zirconium oxide, zirconium hydrogenphosphate, and zirconium hydroxide sulfated), into the polymer blend to produce organic/organic/inorganic tri-phase proton exchange membranes. Following the same fashion of our previous work, high-

throughput techniques involving custom-developed high-throughput characterization tools are used to assess the proton conductivity and mechanical properties of the PVDF/PE zirconium-based composite membranes.

4.2 Experimental

4.2.1 Composite membrane synthesis and protonation

Organic/organic/inorganic tri-phase nanocomposite proton-conducting composite membranes were prepared by mixing zirconium-based nanoparticles and individual blends of five Kynar® PVDF grades and a sulfonated acrylic polyelectrolyte (PE) consisting of a random copolymer of 2-sulfoethyl methacrylate (SEM) (~69wt%), 2-hydroxyethyl methacrylate (HEMA) (~15wt%), methyl methacrylate (MMA) (~8wt%), and styrene (~7wt%); and an equivalent weight of 280 gr PE/mol SO_3H. The five different grades of PVDF, including two PVDF homopolymers (Kynar® 500 and Kynar® 731), and three copolymers of PVDF and hexafluoropropylene (PVDF:HFP) (Kynar® 2801, Kynar® 2821, and Kynar® 2851) (Arkema Inc.); were dissolved in 1-methyl-2-pyrrolidinone (NMP) (Sigma-Aldrich Co., assay≥99.5%) to a total concentration of 10wt% per solution. These PVDF solutions were mixed with a stock solution of the PE (25wt% total solids in NMP) at a fixed mass ratio (dry base) of 65:35 (PVDF:PE, acid form). Three different types of zirconium-based particles were utilized; namely, zirconium(IV) oxide nanopowder (ZrO_2) (particle size <100 nm), zirconium(IV) hydroxide sulfated ($Zr(H_2SO_4)_4$), and zirconium(IV) hydrogenphosphate ($Zr(HPO_4)_2$)

(Sigma-Aldrich Co.). The size of the mesoporous zirconium(IV) hydroxide sulfated and zirconium(IV) hydrogenphosphate particles was further reduced by crushing them using a zirconia mortar and pestle; the zirconium oxide nanopowder was utilized as received. Final particle size was approximately 100-300 nm for zirconium(IV) hydroxide sulfated and 200-1000 nm for zirconium(IV) hydrogenphosphate. For the sake of simplicity for the remainder of this work zirconium oxide and the modified sulfated zirconium hydroxide and zirconium hydrogenphosphate will be referred to as ZrO, ZrS, and ZrHP respectively. Prior to mixing with the PVDF/PE blends the nanoparticles were de-agglomerated and suspended in NMP by vigorous stirring for 6 h, followed by overnight sonication in an ultrasonic bath, and 20 min "strong" sonication using a horn-type sonicator. Each nanoparticle suspension type was mixed with every PVDF/PE blend at 0.5 (low), 1 (medium), and 5wt% (high) (dry base) to give a total of 45 different mixtures (in addition to five reference PVDF/PE blends without nanoparticles). The PVDF/PE/ZrX (X= O, P, HP) mixtures were combined with Desmodur N-3300A (Bayer AG.), a 1,6-hexamethylene diisocyanate-derived triisocyanate crosslinker, at a 1:0.8 OH:NCO ratio (80mol% of the stoichiometric amount of crosslinker needed to react with all the polyelectrolyte hydroxyl groups). The final blends were thoroughly mixed at room temperature under an inert nitrogen atmosphere for approximately 30 minutes, followed by a degassing and re-dispersion of the nanoparticles by sonication (~15 min) immediately before film coating. Coating was performed using a knife-edge apparatus [25] to spread liquid PVDF/PE/ZrX films onto silicon <100> substrates (Silicon, Inc.) previously cleaned for 2 hours in Piranha solution (70% H_2SO_4, 9% H_2O_2, 21% H_2O) at

80°C. The resulting films were cured at 175°C for 20 minutes in a forced convection oven to crosslink the PE and remove excess NMP. Cured composite membranes were detached from the silicon substrates by immersion in DI water at room temperature.

Prior to protonation, free-standing composite membranes were washed in a 1M HCl solution at 80°C for 2 hours, followed by a 15-minute rinse in DI water. The acid-washed membranes were protonated by immersion in 1M H_2SO_4 at 80°C for 2 hours, followed by removal of excess sulfuric acid by several successive 15-minute rinses in DI water until the pH of the rinse water was above 4. Conditioning of protonated composite membranes, as well as nanoparticle-free PVDF/PE references, was carried out by immersion in boiling 18.2 MΩ water for one hour to allow complete membrane swelling. Swollen membranes were stored in 18.2 MΩ water until conductivity and mechanical property measurements were performed.

4.2.2 Composite membranes characterization

4.2.2.1 High throughput measurement of proton conductivity and mechanical properties

Proton conductivity measurements were performed by AC electrochemical impedance spectroscopy (EIS) using a custom automated 4-point probe high-throughput conductivity measuring device (HTC) designed in our lab [24]. Conductivity measurements of composite membranes and reference membranes submerged in 18.2 MΩ water at approximately 25°C were performed in potentiostatic mode with an

excitation signal of 1000 Hz and 30 mV (~20 mV RMS), and a response signal integration time of 5000 cycles following a 5 second stabilization period.

Characterization of mechanical properties was carried out using a modified high-throughput mechanical testing apparatus (HTMECH) based on a previous design developed in our lab [8, 26]. All mechanical characterization tests were performed at a constant speed of 10 mm/s using a 1.24 mm diameter needle (needle to isolation plate hole diameter ratio: 0.413). Sampling rate of the load cell signal was set to 5000 samples per second. All membranes were tested in a fully hydrated state. As otherwise stated, conditioning and analysis of raw data from HTMECH tests was carried out via either undecimated wavelet transform with multiple-level rescaling to estimate noise variance (noise was not assumed white), universal threshold, and an orthogonal 8th order Symlet (Sym8) wavelet type; or a non-causal zero-phase IIR filter using 1st order Chebyshev coefficients, a passband ripple of 0.3 dB, and a cutoff frequency of 10 Hz. Bisquare fitting sensitivity was set to 95% for linear fitting of elastic modulus.

Detailed information about the operation of the HTC and HTMECH systems can be found in the references provided.

4.2.2.2 X-Ray diffraction (XRD)

X-ray diffraction spectra of composite membranes and nanoparticle powders were recorded using a PANalytical X'Pert PRO diffractometer (PANalytical). The incident beam configuration consisted of a Cu-anode tube (λ CuKα_1 = 1.540598 Å,λ CuKα_2 =

1.544426 Å) operated at 45 kV and 40 mA with a fixed 1/16°(0.19 mm) divergence slit, a 0.04 rad Soller slit, and a nickel β-filter to remove CuKβ radiation. The detector, a PANalytical X'Celerometer, was equipped with a 10 mm anti-scatter slit and a 0.04 rad Soller slit. Data was collected over a 2θ range of 1°-65° using a step size of 0.033°.

4.2.2.3 Fourier transform infrared spectroscopy (FT-IR)

Infrared absorption spectra of composite membranes were collected at room temperature with a Bruker Equinox 55 spectrometer (Bruker Optics Inc.) coupled with a KBr beam splitter. The spectra were recorded in the range of 400-5000 cm^{-1} at a resolution of 4 cm^{-1} and averaged 128 times.

4.2.2.4 Scanning electron microscopy (SEM)

High resolution images of the cross-sectional area of composite membranes were obtained using a LEO 1530 thermally assisted field emission scanning electron microscope (LEO Electron Microscopy Group), operated at 10keV. Membrane samples for SEM imaging where prepared by cryogenic breaking in liquid nitrogen followed by vacuum metallization with gold.

4.2.3 Statistical analysis

An unbalanced univariate general linear model (GLM) (2 and 3-way, type III sums of squares) was used for evaluation of significant factors; $p < 0.05$ was defined as

significant (5% significance level). Pairwise comparisons of significant factors from 3-way GLM tests were performed by comparisons of unweighted means of main effects with Sidak-adjusted confidence intervals; while Tamhane's T2 post hoc test was utilized for pairwise comparisons of significant factors from 2-way GLM tests. All results are expressed as mean ± standard error of the mean (± S.E.M.) or as mean ± 95% confidence intervals, according to indicated.

4.3 Results and Discussion

4.3.1 Microstructure of composite membranes

The structure of the zirconium-based additives (ZrX) is of relevance in the characterization of the composite membranes because of their organic/inorganic hybrid nature. Consequently, a preliminary study of the different solid zirconium-based particles, via powder X-ray diffraction, was completed prior to membrane characterization. The XRD spectra obtained are reproduced in Figure 4.1. The crystalline reflections (Bragg peaks) in the zirconia (ZrO) spectrum, particularly those located at scattering angles (2θ) of 28.2°, 30.2°, and 31.5°, indicate a mixed crystalline form of monoclinic and tetragonal ZrO phases [23, 27]. In contrast, ZrHP and ZrS are characterized by an amorphous halo with absence of crystalline reflections. In the case of ZrHP the amorphous spectrum indicates a disordered layer aggregation, and thus, the absence of lamellar α-ZrHP and/or γ-ZrHP. From a practical point of view, this may be beneficial for the overall proton conductivity of ZrHP-based composite membranes as

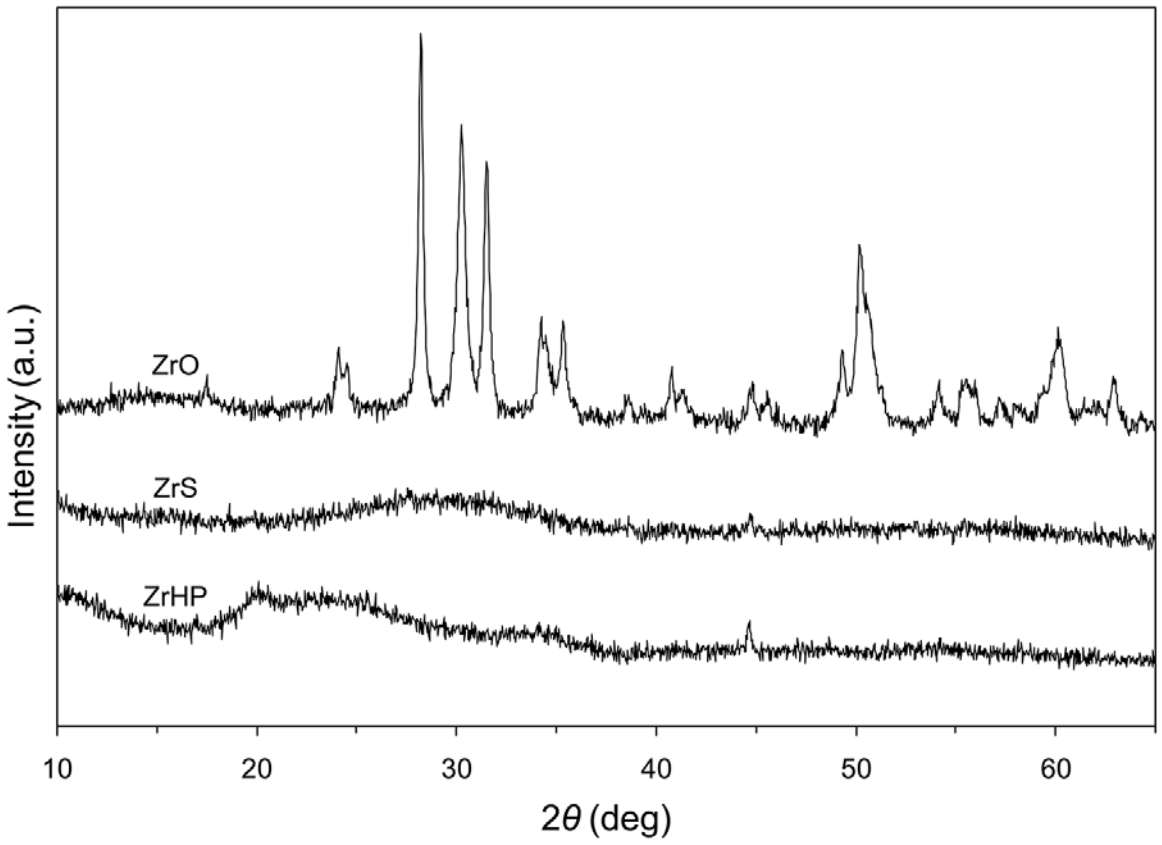

Figure 4.1 Wide angle X-ray diffraction spectra of ZrO, ZrS, and ZrHP nanoparticle powders.

amorphous ZrHP exhibits higher conductivity than comparable crystalline and semi-crystalline α-ZrHP and γ-ZrHP (1-5×10^{-3} vs. 1.8×10^{-5} and 2×10^{-4} S/cm at 100°C and 95%RH, respectively [21]). Similarly, conductivity of membranes based on amorphous ZrS could potentially benefit from a larger number of surface acid sites exposed, given that amorphous materials generally exhibit larger surface area than crystalline counterparts [28].

It has been shown that polymer characteristics, such as crystalline structure, can be affected by salt or acid complexation and/or incorporation of inorganic fillers [29, 30]. Thus, similarly to the characterization of zirconium-based additives, the structure of the of tri-phase composite membranes with different particle loadings, as well as of control samples including pure PVDF films, PVDF/PE membranes, and PVDF/ZrX films; was analyzed by X-ray diffraction (Figure 4.2 and Figure 4.3). The crystalline reflections in the spectrum of pristine solvent-cast PVDF films, prepared at identical conditions as the composite membranes, at scattering angles (2θ) of 17.8°, 18.4°, 19.9°, and 26.6° indicate a predominant crystalline α-phase [8, 31]. An evident decline in the crystallinity of the PVDF by incorporation of zirconium-based particles is noticed from the reduced intensity and broadening of the Bragg peaks. In addition, a shoulder to the right of the 19.9° Bragg peak suggests the formation of β-phase PVDF crystals in presence of ZrX. This is confirmed by the appearance of distinctive β-phase absorption bands at 510 cm^{-1}, ferroelectric all-trans conformation CF_2 bending, and 842 cm^{-1} [8, 32] in the FT-IR spectrum of the control sample (Figure 4.4). Addition of PE to the PVDF matrix results in a complete paraelectric to ferroelectric transition of the PVDF crystalline phase

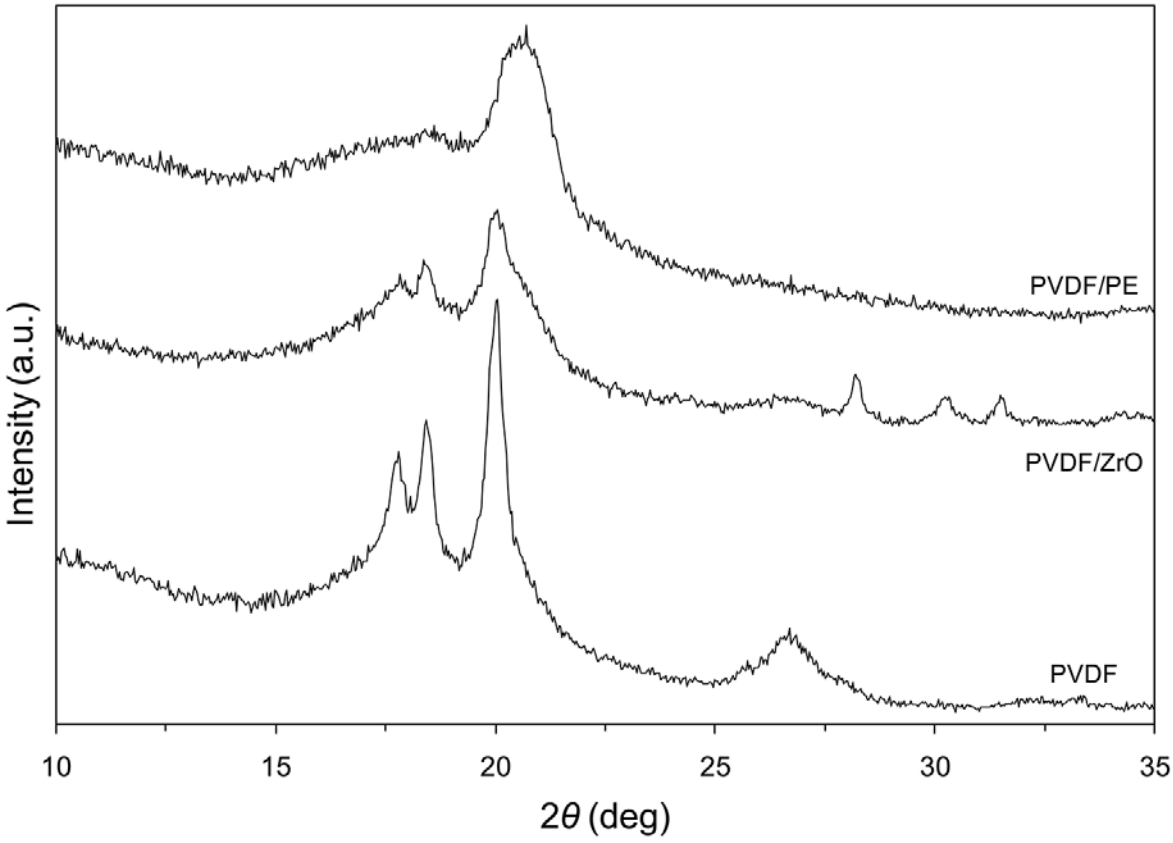

Figure 4.2 Wide angle X-ray diffraction spectra of pure and modified PVDF films. All the spectra correspond to Kynar® 731-based films (other PVDF grades exhibited identical behavior). The representative spectrum of the nanoparticle modified PVDF corresponds to ZrO.

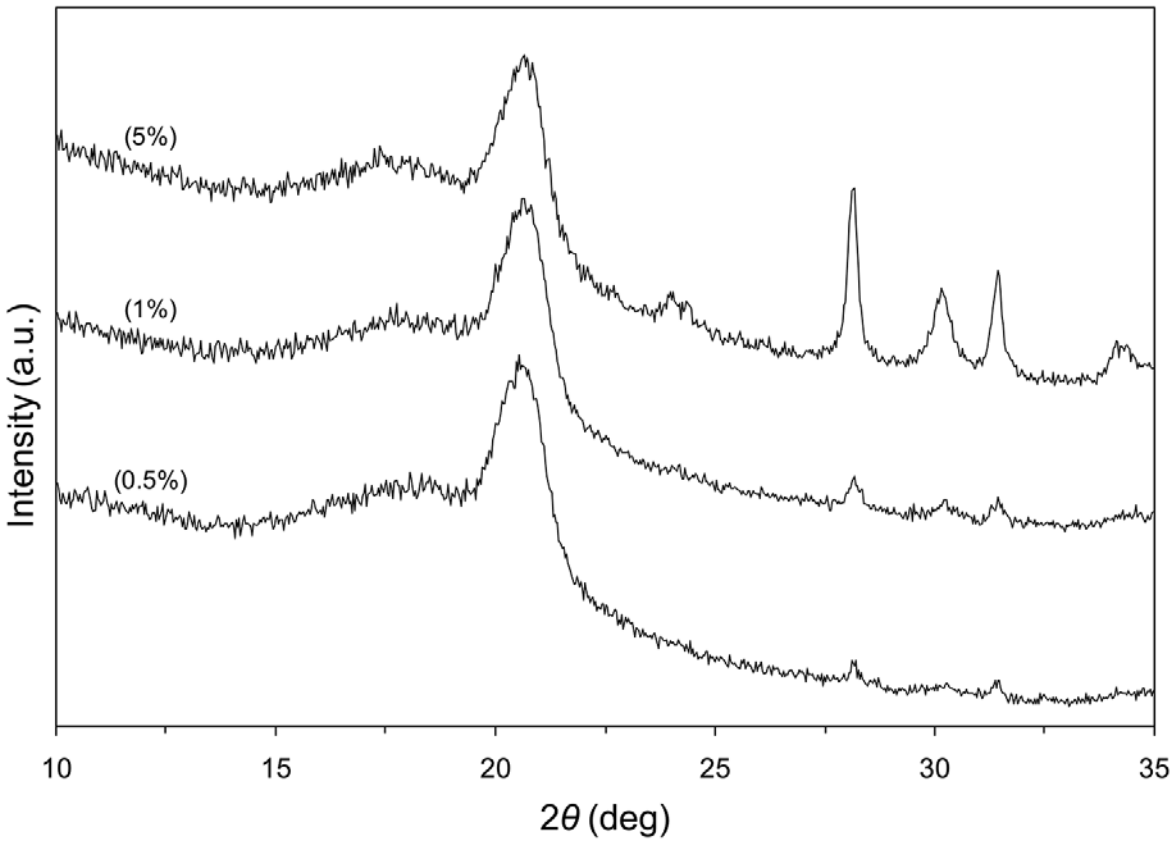

Figure 4.3 Representative wide angle X-ray diffraction spectra of composite membranes with different nanoparticle loadings. All the spectra correspond to Kynar® 731-based films (other PVDF grades exhibited identical behavior) and ZrO nanoparticles.

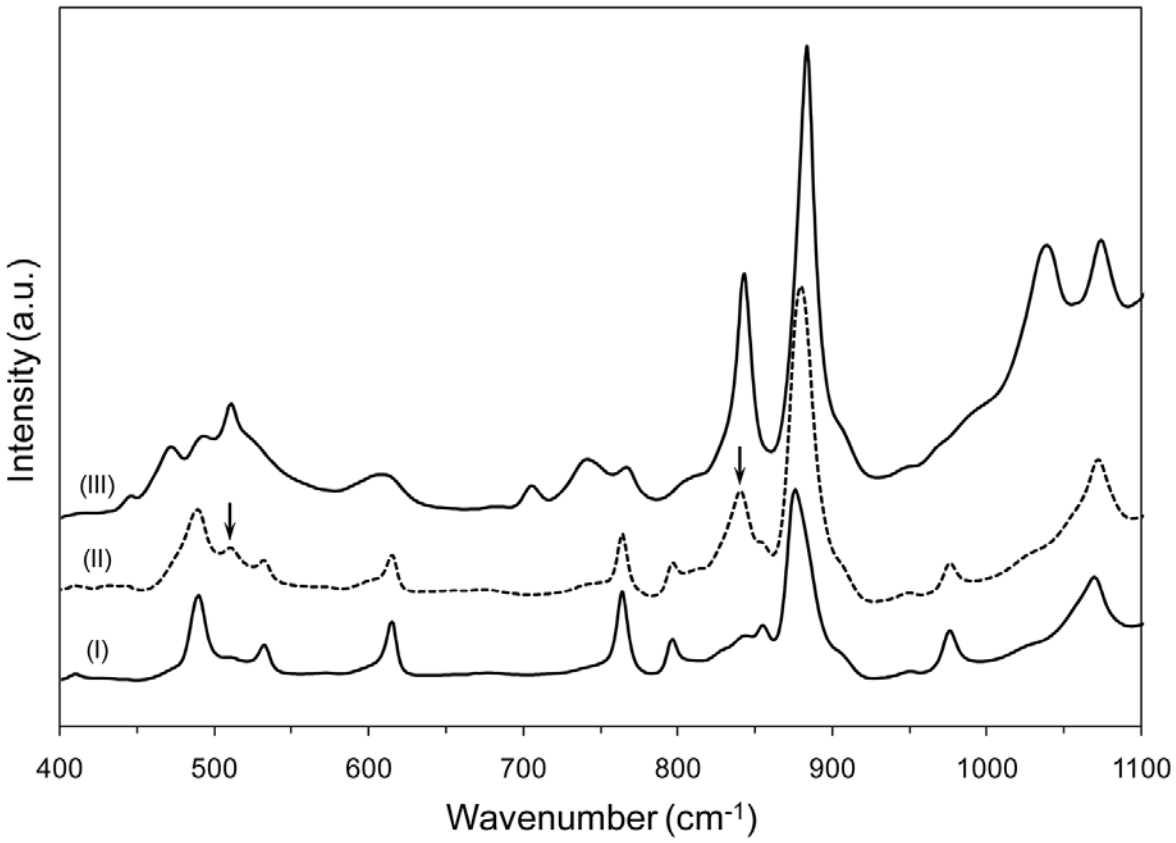

Figure 4.4 FT-IR spectra in the range of 400 to 1100 cm^{-1} corresponding to the pure and modified PVDF films shown in Figure 4.2: (I) PVDF, (II) PVDF/ZrO, and (III) PVDF/PE. The arrows indicate the appearance of characteristic PVDF β-phase bands at 510 cm^{-1} and 842 cm^{-1} as a result of the incorporation of nanoparticles.

characterized by a crystalline reflection at (2θ) 20.6° [8, 31], and confirmed by the disappearance of the non-polar trans-gauche CF_2 bending band at 532 cm^{-1} in the FT-IR of the PVDF/PE membrane spectrum. In summary, the incorporation of either PE or ZrX into the PVDF matrix disturbs the PVDF crystalline structure by inducing α- to β-phase transitions; as a result, the β-phase polymorph is prevalent in the PVDF support matrix of the composite membranes, as seen in Figure 4.3. The diffraction peaks at 28.2°, 30.2°, and 31.5° in the representative XRD spectra of composite membranes correspond to ZrO particles embedded in the polymer matrix. The intensity variation of these crystalline reflections is a clear indicator of different particle loadings. Small angle X-ray diffraction measurements of the zirconium-based additives (not shown) revealed no mesostructure and no basal plane diffraction peaks, in agreement with the amorphous structure of ZrHP and ZrS, and indicating a non-lamellar structure for the crystalline ZrO (or if a lamellar structure exists, the interlayer distance exceeds the largest layered spacing that can be determined by the X-ray diffractometer used).

A foremost concern when preparing polymeric composites by addition of an inorganic component to a polymer solution or dispersion, is the formation of a highly disperse solid phase within the polymer matrix. Consequently, SEM imaging was employed to assess the dispersion of the zirconium-based additives in the PVDF/PE polymer matrix of the composite membranes (Figure 4.5 through Figure 4.9). It is readily seen that the particles aggregate and form agglomerates or clusters that are distributed non-homogeneously throughout the membrane, particularly at high loadings. A critical parameter in the dispersion process is the magnitude of the inter-particle forces relative

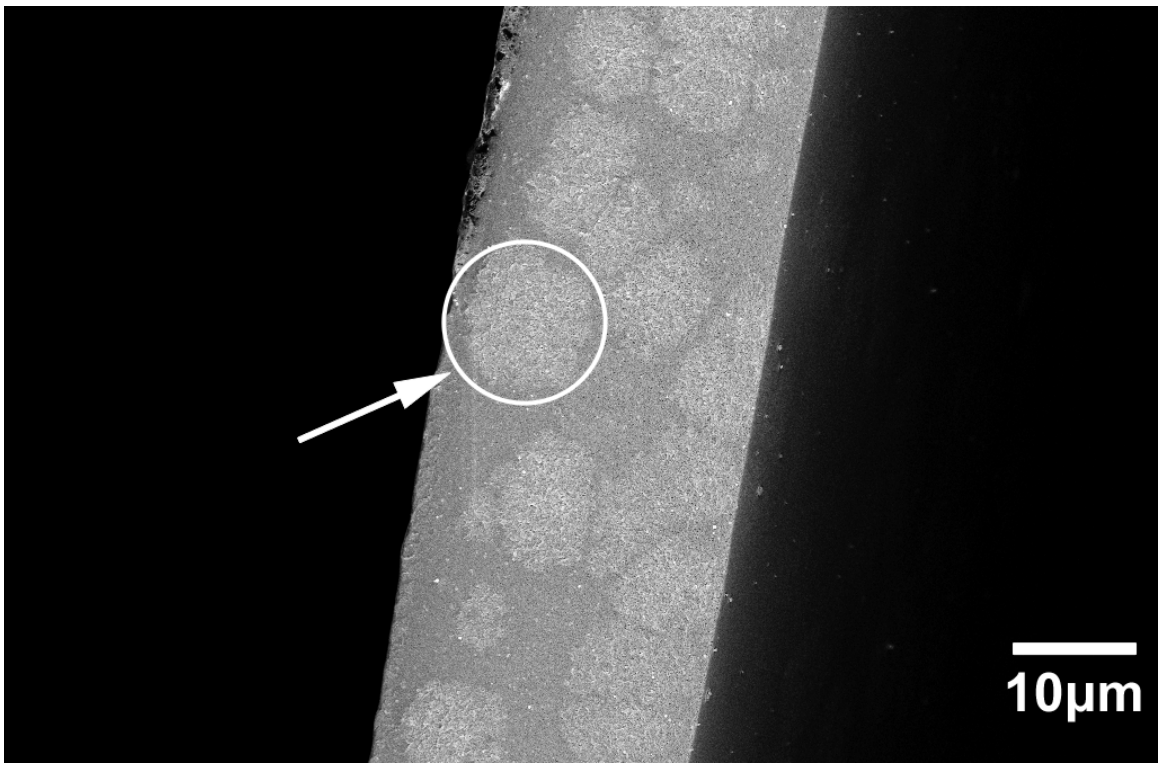

Figure 4.5 SEM image of the cross-sectional area of PVDF/PE/ZrHP (5wt%) composite membrane, EHT 10 kV. The circled area pointed by the arrow indicates a large cluster of aggregated nanoparticles.

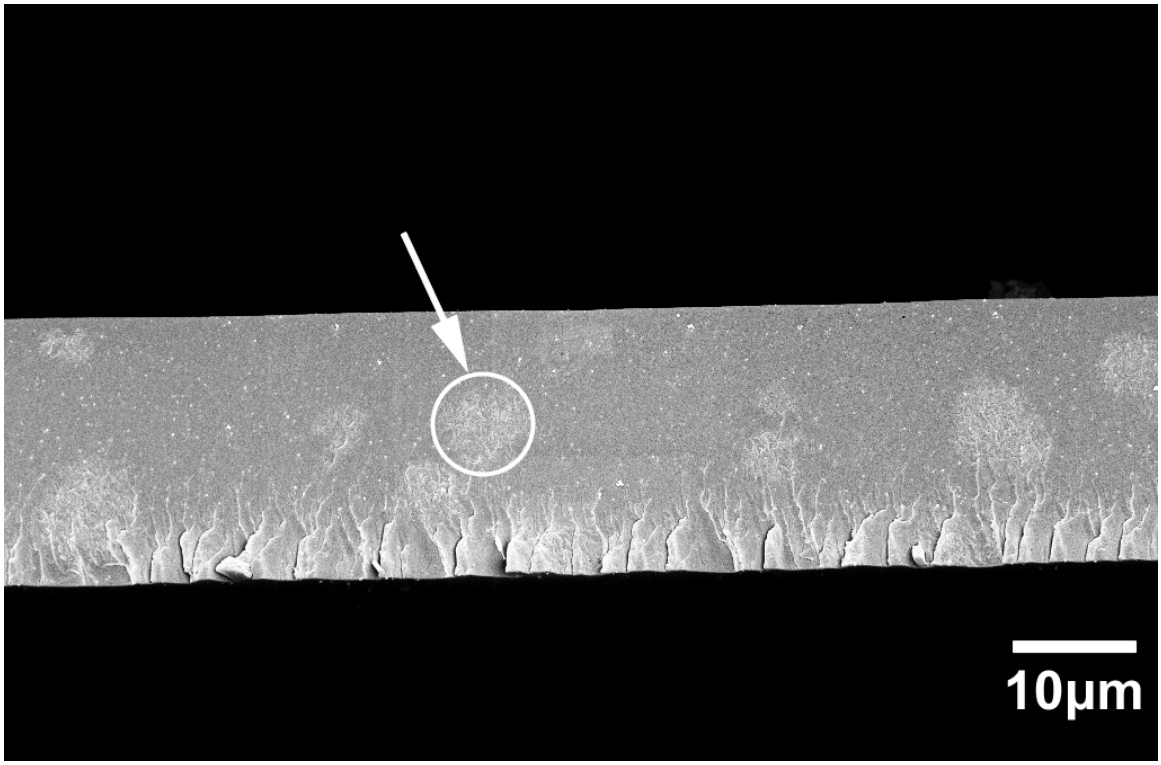

Figure 4.6 SEM image of the cross-sectional area of PVDF/PE/ZrHP (1wt%) composite membrane, EHT 10 kV. The circled area pointed by the arrow indicates a large cluster of aggregated nanoparticles.

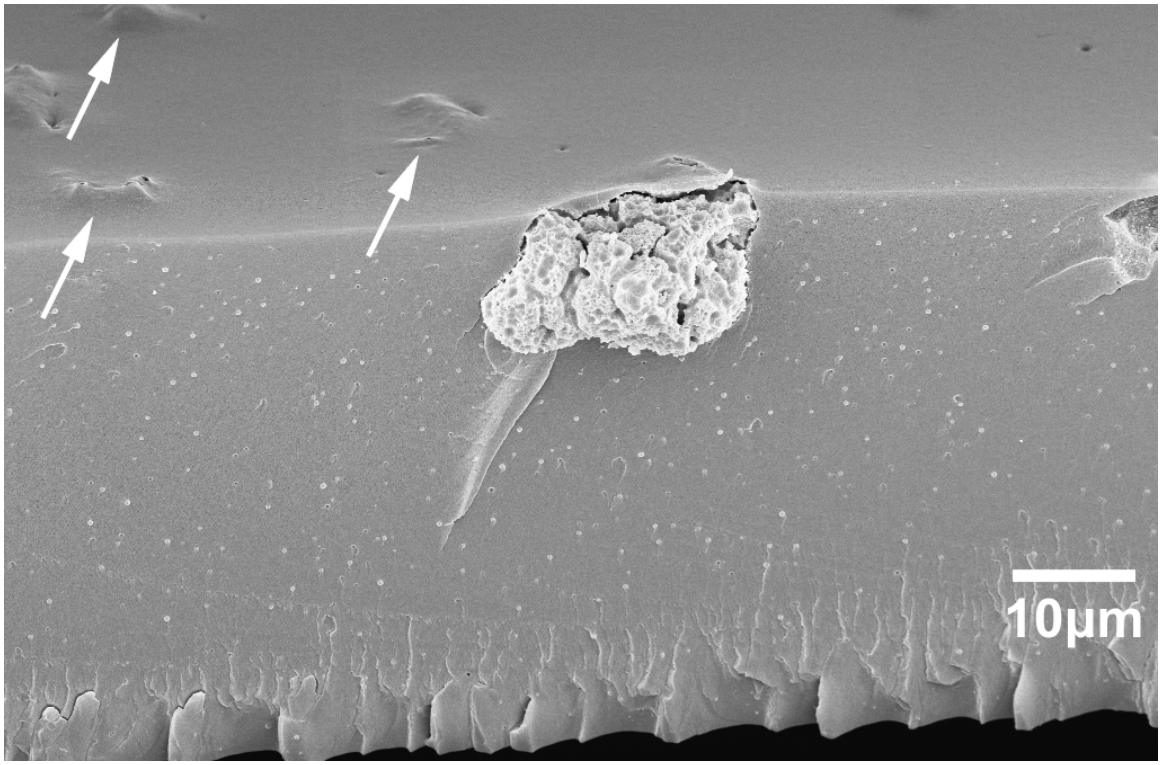

Figure 4.7 SEM image of the cross-sectional area of PVDF/PE/ZrS (5wt%) composite membrane, EHT 10 kV. The arrows indicate membrane defects created by agglomerates below the membrane surface similar to the one in the front plane of the image. The well dispersed small particles of about 300-400nm present across the whole membrane thickness correspond to polyelectrolyte clusters [8].

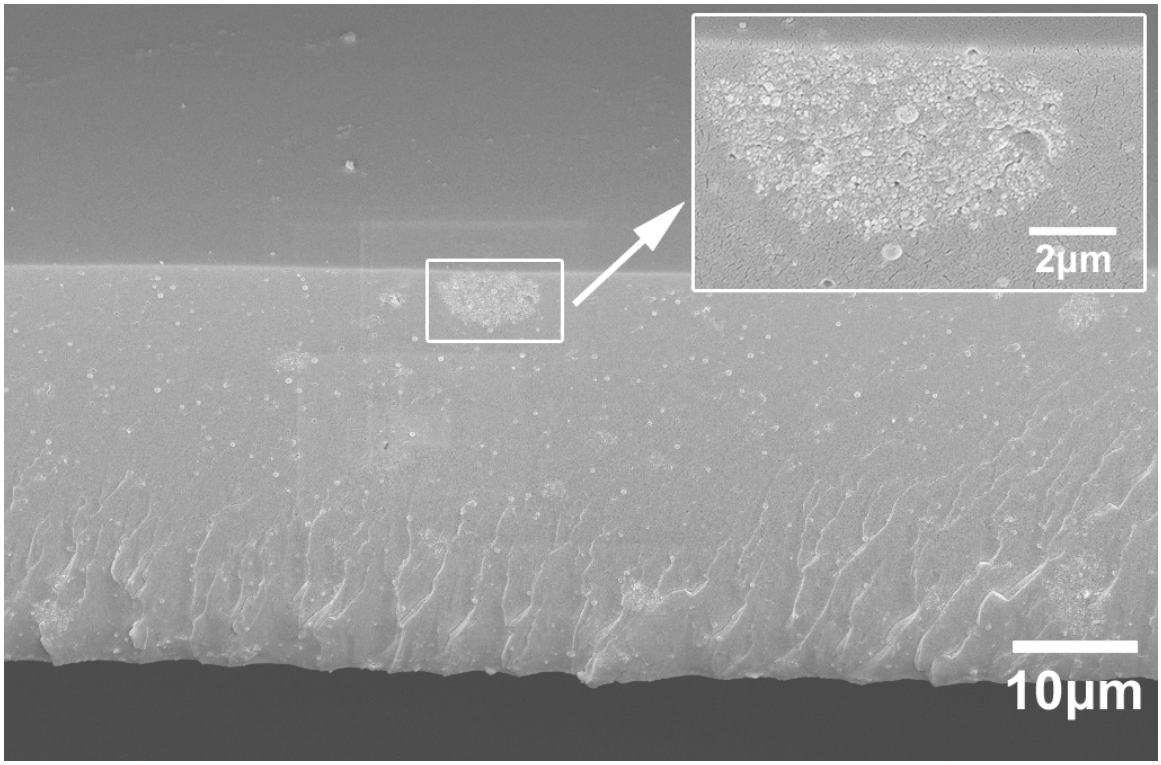

Figure 4.8 SEM image of the cross-sectional area of PVDF/PE/ZrO (5wt%) composite membrane, EHT 10 kV. The enclosed area (zoomed-in in the inset) highlights the relatively smaller agglomerates of ZrO. The well dispersed small particles of about 300-400nm present across the whole membrane thickness correspond to polyelectrolyte clusters [8].

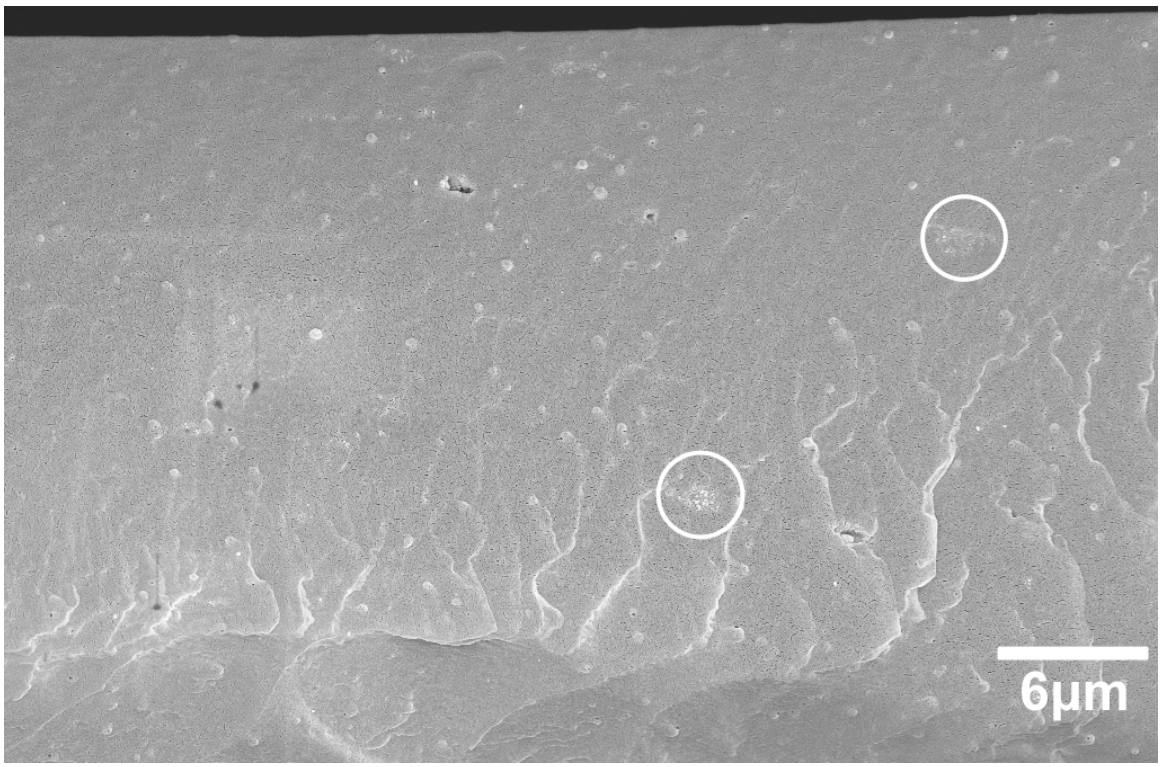

Figure 4.9 SEM image of the cross-sectional area of PVDF/PE/ZrO (1wt%) composite membrane, EHT 10 kV. The enclosed areas highlight the relatively smaller agglomerates of ZrO. The well dispersed small particles of about 300-400nm present across the whole membrane thickness correspond to polyelectrolyte clusters [8].

to those between the particles and the suspending medium [9, 33]. For instance, unfavorable effects can arise due to the competition between the entropic and enthalpic constraints associated with repulsive forces between species of different size and geometry, van der Waals attractions, Coulomb forces, and/or specific polymer-particle and inter-particle attractive/repulsive interactions [33, 34]. Therefore, regardless of possible attractive interactions based on hydrogen bonding and/or dipole-dipole interactions between the ZrX and the PVDF polar groups that can stabilize the solid phase dispersion at low particle loadings, the aggregation behavior witnessed in the PVDF/PE/ZrX composite membranes at medium and high particle mass fractions may be explained by a general unfavorable interaction between the hydrophilic surface of the ZrX particles and the hydrophobic polymer matrix. Due to the large surface-to-volume ratio of the nanoparticles this incompatibility is greatly amplified leading to serious aggregation, especially when no surface modifiers or compatibilizers are utilized. Similarly, In the case of ZrO particles, a reduced surface-to-volume ratio owing to their crystalline form might explain the better dispersion of this additive at all mass fractions when compared to ZrS and ZrHP (Figure 4.8 and Figure 4.9).

Alternatives to improve the nanoparticle dispersion in the PVDF/PE matrices, such as compatibilization and pre-exfoliation of zirconium-based nanoparticles via organomodification with tetra-*n*-butylammonium hydroxide [16, 35], and formation of pre-dispersed particle gels in NMP [36] compatible with the PVDF/PE blends; are being considered for future work.

4.3.2 Proton conductivity

The proton conductivity from HTC screening of 45 dissimilar zirconium-based composite membranes, as well as five PVDF/PE reference membranes, is shown in Figure 4.10 through Figure 4.14. An initial assessment of the plots reveals higher overall conductivity values for membranes containing PVDF:HFP copolymers, in agreement with our previous study of non-hybrid PVDF/PE proton exchange membranes [8]. It also appears to be a general reduction in proton conductivity in composite membranes with high content of nanoparticles with respect to corresponding nanoparticle-free references, which might be directly related to the particle aggregation and clustering noticed at high particle mass fractions. In addition, a seemingly beneficial effect from the incorporation of zirconium-based additives to the PVDF/PE blends is evidenced at low to medium nanoparticle loadings in composite membranes containing PVDF homopolymers (Kynar® PVDF 500 and 731). However, in order to support any conclusive remarks, conductivity data from composite membranes was subjected to statistical analysis using an unbalanced general linear model (GLM). The initial global analysis of conductivity (3-way GLM) revealed statistically significant effects of nanoparticle concentration ($F_{(2,1181)} = 54.07$, $p < 0.001$); nanoparticle type ($F_{(2,1181)} = 20.64$, $p < 0.001$), presumably related with dissimilar acidity among the different zirconium-based nanoparticles; and PVDF grade ($F_{(4,1181)} = 172.58$, $p < 0.001$). Figure 4.15 shows plots of unweighted means of proton conductivity (from the GLM analysis) for the composite membranes as function of nanoparticle type and nanoparticle mass fraction (both identified as significant factors). The effect of the latter is promptly seen as the lowest unweighted mean of

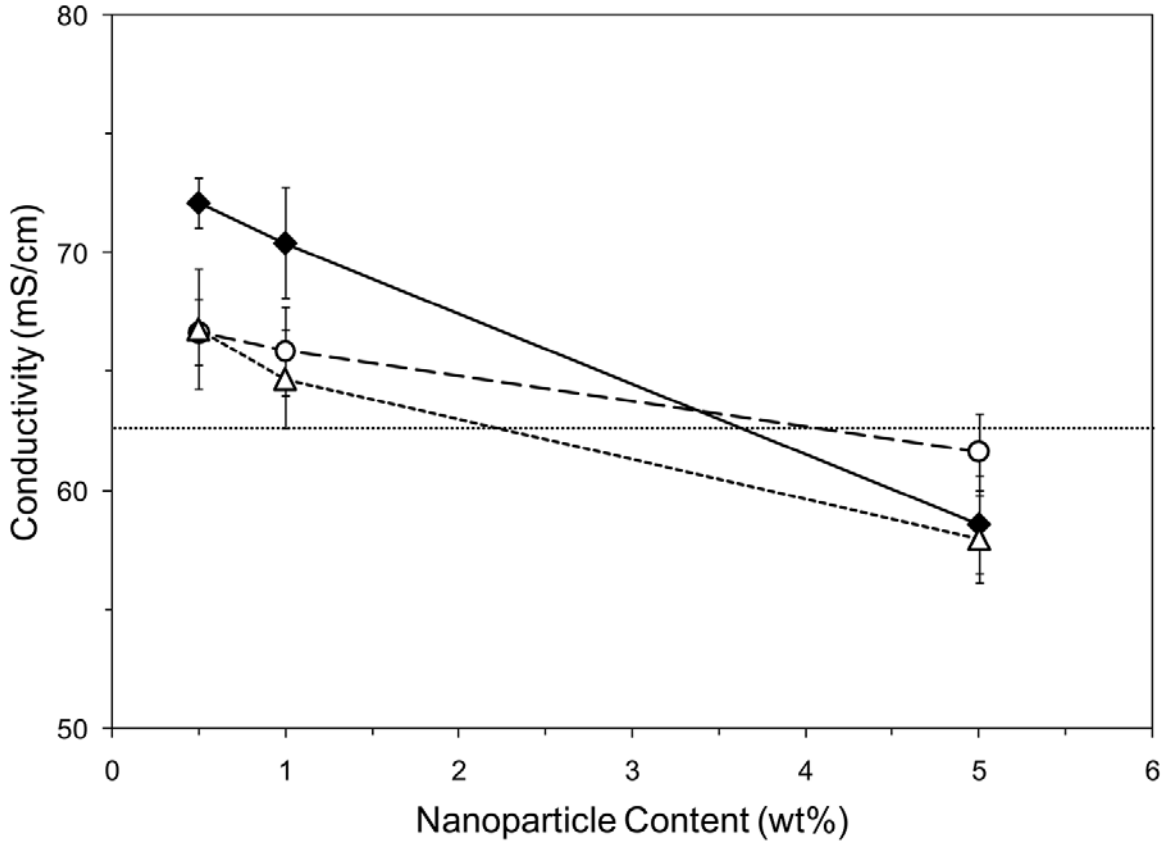

Figure 4.10 Proton conductivity of PVDF/PE/ZrX composite membranes (ZrHP ◆, ZrO ○, ZrS △) based on Kynar® 500 (PVDF homopolymer). The horizontal dotted line (.....) represents the reference non-hybrid PVDF/PE membrane for the corresponding PVDF grade. Testing conditions: 18.2 MΩ water at 25°C. Values are presented as averages ± 95% confidence intervals.

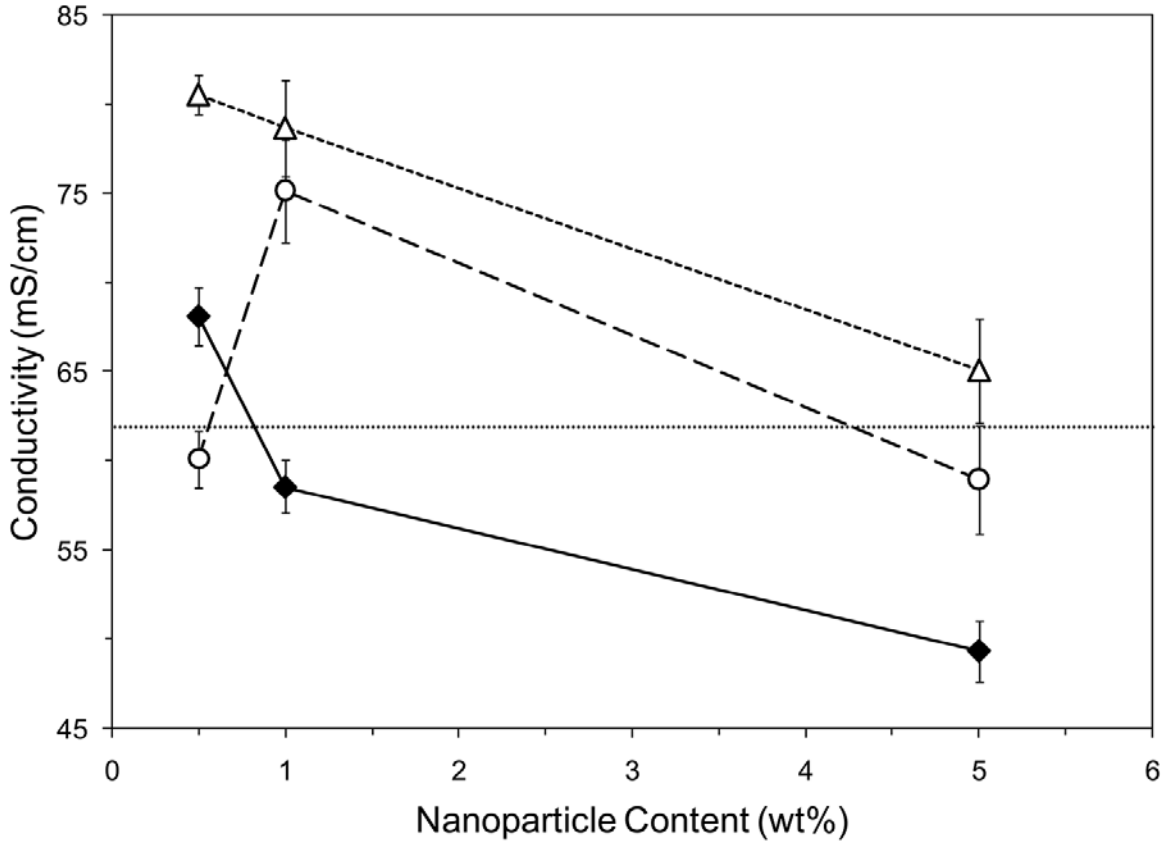

Figure 4.11 Proton conductivity of PVDF/PE/ZrX composite membranes (ZrHP ◆, ZrO ○, ZrS △) based on Kynar® 731 (PVDF homopolymer). The horizontal dotted line (.....) represents the reference non-hybrid PVDF/PE membrane for the corresponding PVDF grade. Testing conditions: 18.2 MΩ water at 25°C. Values are presented as averages ± 95% confidence intervals.

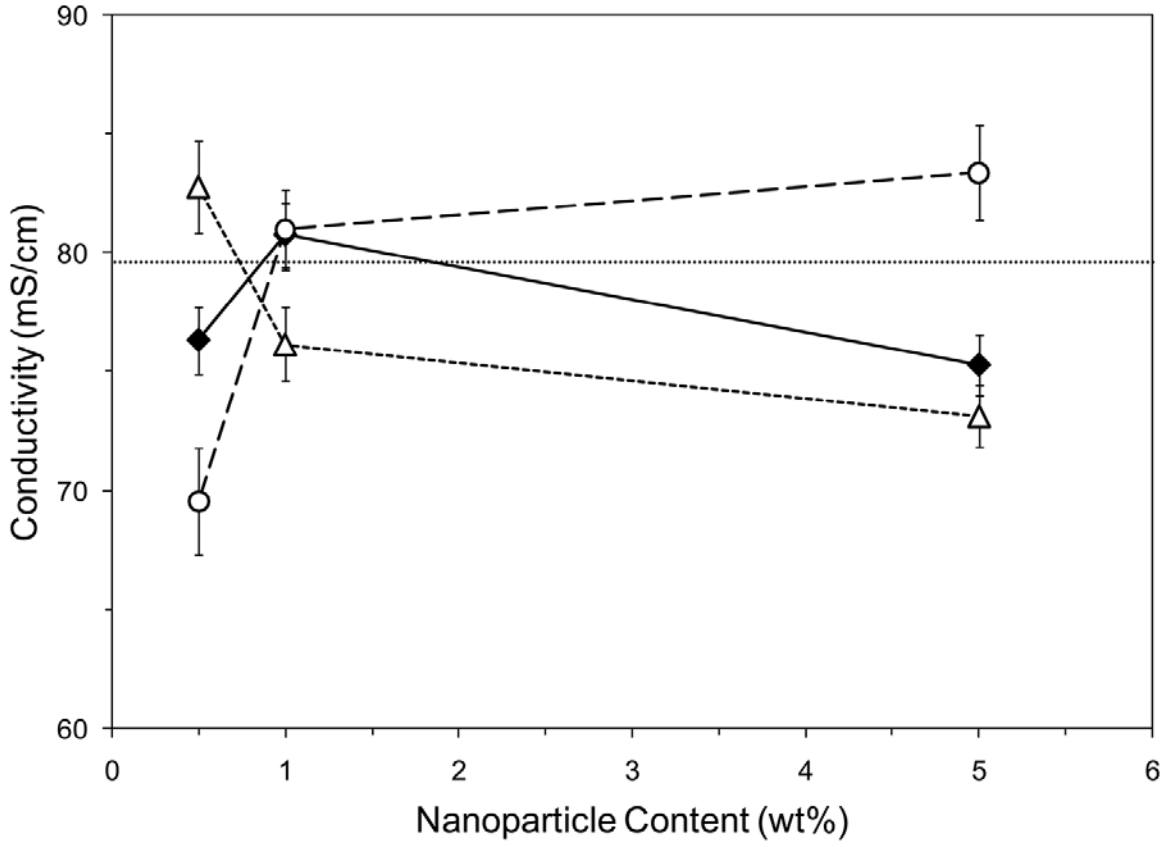

Figure 4.12 Proton conductivity of PVDF/PE/ZrX composite membranes (ZrHP ◆, ZrO ○, ZrS △) based on Kynar® 2801 (PVDF:HFP copolymer). The horizontal dotted line (.....) represents the reference non-hybrid PVDF/PE membrane for the corresponding PVDF grade. Testing conditions: 18.2 MΩ water at 25°C. Values are presented as averages ± 95% confidence intervals.

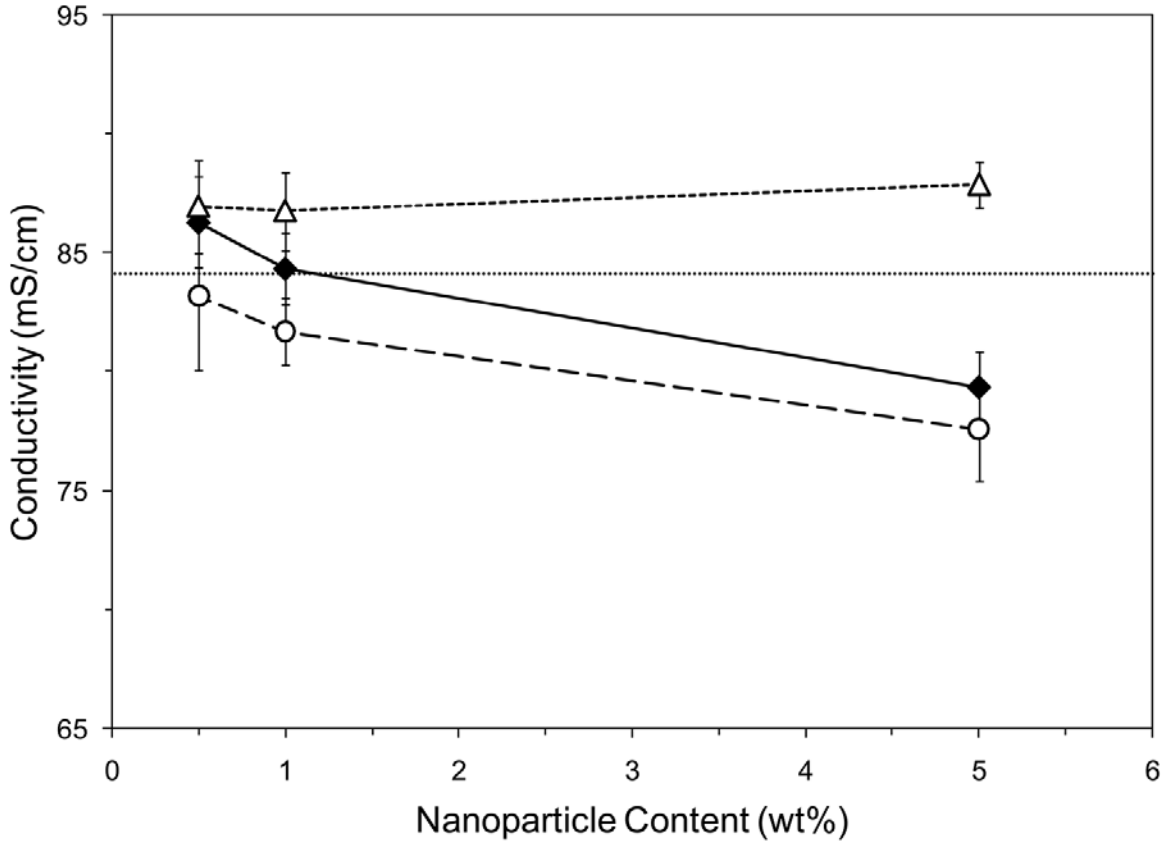

Figure 4.13 Proton conductivity of PVDF/PE/ZrX composite membranes (ZrHP ◆, ZrO ○, ZrS △) based on Kynar® 2821 (PVDF:HFP copolymer). The horizontal dotted line (.....) represents the reference non-hybrid PVDF/PE membrane for the corresponding PVDF grade. Testing conditions: 18.2 MΩ water at 25°C. Values are presented as averages ± 95% confidence intervals.

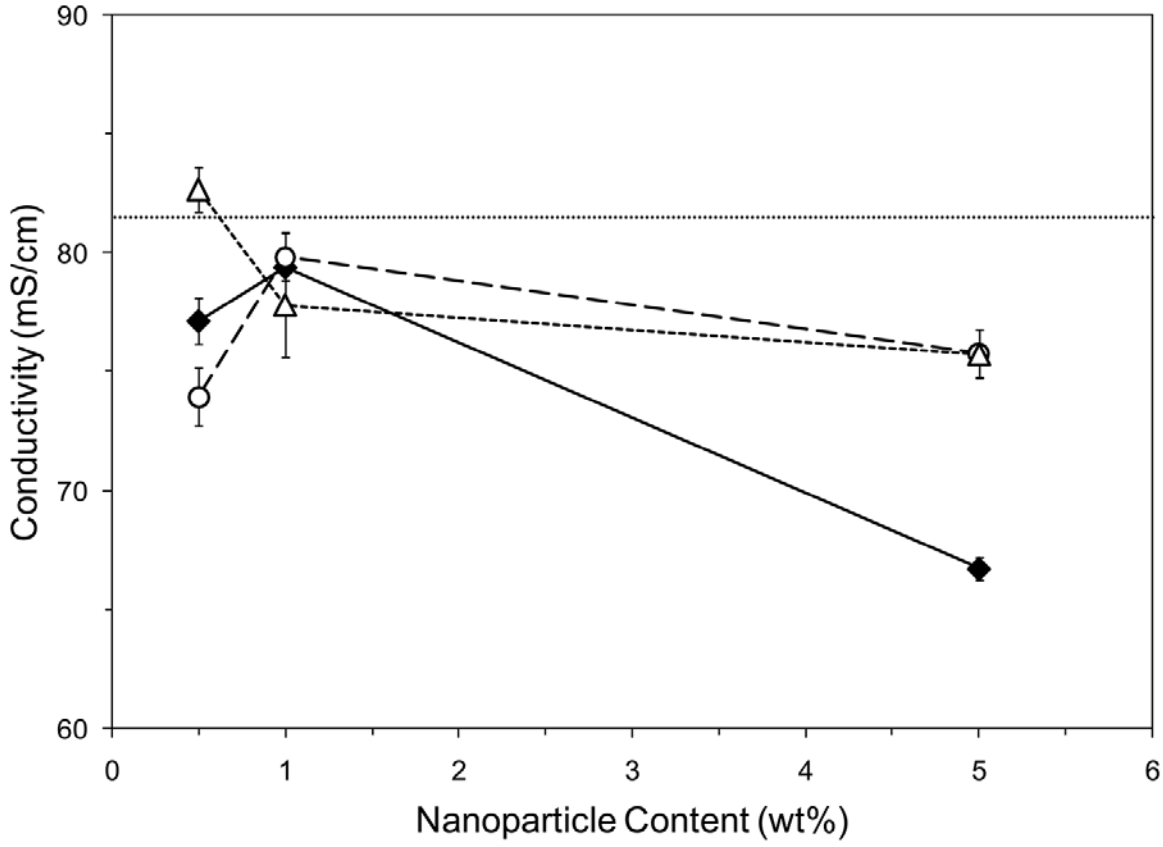

Figure 4.14 Proton conductivity of PVDF/PE/ZrX composite membranes (ZrHP ◆, ZrO ○, ZrS △) based on Kynar® 2851 (PVDF:HFP copolymer). The horizontal dotted line (.....) represents the reference non-hybrid PVDF/PE membrane for the corresponding PVDF grade. Testing conditions: 18.2 MΩ water at 25°C. Values are presented as averages ± 95% confidence intervals.

conductivity corresponds to a nanoparticle loading of 5wt%, supporting the abovementioned reduction in conductivity ascribed to aggregation of the solid phase at high nanoparticle contents. In addition, a slight overall net gain in conductivity (2-3%) with respect to non-hybrid PVDF/PE references is noticed for composite membranes containing 0.5wt% and 1wt% zirconium-based additives (Figure 4.15, right). A clear variation in mean conductivity according to nanoparticle type is evidenced as well (Figure 4.15, left), with ZrS having a noticeable advantage over ZrO and ZrHP. This behavior is anticipated as the acidity of sulfated zirconia solids is among the strongest of all known solid superacids (Hammet acidity function $H_0 \leq -16.04$) [12, 23, 37, 38]. Moreover, the small difference in conductivity noticed between ZrO- and ZrHP-based membranes is in agreement with a slightly improved conductivity observed in ZrO solid acid conductors compared to ZrHP [13].

In a recent study performed over 80 different proton exchange membranes of PVDF/PE blends we determined that proton conductivity is not completely decoupled from the inert PVDF phase, and that a direct relationship between conductivity and the crystalline characteristics of the PVDF exists [8]. Particularly, membranes containing PVDF homopolymers with high crystallinity and big crystallites had lower proton conductivity. To explain this effect we proposed that sizeable dense PVDF regions, arising from the melting of highly concentrated large crystallites in the homopolymer-based matrix during membrane crosslinking, precluded the segmental motion and rearrangement of PE chains. This in turn resulted in a semi-interpenetrated network with less branched proton conducting channels; and thus, reduced conductivity

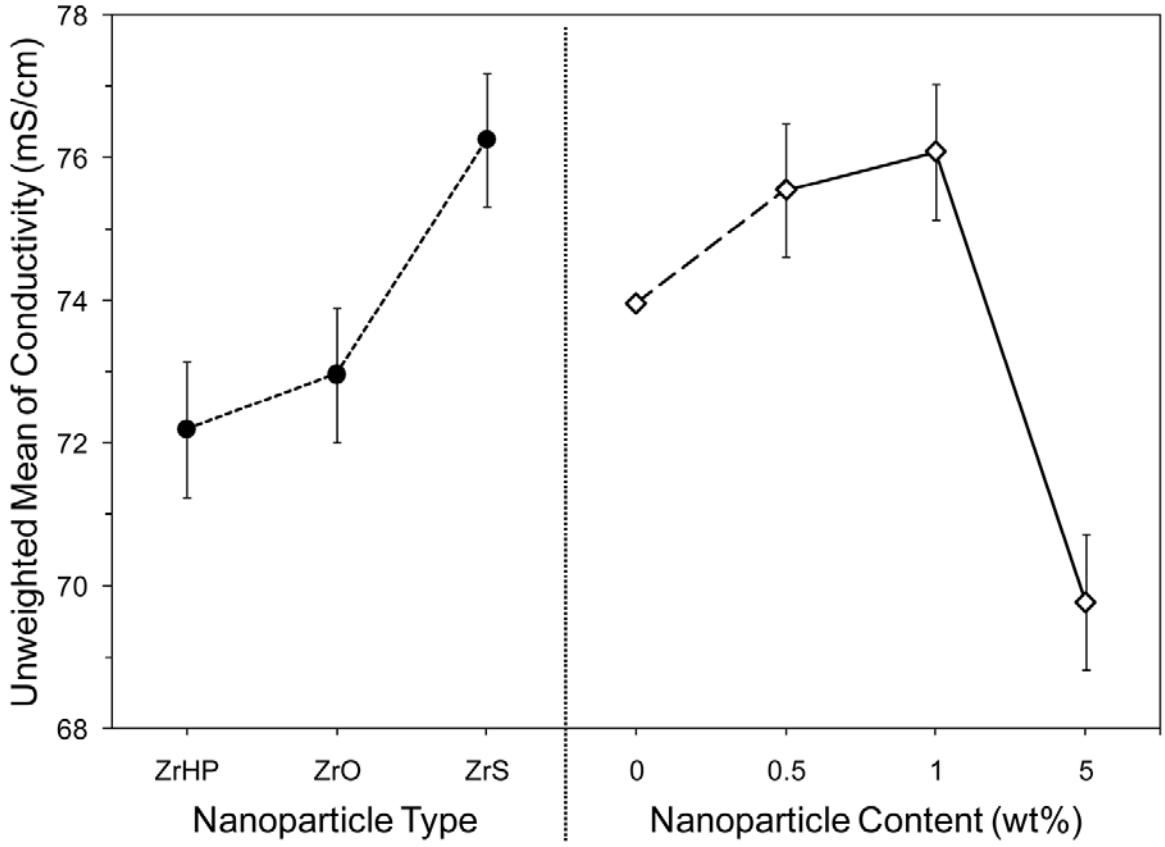

Figure 4.15 Global unweighted means of conductivity, estimated from and 3-way univariate unbalanced GLM analysis (full factorial model), as a function of nanoparticle type (left) and nanoparticle content (right). Error bars represent the upper and lower bounds of 95% confidence intervals.

(Figure 4.16). Interestingly, statistically significant (2-way GLM by PVDF type, $p < 0.05$) conductivity increments resulting from the addition of zirconium-based acid inorganic fillers to PVDF/PE blends occurred *only* in membranes containing PVDF homopolymers (at low and medium nanoparticle loadings) (Figure 4.10 and Figure 4.11). Specifically, membranes based on Kynar® 500 exhibited overall conductivity increments of 9.5% and 7%, while those containing Kynar® 731 showed improvements of 12.4% and 14.3% at nanoparticle contents of 0.5wt% and 1wt%, respectively (comparison of unweighted means from independent 2-way GLM). Surface proton transport is the dominant transport mechanism in solid acids [13] owing to exposed acid sites on the surface of the solid that constitute hydrophilic centers for hydrogen bonding and dipole-dipole interactions, and allow the formation of a water layer around the particle where water assisted transport is likely to be take place (increase in the concentration of mobile protons). Therefore, the increase in conductivity observed in PVDF homopolymer-based composite membranes is presumably explained by a "healing" effect resulting from proton-conducting paths provided by the hydration layer of the nanoparticles that link non-connected PE channels (Figure 4.17). The reason why the nanoparticle types responsible for the largest conductivity increment in homopolymer -based composite membranes are different (i.e., ZrHP for Kynar® 500 and ZrS for Kynar® 731) is not completely understood. However, besides the aforementioned particle dispersion issues, it may be attributed to particle size effects and dissimilar PVDF-particle interactions as Kynar® 731, contrary to Kynar® 500, is *not* fully molten during the membrane crosslinking process [8].

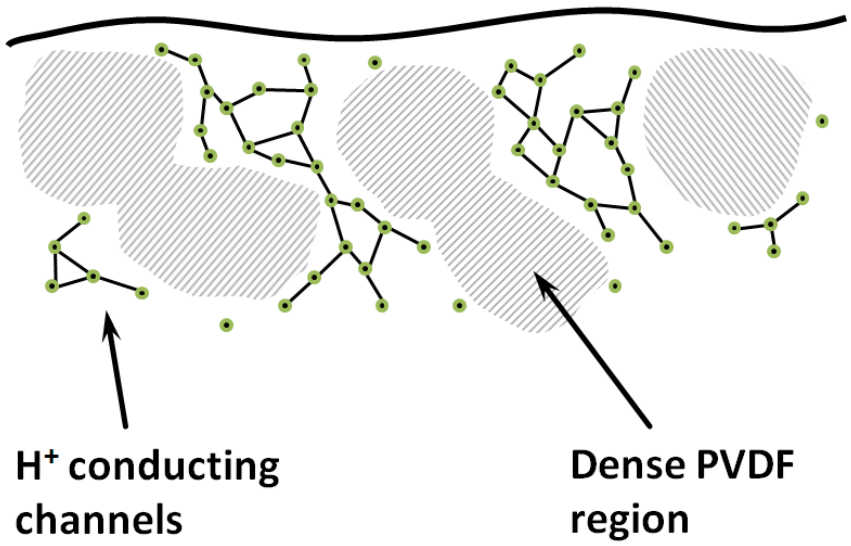

Figure 4.16 Cartoon schematic of the PVDF/PE membrane morphology after crosslinking and solvent evaporation (large dense PVDF regions are characteristic of highly crystalline PVDF homopolymers [8]).

Conductivity of PVDF:HFP copolymer-based composite membranes at low and medium nanoparticle loadings was either non-statistically significant (2-way GLM by PVDF type, $p > 0.05$) or slightly detrimental. The former case suggests that the insertion of zirconium-based additives does not considerably alter the local arrangement of water molecules, and therefore does not have an important effect in the overall membrane conductivity. A similar effect has been noticed in Nafion® membranes containing zirconium phosphate nanofiller, where the local dynamics of water molecules in the composite membrane is quite similar to that of simple hydrated Nafion®, so the dynamical properties of protons at a molecular level (i.e., proton jumping) remain

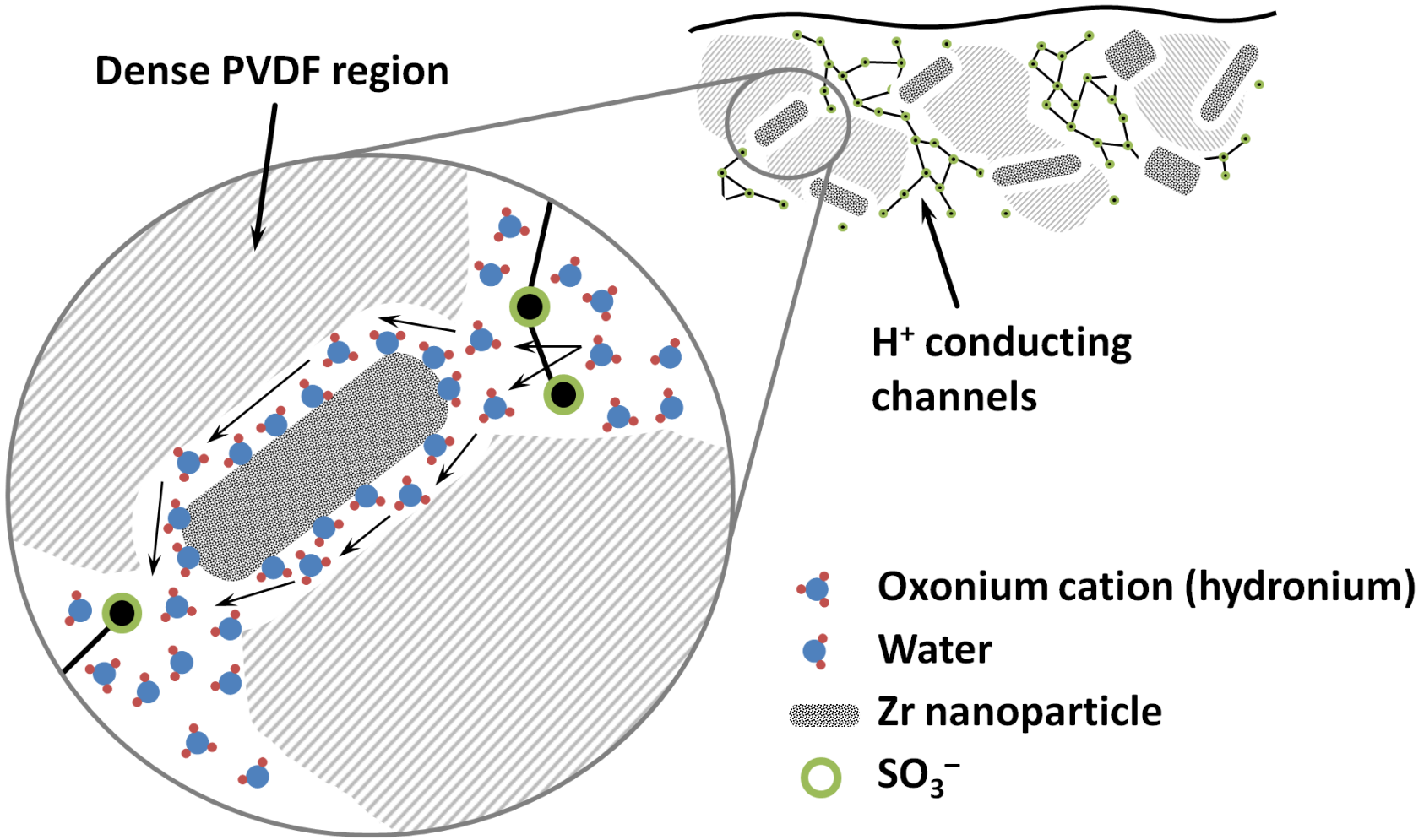

Figure 4.17 Cartoon representation of the effect of the incorporation of zirconium-based solid acid nanoparticles in PVDF/PE membranes. The zoomed area illustrates the Interconnection of separated proton-conducting channels by means of the hydration layer of nanoparticles embedded in dense PVDF regions ("healing" effect).

unchanged with the incorporation of the nanofiller [39]. The case of reduced conductivity may be explained by an increment of diffusional resistance as nanoparticles (or nanoparticle agglomerates) occupy the volume that would otherwise correspond to proton conducting channels. The lack of a defined trend of these conditions at different particle contents further emphasizes the suboptimal particle dispersion within the PVDF/PE matrices (even at low particle loadings) that was highlighted in the previous section; and stresses the need of particle compatibilization and/or pre-exfoliation approaches for the preparation of the composite membranes. Regarding the very few cases where high nanoparticle mass fraction resulted in enhanced conductivity, these might be explained by the fortuitous formation of particle-particle paths from contiguous nanoparticle agglomerates that connect the external faces of the membrane.

Besides the possibility of increasing mechanical strength and chemical stability, one of the main goals of incorporating solid acid particles in polymeric proton exchange membranes is to reduce the susceptibility of the membranes to changes in the degree of hydration, and improve their performance at intermediate operation temperatures (100-200°C). However, as of now, our HTC conductivity screening system unfortunately does not have the capability of performing readings at high temperatures; thus conductivity measurements of the PVDF/PE/ZrX composite membranes are limited to the room temperature values presented. Hardware modifications to equip the system with high temperature operating capabilities are being considered.

4.3.3 Mechanical properties

Controlling the amount of inorganic additives and their degree of dispersion in a polymer matrix are fundamental factors leading to adequate mechanical properties of composite membranes in terms of flexibility and tear strength. Consequently, mechanical characterization of the composite membranes focused on two variables; namely, elastic modulus and toughness. It is important to underline that contrary to uniaxial deformation, typical of conventional mechanical characterization systems, membranes undergo axisymmetric biaxial deformation in HTMECH tests. Therefore care must be taken if the results presented herein are to be compared to uniaxial tensile tests, as differences in mechanical response should be expected between both deformation models.

The corresponding profiles of elastic modulus and toughness of the composite membranes as a function of nanoparticle mass fraction are shown in Figure 4.18 through Figure 4.27. A statistical analysis akin to that performed for proton conductivity revealed significant effects of nanoparticle content ($F_{(2,1105)} = 37.19$, $p < 0.001$), nanoparticle type ($F_{(2,1105)} = 11.3$, $p < 0.001$), and PVDF grade ($F_{(4,1105)} = 249.52$, $p < 0.001$) on membrane elastic modulus; however, the "practical" effect of nanoparticle content and type is weak in comparison to the effect of PVDF grade ($\eta_p^2 \leq 0.06$ vs. $\eta_p^2 = 0.48$, η_p^2: partial eta squared statistic). This is expected as the PVDF support matrix confers the tensile properties to the membranes. Likewise, significant effects of nanoparticle content ($F_{(2,1105)} = 221.58$, $p < 0.001$), nanoparticle type ($F_{(2,1105)} = 129.94$, $p < 0.001$), and PVDF grade ($F_{(4,1105)} = 66.05$, $p < 0.001$) on membrane toughness were identified; however, contrary to

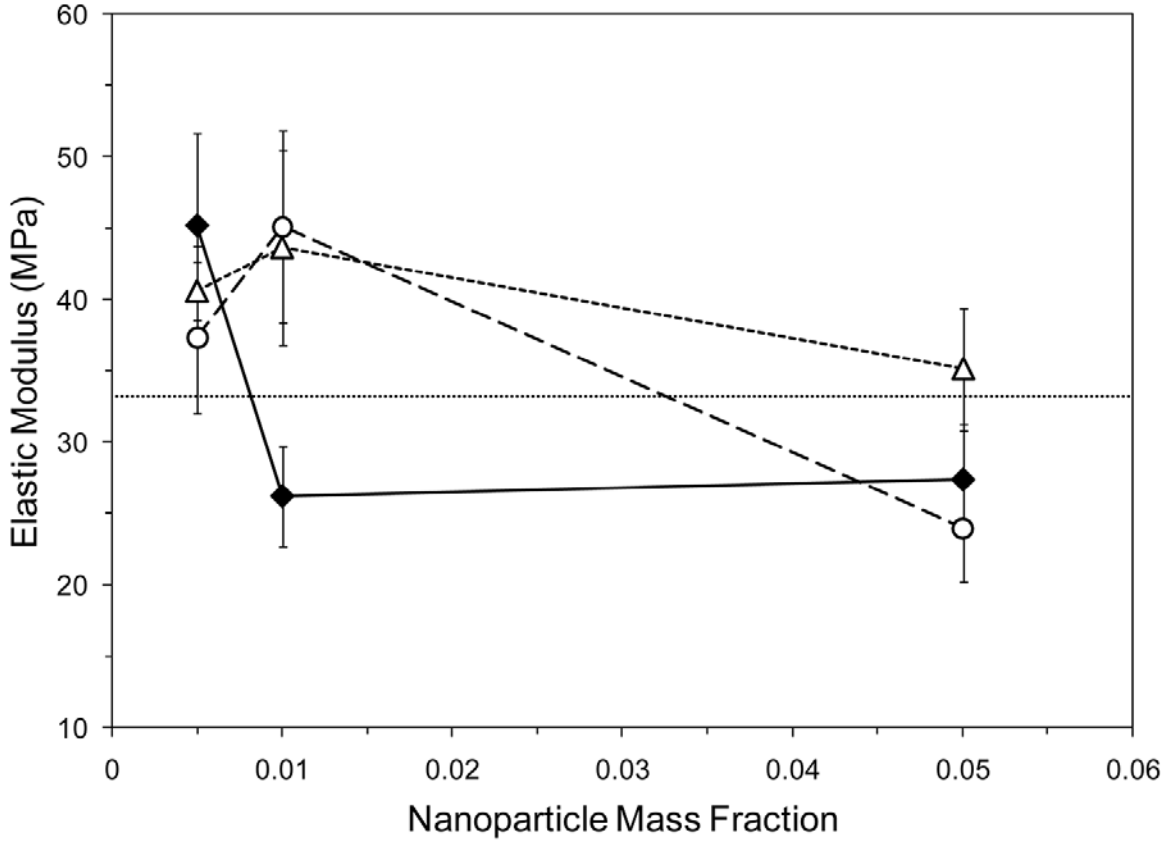

Figure 4.18 Elastic modulus (biaxial) of PVDF/PE/ZrX composite membranes (ZrHP ◆, ZrO ○, ZrS △) based on Kynar® 500 (PVDF homopolymer). The horizontal dotted line (·····) represents the reference non-hybrid PVDF/PE membrane for the corresponding PVDF grade. Values are presented as averages ± 95% confidence intervals.

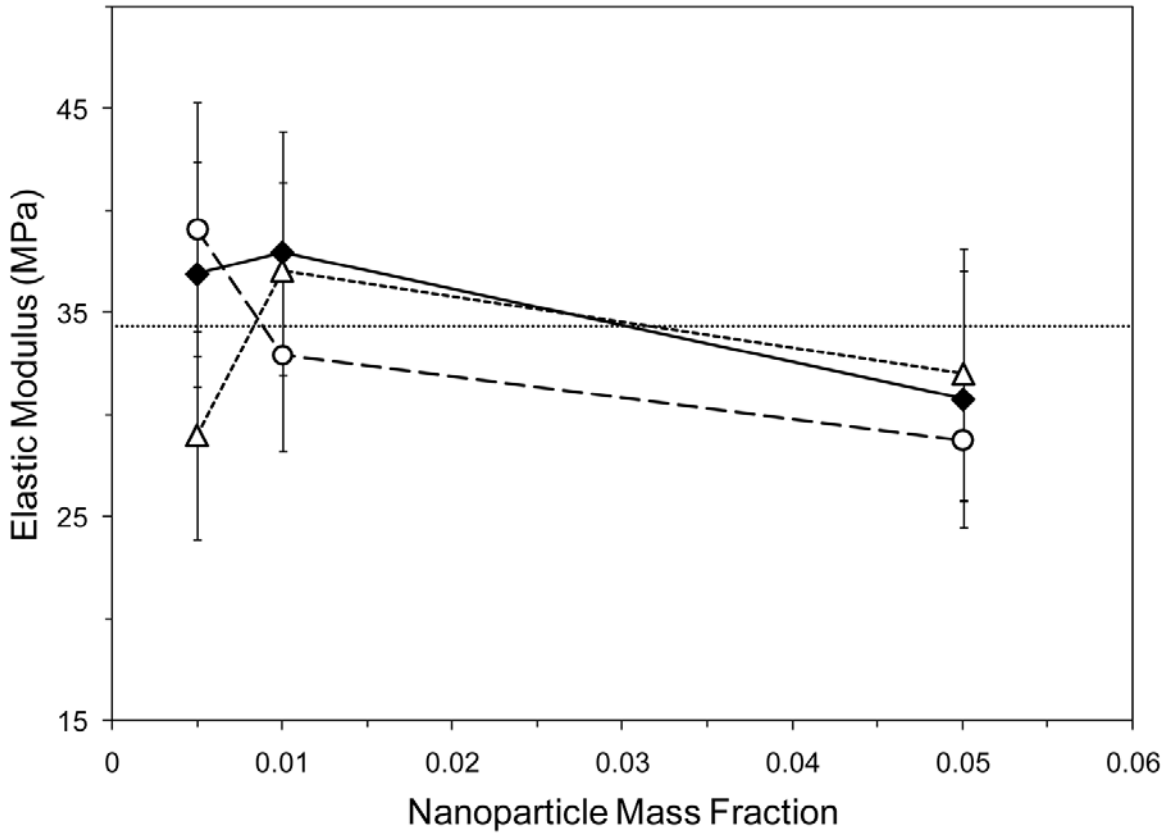

Figure 4.19 Elastic modulus (biaxial) of PVDF/PE/ZrX composite membranes (ZrHP ◆, ZrO ○, ZrS △) based on Kynar® 731 (PVDF homopolymer). The horizontal dotted line (·····) represents the reference non-hybrid PVDF/PE membrane for the corresponding PVDF grade. Values are presented as averages ± 95% confidence intervals.

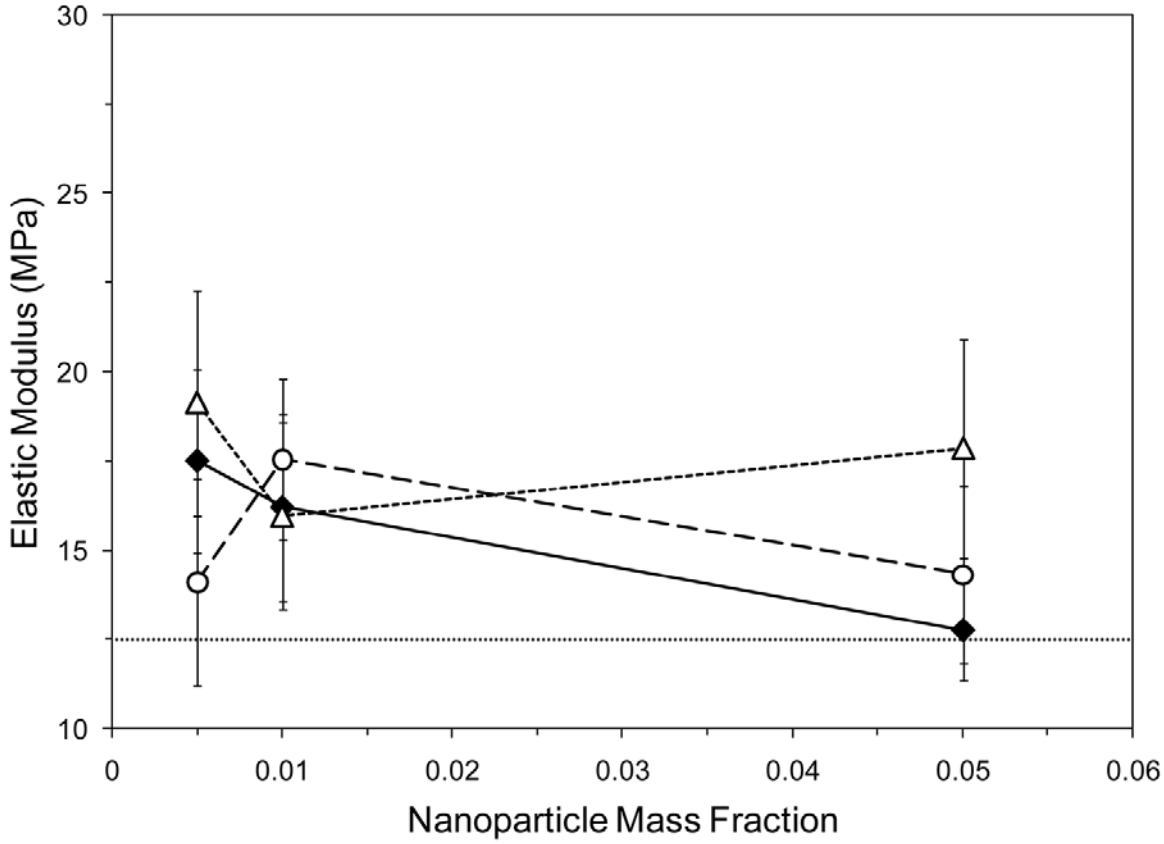

Figure 4.20 Elastic modulus (biaxial) of PVDF/PE/ZrX composite membranes (ZrHP ◆, ZrO ○, ZrS △) based on Kynar® 2801 (PVDF:HFP copolymer). The horizontal dotted line (·····) represents the reference non-hybrid PVDF/PE membrane for the corresponding PVDF grade. Values are presented as averages ± 95% confidence intervals.

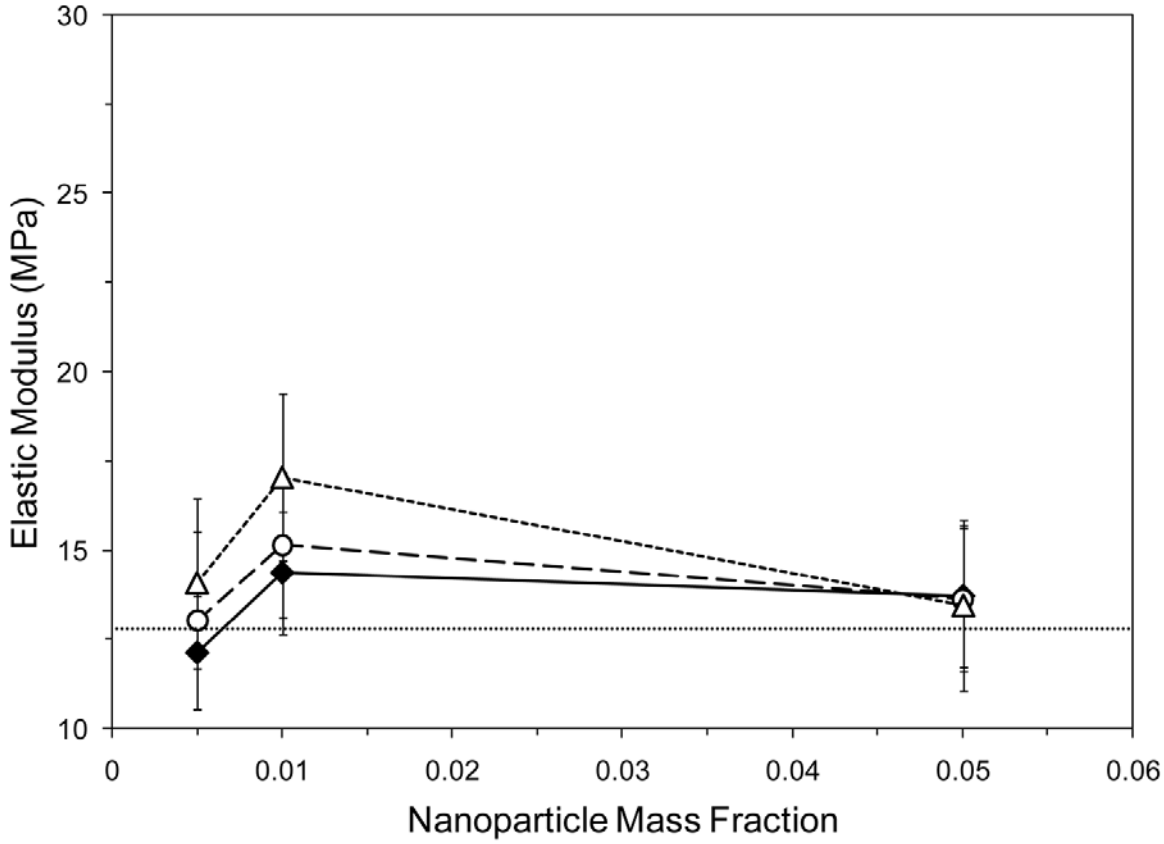

Figure 4.21 Elastic modulus (biaxial) of PVDF/PE/ZrX composite membranes (ZrHP —◆—, ZrO —○—, ZrS - -△- -) based on Kynar® 2821 (PVDF:HFP copolymer). The horizontal dotted line (·····) represents the reference non-hybrid PVDF/PE membrane for the corresponding PVDF grade. Values are presented as averages ± 95% confidence intervals.

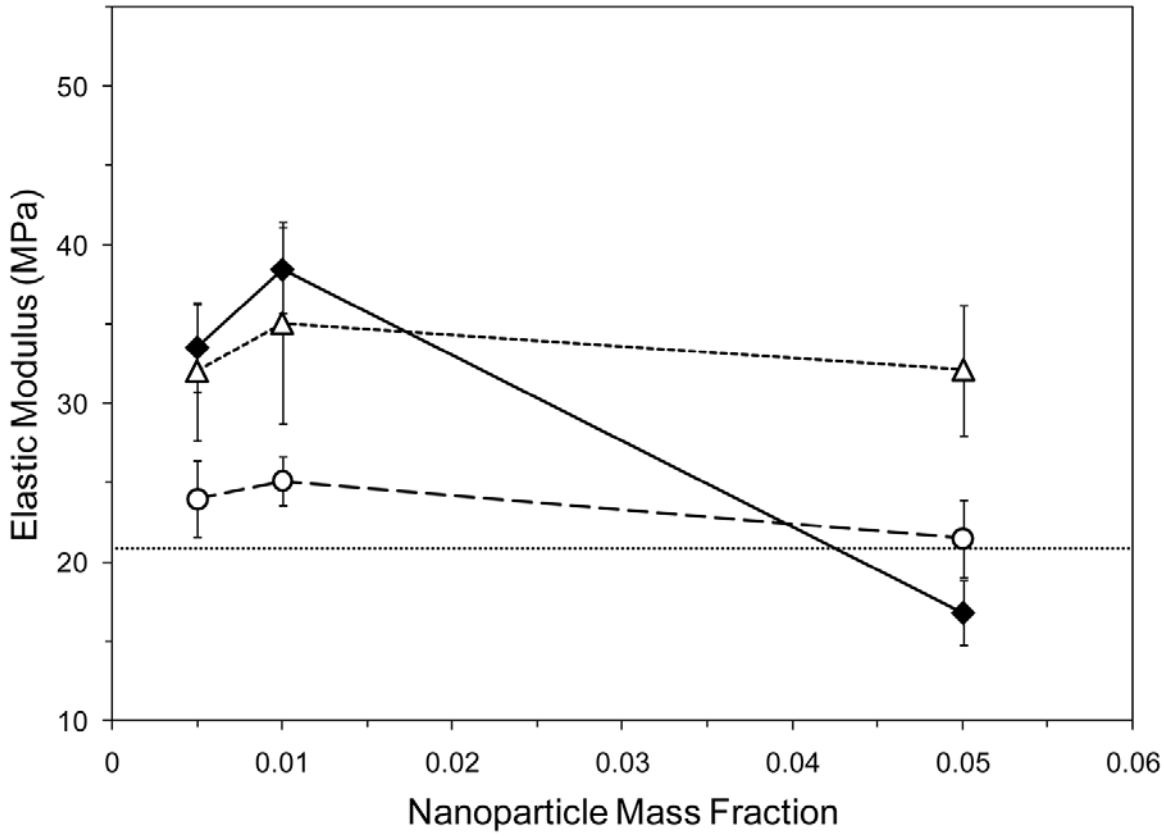

Figure 4.22 Elastic modulus (biaxial) of PVDF/PE/ZrX composite membranes (ZrHP —◆—, ZrO —○—, ZrS -△-) based on Kynar® 2851 (PVDF:HFP copolymer). The horizontal dotted line (·····) represents the reference non-hybrid PVDF/PE membrane for the corresponding PVDF grade. Values are presented as averages ± 95% confidence intervals.

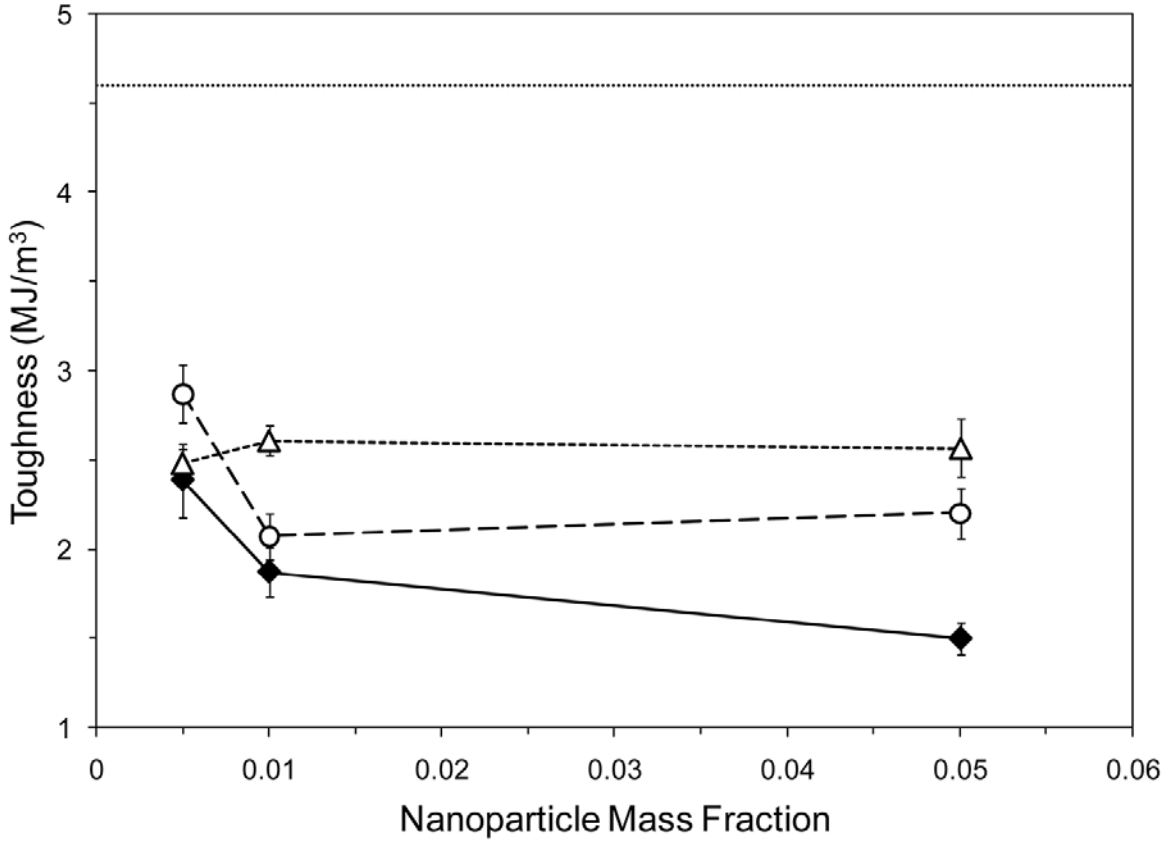

Figure 4.23 Toughness (biaxial) of PVDF/PE/ZrX composite membranes (ZrHP ◆, ZrO ○, ZrS △) based on Kynar® 500 (PVDF homopolymer). The horizontal dotted line (.....) represents the reference non-hybrid PVDF/PE membrane for the corresponding PVDF grade. Values are presented as averages ± 95% confidence intervals.

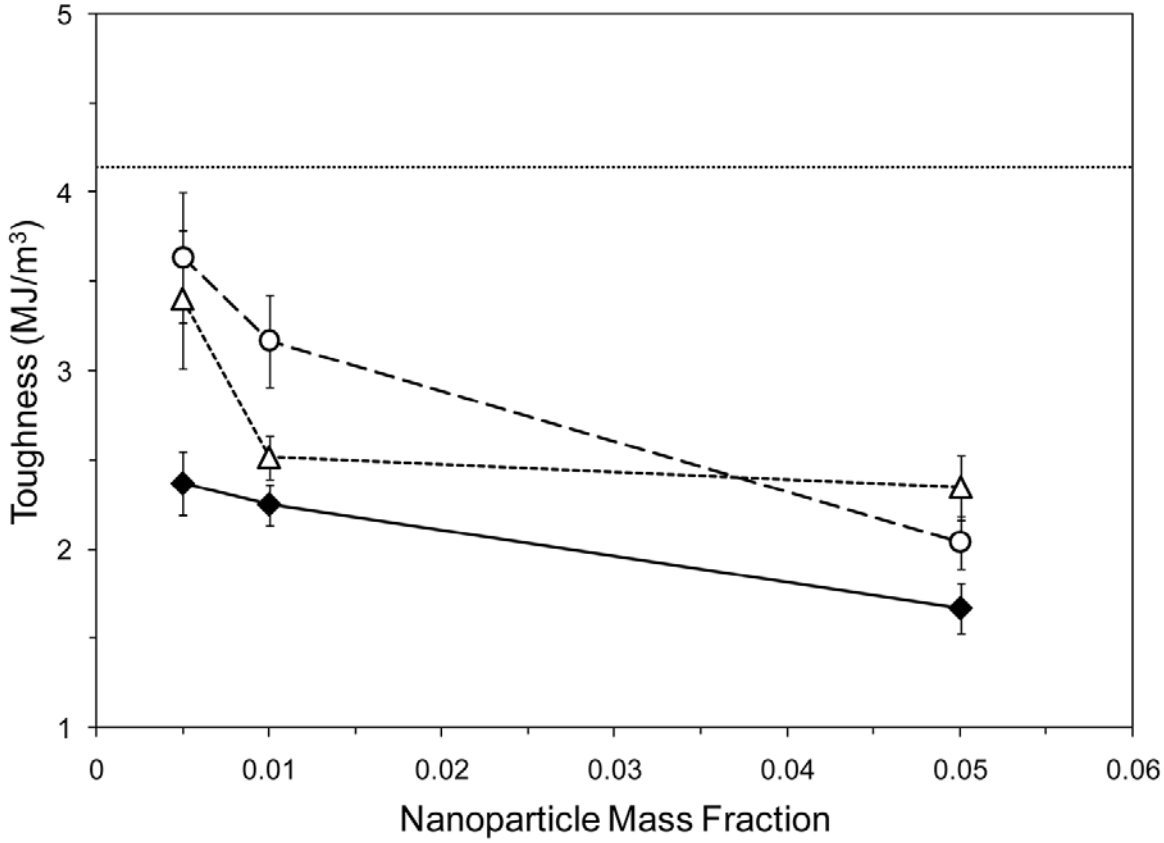

Figure 4.24 Toughness (biaxial) of PVDF/PE/ZrX composite membranes (ZrHP ◆, ZrO ○, ZrS △) based on Kynar® 731 (PVDF homopolymer). The horizontal dotted line (.....) represents the reference non-hybrid PVDF/PE membrane for the corresponding PVDF grade. Values are presented as averages ± 95% confidence intervals.

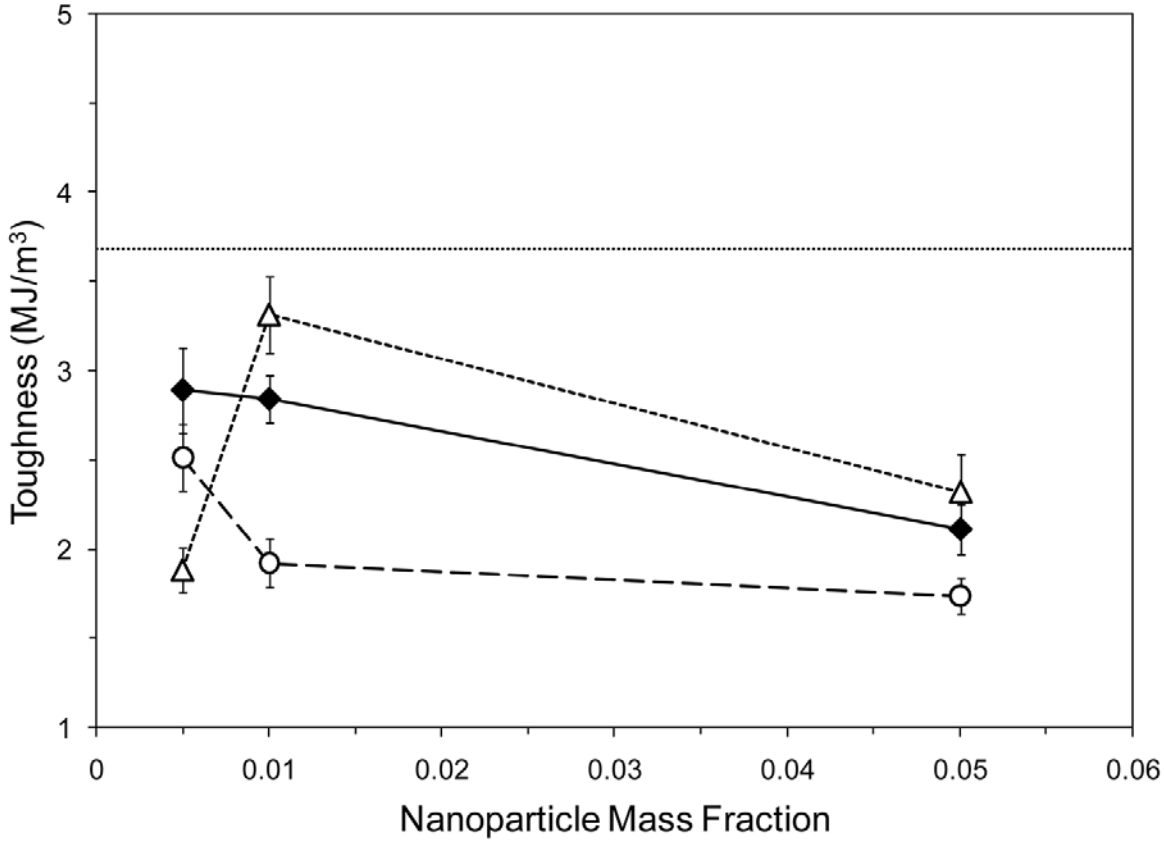

Figure 4.25 Toughness (biaxial) of PVDF/PE/ZrX composite membranes (ZrHP ◆, ZrO ○, ZrS △) based on Kynar® 2801 (PVDF:HFP copolymer). The horizontal dotted line (.....) represents the reference non-hybrid PVDF/PE membrane for the corresponding PVDF grade. Values are presented as averages ± 95% confidence intervals.

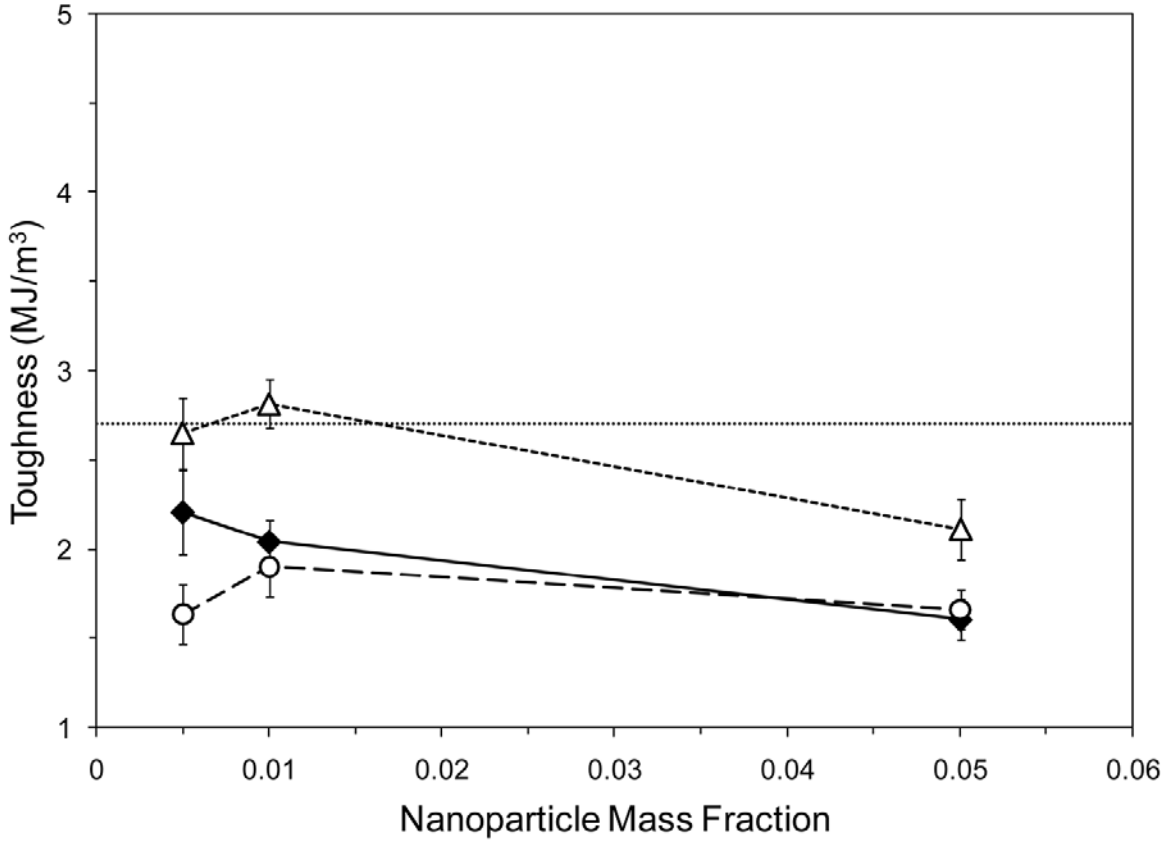

Figure 4.26 Toughness (biaxial) of PVDF/PE/ZrX composite membranes (ZrHP ◆, ZrO ○, ZrS △) based on Kynar® 2821 (PVDF:HFP copolymer). The horizontal dotted line (.....) represents the reference non-hybrid PVDF/PE membrane for the corresponding PVDF grade. Values are presented as averages ± 95% confidence intervals.

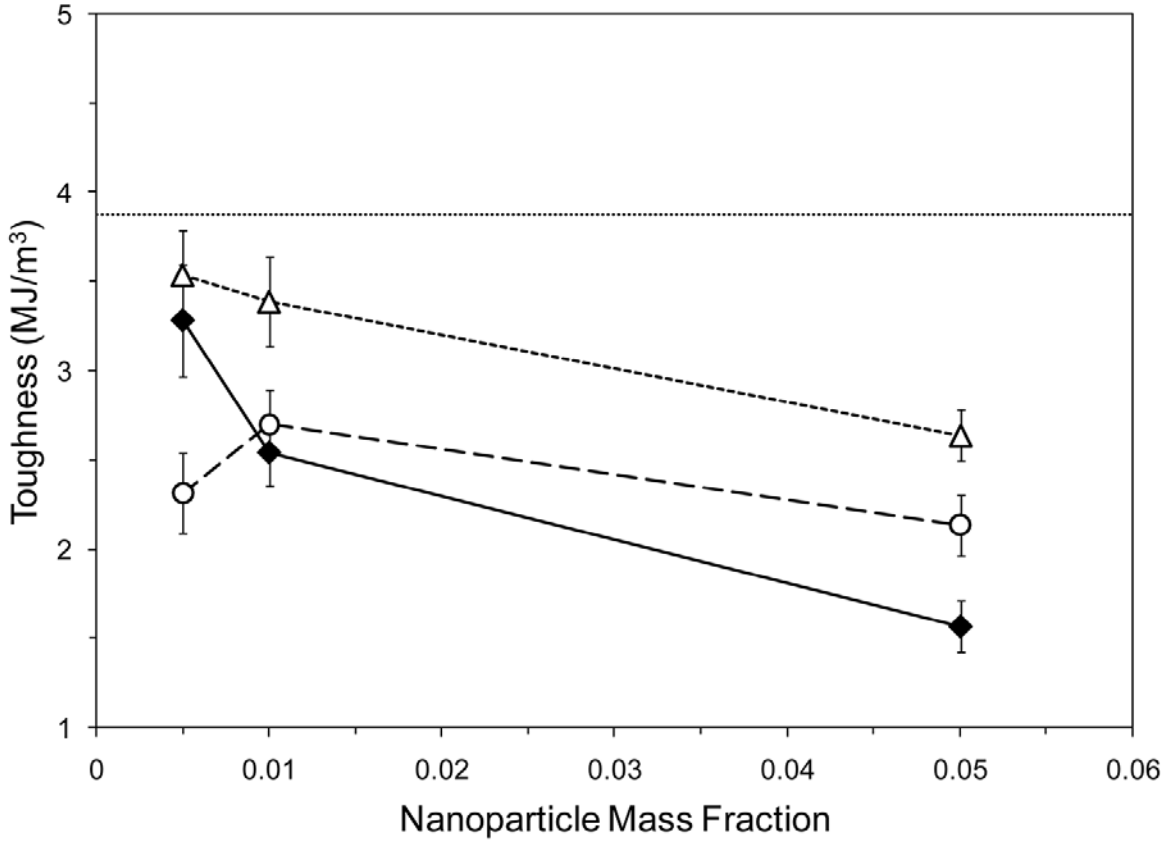

Figure 4.27 Toughness (biaxial) of PVDF/PE/ZrX composite membranes (ZrHP ◆, ZrO ○, ZrS △) based on Kynar® 2851 (PVDF:HFP copolymer). The horizontal dotted line (.....) represents the reference non-hybrid PVDF/PE membrane for the corresponding PVDF grade. Values are presented as averages ± 95% confidence intervals.

their effect on the membrane elastic modulus, the nanoparticle type and content have an important effect on toughness. Generally the size of nanoparticles is too small to provide toughening through a crack-bridging mechanism, and they cannot effectively enhance crack trajectory tortuosity [40]; therefore, the strong effect of nanoparticle type and content on toughness may be directly related with factors such as membrane stiffening and/or defect sites arising from the insertion of nanoparticles.

Despite the reduced effect of nanoparticle content on the membrane elastic modulus, an apparently reinforcing effect in comparison to non-hybrid membranes is evidenced at low to medium particle loadings. The effect is especially manifest in composite membranes containing flexible PVDF:HFP copolymers (statistically significant, 2-way GLM by PVDF type, $p < 0.05$), thus suggesting an increment in membrane stiffness. On the contrary, toughness diminished for all composite membranes at all nanoparticle contents (statistically significant, 2-way GLM by PVDF type, $p < 0.001$), presumably due to the abovementioned membrane stiffening and high density of membrane defects at high particle loadings due to solid-phase aggregation (Figure 4.5 through Figure 4.9). To further visualize the effect of inorganic zirconium-based nanofillers on the mechanical properties of composite membranes, the global unweighted means of elastic modulus and toughness are presented in Figure 4.28. A clear reinforcing stiffening effect with respect to reference PVDF/PE membranes, characterized by an overall elastic modulus increase of 19.5% and 22.5%, is evidenced at nanoparticle loadings of 0.5wt% and 1wt%, respectively. This stiffening correlates perfectly with an overall reduction in membrane toughness (29.7% and 33.4% decline)

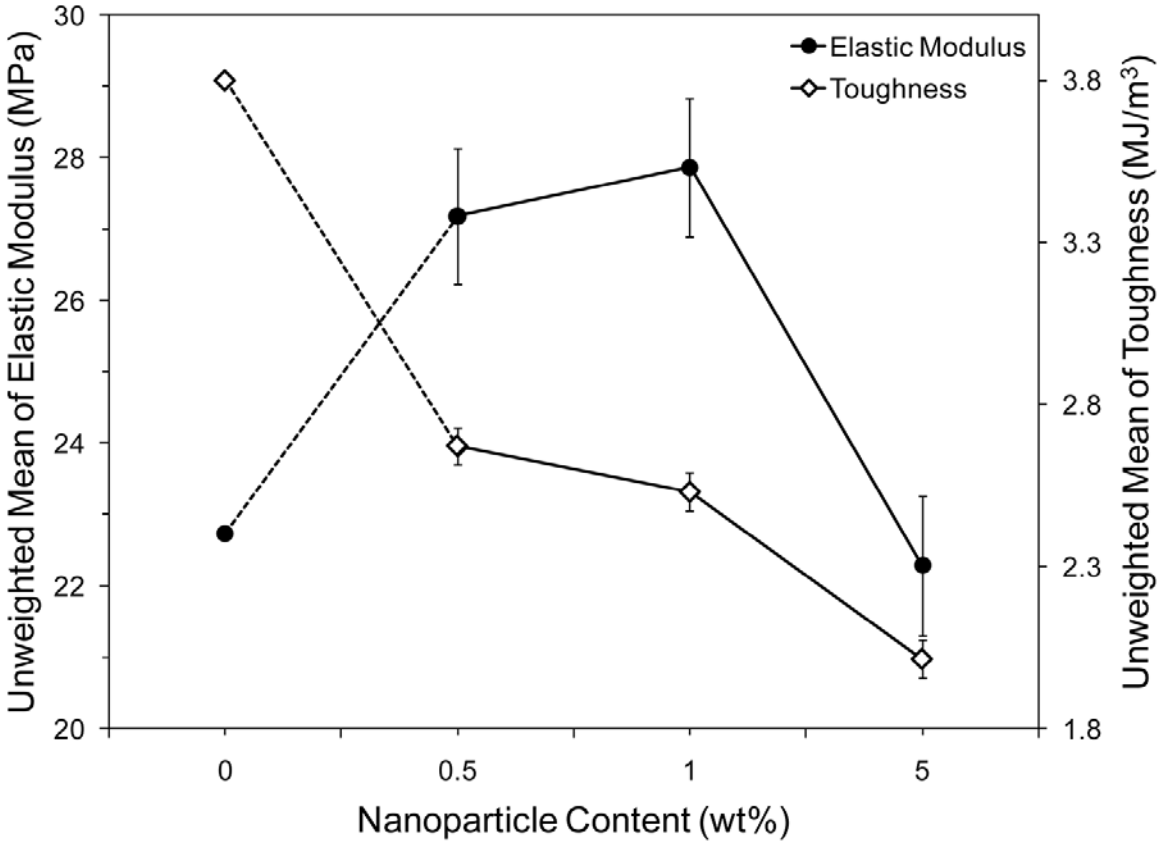

Figure 4.28 Global unweighted means of elastic modulus and toughness, estimated from 3-way univariate unbalanced GLM analysis (full factorial model), as a function of nanoparticle content. Error bars represent the upper and lower bounds of 95% confidence intervals.

at identical nanoparticle contents. These results are in accordance with the mechanical behavior observed in other organic/inorganic systems where nanocomposites stiffen efficiently but tend to fail prematurely as a result of toughness reduction [33, 40]. Moreover, similar outcomes have been observed in poly(arylene ether sulfone)-based polyelectrolyte systems that incorporate zirconium hydrogen phosphate nanoparticles [15].

The abrupt reduction in the overall elastic modulus (22.5% increase to 2% decrease) and further toughness decline (33.4% to 46.9% reduction) at the transition from medium to high nanoparticle loadings, confirms the formation of membrane defects derived from particle agglomerates that adversely affect the energy absorption capability of the membrane during mechanical deformation.

4.4 Conclusions

Proton-conducting tri-phase composite membranes were fabricated by incorporating zirconium oxide, zirconium hydroxide sulfated, and zirconium hydrogenphosphate nanoparticles to polymeric blends of numerous PVDF grades and a crosslinked sulfonated acrylic polyelectrolyte. The proton conductivity and mechanical properties of the membranes were assayed by means of custom designed electrochemical impedance spectroscopy and biaxial axisymmetric deformation high-throughput screening tools. Compared to non-hybrid PVDF/PE reference membranes, the resulting composite membranes exhibited overall improved conductivity at low to

medium particle loadings. A particular beneficial effect in conductivity from the added nanofillers was observed in composite membranes prepared from highly crystalline PVDF homopolymers (i.e., Kynar® 500 and 731), where the hydration layer of the embedded nanoparticles constituted a proton-conducting route that allowed the interconnection of PE channels previously separated by dense PVDF areas resulting from large PVDF crystallites. Tensile properties were similarly enhanced by the insertion of inorganic nanofillers, especially in membranes containing more flexible PVDF:HFP copolymers (i.e., Kynar® 2801, 2821, and 2851) where a reinforcing stiffening effect was evident at low to medium nanoparticle loadings. This increment in the elastic modulus was, however, detrimental for membrane toughness throughout the whole range of PVDF grades and particle loadings. Nanoparticle dispersion was thermodynamically limited as unfavorable particle-polymer interactions resulted in severe aggregation of the solid-phase at high particle contents. Since the degree of nanoparticle dispersion is critical for modulus and strength development, all mechanical properties were significantly lessened at high nanoparticle loadings. Proton conductivity was similarly affected since instead of providing an internal scaffold that stabilizes and enhance the ionic cluster volume, aggregated nanoparticles resulted in increased diffusional resistance by occupying the volume otherwise corresponding to proton-conducting channels.

As a proof of concept of incorporating proton-conducting inorganic nanofillers to non-covalently linked polymer blends, the results obtained herein are encouraging. Addressing particle dispersion issues, as well as critical concentration, by perhaps

forming pre-dispersed zirconium-based particle gels in NMP that are compatible with both the PVDF and neutralized PE solutions; and using acrylic polyelectrolytes of significantly lower equivalent weight and higher conductivity [8], may result in promising alternative cost-effective proton exchange membranes.

4.5 References

1. Barbir, F., *Transition to renewable energy systems with hydrogen as an energy carrier.* Energy, 2009. **34**: p. 308-312.

2. Neef, H.-J., *International overview of hydrogen and fuel cell research.* Energy, 2009. **34**: p. 327-333.

3. U.S. Department of Energy Office of Science, *Basic Research Needs for the Hydrogen Economy: Report of the Basic Energy Sciences Workshop on Hydrogen Production, Storage, and Use.* 2004. p. 178.

4. Sopian, K. and Daud, W.R.W., *Challenges and future developments in proton exchange membrane fuel cells.* Renewable Energy, 2006. **31**: p. 719-727.

5. Hickner, M.A., et al., *Alternative Polymer Systems for Proton Exchange Membranes (PEMs).* Chemical Reviews, 2004. **104**: p. 4587-4612.

6. Dobrovol'skii, Y.A., et al., *Proton-Exchange Membranes for Hydrogen-Air Fuel Cells.* Russian Journal of General Chemistry, 2007. **77**(4): p. 766-777.

7. Meier-Haack, J., et al., *Membranes from sulfonated block copolymers for use in fuel cells.* Separation and Purification Technology, 2005. **41**: p. 207-220.

8. Zapata, P. and Meredith, J.C., *High Throughput Study of Novel PVDF/Acrylic Polyelectrolyte Semi-Interpenetrated Network Proton Exchange Membranes.* To be submitted for publication, 2009.

9. Scherer, G.G., ed. *Fuel Cells I.* Advances in Polymer Science, ed. A. Abe, et al. Vol. 215. 2008, Springer-Verlag Berlin Heidelberg. 268.

10. Savadogo, O., *Emerging membranes for electrochemical systems Part II. High temperature composite membranes for polymer electrolyte fuel cell (PEFC) applications.* Journal of Power Sources, 2004. **127**: p. 135-161.

11. Neburchilov, V., et al., *A review of polymer electrolyte membranes for direct methanol fuel cells.* Journal of Power Sources, 2007. **169**: p. 221-238.

12. Thampan, T.M., et al., *Systematic Approach to Design Higher Temperature Composite PEMs.* Journal of The Electrochemical Society, 2005. **152**(2): p. A316-A325.

13. Hogarth, W.H.J., Costa, J.C.D.d., and Lu, G.Q.M., *Solid Acid Membranes for High Temperature (>140°C) Proton Exchange Membrane Fuel Cells.* Journal of Power Sources, 2005. **142**: p. 223-237.

14. Kim, J.-D., Mori, T., and Honma, I., *Organic–Inorganic Hybrid Membranes for a PEMFC Operation at Intermediate Temperatures.* Journal of The Electrochemical Society, 2006. **153**(3): p. A508-A514.

15. Hill, M.L., et al., *Zirconium hydrogen phosphate/disulfonated poly(arylene ether sulfone) copolymer composite membranes for proton exchange membrane fuel cells.* Journal of Membrane Science, 2006. **283**: p. 102-108.

16. Kuan, H.-C., et al., *Preparation of Exfoliated Zirconium Phosphate/Nafion Organic-Inorganic Hybrid Proton Exchange Membranes.* Electrochemical and Solid-State Letters, 2006. **9**(2): p. A76-A79.

17. Bi, C., et al., *Fabrication and investigation of SiO_2 supported sulfated zirconia/Nafion® self-humidifying membrane for proton exchange membrane fuel cell applications.* Journal of Power Sources, 2008. **184**: p. 197-203.

18. Tchicaya-Bouckary, L., Jones, D.J., and Rozière, J., *Hybrid Polyaryletherketone Membranes for Fuel Cell Applications.* Fuel Cells, 2002. **2**(1): p. 40-45.

19. Alberti, G., et al., *New Preparation Methods for Composite Membranes for Medium Temperature Fuel Cells Based on Precursor Solutions of Insoluble Inorganic Compounds.* Fuel Cells, 2005. **5**(3): p. 366-374.

20. Gaowen, Z. and Zhentao, Z., *Organic/inorganic composite membranes for application in DMFC.* Journal of Membrane Science, 2005. **261**: p. 107-113.

21. Alberti, G. and Casciola, M., *Composite membranes for Medium-Temperature PEM Fuel Cells.* Annual Review of Materials Research, 2003. **33**: p. 129-154.

22. Hogarth, W.H.J., et al., *Proton conductivity of mesoporous sol–gel zirconium phosphates for fuel cell applications.* Journal of Materials Chemistry, 2005. **15**: p. 754-758.

23. Tominaka, S., et al., *Sulfated zirconia nanoparticles as a proton conductor for fuel cell electrodes.* Journal of Power Sources, 2008. **185**: p. 656-663.

24. Zapata, P., Basak, P., and Meredith, J.C., *High-Throughput Screening of Ionic Conductivity in Polymer Membranes.* Electrochimica Acta, 2009. **10.1016/j.electacta.2009.02.009**.

25. Meredith, J.C., Karim, A., and Amis, E.J., *Combinatorial Methods for Investigations in Polymer Materials Science.* MRS Bulletin, 2002. **27**(4): p. 330-335.

26. Sormana, J.-L., Chattopadhyay, S., and Meredith, J.C., *High-throughput mechanical characterization of free-standing polymer films.* Review of Scientific Instruments, 2005. **76**: p. 062214.

27. Tatsumi, T., Matsuhashi, H., and Arata, K., *A Study of the Preparation Procedures of Sulfated Zirconia Prepared from Zirconia Gel. The Effect of the pH of the Mother Solution on the Isomerization Activity of n-Pentane.* Bulletin of the Chemical Society of Japan, 1996. **69**(5): p. 1191-1194.

28. Ludmány, A., et al., *Amorphous titanium hydrogenphosphate—an inorganic sorbent and a catalyst.* Applied Catalysis A: General, 2004. **267**: p. 149-156.

29. Kumar, G.G., et al., *Structural characterization of PVdF-HFP/PEG/Al_2O_3 proton conducting membranes for fuel cells.* Journal of Membrane Science, 2007. **303**: p. 126-131.

30. Rajendran, S., Sivakumar, P., and Babu, R.S., *Investigation on poly (vinylidene fluoride) based gel polymer electrolytes.* Bulletin of Materials Science, 2006. **29**(7): p. 673-678.

31. Mhalgi, M.V., Khakhar, D.V., and Misra, A., *Stretching Induced Phase Transformations in Melt Extruded Poly(vinylidene fluoride) Cast Films: Effect of Cast Roll Temperature and Speed.* Polymer Engineering and Science, 2007. **47**(12): p. 1992-2004.

32. Gregorio, R.J., *Determination of the α, β, and γ Crystalline Phases of Poly(vinylidene fluoride) Films Prepared at Different Conditions.* Journal of Applied Polymer Science, 2006. **100**: p. 3272-3279.

33. Goettler, L.A., Lee, K.Y., and Thakkar, H., *Layered Silicate Reinforced Polymer Nanocomposites: Development and Applications.* Polymer Reviews, 2007. **47**(2): p. 291-317.

34. Hooper, J.B., et al., *Structure, surface excess and effective interactions in polymer nanocomposite melts and concentrated solutions.* Journal of Chemical Physics, 2004. **121**(14): p. 6986-6997.

35. Sun, L., et al., *Preparation of Exfoliated Epoxy/α-Zirconium Phosphate Nanocomposites Containing High Aspect Ratio Nanoplatelets.* Chemistry of Materials, 2007. **19**(7): p. 1749-1754.

36. Casciola, M., et al., *Gels of zirconium phosphate in organic solvents and their use for the preparation of polymeric nanocomposites.* Journal of Materials Chemistry, 2005. **15**: p. 4262-4267.

37. Eley, D.D., Pines, H., and Weisz, P.B., eds. *Advances in Catalysis*. Vol. 37. 1990, Academic Press, Inc.: San Diego. 329.

38. Fraenkel, D., *Acid Strength of Sulfated Zirconia Inferred from Catalytic Isobutane Conversion.* Chemistry Letters, 1999. **28**(9): p. 917-918.

39. Paciaroni, A., et al., *Dynamics of water confined in fuel cell Nafion membranes containing zirconium phosphate nanofiller.* Journal of Physics: Condensed Matter, 2006. **18**: p. S2029-S2038.

40. Zerda, A.S., Caskey, T.C., and Lesser, A.J., *Highly Concentrated, Intercalated Silicate Nanocomposites: Synthesis and Characterization.* Macromolecules, 2003. **36**(5): p. 1603-1608.

Chapter 5
Conclusions and Recommendations for Future Study

Candidate proton exchange membrane (PEM) materials from blends of poly(vinylidene fluoride) (PVDF) and sulfonated acrylic polyelectrolytes (PE), and nanocomposites of the same incorporating zirconium-based nanoparticles have been studied and characterized using high-throughput screening techniques. The use of such techniques in the study of novel materials for fuel cell applications proved as an advantageous and unique approach to assay material attributes such as ionic conductivity and mechanical properties. Following the success of high-throughput methodologies in numerous areas, where they have been effectively utilized for efficient and rapid property characterization, the endeavor of developing new PEM materials can greatly benefit from the ability of such techniques to streamline the screening process, and create a suitable framework to address the large variable space involved. Particularly, high-throughput primary screening may enable the "discovery" of parameters where hypotheses can be tested optimally in secondary (low-throughput, high accuracy) experiments, allowing to understand the underlying mechanisms of material behavior and develop structure-property relationships. Given the complex nature and breadth of parameters comprised in multivariate systems and *de novo*

material syntheses, the parameter space simplification offered by high-throughput techniques is an important advance.

5.1 Conclusions

The main advances and findings in this work are summarized below, followed by detailed elaborations in the succeeding sections:

- Development of a novel automated high-throughput ionic conductivity measurement tool, and modification/improvement of a high-throughput device for screening mechanical properties.
- Rapid high-throughput screening of collections of numerous unique membranes of semi-interpenetrated networks of inert PVDF and covalently crosslinked proton-conducting sulfonated acrylic polyelectrolytes.
- Maximum effective (statistically significant) mass fraction of polyelectrolyte beneficial for proton conductivity has been identified in PVDF/PE membranes.
- Proton-conducting attributes of PVDF/PE membranes are not fully decoupled from the inert phase; namely, the crystalline characteristics of the PVDF support matrix have a significant effect on proton conductivity.
- Development and screening of novel "tri-phase" organic/organic/inorganic composite membranes consisting inorganic zirconium-based nanoparticles embedded in PVDF/acrylic polyelectrolyte blends.

- Hydrophilic zirconium nanoparticles improve the proton conductivity of membranes based on highly crystalline PVDF by providing a path through hydration layers that link less branched proton-conducting channels.
- Zirconium nanoparticles improve the elastic modulus of membranes based on PVDF:HFP copolymers, making them stiffer and less prone to deformation. However, toughness is reduced by the presence of the nanoparticles in both PVDF- and PVDF:HFP-based membranes.

5.1.1 High-throughput conductivity characterization system (HTC)

A novel automated high-throughput ionic conductivity measuring device has been developed in this work [1] (chapter 2). The device, based on AC electrochemical impedance spectroscopy (EIS), utilizes a miniature probe with four co-linear point-contact electrodes (four-point probe). The non-typical arrangement/geometry of the system to assay the ionic conductivity of thin polymeric membranes, required the development of a model based on assumptions of isotropic current distributions in the form of cylindrical iso-current density surfaces within the membrane, when the latter is excited by a an AC perturbation signal. Due to the reduced level of the perturbation signals necessary in EIS measurements (mV and μA range) in order to obtain a linear response, a custom sine-correlation signal filtering approach was implemented in the HTC system to filter noise, and decouple DC offsets and high order harmonics from the fundamental response signal. In addition, a localized high-precision thickness

measurement system was integrated to the HTC to further improve the accuracy of the conductivity readings.

The HTC was proposed as an alternative to standard conductivity cells and was demonstrated to offer significant reductions in sample size and speed with no accuracy penalty. For instance, validation conductivity measurements of small Nafion® 112 standards were only within 1.8% of the value reported by the manufacturer under identical testing conditions (84.5 ± 0.54 mS/cm average vs. 83 mS/cm, at 1000 Hz in 18.2 MΩ water at 25°C). Further conductivity screening of approximately 80 dissimilar PVDF/PE blends [1, 2] (chapters 2 and 3) demonstrated the suitability of the HTC system for high-throughput ionic conductivity studies. It is important to notice, however, that owing to the actual I-V current measurement setup juxtaposed with the small amplitude of the perturbation signals, the HTC signal analysis algorithm can only readily resolve the fundamental response signal for frequencies above 500 Hz. For excitation frequencies below 500 Hz the conductivity readings of the HTC should not be relied upon, unless an I-V autobalancing bridge is used to estimate the current of excitation signal (see section 5.2.2).

While initially intended for the characterization of combinatorial libraries of ionic-conducting materials (found to be unsuitable for the study of polyelectrolytes. See appendix A), the HTC proved to be extremely useful to screen uniform samples; particularly to evaluate homogeneity in terms of ionic conductivity (see section 2.3.1). The usefulness of the HTC system goes beyond this investigation and can easily be implemented in other studies where rapid screening of ionic conductivity is required.

5.1.2 Poly(vinylidene fluoride) and acrylic polyelectrolyte blends

Candidate materials for proton exchange membranes were fabricated from blends of multiple PVDF grades and two sulfonated acrylic polyelectrolytes of dissimilar equivalent weight. The property characterization of these blends (80x) was not trivial owing to the inherent large amount of possible combinations between the components. To facilitate this task high-throughput screening techniques coupled with appropriate statistical analysis were utilized [1, 2] (chapters 2 and 3).

Besides enabling the ability to use engineering thermoplastics and/or commercially available polymers, one of rationales behind developing materials for PEMs from blends of inert and proton-conducting components is to decouple mechanical and proton conductivity properties so that they can be individually optimized. However, statistical analysis of the conductivity data spaces generated from the HTC screening of PVDF/PE blends revealed that, contrary to what was initially thought, conductivity was not completely decoupled from the properties of the PVDF grade used as the inert support matrix in the membranes. What is more, a partial eta squared statistic (η_p^2) of 0.293 indicated that the practical significance of the effect of PVDF grade on the PVDF/PE membranes proton conductivity was considerable (PVDF grade by itself accounted for about 30% of the overall conductivity variance).

Unweighted conductivity means from a GLM analysis of conductivity data revealed that conductivity was favored in membranes containing PVDF:HFP copolymers over those containing PVDF homopolymers. A univocal correspondence was found between this statistical result and the crystalline properties of the different

PVDF grades; namely, PVDF:HFP copolymers (present in the membranes with the highest conductivities) exhibited the lowest crystallinity and smallest crystallite size (compared to PVDF homopolymers). A synergistic effect on proton conductivity was also noticed between the aforementioned PVDF crystalline characteristics and melt viscosity, as higher melt viscosity resulted in lower conductivity. Specifically, the maximum overall conductivity was attained by membranes containing Kynar® 2821 PVDF:HFP copolymer (X_C = 24.8%, D = 152.4 Å, η_M = 8.6 kP), whereas the lowest by those based on Kynar® 731 PVDF homopolymer (X_C = 69.1%, D = 200.2 Å, η_M = 16.9 kP). A model suggesting precluded segmental motion of the PE chains due to high melt viscosity and the formation of dense PVDF areas generated by molten crystallites, which results in reduced crosslinking and branching of the proton conducting channels, was proposed to explain the lower conductivity of PVDF homopolymer-based membranes.

Additional statistical analysis of simple effects of PE content on conductivity revealed that a maximum effective amount of PE exists in the range of 55-60wt% (neutralized form PE). This effect is directly attributed to the formation of droplet-like PE clusters (microphase separation) at high PE mass fractions. This is in turn associated with the PE neutralization degree necessary for the compatibilization of the PVDF and PE phases. Consequently, increasing the PE content above 55-60wt% is not expected to produce statistically significant improvements in proton conductivity; in fact, the effect could be detrimental due to increased clustering. If the PE neutralization degree is to be further reduced from the actual value used in this study (0.95), coalescence of PE domains is expected to occur at even lower PE mass fractions.

Mechanical properties of PVDF/PE membranes were directly associated with those of the PVDF grade incorporated in the membrane, as well as the PE mass fraction. No strong influence of PE type was evident ($0.03 \leq \eta_p^2 \leq 0.11$). A remarkable exponential-decay fit was found for multiple mechanical properties (i.e., elastic modulus, tensile strength, and toughness) as a function of PE mass fraction. Although not completely understood, this model could provide some insights on the phase behavior of PVDF/PE blends with the aid of additional studies (e.g., blends with different PE mass fraction ranges and blends with PEs of multiple neutralization degrees).

PVDF/PE membranes exhibit acceptable conductivity and mechanical properties and compare favorably to standard perfluorosulfonic acid-based PEMs; however, characterization of additional properties (e.g., durability, selectivity, etc) is necessary to ascertain their suitability as proton exchange membranes (see section 5.2.1.2).

5.1.3 Zirconium-based nanocomposites

Organic/organic/inorganic tri-phase nanocomposite membranes were prepared from poly(vinylidene fluoride), a sulfonated acrylic polyelectrolyte, and various types of zirconium-based nanoparticles; namely, zirconium(IV) oxide (ZrO_2), zirconium(IV) hydroxide sulfated ($Zr(H_2SO_4)_4$), and zirconium(IV) hydrogenphosphate ($Zr(HPO_4)_2$). Approximately 50 nanocomposite membrane types were fabricated and characterized [3] (chapter 4).

The incorporation of zirconium nanoparticles to PVDF/PE blends creates a tri-phase system not common in standard approaches for the development of composite

materials for PEMs (see section 1.3.4.2). The main advantage arising from such tri-phase systems is the ability to have the benefits inherent from blending inert/ionic conducting polymers (partial decoupling of proton conductivity and mechanical properties), while providing an internal scaffold responsible for improved tensile properties, as well as stabilization and enhancement of the ionic cluster volume for increased conductivity. This effect in conductivity was particularly noteworthy in membranes containing PVDF homopolymers (Kynar® 500 and 731) at low to medium nanoparticle mass fractions, as a presumable "healing" effect resulted from ion-conducting paths formed by the hydration layers of the nanoparticles across dense PVDF areas. These paths provide a linkage between non-crosslinked PE channels, resulting in an increased "effective branching"; and thus, enhanced conductivity. Improved conductivity of PVDF homopolymer-based composite membranes reached levels comparable to those of PVDF:HFP copolymer-based membranes. On the other hand, the effect of additional proton conducting paths and/or acid sites was not statistically significant in PVDF:HFP copolymer-based membranes (or even slightly detrimental in some cases), owing to a highly branched network of proton-conducting channels where additional interconnection (or effective branching) does not result in significant increments of conductivity.

Concerning the mechanical properties of the composite membranes, the inclusion of nanoparticles into the PVDF/PE matrix resulted in an improvement of tensile properties characterized by a reinforcing stiffening effect, particularly manifest in PVDF:HFP copolymer-based membranes, at low to medium nanoparticle loadings. In

contrast, a general decline in toughness was evident for all membranes. This is thought to be occasioned by the aforementioned stiffening effect and/or the formation of small membrane defects derived from particle agglomerates.

Nanoparticle dispersion was thermodynamically limited by unfavorable particle-polymer interactions. This resulted in severe aggregation of the solid-phase at high particle loadings. Consequently, proton conductivity declined due to increased diffusional resistance resulting from large agglomerates of nanoparticles. Similarly, akin to proton conductivity, all mechanical properties exhibited a noticeable diminution at high particle loadings as a result of membrane defects arising from particle clusters.

5.2 Recommendations for future study

5.2.1 PVDF/PE membranes: preparation and characterization

There are several factors to consider in order to give continuity to the present work and elicit new studies.

5.2.1.1 Membrane preparation

High crystallinity and relatively big crystallite size typical of PVDF homopolymers are detrimental for proton conductivity in PVDF/PE blends. On the other hand, several PVDF homopolymers exhibit some appealing mechanical properties such as high elastic modulus and high tensile strength. However, the tradeoff of proton conductivity arising from the use of PVDF homopolymers is not completely justified by the enhanced

mechanical properties. Thermal pretreatment of the PVDF prior to blending with the polyelectrolyte would be a plausible approach to circumvent this issue and allow the use of high elastic modulus PVDF homopolymers without having an adverse effect on conductivity. Specifically, the PVDF could be heated above its melting temperature followed by ultra-fast quenching to preclude the growth of crystallites. Although heat-induce re-crystallization of this "glassy" PVDF is a possibility during the PVDF/PE membrane manufacturing (curing process), it is unlikely to happen due to the very fast heating to temperatures above the PVDF melting point.

A 1,6-hexamethylene diisocyanate-derived triisocyanate crosslinker is used to create the branched network of proton-conducting channels. It would be worthwhile to evaluate different types of crosslinker (e.g., crosslinkers with shorter more rigid aliphatic chains, or longer more flexible chains, or incorporating rigid aromatic groups, etc.) and their effect of conductivity. The effect of the degree of crosslinking (NCO:OH ratio) should be considered as well.

As previously mentioned, post-sulfonation of existing polymers is one of the main approaches in the development of new PEM materials [4-6]. With this in mind, and considering the advantages of polymer blending for PEM material design, partial sulfonation of the inert PVDF phase in the PVDF/PE blends could be a reasonable new approach to combine the benefits of both worlds and further improve the conductivity of PVDF/PE membranes without sacrificing their mechanical integrity (clearly the maximum PVDF post-sulfonation that has no considerable impact on mechanical properties has to be determined).

Aggregation and precipitation of the inorganic phase was noticed in the fabrication of nanocomposites, owing to non-favorable solvent- and/or polymer-particle interactions. Other manufacturing techniques besides sonication-dispersion could be assayed to overcome this issue, including for example: *in situ* sol-gel manufacturing [7], surface modification of the nanoparticles for enhanced solvent-particle compatibility (e.g., organomodification with tetra-*n*-butylammonium hydroxide [8, 9]), or pre-exfoliated nanoparticles in gels or solvent-substituted gels, which is especially advantageous when casting from polymer solutions or blends is the only way to obtain a free-standing polymeric film [10]. Another advisable approach would be to modify the nanoparticle surface with crosslinkable groups, so that the particle becomes a constitutive part of the actual proton-conducting network. An anticipated advantage of covalently connecting the polyelectrolyte chains to the nanoparticles could be anchorage of the proton-conducting network to the inert PVDF phase, which could result in enhanced stability and degradation resistance due to reduced loss of active ionic domains in oxidative environments.

5.2.1.2 Membrane characterization

Additional characterization of the PVDF/PE membranes is necessary to better understand their underlying structure-property relationships, as well as to establish the suitability of these membranes for actual fuel cell applications. Such characterizations include:

- Study of the structure of hydrophilic domains of proton conducting channels and their correlation with the membrane overall conductivity. This can be carried out using transmission electron microscopy (TEM), or atomic force microscopy (AFM). For instance, the latter has been previously used to characterize the hydrophilic domains in Nafion and other PFSA-based membranes [11].
- Assessment of microstructure effects on conductivity and mechanical properties via variations in the compatibilization degree of the PE and PVDF phases (PE neutralization level).
- Perform swelling studies to estimate the dimensional changes of the membranes when hydrated (critical for usability in a fuel cell stack).
- One of the main advantages of nanocomposite PEMs, besides mechanical enhancement, is their usability at lower hydration conditions than those required by pure polymer electrolytes. Therefore, a study of the performance of PVDF/PE/Zr-X nanocomposites at high temperatures and partial drying conditions would be an important addition to the high-throughput mechanical and low temperature proton conductivity characterization presented in this work.

5.2.1.3 Next steps: feasibility evaluation

There are numerous additional factors that dictate the applicability of a particular PEM material in PEMFCs. For example, materials exhibiting excellent conductivity

performance have been shown to have poor adhesion to the electrodes in the MEA [12], generating unfavorable high frequency resistance and decreased cell life span due to delamination of the MEA. For this reason the next steps towards a complete assessment of the suitability of the PVDF/PE membranes and zirconium-based nanocomposites include electrode compatibility studies, MEA fabrication and testing, and *in-situ* fuel cell stack evaluation.

5.2.2 High-throughput conductivity characterization system (HTC)

The conductivity of a material determined using a co-linear four-point probe arrangement is generally given by:

$$\sigma\big|_{Z''\to 0} = \frac{1}{Z_{(jw)}} \cdot G(h, x_i) \qquad 5.1$$

where $G(h,x_i)$ is a proportionality constant that depends on the geometry of the measurement. In the case of the HTC system this proportionality constant is given by the assumption of cylindrical iso-current density surfaces (see section 2.2.1.1):

$$G(h, x_i) = -\frac{1}{2\pi h}\left[\ln\left(\frac{x_1}{x_2 + x_3}\right) - \ln\left(\frac{x_1 + x_2}{x_3}\right)\right] \qquad 5.2$$

In reality the current injected at a point source propagates spherically within the sample (i.e., spherical iso-current density surfaces). The basis of assuming cylindrical iso-current density surfaces in the development of the aforementioned working model

for the HTC is the fact that in very thin membranes, compared to the inter-electrode spacing, the curvature of the spherical surfaces is negligible, thus approximating a cylindrical shape within the thickness of the membrane. HTC conductivity measurements were in excellent agreement with accepted values of validation standards; however, as new ionic conducting materials are developed thickness can become an issue (e.g., thicker membranes designed specifically for direct methanol fuel cells, or membranes exhibiting considerable swelling), resulting in noticeable discrepancies between the actual and the measured conductivity and limiting the applicability of the HTC as a general conductivity measuring tool.

A solution to this issue is the use of thickness-dependent correction factors based on the theoretical solution of the equivalent electric field. Using this approach the model given by Equations 5.1 and 5.2 is replaced by the following general expression (for equally spaced electrodes, $x_i = x_{i+1} = x$):

$$\sigma\big|_{Z'\to 0} = \frac{1}{Z_{(jw)}} \frac{1}{2\pi x} \cdot f(\tau) \qquad 5.3$$

where τ is the ratio of the membrane thickness to the inter-electrode spacing (h / x), and $f(\tau)$ is a thickness correction factor given by [13]:

$$f(\tau) = 1 + \frac{4}{\tau} \sum_{n=1}^{\infty} \left[\frac{1}{\sqrt{\left(\tau^{-2} + 4n^2\right)}} - \frac{1}{\sqrt{\left(4\tau^{-2} + 4n^2\right)}} \right] \qquad 5.4$$

In the limit of very thin membranes compared to the inter-electrode distance ($\tau \to 0$) $f(\tau)$ approaches:

$$f(\tau)\Big|_{\tau\to 0} = \frac{2x}{h}\ln(2) \qquad 5.5$$

which yields the same identical result as the HTC model given by Equations 5.1 and 5.2 for the case of identical inter-electrode spacing ($x_i = x_{i+1} = x$). Although implementing the thickness correction factor given in Equation 5.4 can overcome inaccuracies arising from the HTC model assumptions and lead to more truthful conductivity measurements for a wider variety of samples, it might not be a practical alternative for causal real-time measurements (computational inefficient) as the series converges slowly for small values of τ.

A different approach more suitable for numerical computation to estimate the thickness correction factor $f(\tau)$ has been proposed by Weller [14] based on mathematical manipulations of the exact solution of the equivalent electric field model for the co-linear four-point probe:

$$f(\tau) \cong f_{(n,m)}(\tau) \equiv 1 + \frac{3}{2}\cdot\left(\sum_{n'=1}^{n} a_{n'} + \int_{n+1}^{\infty} a_{n'}dn' - \sum_{q=1}^{m}\left(\frac{B_q}{q!}\right)\frac{\partial^{(q-1)}a_{n'}}{\partial n'^{(q-1)}}\bigg|_{n'=n+1}\right) \qquad 5.6$$

where $n \geq 0$, $m \geq 1$, $a_n = \left[\left(1+n^2\tau^2\right)\sqrt{1/4+n^2\tau^2} + \left(1/4+n^2\tau^2\right)\sqrt{1+n^2\tau^2}\right]^{-1}$, and B_q is the qth Bernoulli number. This correction becomes more exact as *m* increases; therefore the

tradeoff between measurement precision and computation time can be adjusted by varying the value of *m*. A way to evaluate the efficacy of the correction algorithm, and determine the appropriate length of the summation, could be to measure the conductivity of standards of known conductivity and various thicknesses (ranging from small to big values of τ) with and without the thickness correction factor and comparing the results with the known conductivity values.

Further considerations (particularly hardware modifications) to broaden the range of action of the HTC system include:

- Use of higher sampling rate DAQ systems capable of analog input/output frequencies suitable for typical AC EIS measurements frequencies (1Hz to 250 kHz), coupled with an I-V autobalancing bridge for robust current measurements in wide frequency ranges (20 Hz to 110 MHz [15]).
- Implementation of *in situ* heating systems to enable high temperature conductivity measurements; which are extremely important to compare the conductivity of membranes at conditions similar to the operational conditions of a PEMFC, and to determine the how conductivity scales with temperature in new PEM materials.
- Conversion of the probe mechanism to a multiplexed array of four-point probes in order to increase the throughput of the system and reduce experimental variance. As mentioned in section 2.2.1.2, the probe used in this study was a proof-of-concept and further refinement is possible now that the proposed

approach proved to be viable. Using a multiplexed array of even smaller miniature for-point probes could increase the density of points acquired in a single sample, and hence amplify the resolution of conductivity maps. It would as well eliminate the need of positioning stages. It is important to notice, however, that the abovementioned thickness correction factor for the conductivity model would imperative in case the inter-electrode distance in the array is further reduced from that of the actual system.

- As demonstrated in section 2.3.1, correct thickness measurement of the swollen membrane is critical to estimate its conductivity. Therefore, non-contact local thickness measurements (e.g., visible-near infrared interferometry) could further improve the accuracy of the HTC conductivity readings.

5.2.3 High-throughput mechanical characterization tool (HTMECH)

Modeling of the HTMECH deformation mechanics has been partially addressed in previous studies in our lab [16]; however, a definite model that can describe the behavior of dissimilar materials under biaxial axisymmetric deformation is not available yet. Even though a considerable advance was made by developing a new data analysis algorithm to extract the mechanical properties from the force vs. time profiles recorded during HTMECH screening, a model of the HTMECH deformation mechanics could allow for more accurate estimation of such properties. For instance, a deformation model could be used in conjunction with regression techniques or optimization approaches

such as sequential quadratic programming to estimate the mechanical properties of a material from the recorded force vs. time profiles.

Further considerations for the HTMECH system:

- The mechanical properties of polymers and other materials are generally affected to a considerable extent by environmental conditions such as humidity and temperature. Therefore, the ability to control of these conditions could be an important addition to the HTMECH system and significantly expand its usability. The use of a custom designed environmental chamber was evaluated for this purpose; however, although providing reasonable humidity control, the prototype enclosure built required to invert the arrangement of the sample retention mechanism and the force sensor, resulting in a reduced signal-to-noise ratio in the measured force profiles.
- Due to noise issues, especially noticeable in force profiles of brittle and/or very thin samples, the actual sample displacement axis (industrial level linear motor) could be replaced with a high precision linear motor (research grade) coupled with a dampening mechanism.
- Similarly as in conductivity measurements, mechanical properties depend directly on the sample thickness; however, in the actual HTMECH design thickness is measured and averaged before the sample is mounted on the retention mechanism (no localized thickness). Consequently, deviations in the estimated mechanical properties tend to increase in non-uniform samples. An in-place non-contact thickness measurement

technique similar to that proposed in the HTC section could provide a solution for this issue.

5.2.4 High throughput data manipulation and analysis

Information collected using the HTC and HTMECH systems (raw data), as well as generated data fields (derived attributes) corresponding to analyzed raw data (e.g., elastic modulus, toughness, etc.), are typically dispersed. This is particularly evident when screening numerous dissimilar samples where several factors are varied at once, as no straightforward correlation between such factors is evident. Unless strong and well defined correlation patterns are seen among the data sets, the right analysis tools are necessary to obtain useful information from the data. For instance, when analyzing the conductivity data of PVDF/PE the use of appropriate statistical tools allowed to isolate the effect of the PVDF type on conductivity, an effect not readily evident when simply "looking" at the data or using typical simultaneous graphical approaches. Furthermore, it was possible to successfully correlate this effect with some of the PVDF crystallinity and viscosity properties; however, only a few properties of the PVDF were assayed and it is not known if others could have been as significant as those found. For this reason, tools such as data manipulation, data reduction via descriptors, and data mining may be a necessary complement for the HTC and HTMECH, and high-throughput techniques in general.

Knowledge discovery in databases or data mining provides a unique approach to integrate scientific information and theory for materials discovery. These techniques

have been proved to be a valuable tool to deal with extremely large and disparate databases derived from combinatorial and high throughput studies [17-20]. The goal of data mining is the extraction of information and insight from massive databases by discovering new patterns or building predictive and/or descriptive models from a given dataset. In few words it helps to know what information is really important. Data manipulation and mining can be performed using techniques such as:

- Data classification (rule induction, classification and regression trees)
- Prediction via regression algorithms (partial least squares, support vector machine)
- Segmentation (two-step clustering, K-means clustering, Kohonen networks)
- Sequencing (rule induction)

In most materials science studies, variables or parameters that are likely to affect a set of properties are identified a priori. This is usually based on predefined selection metrics and performance criteria, theoretical considerations, and/or analysis based on prior experience. However, it is difficult to integrate information simultaneously from multivariate data, especially when phenomenological relationships cannot always be explained in advance. Hence, prior to data mining, the data space dimensionality can be reduced via descriptors (descriptors can, for instance, be physicochemical properties like crystallinity, and processing variables like annealing temperature). One basic approach to address data description is to use principal component analysis (PCA). This is a

common widespread technique for reducing the size of high-dimensional data spaces, such as those often arising from high-throughput experimentation, with minimal loss of information. What is more, when large numbers of descriptors are obtained, further simplification can be performed by scatter maps screening and/or linear combinations of the PCA original descriptor set.

5.3 References

1. Zapata, P., Basak, P., and Meredith, J.C., *High-Throughput Screening of Ionic Conductivity in Polymer Membranes.* Electrochimica Acta, 2009. **10.1016/j.electacta.2009.02.009**.

2. Zapata, P. and Meredith, J.C., *High Throughput Study of Novel PVDF/Acrylic Polyelectrolyte Semi-Interpenetrated Network Proton Exchange Membranes.* To be submitted for publication, 2009.

3. Zapata, P. and Meredith, J.C., *in preparation.*

4. Hickner, M.A., et al., *Alternative Polymer Systems for Proton Exchange Membranes (PEMs).* Chemical Reviews, 2004. **104**: p. 4587-4612.

5. Kerres, J.A., *Development of ionomer membranes for fuel cells.* Journal of Membrane Science, 2001. **185**: p. 3-27.

6. Meier-Haack, J., et al., *Membranes from sulfonated block copolymers for use in fuel cells (review).* Separation and Purification Technology, 2005. **41**: p. 207-220.

7. Kim, J.-D., Mori, T., and Honma, I., *Organic–Inorganic Hybrid Membranes for a PEMFC Operation at Intermediate Temperatures.* Journal of The Electrochemical Society, 2006. **153**(3): p. A508-A514.

8. Kuan, H.-C., et al., *Preparation of Exfoliated Zirconium Phosphate/Nafion Organic-Inorganic Hybrid Proton Exchange Membranes.* Electrochemical and Solid-State Letters, 2006. **9**(2): p. A76-A79.

9. Sun, L., et al., *Preparation of Exfoliated Epoxy/α-Zirconium Phosphate Nanocomposites Containing High Aspect Ratio Nanoplatelets.* Chemistry of Materials, 2007. **19**(7): p. 1749-1754.

10. Casciola, M., et al., *Gels of zirconium phosphate in organic solvents and their use for the preparation of polymeric nanocomposites.* Journal of Materials Chemistry, 2005. **15**: p. 4262-4267.

11. McLean, R.S., Doyle, M., and Sauer, B.B., *High-Resolution Imaging of Ionic Domains and Crystal Morphology in Ionomers Using AFM Techniques.* Macromolecules, 2000. **33**: p. 6541-6550.

12. Kerres, J., et al., *Synthesis and characterization of polyaryl blend membranes having different composition, different covalent and/or ionical cross-linking density, and their application to DMFC.* Desalination, 2002. **147**(1-3): p. 173-178.

13. Valdes, L.B., *Resistivity Measurements on Germanium for Transistors.* Proceedings of the IRE, 1954: p. 420-427.

14. Weller, R.A., *An algorithm for computing linear four-point probe thickness correction factors.* Review of Scientific Instruments, 2001. **72**(9): p. 3580-3586.

15. *Agilent Technologies Impedance Measurement Handbook (Agilent application note 5950-3000)*. 2006, Agilent. p. 126.

16. Sormana, J.-L., Chattopadhyay, S., and Meredith, J.C., *High-throughput mechanical characterization of free-standing polymer films.* Review of Scientific Instruments, 2005. **76**: p. 062214.

17. Kyrylyuk, A.V., Case, F.H., and Fraaije, J.G.E.M.H., *Property Prediction and Hybrid Modeling for Combinatorial Materials.* QSAR & Combinatorial Science, 2005. **24**(1): p. 131-137.

18. Ohrenberg, A., et al., *Application of Data Mining and Evolutionary Optimization in Catalyst Discovery and High-Throughput Experimentation – Techniques, Strategies, and Software.* QSAR & Combinatorial Science, 2005. **24**: p. 29-37.

19. Rajan, K., *Materials informatics.* Materials Today, 2005. **8**(10): p. 38-45.

20. Kyrylyuk, A.V., Case, F.H., and Fraaije, J.G.E.M.H., *Property Prediction and Hybrid Modeling for Combinatorial Materials.* QSAR & Combinatorial Science, 2005. **24**: p. 131-137.

Appendix A
Combinatorial Libraries

Combinatorial methods have become a valuable approach to accelerate the development and optimization of materials; including: biodegradable and/or biocompatible materials, catalysts, electrolytes, organic/inorganic composite materials, polymeric materials, pharmaceuticals, optical and magnetic materials, among others. For this reason the original objective of this work included the use of these methods in juxtaposition with high throughput techniques to accelerate the development, screening, and characterization of PVDF/PE proton exchange membranes.

Initial work involved the creation of combinatorial libraries of PVDF/PE with continuous linear composition gradients (variable PVDF:PE ratio along the length of the library). For this task a composition gradient film coating procedure previously developed [1] was utilized (Figure A.1). Although this method has been successfully utilized in the past to create continuous composition gradients of polymer blends, it was not suitable for the mixture of PVDF and acrylic polyelectrolytes due to multiple reasons. Particularly, the high viscosity of the polymer solutions precluded their proper mixing in the CSTR-like mixer in the initial stage of the library manufacturing process (stage (a) in Figure A.1). What is more, a large viscosity mismatch between the two

solutions resulted in flow instabilities during the coating stage (stage (c) in Figure A.1), which gave place to random non-parallel transitions along the gradient direction.

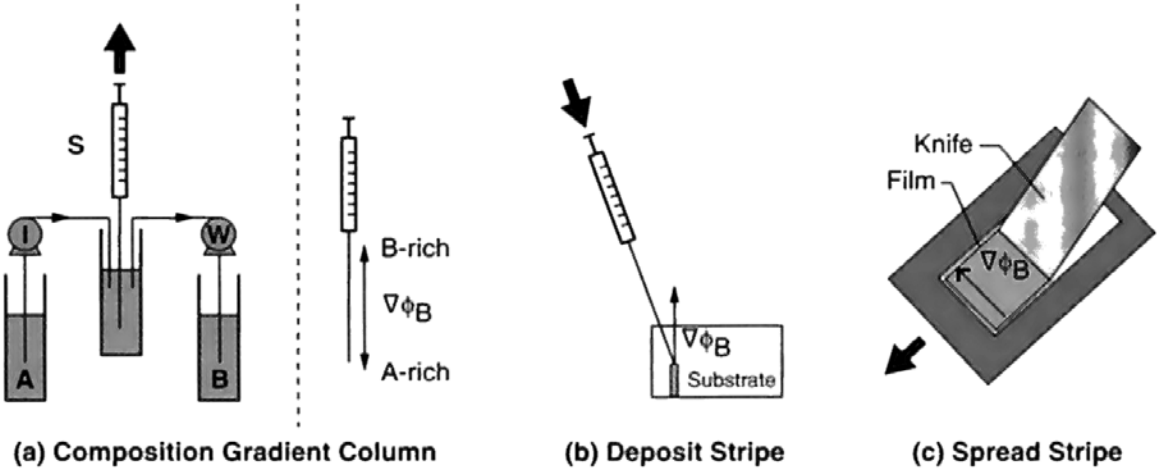

Figure A.1 Schematic of the composition gradient film coating procedure [1].

To overcome these issues a new microchannel direct gradient infusion technique was developed (Figure A.2). The approach is based on a microfluidic channel blade designed following a generalized Murray's law to determine the optimum ratios between the width of parent and daughter channels [2]. Briefly a branching parameter ($X = d_0^3 / 2d_1^3$) is defined based on the original Murray's law derived using the principle of minimum work. From this, by analogy to circular-cross section channels, a model is derived to estimate the optimum width of bifurcated channels with non-circular cross section (e.g., square or rectangular channels) in the microfluidic system (constant depth). The model is given by:

$$\alpha_n(1+\alpha_n)\mathrm{Po}(\alpha_n) = (2X)^n \alpha_0(1+\alpha_0)\mathrm{Po}(\alpha_0) \qquad \text{A.1}$$

$$\mathrm{Po}(\alpha_n) = 24\left[1 - \frac{192}{\pi^5 \alpha_n} \sum_{i=1,3,5\ldots}^{\infty} \frac{1}{i^5} \tanh\left(\frac{i\pi\alpha_n}{2}\right)\right]^{-1} \left(1 + \frac{1}{\alpha_n}\right)^{-2} \qquad \text{A.2}$$

where α_n is the aspect ratio (depth/width) of the nth bifurcation level, $\mathrm{Po}(\alpha_n)$ is the Poiseuille number, and X is the branching parameter.

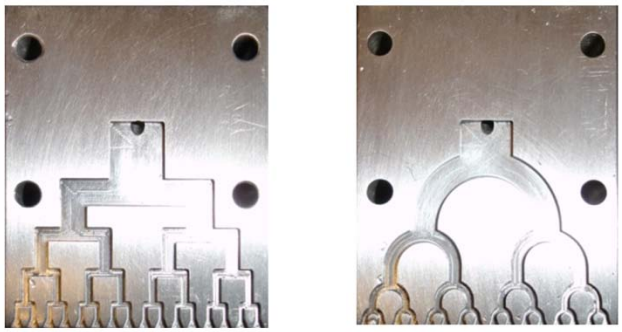

Figure A.2 Microchannel blades used in the direct gradient infusion technique to create continuous composition gradient libraries (the design is based on the generalized Murray's law [2]).

In the direct gradient infusion system (Figure A.3) the blade is held stationary above a moving stage and connected to a high-shear CSTR-like ultra-low volume chamber (the volume is reduced in order to minimize dead mixing zones and residence time). The chamber is fed by automatic controlled-rate pumps at rates that vary according a predefined mass balance model to follow a particular time-composition variation inside the mixing chamber (generally this variation was set as linear in order to

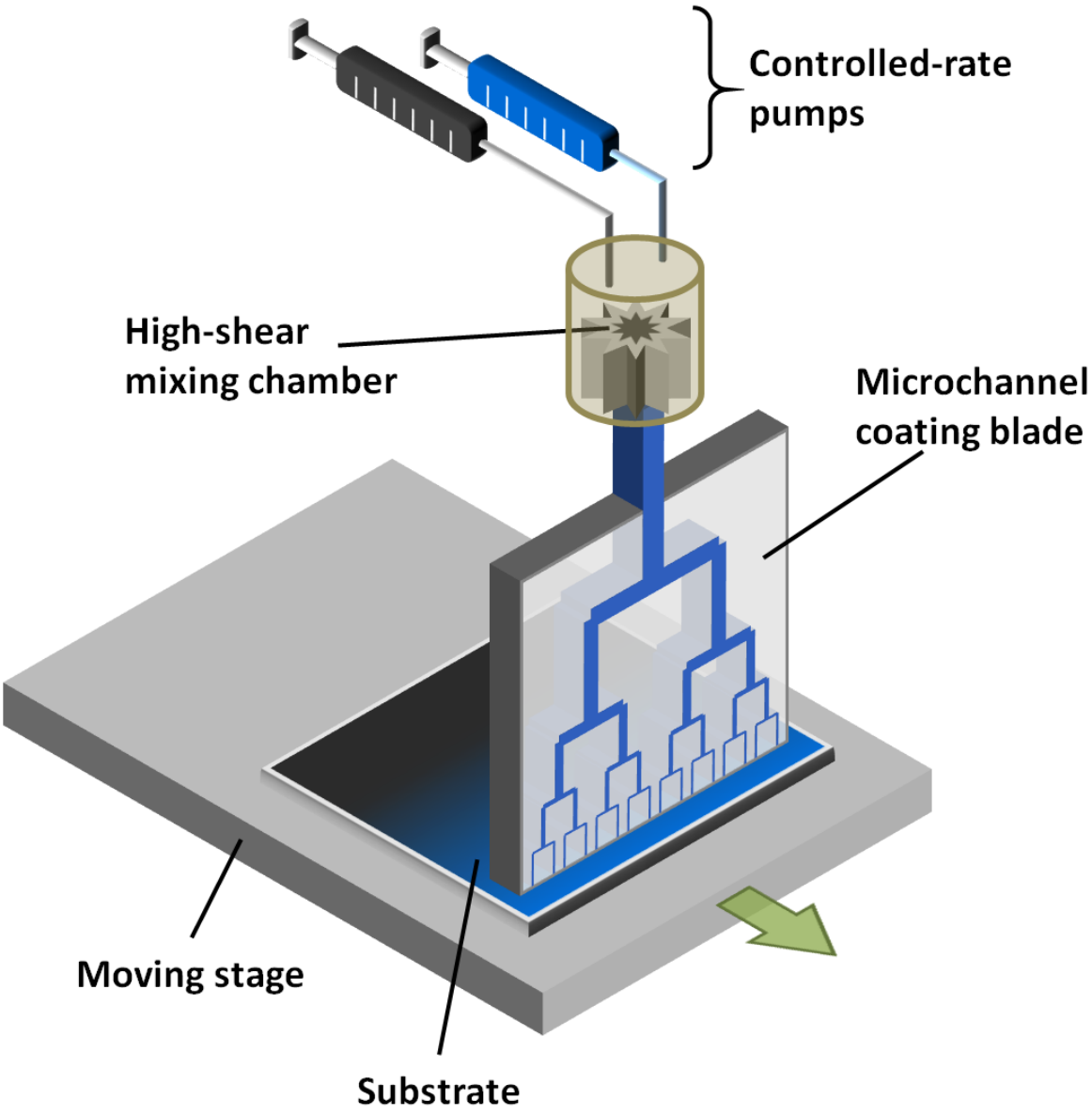

Figure A.3 Schematic of the direct gradient infusion system for the fabrication of composition gradient libraries.

produce linear gradient libraries). The mixed polymer solution is continuously fed into the microchannel network inside the blade, while simultaneously a substrate (e.g., glass or silicon) mounted over the positioning stage moves underneath the outlet ports of the blade.

The direct gradient infusion system was validated using multiple polymer blends at numerous viscosity ranges and ratios to create linear composition gradient libraries. A representative example, using a blend of poly(methyl methacrylate) (PMMA) and poly(ethylene oxide) (PEO), is shown in Figure A.4.

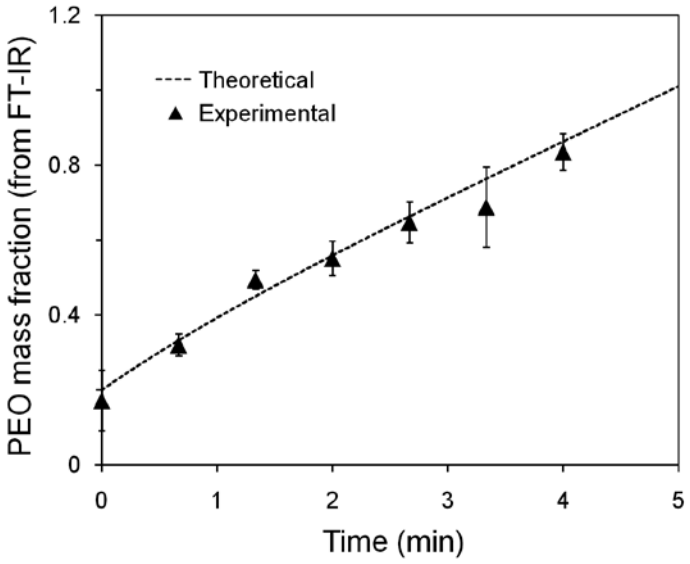

Figure A.4 Microchannel direct gradient infusion PMMA-PEO model system.

Following validation, prototype gradient libraries of PVDF/PE were manufactured to evaluate the applicability of the combinatorial approach for the study of mechanical properties and proton conductivity of these polymer blend system. One of the most

prevalent requirements for the proper operation of proton exchange membranes is humidification; that is, the membrane needs to be hydrated so that proton transport mechanisms can take place. A common "side effect" of membrane hydration is swelling (from water uptake), which is translated in dimensional changes in the membrane. The swelling degree, and hence the extent of dimensional change of the membrane, depends directly on the concentration of the hydrophilic sites responsible for proton conduction (generally acid groups such as sulfonic acid). In the PVDF/PE system the PE is the component containing the sulfonic acid groups responsible for proton conduction. The density of these groups in the PVDF/PE combinatorial libraries varies as the ratio of PVDF to PE changes from one end to the other in the library. This originated an unwanted asymmetric membrane deformation (Figure A.5) when in a hydrated state that precluded the use of composition gradient combinatorial libraries to evaluate proton conductivity and mechanical properties (both are measured in the hydrated state) of the PVDF/PE system. The main impediment arising from the asymmetric swelling of the PVDF/PE combinatorial libraries was the extreme difficulty to correlate a particular measurement with the underlying composition of the testing location. Due to the variable nature of the libraries experimental variance must be kept at a minimum in order to adequately correlate measurements with the variable used for the creation of the library. Therefore, any additional variance induced by trying to associate conductivity or mechanical property measurements with PVDF/PE ratios over the asymmetrically swollen membranes, would have resulted in masking of the true effect of the composition variable.

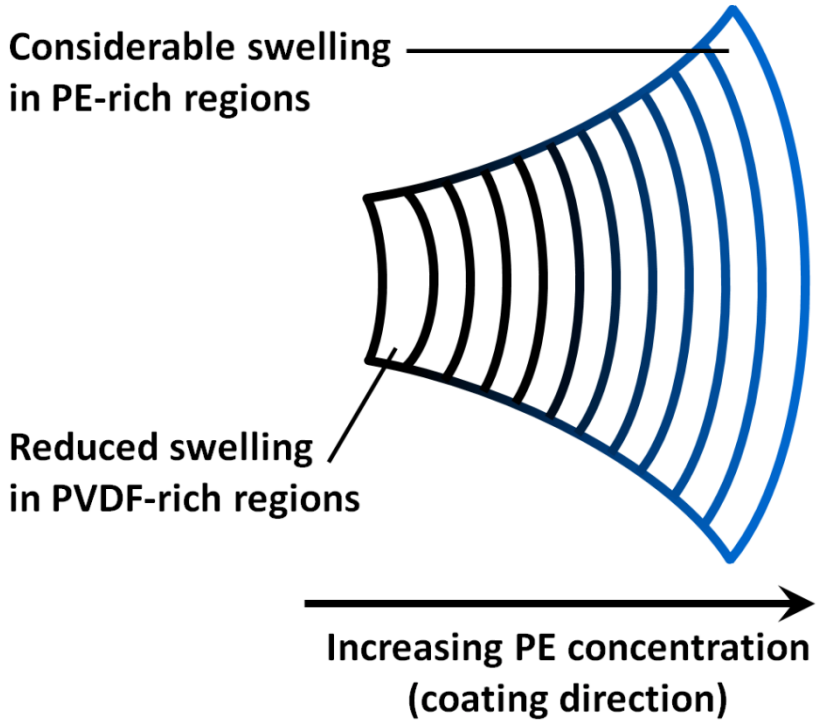

Figure A.5 Cartoon schematic depicting the asymmetric membrane deformation of PVDF/PE combinatorial membranes caused by uneven swelling degree due to variable PE content.

Despite the drawbacks encountered in the combinatorial study of polyelectrolytes, the direct gradient infusion technique constitutes a valuable tool for the study of other polymer blend systems that are not subject of dimensional variations.

A.1 References

1. Meredith, J.C., Karim, A., and Amis, E.J., *High-Throughput Measurement of Polymer Blend Phase Behavior.* Macromolecules, 2000. **33**: p. 5760-5762.

2. Emerson, D.R., et al., *Biomimetic design of microfluidic manifolds based on a generalised Murray's law.* Lab on a Chip, 2006. **6**: p. 447-454.

VITA

Pedro José Zapata Betancur was born on January 24, 1977 in Medellín, Colombia to Pedro José Zapata Villa and Luisa Betancur Alzate. He obtained his Bachelor's degree in Chemical Engineering from the Universidad Pontificia Bolivariana (Facultad de Ingeniería Química) in 1999. After graduating he worked at Colorquimica S.A. in his hometown of Medellín, Colombia, until fall of 2001, when he joined the School of Chemical & Biomolecular Engineering at the Georgia Institute of Technology to pursue graduate studies. He later obtained his Master's degree in Chemical & Biomolecular Engineering in 2004 under the guidance of Dr. J. Carson Meredith. His worked focused on high throughput and combinatorial study of cell response to polymer blend phase separation. Still under the guidance of Dr. J. Carson Meredith, he continued his graduate education at the Georgia Institute of Technology to pursue his Ph.D degree. He worked in the area of polymer electrolyte membranes for proton exchange membrane fuel cells. While pursuing his Ph.D degree he interned at Arkema Inc. during the summer and fall of 2006. He will work at Intel in Portland, Oregon, after graduating with a PhD in Chemical & Biomolecular Engineering in spring 2009.